HAL open science

Nonlinear features of instabilities, turbulence and transport in hot plasmas

Maxime Lesur

To cite this version:

Maxime Lesur. Nonlinear features of instabilities, turbulence and transport in hot plasmas. Plasma Physics [physics.plasm-ph]. Université de Lorraine, 2020. tel-02882428v2

HAL Id: tel-02882428

https://hal.science/tel-02882428v2

Submitted on 5 Jul 2020

HAL is a multi-disciplinary open access archive for the deposit and dissemination of scientific research documents, whether they are published or not. The documents may come from teaching and research institutions in France or abroad, or from public or private research centers.

L'archive ouverte pluridisciplinaire **HAL**, est destinée au dépôt et à la diffusion de documents scientifiques de niveau recherche, publiés ou non, émanant des établissements d'enseignement et de recherche français ou étrangers, des laboratoires publics ou privés.

Thèse d'Habilitation à Diriger des Recherches
de l'Université de Lorraine

Spécialité : Physique des Plasmas

Nonlinear features of instabilities, turbulence and transport in hot plasmas

par

Maxime Lesur

Soutenue le 25 mai 2020 devant un jury composé de

L. Vermare	Chargée de Recherche HDR, Laboratoire de Physique des Plasmas, Palaiseau	Rapportrice
P. Lauber	Privatdozent HDR, Max-Planck-Institut für Plasmaphysik, Garching bei München	Rapporteur
L. Villard	Professeur Ecole Polytechnique Fédérale de Lausanne, Lausanne	Rapporteur
X. Garbet	Directeur de Recherche, Commissariat à l'Energie Atomique, Cadarache	Examinateur
H. Wilson	Professeur, University of York, Heslington York	Examinateur
E. Gravier	Professeur, Université de Lorraine, Nancy	Examinateur

Acknowledgements

I am sincerely grateful to the three referees, Laure Velmare, Philipp Lauber, and Laurent Villard, who took the time to read this manuscript carefully and write detailed reports. I thank also the other members of the jury, Xavier Garbet, Etienne Gravier, and Howard Wilson. The jury provided insightful questions and comments, which will help me adjust the directions of future research.

During these 10 years of research since obtaining my PhD, I have been given constant freedom in pursuing the fundamental topics I was most interested in, but also many opportunities to connect them with recent experimental observations. I am extremely grateful for the trust and support of my mentors, in chronological order, doctor Yasuhiro Idomura, doctor Xavier Garbet, professor Patrick H. Diamond, the late professor Sanae-I. Itoh, professor Kimitaka Itoh, and professor Etienne Gravier, who also sponsored my HDR candidacy. I also thank the institutions, hierarchies and funding bodies of the Japan Atomic Energy Agency (JAEA) in Tokyo, the Institute for Magnetic Fusion Research (IRFM) in Cadarache, the World-Class-Institute (WCI) Center for Fusion Theory in Daejeon, the Research Institute for Applied Mechanics (RIAM - Kyushu U.) in Fukuoka, and the Institut Jean Lamour (IJL) in Nancy.

Parts of the work presented in this manuscript were performed by master and PhD students. Let me thank my two PhD students : Julien Médina and Kyungtak Lim ; the students whose M2 internship I supervised : Sebastian Hendricks, Djerroud Chabha, and Nicolas Berkenheier ; and the students whose M1 internship I supervised : Chen Xiang, Soni Kunal, Francis Devasagayam, Hanne Thienpondt, and Alejandro Guillevic.

I am also grateful to my co-authors, colleagues, and people I met in conferences or seminars, who contributed to the present work. Special thanks to the organizers and participants of the Festival de Théorie, where I learn so much every two years.

Warmest thoughts to my family, Ula, Neo, Tamaki, and my friends, for their unfaltering support.

The various parts of this work were supported throughout the years by the JAEA Foreign Researcher Inviting Program and the MEXT under Grant No. 22866086 ; by the European Communities under the contract of Association between EURATOM and CEA ; by the WCI Program of the NRF of Korea funded by the Ministry of Education, Science and Technology of Korea (WCI 2009-001) ; by CMTFO via U.S. DoE Grant No. DE-FG02-04ER54738 ; by the JSPS, Japan (16K18335, 16H02442, 15K18305, 15H02155, 21224014, 23244113, 25887041, and 15H02335), by the collaboration programs of the RIAM of Kyushu University and of NIFS (NIFS14KNST072, NIFS15KNST089) and Asada Science Foundation ; by the the EUROfusion Consortium via the French Research Federation for Magnetic Fusion Studies (FR-FCM) ; by the Euratom research and training programme 2014-2018 under Grant Agreement No. 633053 for the project WP17-ENRCEA-02 ; and by the Agence Nationale de la Recherche under project GRANUL (ANR-19-CE30-0005). The views and opinions expressed herein do not necessarily reflect those of the European Commission.

Computations were performed on Altix3700 and BX900 systems at JAEA ; on Norma system at CEA ; on the Kraken system at NFRI ; on the Plasma Simulator at NIFS ; on the XT and SX systems at Kyushu University ; on the HPC resources of IDRIS (ADA and Jean-Zay) under Allocation No. 2017-27862 made by GENCI ; on Asterix and EXPLOR systems at Lorraine University under Project No. 2017M4XXX0251 ; and on CINECA Marconi supercomputer within the framework of the GSNTIT and GSNTITS projects.

Abstract

Resonant interactions between waves and particles often play major roles in collisionless, or high-temperature plasmas. In this manuscript, I focus on a kinetic nonlinear effect, due to these resonances : the self-trapping of charged particles by their own electrostatic potential. This self-trapping leads to a formation of structures resembling vortices, in the phase-space of the particle distribution function (real space + velocity space). Based on the dynamics in phase-space, we clarify the mechanisms of phenomenon that can seem counter-intuitive from the point-of-view of an observer in real-space. This manuscript focuses on three types of waves : waves driven by supra-thermal particles in fusion plasmas, ion-acoustic waves in space plasmas, and drift-waves driven by trapped particles in tokamaks. I describe the impact of phase-space structures on stability and the nonlinear evolution of waves, as well as turbulence properties, particle transport, anomalous resistivity, and turbulent heating associated with these waves. I propose several experimental applications of phase-space structures as diagnostic and mean of control. Finally, I describe the outline of a long-term research project, which aims at developing a turbulence theory in a regime dominated by phase-space structures.

Résumé

Les plasmas chauds sont souvent le lieu d'importantes interactions résonantes entre ondes et particules. Dans ce manuscrit, je me focalise sur un effet cinétique non-linéaire, lié à ces résonances : l'auto-piégeage de particules chargées par leur propre potentiel électrique. Cet auto-piégeage conduit à la formation de structures semblables à des vortex, mais dans l'espace des phases de la fonction de distribution des particules (espace réel + espace des vitesses). En étudiant la dynamique des particules dans l'espace des phases, je propose de clarifier les mécanismes de phénomènes qui semblent contre-intuitifs du point de vue d'un observateur de l'espace réel. Je me concentre sur trois types d'ondes : les ondes engendrées par des particules supra-thermiques dans les plasmas de fusion, les ondes acoustiques ioniques dans les plasmas astrophysiques, et les ondes de dérives dues aux particules piégées dans les tokamaks. Je décrie l'impact des structures de l'espace des phases sur la stabilité et l'évolution non-linéaire des ondes, ainsi que sur les propriétés de la turbulence, le transport de particules, la résistivité anormale, et le chauffage turbulent associés à ces ondes. Je propose également quelques applications expérimentales des structures de l'espace des phases comme diagnostic et moyen de contrôle. Enfin, je décris les grandes lignes d'un projet de recherche sur le plus long terme qui vise à développer une théorie de la turbulence dans un régime dominé par les structures de l'espace des phases.

Table des matières

1 Introduction **1**
1.1 Hot plasmas . . . 1
1.1.1 Plasmas : ubiquitous, electromagnetic fluids . . . 1
1.1.2 Hot plasmas, and the Vlasov equation . . . 1
1.2 Turbulence . . . 2
1.2.1 Turbulence in hot plasmas . . . 2
1.2.2 Socio-economic impacts of a successful theory of hot plasma turbulence 3
1.2.3 Conventional turbulence theories . . . 3
1.3 Phase-space structures . . . 4
1.3.1 Phase-space holes . . . 4
1.3.2 Kubo number and granulation theory . . . 5
1.4 Magnetic confinement nuclear fusion . . . 5
1.4.1 Towards a clean, safe, and efficient energy source . . . 5
1.4.2 Energetic particles in MCF . . . 6
1.4.3 Turbulence in MCF . . . 6
1.5 Outline of this manuscript . . . 7

2 Vlasov plasmas **8**
2.1 Foundations of the Vlasov equation . . . 8
2.2 From linear to nonlinear theories . . . 9
2.2.1 Equilibrium . . . 9
2.2.2 Linear theory . . . 10
2.2.3 Nonlinear flux . . . 10
2.2.4 Quasi-linear theory . . . 11
2.2.5 Nonlinear theories . . . 13
2.3 Invariants . . . 15
2.3.1 Entropy . . . 15
2.3.2 Phasestrophy . . . 16
2.3.3 The Energy-Phasestrophy relation . . . 16

3 Subcritical instabilities **18**
3.1 Introduction . . . 18
3.2 Concepts of subcritical instability . . . 19
3.3 Subcritical instabilities in neutral fluids . . . 22
3.3.1 Experimental measurement of subcritical bifurcation . . . 23
3.3.2 Physical mechanism of subcritical growth in neutral fluids . . . 24
3.4 Subcritical instabilities in plasmas . . . 25
3.4.1 Fluid-like subcritical instabilities in plasmas . . . 26
3.4.2 Kinetic subcritical instabilities . . . 26
3.4.3 Hybrid Fluid-Kinetic subcritical instabilities . . . 30
3.5 Conclusions . . . 30

4 Energetic-particle-driven modes in 1D **31**
4.1 From 3D to 1D . . . 33
4.1.1 Reduction of the perturbed Hamiltonian . . . 33
4.1.2 Reduction of the collision operator . . . 34
4.1.3 Reduction of the background damping mechanisms . . . 35
4.1.4 Limitations . . . 35
4.2 The Berk-Breizman model . . . 37
4.2.1 Normalization . . . 37
4.2.2 Full-f BB model . . . 37
4.2.3 δf BB model . . . 39
4.2.4 The COBBLES code . . . 40
4.2.5 The PICKLES code . . . 41
4.3 Single mode . . . 43
4.3.1 Nonlinear analytic theory . . . 43
4.3.2 Subcritical instability . . . 48
4.3.3 Phenomenology . . . 51
4.3.4 Chirping lifetime . . . 58
4.3.5 Chirping period . . . 60
4.3.6 Analysis of experimental chirping modes . . . 66
4.4 Fluid coupling with another mode . . . 72
4.4.1 Introduction . . . 72
4.4.2 Expanding the Berk-Breizman model . . . 73
4.4.3 Fluid and kinetic nonlinearities . . . 75
4.4.4 Phenomenology . . . 76
4.4.5 Fluid limit . . . 79
4.4.6 Application to EGAMs on the LHD . . . 81
4.4.7 Summary . . . 85
4.5 Many modes . . . 87
4.5.1 Vlasov-Poisson limit . . . 87
4.5.2 Secondary bump-on-tail instability . . . 88

5 Ion-acoustic turbulence in 1D **91**
5.1 Model . . . 92
5.1.1 Model description . . . 92
5.1.2 Numerical simulations . . . 92
5.2 Energy-phasestrophy relation . . . 92
5.3 Subcritical CDIA turbulence . . . 93
5.3.1 Ensemble of waves . . . 94
5.3.2 Single seed PS structure . . . 97
5.3.3 Ensemble of many PS structures . . . 100
5.3.4 Partial summary . . . 104
5.3.5 Discussions . . . 104
5.4 Phase-space jets . . . 106
5.4.1 Small mass ratio . . . 106
5.4.2 Large mass ratio . . . 110
5.4.3 Large system size . . . 112
5.4.4 Driven system . . . 113
5.4.5 Conclusion . . . 116

6 Trapped-particle-driven 2D turbulence **117**
6.1 Model . . . 119
6.1.1 Bounce-averaged gyrokinetics . . . 119
6.1.2 The TERESA code . . . 120
6.1.3 Recent developments . . . 121
6.1.4 Caveats . . . 123
6.2 Linear instabilities . . . 124
6.2.1 Impact of electron dissipation . . . 124

6.2.2 Energy-space structure . . . 127
6.3 Single-mode saturation . . . 128
6.4 Turbulence and transport . . . 129
6.4.1 Impacts of electron dissipation . . . 129
6.4.2 Anatomy of transport in energy space . . . 130
6.4.3 Characterization by test particles . . . 135
6.4.4 Control of turbulent transport . . . 137
6.4.5 Impurity transport . . . 138

7 Conclusions and outlook **141**
7.1 Conclusions . . . 141
7.2 Outlook . . . 145
7.2.1 Phase-space turbulence, and granulation . . . 145
7.2.2 Other projects . . . 147

A Résumé en langue française (Summary in french) **148**
A.1 Thèmes de recherche . . . 148
A.1.1 Contexte . . . 148
A.1.2 Vue d'ensemble . . . 149
A.1.3 Vortex dans l'espace des phases . . . 149
A.1.4 Anatomie du transport turbulent . . . 152
A.2 Projet de recherche . . . 154
A.2.1 Résumé . . . 154
A.2.2 Objectif . . . 154
A.2.3 Approche numérique . . . 154
A.2.4 Approche expérimentale . . . 155
A.2.5 Impacts . . . 155
A.2.6 Autres activités . . . 155

Chapter 1

Introduction

This manuscript is a review of my main contributions to the research on instabilities, turbulence and transport in high-temperature and collisionless plasmas, and in particular on underlying nonlinear mechanisms. It is based on kinetic models, which take into account the statistics of particle dynamics in phase-space. My research mainly focuses on the context of magnetic confinement thermonuclear fusion, which is introduced in this chapter, but also finds applications in space plasmas and laser/plasma interactions.

Although this manuscript includes some unpublished work [1] it is in large part based on a selection of published peer-reviewed papers, which I authored or co-authored. I selected the papers which together form a coherent structure (albeit not as self-coherent as phase-space structures...). We emphasize both useful analogies and essential differences, and use self-consistent notations throughout.

Let me first introduce the context and basic concepts.

1.1 Hot plasmas

1.1.1 Plasmas: ubiquitous, electromagnetic fluids

Unlike neutral gases, plasmas are electromagnetic in nature. They are characterized by a significant degree of ionization, a process by which electrons "free" themselves from their atomic orbits. Therefore a plasma can be thought of as a collection of free, negative and positive charge-carrying particles (and a fraction of neutral particles, very small in the case of a hot plasma). Although quasi-neutral as a whole, a plasma responds to, and generates, an electromagnetic field, in a self-consistent way. Collective effects dominate plasma behaviour: the motion of a typical particle is governed by electromagnetic interactions with a very large number of distant particles, rather than by binary Coulomb interactions with neighbours. This can be opposed to the strong coupling between individual particles, which governs the behaviour of neutral fluids.

1.1.2 Hot plasmas, and the Vlasov equation

Temperature is a property of the energy distribution of particles. In a plasma, we consider the temperature of each species separately (e.g. electrons only, or hydrogen ions only). When the frequency of collisions is high enough, the particles of a species are smoothly distributed in energy, in a way very similar to neutral gas. A fluid-like description of the plasma, where the energy distribution of each species is replaced by a few of its moments (e.g. density, mean velocity and temperature), is then accurate. In hot plasmas, however, collisions are extremely rare. More precisely, the collisional mean-free-path (the average length it takes a particle to have its direction significantly changed by binary interactions with other particles) is much larger than the wavelengths of dominant electromagnetic waves. As

1. Unpublished parts can be found in particular: in chapter 2 on quasilinear and nonlinear analysis of the Vlasov equation, in subsection 4.3.4 on chirping lifetime, in subsection 4.3.6 on analysis of MAST data, in subsection 6.1.3 on recent developments of the TERESA code, and the projects I propose in chapter 7

a consequence, particles interact resonantly with waves, thereby introducing additional degrees of freedom in the energy distribution and leading to strong departures from a smooth, fluid-like, Gaussian velocity-distribution. Such mechanisms must be described by a kinetic model. In the collisionless limit, the plasma is adequately modeled by the Vlasov equation (along with Maxwell equations), which describes the time evolution of the particle distribution function, f, in a 6D phase-space (3 positions and 3 velocities). The gyrokinetic model is a variant of the Vlasov-Maxwell system in magnetized plasmas, where the fast cyclotron motion is averaged out, taking advantage of the presence of a strong magnetic field, which guides the particles on the lowest order. This leads to a 5D model, with a 4D phase-space parameterized by an invariant of the motion.

Vlasov plasmas are relevant in astrophysical, space, laser, and magnetic confinement plasmas. In interplanetary and interstellar media, the absolute temperature is high enough that the thermal kinetic energy is much larger than the potential energy of interaction between charged particles, owing to the low density. In the literature, the terminology can be: "hot", "weakly coupled", "Vlasov", or "collisionless" [2]. In magnetic confinement experiments, the temperature of the core is up to the order of 100 million degrees (for both ions and electrons), one order-of-magnitude higher than the Sun's core. Such plasmas are confined in a strongly inhomogeneous configuration (over a few meters, the temperature varies by 5 orders-of-magnitude) by strong magnetic fields. The collisional mean-free-path is measured in kilometers. Such plasmas are often far out of thermodynamical equilibrium. They feature rich and complex dynamics, both transitively and in asymptotic times (quasi-steady state). This is not limited to fluctuations. The mean fields of plasma (e.g. local means of density, temperature, magnetic fields) are highly dynamical as well.

1.2 Turbulence

1.2.1 Turbulence in hot plasmas

Laboratory experiments and satellite measurements have long demonstrated that most hot plasmas of interest are turbulent: they feature microscopic fluctuations on a broad range of scales, with energy flowing between scales. Resulting from these fluctuations, the particle motion is chaotic, with similarities to a random walk. In inhomogeneous plasmas, one expected impact is the diffusion of mean field gradients. Indeed, experiments demonstrate that microscopic turbulence has major macroscopic impacts on the mean fields, such as

— the transport of particles, momentum and heat (turbulent mixing), anomalous diffusion,
— the formation of mesoscale and macroscale structures (turbulent structure formation), such as zonal flows [3],
— the coupling between different directions of mean flows.

Hot plasma turbulence plays a key role in a broad range of contexts. The present work is more closely linked to:

— magnetic confinement fusion plasmas (in particular drift wave, and interchange turbulence)
— laser-plasma interactions (in particular Rayleigh-Taylor turbulence)
— the solar wind, which permeates the space between the Sun and the Earth.
— structure formation (stars, accretion disks around black holes) in the interstellar medium.

Turbulence theories attempt to model the statistics of microscopic fluctuations of the whole plasma and fields. The starting point is the whole plasma setup (the mean plasma fields and electromagnetic fields, the boundary conditions, and external sources and sinks of particles and energy). The goal is to predict the statistics of microscopic fluctuations, and their macroscopic impacts, including large-scale structure formation, and turbulent mixing.

2. For the title of this manuscript we choose the term "hot" by default, since other denominations are not fool-proof either

3. Zonal flows (like the flows visible on the surface of Jupiter) are of particular interest because they act like barriers, which locally suppress turbulent mixing

1.2.2 Socio-economic impacts of a successful theory of hot plasma turbulence

A distilled understanding of this physics is key in the future of clean energy generation, space weather, space travel, space plasma physics, and astrophysics. Let us describe a few examples, relevant to our long-term objectives.

— Controlling turbulence in the core of magnetic confinement plasmas would be a major step in enabling viable fusion reactors [OKWZ16]. The design of the largest fusion experiment (ITER) was based on the extrapolation of empirical laws, which were obtained by measurements in much smaller devices. A theory capable of predicting the macroscopic impacts of turbulence, would mitigate the risks of extrapolation, yield new means of control [KLP+97], expedite the design of future commercial reactors, and significantly reduce their cost. Indeed, the minimum size of a tokamak is determined by turbulent transport. We can make a very rough estimation in a simple limit where heat transport is described by a heat diffusion coefficient χ. Then the radius must be proportional to $\chi^{1/2}$, and the machine cost very roughly proportional to $\chi^{3/2}$. In this sense, a 10% reduction of turbulence is potentially worth billions of euros.

— Inertial confinement is an alternative approach to fusion, where a small solid target is impacted by an array of powerful lasers. The target turns into a plasma and implodes. A better understanding of turbulence is crucial to optimize the experimental setup and design the target.

— The design of electric propulsion thrusters, such as Hall effect thrusters, suffers from a lack of understanding of anomalous (turbulent) erosion of a key component. Predicting this macroscopic impact of plasma turbulence would expedite their design and lead to an increase in range of space missions [Che07].

— Understanding turbulence in the solar wind [BC13], coupled with solar flares [JAD15], is crucial in the emerging discipline of space weather. Space weather could provide early warnings of: 1. solar radiation storms, which have been shown to damage electronic equipment in satellites, and cause radio blackouts on EarthHF radio, GPS systems and power grid ; and 2. geomagnetic storms, which cause beautiful auroras, but temporarily degrade the accuracy of GPS systems, and can impact power grid operation, even far from the poles.

1.2.3 Conventional turbulence theories

In the early years, plasma turbulence theories were based on concepts of self-similarity by analogy with neutral fluid turbulence: cascades in wave-number space [Kol41b], coupled with mixing-length estimates in real space [Pra25]. Decades of progress showed that hot plasma turbulence theory had to depart from fluid turbulence theories, due to important kinetic effects. In particular, quasi-linear theory was developed to include resonant energy exchanges between waves and particles [DP61, VVS61]. Lowest-order nonlinear corrections were later included in weak-turbulence and strong-turbulence theories [Kad64]. In the following decades, sophisticated formalisms have been built, which furthered the understanding of nonlinearities and high-order statistics in plasma turbulence [YII02b, DII10, Kro15].

These theories are extremely valuable in specific cases, in particular to predict the self-organisation of macroscale flows (a challenge that brute-force numerical simulations are struggling with). However, in terms of fluctuation statistics, and macroscopic impacts in general, the agreement (even qualitative) with experimental observations is limited. Quasi-linear and alike theories cannot address essential aspects of turbulent mixing, such as abrupt events, non-local transport, and the impacts of electrostatic trapping, which are described in this manuscript.

In parallel, direct numerical simulations of the gyrokinetic equations have been applied to investigate the phenomenology of turbulent transport. However, agreement between simulation and experiment remains exceptional, local in space, and rely on arbitrary adjustments of input parameters as well. The origin(s) of these discrepancies is (are) unclear. In my research, I focus on an important caveat of conventional turbulence theories and modelling:

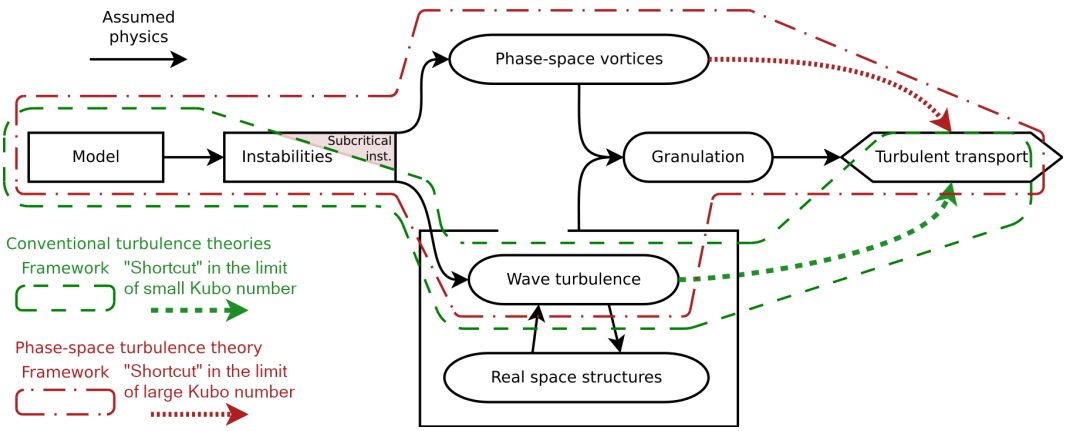

Figure 1.1 – Cartoon of the framework of phase-space turbulence and granulation. "Real space structures" include e.g. zonal flows. Conventional turbulence theories, which assume that plasmas respond to perturbations as an ensemble of random-phase waves (wave turbulence), take a questionable shortcut represented here by a dashed arrow.

they do not properly account for non-wave-like, microscopic structures in phase-space (PS), such as PS vortices [RB67]. Fig. 1.1 illustrates the limit of the framework of conventional turbulence theories.

Since the gyrokinetic model includes the full nonlinearity of wave-particle interactions, gyrokinetic simulations should in principle include microscopic PS structures. However that is only true in a limit of low numerical diffusion, and accurate discretization of the whole phase-space. In practice, this makes microscopic PS structures inaccessible to heavy gyrokinetic codes, given current computation capabilities. Analytic theories don't suffer from numerical diffusion, but to make calculations tractable, they assume that the plasma responds to perturbations as an ensemble of waves with random phases (except to describe nonlinearities in wave-number space - e.g. mode-mode coupling). This wipes out PS structures.

1.3 Phase-space structures

1.3.1 Phase-space holes

PS structures are well known in contexts other than micro-turbulence: e.g. the two-beam instability, the bump-on-tail instability, Weibel instabilities. We describe several kinds of PS structures throughout this manuscript. The most ubiquitous PS structure is a vortex-like island of negative phase-space density fluctuation, $\delta f < 0$, which is called a PS hole. PS holes result from the localized trapping of particles by their own electrostatic potential, which is a fundamental kinetic nonlinearity in the Vlasov equation. Fig. 1.2 illustrates this mechanism for an ion hole in a 1D plasma. A PS hole is akin to a Bernstein-Greene-Kruskal (BGK) mode [BGK57], however it is not locked to the resonant velocity. On the contrary, PS holes display rich dynamics. Interestingly, PS holes self-organize in a way strongly analogous to self-gravitating matter.

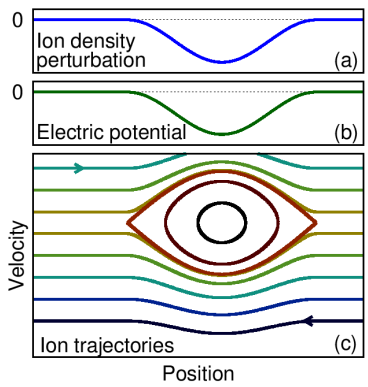

Figure 1.2 – Phase-space hole. (a) Ion density fluctuation. (b) Electrostatic potential. (c) Ion trajectories.

PS holes were predicted by simulation [RB67], interpreted by theory [Sch79, Dup82], and experimentally observed in a wide range of space and laboratory plasmas [ES06]: linear and toroidal plasma devices, magneto-

sphere, interplanetary space, and during magnetic reconnexion. In homogeneous plasmas, numerical simulations have shown that when a few PS holes of similar size are present, they can interact and merge [RB67]. Most simulations studied regimes with only a handful of PS holes. However, in 2014, I have shown that a large number of small PS holes have much stronger impacts than a small number of large PS holes [LDK14a]. Some simulations with a moderate number of PS holes were performed [GDSR09], but stochastic PS dynamics was only transient. Since PS holes tend to coalesce and merge, in decaying turbulence they are bound to eventually form one large vortex. More work is needed to describe the statistical steady-state of stirred (flux-driven) turbulence including PS holes in large systems.

In inhomogeneous plasma turbulence, where particles undergo a secular drift, the concept of PS hole was generalized as drift-holes [TDH90]. Analytic theory predicts the existence of drift-holes, over a broad range of conditions. The context here is that of drift-wave turbulence, including magnetic curvature, which can be generalized to interchange turbulence. As evidenced by recent work on the effect of shear flows [KD12], the interest for drift-holes has never faded. However, drift-holes were never observed in any simulation. I argue that the culprit is numerical dissipation, on which PS structures are very sensitive.

1.3.2 Kubo number and granulation theory

The Kubo number K is a dimensionless quantity, which characterizes the regime of transport. The Kubo number can be defined from the point-of-view of either real space or PS. In the context of PS dynamics in Vlasov turbulence, the Kubo number can be estimated as $K = \tau_{\mathrm{ac}}/\tau_{\mathrm{tr}}$. Here τ_{ac} is the autocorrelation time of the turbulent spectrum of electrostatic fluctuations, and τ_{tr} is the typical quasi-period of a PS orbit of particles trapped in a PS vortex.

Quasilinear theory assumes the $K \ll 1$ limit. Meanwhile, mixing-length theory corresponds to $K \sim 1$. The usual practice of combining both theories in order to calculate turbulent relaxation, is therefore questionable. Dupree pioneered an analytic turbulence theory called granulation theory [Dup72], to treat the $K \sim 1$ regime properly (by including non-wave-like fluctuations). He argued that PS structure formation competes against decorrelation by random-phases wave turbulence. In the statistical steady state, this yields granulated fluctuations: evolving clusters of particles, correlated by resonances. In a sense, Dupree's theory is a kinetic generalization, to collisionless plasmas, of the concept of eddies in fluids.

Building on Dupree's seminal work, analytic theories have predicted essential impacts of granulation: intermittency of turbulence [TDH90], flow coupling, jamitons, non-local transport, non-diffusive transport, and subcritical diffusion [KID+17]. These are hot issues of plasma turbulence. Time is ripe to perform a numerical investigation, before designing a way to discriminate from other candidate mechanisms in experimental data.

1.4 Magnetic confinement nuclear fusion

1.4.1 Towards a clean, safe, and efficient energy source

When asked by a journalist the question "Which scientific discovery or advance would you like to see in your lifetime?", Stephen Hawking gave the following answer, "I would like nuclear fusion to become a practical power source. It would provide an inexhaustible supply of energy, without pollution or global warming." [Haw10]. Indeed, the global energy crisis could be alleviated by a clean, safe and efficient energy source. A promising approach is to heat a plasma of hydrogen isotopes at 150 million degrees, and confine it in a donut-shaped magnetic field. After decades of exponential progress, this is routinely done in several magnetic fusion experiments (tokamaks and stellerators) around the world. Magnetic-confinement fusion (MCF) energy is:

— Clean. Although fusion is a nuclear process, it does not involve any high-activity nor long-lived nuclear waste. The burnt fuel is inert helium. Tritium, which is used in the reaction, is radioactive, but orders-of-magnitude less so (with its 12.3 years half-life) than uranium. High-energy neutrons will activate containing walls. However,

this waste is classified as low to medium activity waste (unlike nuclear fission). The deuterium and tritium derived from a bathtub of seawater and from the lithium in one laptop battery are enough to provide the energy needs of an average American adult, for life.

— Safe. Unlike nuclear fission, fusion is inherently safe. Since the fuel is a plasma of hydrogen isotopes in a quasi-void (average density: $10^{20}\mathrm{m}^{-3}$), the total mass inside a reactor is less than a gram. Any disturbance causes the plasma to immediately cool down, halting fusion reactions. The same reason, which makes fusion so safe, makes fusion so challenging. However, we should point out that, if the disturbance halting fusion reactions is a major disruption, this could severely damage the device. Currently, there are significant research efforts on early detection and mitigation of disruptions.

— Not efficient yet. No experiment has ever reached break-even (extracting more energy from fusion reactions than the energy required to sustain the plasma). After decades of progress, starting from less than a Watt in the 70's, a record of 16MW generated from 25MW of input power was obtained (in the tokamak JET in 1997). The largest magnetic fusion experiment, ITER, is being built in Cadarache, France. ITER aims at reaching break even for the first time in 2035, generating 500MW from an input of 50MW. Improving turbulence theories is useful not only for tokamaks, but also for all magnetic fusion devices. This includes stellerators, and new compact designs, which take advantage of breakthrough in superconducting coils [SBP+15].

1.4.2 Energetic particles in MCF

In an ignited toroidal MCF plasma operating with a deuterium-tritium mix, the confinement of α-particles is critical to prevent damages on the first-wall and to achieve break-even. The reason is that these high energy particles must be kept long enough in the plasma core to allow enough of their energy to heat thermal populations by slowing-down processes. Additionally, neutral beam injection is an important heating scheme, which provides another source of Energetic Particles (EPs). A major concern is that EPs can excite macroscopic plasma instabilities in the frequency range of Alfvén Eigenmodes (AEs) or geodesic acoustic modes (EGAM), which significantly enhance their transport, and couple with background turbulence. They impact fuelling and the wall integrity, and ultimately the efficiency of a fusion reactor.

Since the recognition of this issue in the 1970's, considerable progress has been made in the theoretical understanding of the principal EP-driven instabilities. However, robust predictions of stability and transport, as well as development of control schemes, require progress on our understanding of their nonlinear physics.

1.4.3 Turbulence in MCF

In MCF devices, the huge temperature gradient between the hot core and the cool edge makes the plasma inevitably turbulent. Turbulence drives the transport of particles and energy from the core to the edge, which degrades required confinement. Turbulence can be mitigated, or channelled. Some methods of control have been discovered empirically. A better theoretical understanding of turbulence would lead to new methods of control.

Numerical simulations of MCF turbulence is challenging, especially because of coupling between disparate scales, from electron cyclotron scale (~ 0.01mm) to device scale (~ 1m). In this context, a single direct numerical simulation (gyrokinetic simulation) is very costly. Simulating a small fraction of the whole plasma, with rough numerical discretization in the velocity space, can consume $\sim 10^8$ core.hours on a modern supercomputer [MIW+15].

In practice, modern gyrokinetic simulations can only afford a limited number of grid points in the velocity (or energy) space, typically ~ 10 to ~ 100. This introduces large numerical diffusion, which may spuriously wash away fine-scales PS structures. A handful of authors have attempted to investigate PS structures with brute-force gyrokinetic simulations, by increasing the number of energy grid points [WS06, TDS+09]. These showed promising results, reinforcing the importance of resolving fine-scale PS structures. However,

these were done at the expense of fine-scales in real space, and the one-shot nature of these extremely costly attempts would not allow the underlying physics to be uncovered. In this sense, investigating the impacts of fine scales in PS is not accessible to brute-force numerical simulations. Based on this reasoning, we propose in Chapter 7 a project to investigate PS structures in MCF numerically by focusing on low-frequency turbulence, which allows a reduction of dimensionality. With this approach, fine-scales in PS become accessible at reasonable computing cost.

1.5 Outline of this manuscript

In chapter 2, we review the foundations of the Vlasov equation for collisionless plasmas, and describe general linear, quasilinear and nonlinear theories. We discuss how invariants can provide important information about the nonlinear behavior. In particular, we introduce the energy-phasestrophy theorem, as a kinetic counterpart of the Charney-Drazin theorem of quasi-geostrophic fluids.

In chapter 3, we describe the fundamental aspects of subcritical instabilities in plasmas, based on systems of increasing complexity: from simple examples of a point-mass in a potential well or a box on a table; to turbulence and instabilities in neutral fluids; and finally to modern applications in magnetized toroidal fusion plasmas. We draw parallels between these systems.

In chapter 4, we describe our main contributions to the nonlinear theory of the Berk-Breizman model, and its application to energetic particle-driven modes in tokamaks and stellerators. We review the nonlinear theory in the case of a single mode, and extend it, in particular in regimes of subcritical instabilities and chirping. We obtain analytical expressions for the subcritical threshold and for the nonlinear growth-rate. We investigate chirping characteristics (velocity, lifetime, period), and apply it to interpret measurements of Alfvén modes. We clarify the mechanism of relaxation oscillations associated with chirping bursts. We develop a model combining kinetic and fluid descriptions to explore how one linearly unstable mode may transfer its energy to another, stable mode, triggering a subcritical instability. Finally, we show that the velocity slope at the boundaries of a BGK phase-space island formed by a primary instable mode can drive the secondary instability of neighboring modes, and develop the corresponding analytic theory.

In chapter 5, we investigate nonlinear properties of current-driven ion-acoustic turbulence in 1D electron-ion plasmas, and in particular the formation and dynamics of PS structures. We find that in subcritical conditions, velocity-space redistribution and anomalous resistivity are due to PS turbulence, which includes not only holes, but also phase-space jets (highly anisotropic structures, with an extent in velocity of the order of the electron thermal velocity).

In chapter 6, we focus on quasi-2D electrostatic turbulence driven by magnetically-trapped particles in the core of axi-symmetric tokamaks. We taken into account inhomogeneities of magnetic field and pressure profiles. We adopt a bounce-averaged gyrokinetic model, and investigate the impact of electron dissipation, and of energy-structures, on turbulent transport. Moreover, we analyze the statistics of test particle trajectories to clarify the nature of transport. Finally, we summarize our recent contributions to the control of zonal flow by heating, and the theory of trapped impurity transport.

Finally, in chapter 7, we summarize the main results developed in this manuscript, and propose a long-term research project to further our understanding of Vlasov turbulence.

Chapter 2

Vlasov plasmas

The kinetic theory of ideal gases assumes that the interactions among molecules are negligible except during collisions. In contrast, hot plasmas are dominated by Coulomb-type long-range interactions, and require another kinetic description.

Boltzmann developed his namesake equation in 1872 to describe the statistical behavior of an out-of-equilibrium thermodynamical system. Jeans applied what is now known as the collisionless Boltzmann equation or the Vlasov equation – depending on the community – to gravitational problems in the context of galactic dynamics [Jea15]. Later Vlasov proposed to apply the equation to systems of charged particles, coupling it with Maxwell equations through charges and currents, and highlighted the importance of long-range interactions: "a system of charged particles is, in essence, not a gas but a distinctive system coupled by long-range forces" [Vla38, Vla68]. Depending on the context, the Vlasov equation was coupled to various equations for self-consistency, yielding systems such as the Vlasov-Poisson, Vlasov-Maxwell, Vlasov-Newton, Vlasov-Einstein, and Vlasov-Yang-Mills systems. In this manuscript, we are mainly concerned with the Vlasov-Poisson system as analyzed by Landau [Lan46], although in this chapter we attempt to keep a formalism general enough to be applicable to the Vlasov-Maxwell system as well.

Formally, most hot plasmas of interest do not rigorously follow the Vlasov equation (that is, even notwithstanding the limitations due to the finite number of particles, and to higher-order correlation effects [Ich68]). They are subject to collisions, sources, sinks (including chemical, atomic and nuclear processes) and possibly external forcing. However, in many cases of interest, it is possible to consider regions of space and time-scales, well separated from those of these additional processes, where the Vlasov equation, or a collisionless Boltzmann equation, is a reasonable approximation or a convenient starting point.

2.1 Foundations of the Vlasov equation

A many-body system can be described by the microscopic distribution $\mathcal{N}(\mathbf{\Gamma}, t) = \sum \delta(\mathbf{\Gamma} - \mathbf{\Gamma}_{\boldsymbol{i}})$, where $\mathbf{\Gamma}_{\boldsymbol{i}}(t)$ is the location in phase-space of a particle i, and the sum is taken over all particles. To simplify the present discussion, we consider a single-species system of $N \gg 1$ particles, without external forces, and normalize the total phase-space volume, assumed constant, to 1. Substituting Newton equations of motion into the partial time derivative of $\mathcal{N}$ yields the Klimontovich-Dupree equation, which involves microscopic electromagnetic fields.

Since it is unfeasible to reproduce any many-body experiment at the microscopic level, it is much more efficient to take an ensemble point-of-view, where distributions and fields are smooth functions of phase-space. At any given time t, the statistical properties are determined by a N-body distribution function F_N in a phase-space of dimension $6N$. Integrating F_N over $6(N-1)$ dimensions yields the one-particle distribution function f_1, or f for concision, which describes the average number of particles within an infinitesimal 6D phase-space volume. This distribution function is also the normalized ensemble average of the microscopic distribution $\mathcal{N}$. Similarly, integrating F_N over $6(N-2)$ dimensions yields the two-body distribution function f_2, which is related to f_1 and an ensemble average of a

product of two microscopic distributions.

Then, in the absence of atomic and nuclear processes, the ensemble average of the Klimontovich-Dupree equation yields a kinetic equation,

$$\frac{\partial f_1}{\partial t} + \dot{\mathbf{\Gamma}} \cdot \frac{\partial f_1}{\partial \mathbf{\Gamma}} = \left.\frac{\mathrm{d} f_1}{\mathrm{d} t}\right|_{\mathrm{coll.}}, \tag{2.1}$$

where $\dot{\mathbf{\Gamma}}$ involves ensemble-averaged electromagnetic fields obtained from velocity moments of f_1 (via Maxwell equations).

In the following, we write f_1 simply as f. The l.h.s. of the kinetic equation, Eq. (2.1), is the Lagrangian derivative of f, in other words the variation of f following collisionless particle orbits. Eq. (2.1) is not a closed equation, because the collision term involves expressions of the form $\langle \mathcal{N}\mathcal{N} \rangle$. Under the Coulomb approximation, which forbids any retardation effect, and which is valid if the thermal velocity is much slower than the speed of light, we can reduce the latter term as a function of f_2. Similarly, the equation which gives the evolution of f_2 involves terms of the form $\langle \mathcal{N}\mathcal{N}\mathcal{N} \rangle$, and so on. Altogether, these equations form a chain called the Bogoliubov-Born-Green-Kirkwood-Yvon (BBGKY) hierarchy equations [Bog46, RR60], for which a closure is required. A collision operator is a statistical operator, which approximates the effects of particle interactions, and provides such closure.

The collision term vanishes in the absence of particle interactions, yielding the Vlasov equation, which is valid on a time-scale much shorter than a collisional time-scale. The result that, in the absence of collisions, f is conserved along particle orbits, can be seen as a direct consequence of Liouville's theorem, which states that the density in phase-space is constant along particle orbits.

2.2 From linear to nonlinear theories

We work in a general set of coordinates $\boldsymbol{q} = (q_1, q_2, \ldots q_n)$ in n dimensions, and its canonically conjugated set $\boldsymbol{p} = (p_1, p_2, \ldots p_n)$. The Vlasov equation can be written in Hamiltonian form,

$$\frac{\partial f}{\partial t} - [H,\, f]_{\boldsymbol{q},\boldsymbol{p}} = 0, \tag{2.2}$$

where the brackets are Poisson brackets,

$$[H,\, f]_{\boldsymbol{q},\boldsymbol{p}} = \frac{\partial H}{\partial \boldsymbol{q}} \cdot \frac{\partial f}{\partial \boldsymbol{p}} - \frac{\partial H}{\partial \boldsymbol{p}} \cdot \frac{\partial f}{\partial \boldsymbol{q}}. \tag{2.3}$$

2.2.1 Equilibrium

The equilibrium motion of a charged particle in a 1D plasma with periodic boundary conditions, or in a tokamak, is integrable [1], and (at least) quasi-periodic. Such n-dimensional systems can be described by a Hamiltonian $H_{\mathrm{eq}}(J_k)$ in a system of n action-angle couples $(\boldsymbol{\alpha},\, \boldsymbol{J})$, which are obtained from $(\boldsymbol{q},\, \boldsymbol{p})$ by a canonical transformation [Arn78]. Here, we note $H_{\mathrm{eq}}(J_k) = H_{\mathrm{eq}}(J_1, J_2, \ldots, J_n)$ for concision. We stress that H_{eq} is a function of all actions, but not necessarily of the vector $\boldsymbol{J}$. The Poisson brackets then take a simple form,

$$[H_{\mathrm{eq}},\, f_{\mathrm{eq}}]_{\boldsymbol{\alpha},\boldsymbol{J}} = -\boldsymbol{\omega}_{\mathbf{eq}} \cdot \frac{\partial f_{\mathrm{eq}}}{\partial \boldsymbol{\alpha}}, \tag{2.4}$$

where $\boldsymbol{\omega}_{\mathbf{eq}} = \partial H_{\mathrm{eq}} / \partial \boldsymbol{J}$ are constant frequencies. The Vlasov equation in the steady state is then consistent with any $f_{\mathrm{eq}}(J_k)$.

1. In a tokamak, the equilibrium motion is formally integrable because of the existence of 3 invariants, but in practice it is only approximately integrable because one of the invariants is expressed as a Taylor expansion in ρ_c/R.

2.2.2 Linear theory

Taking into account turbulent fluctuations of the electromagnetic fields, the motion is not integrable anymore. However, it is still convenient to use the action-angle couples obtained from the equilibrium motion. The main advantage is that the linear part of the Vlasov equation simplifies radically.

We write the Hamiltonian as $H = H_{\rm eq} + \delta H$, where $\delta H(\alpha_k, J_k)$ is the perturbation, and similarly $f = f_{\rm eq} + \delta f$ for the distribution function. The linearized Vlasov equation,

$$\frac{\partial \delta f}{\partial t} \; - \; [H_{\rm eq},\, \delta f]_{\boldsymbol{\alpha},\boldsymbol{J}} \; - \; [\delta H,\, f_{\rm eq}]_{\boldsymbol{\alpha},\boldsymbol{J}} \; = \; 0, \tag{2.5}$$

yields

$$\frac{\partial \delta f}{\partial t} \; + \; \boldsymbol{\omega_{\rm eq}} \cdot \frac{\partial \delta f}{\partial \boldsymbol{\alpha}} \; = \; \frac{\partial \delta H}{\partial \boldsymbol{\alpha}} \cdot \frac{\partial f_{\rm eq}}{\partial \boldsymbol{J}}. \tag{2.6}$$

Since the system is quasi-periodic, we can decompose the perturbation as a Fourier series in each α_k. To simplify the calculations in this section, we also apply the Fourier transform in time,

$$\delta H = \sum_{\boldsymbol{n},\omega} \hat{H}_{\boldsymbol{n},\omega} e^{\imath(\boldsymbol{n}\,\cdot\,\boldsymbol{\alpha} - \omega t)}, \tag{2.7}$$

and similarly for δf. We have to keep in mind that the Laplace transform should be used instead [Lan46]. To resolve this issue, we will make the usual ansatz of treating the frequency as complex, $\omega = \omega_r + \imath\gamma$ and applying the Landau prescription in the dispersion relation. The Fourier transform of Eq. (2.6) yields a simple expression for the linear response of the perturbed distribution function,

$$\hat{f}_{\boldsymbol{n},\omega} \; = \; -\frac{\boldsymbol{n}\cdot\partial_{\boldsymbol{J}} f_{\rm eq}}{\omega - \boldsymbol{n}\cdot\boldsymbol{\omega_{\rm eq}}} \hat{H}_{\boldsymbol{n},\omega}. \tag{2.8}$$

Therefore, in action-angle variables, resonances take a simple form,

$$\omega = \boldsymbol{n}\cdot\boldsymbol{\omega_{\rm eq}}. \tag{2.9}$$

The drawback is that Maxwell equations, which close the system, can take complicated forms in these variables. However, this is not a major hurdle in general. Formally, Maxwell equations provide a second relation between $\hat{H}_{\boldsymbol{n},\omega}$ and $\hat{f}_{\boldsymbol{n},\omega}$, which, combined with Eq. (2.8), yields a dispersion relation $\omega(\boldsymbol{n})$ for any given $f_{\rm eq}(J_k)$. Solving this dispersion relation yields the linear frequency ω_r and growth-rate γ.

2.2.3 Nonlinear flux

The Vlasov equation in angle-action variables,

$$\frac{\partial f}{\partial t} \; + \; \frac{\partial H}{\partial \boldsymbol{J}} \cdot \frac{\partial f}{\partial \boldsymbol{\alpha}} \; - \; \frac{\partial H}{\partial \boldsymbol{\alpha}} \cdot \frac{\partial f}{\partial \boldsymbol{J}} \; = \; 0, \tag{2.10}$$

can be put in a conservative form,

$$\frac{\partial f}{\partial t} \; + \; \frac{\partial}{\partial \boldsymbol{\alpha}} \cdot \left[\frac{\partial H}{\partial \boldsymbol{J}} f\right] \; - \; \frac{\partial}{\partial \boldsymbol{J}} \cdot \left[\frac{\partial H}{\partial \boldsymbol{\alpha}} f\right] \; = \; 0. \tag{2.11}$$

Averaging over all angles yields,

$$\frac{\partial \langle f \rangle}{\partial t} \; + \; \frac{\partial}{\partial \boldsymbol{J}} \cdot \boldsymbol{\Lambda} \; = \; 0. \tag{2.12}$$

where $\boldsymbol{\Lambda} = \left\langle \dot{\boldsymbol{J}}\, \delta f \right\rangle = \left\langle -\frac{\partial \delta H}{\partial \boldsymbol{\alpha}} \delta f \right\rangle$ is the flux of phase-space density in the directions of the actions.

2.2.4 Quasi-linear theory

Substituting the linear solution yields a first estimate of the flux,

$$\boldsymbol{\Lambda}^{\mathrm{L}} \;=\; -\sum_{\boldsymbol{n}} \imath \boldsymbol{n} \left|\hat{H}_{\boldsymbol{n},\omega}\right|^2 \frac{\boldsymbol{n}\cdot\partial_{\boldsymbol{J}} f_{\mathrm{eq}}}{\omega - \boldsymbol{n}\cdot\boldsymbol{\omega}_{\mathbf{eq}}}. \tag{2.13}$$

Although the latter expression involves the complex ω, using the symmetries between $\boldsymbol{n}$ and $-\boldsymbol{n}$ yields an expression involving real quantities only,

$$\boldsymbol{\Lambda}^{\mathrm{L}} \;=\; \sum_{\boldsymbol{n}} \boldsymbol{n} \left|\hat{H}_{\boldsymbol{n},\omega}\right|^2 \frac{\omega_r(\boldsymbol{n}) - \boldsymbol{n}\cdot\boldsymbol{\omega}_{\mathbf{eq}}}{\left[\omega_r(\boldsymbol{n}) - \boldsymbol{n}\cdot\boldsymbol{\omega}_{\mathbf{eq}}\right]^2 + \left[\gamma(\boldsymbol{n})\right]^2} \boldsymbol{n}\cdot\partial_{\boldsymbol{J}} f_{\mathrm{eq}}. \tag{2.14}$$

Note that the flux in the direction of any action J_j involves in principle gradients of the equilibrium distribution function in all directions.

The superscript ^{L} emphasizes the fact that no nonlinearity whatsoever is taken into account in this expression of the flux. Quasi-linear theory [RF61, VVS61, DP61, SG69] provides a way to take into account some of the nonlinear terms, and the evolution of mean profiles ($\langle f\rangle = f_{\mathrm{eq}} + \hat{f}_{\mathbf{0}}$) and mean fields ($\langle H\rangle = H_{\mathrm{eq}} + \hat{H}_{\mathbf{0}}$).

More precisely, we do not make a Fourier transform in time. We treat the time evolution more carefully. The Fourier transform in $\boldsymbol{\alpha}$ of the Vlasov equation, Eq. (2.10), yields

$$\begin{aligned}\frac{\partial \hat{f}_{\boldsymbol{n}}}{\partial t} \;+\; \imath \boldsymbol{n}\cdot\boldsymbol{\omega}_{\mathbf{eq}}\, \hat{f}_{\boldsymbol{n}} \;-\; \imath \boldsymbol{n}\cdot \frac{\partial f_{\mathrm{eq}}}{\partial \boldsymbol{J}}\, \hat{H}_{\boldsymbol{n}} \;&=\\ &+ \sum_{\boldsymbol{n}'} \imath(\boldsymbol{n}-\boldsymbol{n}')\cdot \frac{\partial \hat{f}_{\boldsymbol{n}'}}{\partial \boldsymbol{J}} \hat{H}_{\boldsymbol{n}-\boldsymbol{n}'} \;-\; \sum_{\boldsymbol{n}'} \imath \boldsymbol{n}'\cdot \frac{\partial \hat{H}_{\boldsymbol{n}-\boldsymbol{n}'}}{\partial \boldsymbol{J}}\, \hat{f}_{\boldsymbol{n}'}.\end{aligned} \tag{2.15}$$

The RHS corresponds to nonlinear wave-wave and wave-particle interactions. In the framework of quasilinear theory, the nonlinear wave-wave and wave-particle interactions are assumed to be weak according to the hypotheses of weak turbulence and of no particle trapped in electrostatic potential. Thus we neglect the nonlinear interactions of the form $\hat{H}_{\boldsymbol{n}-\boldsymbol{n}'}\hat{f}_{\boldsymbol{n}'}$ except for $\boldsymbol{n} = \mathbf{0}$, $\boldsymbol{n}' = \mathbf{0}$, or $\boldsymbol{n}' = \boldsymbol{n}$. Therefore, for $\boldsymbol{n} \neq \mathbf{0}$, Eq. (2.15) is approximated by

$$\frac{\partial \hat{f}_{\boldsymbol{n}}}{\partial t} \;+\; \imath\, \omega_{R,\boldsymbol{n}}\, \hat{f}_{\boldsymbol{n}} \;=\; \imath \boldsymbol{n}\cdot \frac{\partial \langle f\rangle}{\partial \boldsymbol{J}} \hat{H}_{\boldsymbol{n}}, \tag{2.16}$$

where

$$\omega_{R,\boldsymbol{n}}(J_k, t) = \boldsymbol{n}\cdot \left(\boldsymbol{\omega}_{\mathbf{eq}} + \frac{\partial \hat{H}_{\mathbf{0}}}{\partial \boldsymbol{J}}\right) \tag{2.17}$$

is the resonant frequency including a Doppler shift induced by mean fields.

Eq. (2.16) is of the form

$$L_{\boldsymbol{n}} \hat{f}_{\boldsymbol{n}} \;=\; \hat{g}_{\boldsymbol{n}}(J_k, t), \tag{2.18}$$

where $L_{\boldsymbol{n}}$ is the linear operator $L_{\boldsymbol{n}} = \partial_t + \imath\, \omega_{R,\boldsymbol{n}}(J_k, t)$, and $\hat{g}_{\boldsymbol{n}} = \imath \boldsymbol{n}\cdot\partial_{\boldsymbol{J}}\langle f\rangle\, \hat{H}_{\boldsymbol{n}}$. To solve this equation, we assume that the evolution of mean fields is much slower than the time-evolution of $\hat{f}_{\boldsymbol{n}}$, in order to neglect the time-evolution of $\omega_{R,\boldsymbol{n}}$. For $\omega_{R,\boldsymbol{n}} = 0$, the solution is trivial. For $\omega_{R,\boldsymbol{n}} \neq 0$, Eq. (2.18) can be solved using Green's function $G_{\boldsymbol{n}}(t,s) = \exp\left[\imath\,(s-t)\omega_{R,\boldsymbol{n}}\right]$, which is such that $L_{\boldsymbol{n}} G_{\boldsymbol{n}} = \delta(s-t)$. The solution is

$$\hat{f}_{\boldsymbol{n}}(J_k, t) \;=\; \int_0^t e^{\imath\,(s-t)\omega_{R,\boldsymbol{n}}}\, \imath \boldsymbol{n}\cdot \frac{\partial \langle f\rangle}{\partial \boldsymbol{J}}(J_k, s)\, \hat{H}_{\boldsymbol{n}}(J_k, s)\, \mathrm{d}s. \tag{2.19}$$

It turns out that the latter expression is also valid for $\omega_{R,\boldsymbol{n}} = 0$.

Each mode is assumed to have a fixed frequency $\omega_{\boldsymbol{n}}$ (obtained from linear theory), and a time-dependent growth rate $\gamma_{\boldsymbol{n}}$,

$$\hat{H}_{\boldsymbol{n}}(J_k, t) \;=\; \hat{H}_{\boldsymbol{n}}(J_k, s) \exp\left[\int_0^t \left(-i\omega_{\boldsymbol{n}} + \gamma_{\boldsymbol{n}}(t')\right) \mathrm{d}t'\right]. \tag{2.20}$$

This assumption is debatable because, as we will see on several occasions in the following chapters, a mode frequency can be significantly modified by nonlinear processes.

For $\boldsymbol{n} = \boldsymbol{0}$, Eq. (2.15) recovers the flux equation, Eq. (2.12), with the flux of phase-space density,

$$\boldsymbol{\Lambda} \;=\; \sum_{\boldsymbol{n}} \imath \boldsymbol{n} \hat{f}_{\boldsymbol{n}} \hat{H}^*_{\boldsymbol{n}}. \tag{2.21}$$

Substituting Eqs. (2.19) and (2.20) yields

$$\boldsymbol{\Lambda}(J_k, t) \;=\; \sum_{\boldsymbol{n}} \left| \hat{H}_{\boldsymbol{n}}(J_k, t) \right|^2 \boldsymbol{n} \left(\boldsymbol{n} \cdot \frac{\partial I_{\boldsymbol{n}}(t)}{\partial \boldsymbol{J}} \right), \tag{2.22}$$

where

$$I_{\boldsymbol{n}}(t) \;=\; \int_0^t e^{\imath(\omega_{R,\boldsymbol{n}} - \omega_{\boldsymbol{n}})(s-t)} \exp\left[\int_t^s \gamma_{\boldsymbol{n}}(t') \mathrm{d}t' \right] \langle f \rangle (J_k, s)\, \mathrm{d}s; \tag{2.23}$$

Since the RHS phase-mixes for $t - s$ larger than a typical growth time γ^{-1} and a typical timescale of relaxation of $\langle f \rangle$, we can approximate $\int_t^s \gamma_{\boldsymbol{n}}(t') \mathrm{d}t'$ by $(s-t)\gamma_{\boldsymbol{n}}(t)$ and $\langle f \rangle (J_k, s)$ by $\langle f \rangle (J_k, t)$. With this approximation,

$$I_{\boldsymbol{n}}(t) \;=\; \frac{1 - e^{-i(\omega_{R,\boldsymbol{n}} - \omega_{\boldsymbol{n}})t - |\gamma_{\boldsymbol{n}}(t)|t}}{i(\omega_{R,\boldsymbol{n}} - \omega_{\boldsymbol{n}}) + |\gamma_{\boldsymbol{n}}(t)|} \langle f \rangle (J_k, t); \tag{2.24}$$

Finally, the time evolution of the averaged distribution function simplifies to

$$\frac{\partial \langle f \rangle}{\partial t} \;=\; \frac{\partial}{\partial \boldsymbol{J}} \cdot \left[\bar{\bar{D}}^{\mathrm{QL}} \frac{\partial \langle f \rangle}{\partial \boldsymbol{J}} \right], \tag{2.25}$$

where $\bar{\bar{D}}^{\mathrm{QL}}$ is the quasi-linear diffusion tensor, whose components are

$$D^{\mathrm{QL}}_{i,j}(J_k, t) \;=\; \sum_{\boldsymbol{n}} n_i n_j \left| \hat{H}_{\boldsymbol{n}}(J_k, t) \right|^2 \mathrm{Im} \frac{1 - e^{-\imath(\omega_{R,\boldsymbol{n}} - \omega_{\boldsymbol{n}})t - |\gamma_{\boldsymbol{n}}(t)|t}}{(\omega_{R,\boldsymbol{n}} - \omega_{\boldsymbol{n}}) - \imath |\gamma_{\boldsymbol{n}}(t)|}. \tag{2.26}$$

The main hypotheses of quasi-linear theory are: weak turbulence (small fluctuations of the profiles compared to the equilibrium), no trapped particles in electrostatic potential 'wells' (with a very large number of electrostatic waves, the resonance region of each waves can overlap so that the particle motion becomes stochastic, and the particle can wander in the velocity phase space [SG69, DII10]) and a small auto-correlation time of the electric field compared to the evolution time of the profiles [ALP79].

At this point, many authors take the time-asymptotic approximation,

$$1 - e^{-|\gamma_{\boldsymbol{n}}|t} e^{-\imath(\omega_{R,\boldsymbol{n}} - \omega_{\boldsymbol{n}})t} \;\approx\; 1, \tag{2.27}$$

which yields

$$D^{\mathrm{QL}}_{i,j}(J_k, t) \;=\; \sum_{\boldsymbol{n}} n_i n_j \left| \hat{H}_{\boldsymbol{n}}(J_k, t) \right|^2 \frac{|\gamma_{\boldsymbol{n}}(t)|}{(\omega_{R,\boldsymbol{n}} - \omega_{\boldsymbol{n}})^2 + \gamma_{\boldsymbol{n}}(t)^2}. \tag{2.28}$$

However, for studying the beginning of the saturation phase, which occurs at a time of the order of $1/\gamma$, the expression Eq. (2.26), as is, can be retained.

Since we are typically interested in density, momentum, or heat fluxes, which are moments of the phase-space density flux $\boldsymbol{\Lambda}$, let us consider Eq. (2.28) in the sense of a distribution. The diffusion coefficient involves a Cauchy-Lorentz distribution, whose limit as $\gamma_{\boldsymbol{n}} \to 0$ is

$$\lim_{\gamma_{\boldsymbol{n}} \to 0} \frac{|\gamma_{\boldsymbol{n}}|}{(\omega_{R,\boldsymbol{n}} - \omega_{\boldsymbol{n}})^2 + \gamma_{\boldsymbol{n}}(t)^2} \;=\; \pi \delta(\omega_{R,\boldsymbol{n}} - \omega_{\boldsymbol{n}}) \tag{2.29}$$

Note that this is the imaginary part of the Plemelj formula – the real part $\mathcal{P}/(\omega_{R,\boldsymbol{n}} - \omega_{\boldsymbol{n}})$ vanishes due to symmetries between $\boldsymbol{n}$ and $-\boldsymbol{n}$.

Conventionally, this approximation is used in the resonant region, assuming $|\gamma_{\boldsymbol{n}}| \ll |\omega_{\boldsymbol{n}}|$. Let us investigate the accuracy of this approximation depending on the parameters. To

illustrate, let us take the example of a 1D Vlasov plasma, with a bump-on-tail distribution of electrons, $f_{\rm eq} = f_{\rm eq}^M + f_{\rm eq}^B$, comprising a maxwellian bulk, and a gaussian beam,

$$f_{\rm eq}^B \;=\; \frac{n_B}{v_{TB}\sqrt{2\pi}}\, e^{-\frac{1}{2}\left(\frac{v-v_B}{v_{TB}}\right)^2} \tag{2.30}$$

The resonant velocity $v_R = \omega/k$ of most unstable Langmuir waves is typically at $v_B - v_{TB}$, where velocity-gradient is maximum (and $v > 0$). Therefore, we may assume for this illustration that $v_R = v_B - v_{TB}$. The system size is $L = 2\pi/k_1$, with periodic boundary conditions. In this context, the angle action variables are $\alpha = k_1 x$ and $J = mv/k_1$. The equilibrium hamiltonian is $H_{\rm eq} = k_1^2 J^2/(2m)$, and the perturbed one is $\delta H = q\phi$. The equilibrium frequency is $\omega_{\rm eq} = k_1 v$, and the resonant frequency for a mode n of wave number $k_n = nk_1$ is simply $\omega_{R,n} = k_n v$. Substituting into Eqs. (2.25) and (2.28), and renormalizing $D^{\rm QL}$ to express diffusion in terms of v instead of J yields

$$\frac{\partial\langle f\rangle}{\partial t} \;=\; \frac{\partial}{\partial v}\left(D^{\rm QL}\frac{\partial\langle f\rangle}{\partial v}\right), \tag{2.31}$$

and

$$D^{\rm QL}(v,t) \;=\; \frac{q^2}{m^2}\sum_n k_n^2\left|\hat{\phi}_n\right|^2 \frac{|\gamma_n|}{(k_n v-\omega_n)^2+\gamma_n^2}. \tag{2.32}$$

Then, for example, the rate of change of momentum is obtained as

$$\frac{{\rm d}p}{{\rm d}t} \;=\; \int \frac{\partial\langle f\rangle}{\partial t} v{\rm d}v \;=\; -\int D^{\rm QL}\frac{\partial\langle f\rangle}{\partial v}\,{\rm d}v. \tag{2.33}$$

Let us ignore the contribution of the maxwellian bulk, and focus on the resonance. We substitute $f_{\rm eq}^B$ for $\langle f\rangle$. The contribution of a given mode n is then proportional to

$$I \;=\; \int \frac{|\gamma|}{(kv-\omega)^2+\gamma^2}\frac{\partial f_{\rm eq}^B}{\partial v}\,{\rm d}v, \tag{2.34}$$

where we have dropped the $_n$ subscript for concision. In the limit of vanishing growth rate, I can be approximated as

$$I_0 \;=\; \frac{\pi}{k}\left.\frac{\partial f_{\rm eq}^B}{\partial v}\right|_{v=\omega/k}, \tag{2.35}$$

where $v_R = \omega/k$ is the resonant velocity. Figure 2.1 shows the value of I/I_0 against the only two remaining parameters in this setup: γ/ω (a), and v_{TB}/v_R (b). As expected, the approximation is increasingly accurate ($I/I_0 \to 1$) with decreasing growthrate. However, for the approximation $I = I_0$ to be accurate, the ratio γ/ω needs to be very small, especially for low thermal spreads of the beam. Since the growth rate is finite, it is more accurate to keep when possible the expression Eq. (2.28), or even Eq. (2.26).

We apply and discuss quasilinear theory in the case of energetic particle-driven modes in Chapter 4, and in the case of trapped particles-driven turbulence in Chapter 6.

2.2.5 Nonlinear theories

Nonlinear hydrodynamic and magneto-hydrodynamic theories provide robust foundations for understanding the long-time behavior of Vlasov plasmas. We can cite the Hasegawa-Mima model [HM78], which provides a good understanding of wave-wave interactions, and large-scale structure formation in 2D turbulence in the long-wavelength limit; and the Hasegawa-Wakatani model [HW83] to take into account viscosity.

Here we discuss nonlinear kinetic effects underlying the Vlasov equation. The literature yields a wealth of information and interpretations provided by numerical simulations and experiments. However, it appears that analytic works are sparser. Although at present I lack the knowledge to provide a comprehensive review, let me cite a few examples, some of which are developed throughout this manuscript.

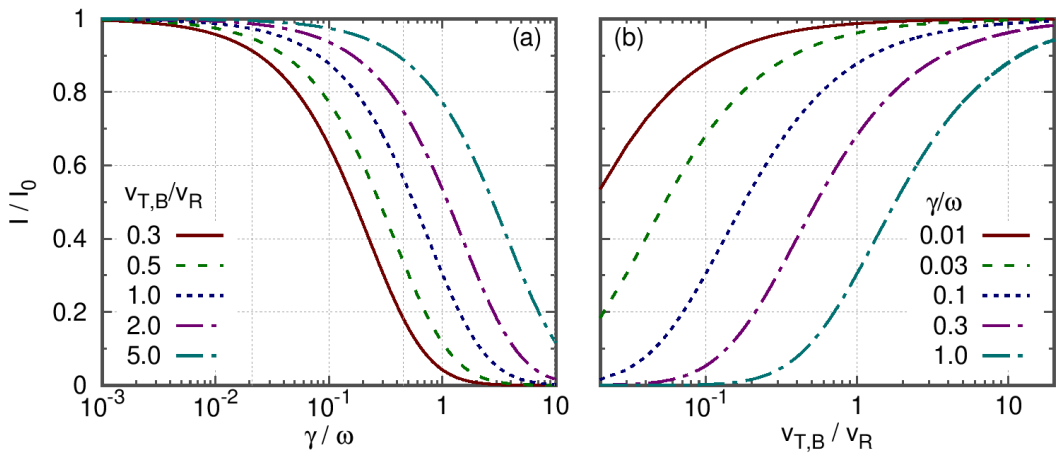

Figure 2.1 – Accuracy of the Dirac δ approximation for the Cauchy-Lorentz distribution in the quasilinear diffusion coefficient. (a) Nonlinear evolution of normalized bounce frequency. (b) Snapshots of distribution function.

The linearly damped case with infinitesimal initial perturbation can be considered as solved. Indeed, Mouhot and Villani used a perturbative approach similar to the Kolmogorov–Arnold–Moser (KAM) theory to demonstrate the possibility of fully nonlinear, long-term relaxation, without entropy increase nor radiation, i.e. nonlinear Landau damping [MV11, Vil14].

Bernstein, Greene and Kruskal constructed a family of fully nonlinear, nonvanishing steady-state solutions, then called as BGK waves, where the distribution is a function of energy [BGK57]. The stability of such solutions remains an open question, as we discuss in chapter 4 (4.5.2). More generally, Sagdeev developed a method based on a pseudo-potential to find fully nonlinear solitary waves [Sag66].

In the presence of a local potentiel well which traps ions (and conversely for electrons) within an eye-shaped separatrix in phase-space (PS), the BGK solution is a PS island, as introduced in chapter 1. Such PS island can evolve into a self-trapped PS structure in many situations [Sch86].

For weakly collisional, quiescent plasmas near thermal equilibrium, the dressed test-particle model [RR60] coupled with the fluctuation-dissipation theorem successfully predicts the fluctuation spectrum and slow relaxation. In this model, particle discreteness plays an essential role of producing incoherent fluctuations by Cerenkov emission. Since it is based on linear response and unperturbed orbits, the dressed test-particle model not only precludes the presence of collective modes, but it gradually loses its validity as linear marginality is approached from the stable end, and nonlinear discreteness noise becomes significant. However, the method can be adapted (see e.g. [DII10]) to the problem of turbulence in collisionless plasmas far from thermal equilibrium, by carrying one or more modifications depending on the regime:

— switching from strictly local (in wavenumber space) to de-localized (and possibly non-local in the sense of non-neighboring scales) emission and absorption,
— accounting for incoherent fluctuations induced by nonlinear coupling, which easily overcome Cerenkov emission,
— coupling the Vlasov equation with a wave kinetic equation to describe the evolution of turbulent spectrum in the presence of sources and sinks,
— replacing linear damping or growth rates by nonlinear ones (when available),
— re-normalizing the Landau propagator to account for resonance broadening by background turbulence [Dup66],
— replacing dressed test particles by self-trapped PS structures in the role of the quasi-particle.

The latter procedure is discussed in chapter 7. It results in relaxation described by an operator with the same structure as Lenard-Balescu.

2.3 Invariants

In general, nonlinear theories take advantage of invariants and balance equations. Several invariants can be identified by noting the following general property. Let $u(\Gamma, t)$ and $v(\Gamma, t)$ be two arbitrary functions, analytic in a phase-space $\Gamma \equiv (\boldsymbol{q}, \boldsymbol{p})$, where either or both of u and v satisfy either periodic or vanishing boundary conditions. And let $w(u, t)$ be an arbitrary function of u and time t. Then, integration by part shows that

$$\int [u,\, v]_\Gamma \; w(u,t)\, \mathrm{d}\Gamma \;=\; 0, \tag{2.36}$$

where integration is over the whole phase-space volume. Substituting $u = f$ and $v = h$ and combining with Vlasov equation yields

$$\int w(f,t)\, \frac{\partial f}{\partial t}\, \mathrm{d}\Gamma \;=\; 0. \tag{2.37}$$

Similarly, substituting $u = h$ and $v = f$ and combining with Vlasov equation yields

$$\int w(h,t)\, \frac{\partial f}{\partial t}\, \mathrm{d}\Gamma \;=\; 0. \tag{2.38}$$

This property can be used to find a series of invariants. Let us cite a few examples.

— Choosing $w = 1$ yields a first invariant: total particle number $\int f \mathrm{d}\Gamma$.

— Choosing $w = h$ yields a relationship between total kinetic energy and the work done on particles by electromagnetic forces, which can be combined with Maxwell equations to find a second invariant: total energy.

— Choosing $w = 1 + \log f$ yields a third invariant: total entropy $\int f \log f \mathrm{d}\Gamma$, which we describe in subsection 2.3.1.

— Choosing $w = f$ yields a fourth invariant: the quantity $\int f^2 \mathrm{d}\Gamma$, which we discuss in subsection 2.3.2.

These invariants provide a good basis for developing nonlinear theories. For example, O'Neil equated the rate of change of kinetic energy to the rate of change of potential energy to calculate the nonlinear evolution of the amplitude of a single mode in the bump-on-tail instability [O'N65].

However, as stated in the introduction of this chapter, in hot plasma physics, we are often faced with open systems and finite collision frequencies. In such systems, some or all of the conservation equations associated with these invariants must be replaced by corresponding balance equations. Nevertheless, balance equations can also yield useful nonlinear theories. For example, a power balance was used to successfully estimate the amplitude of saturation of a single mode in the bump-on-tail instability with external dissipation and collisions [BB90a], as we will describe in chapter 4 (4.3.1).

2.3.1 Entropy

Although the Vlasov equation conserves total entropy $\int f \log f \mathrm{d}\Gamma$, this is not true for real plasmas nor numerical simulations of Vlasov plasmas. Real plasmas are many-body systems with a finite number of particles, which introduces irreversible heating. Numerical simulations of the Vlasov equation are enabled by some level of discretization, truncation, or filtering, which also yields entropy production. Entropy is also produced by irreversible resonant quasi-linear diffusion, which is coarse-grained averaged and requires chaos.

Entropy production is practically irreducible in kinetic numerical simulations of collisionless turbulence. In Ref. [Les16], I demonstrate that the irreducible part of spurious entropy can amount to a large fraction of total entropy. The argument is based on a simulation of collisionless ion-acoustic turbulence, where a significant error (15%) in entropy conservation is found, independently of the numerical method, scheme, or number of grid points. A collision operator solves the issue, but only for collision frequencies so large that they significantly modify the macroscopic behavior.

2.3.2 Phasestrophy

Self-trapped structures in phase-space resemble vortices in 2D ideal fluid turbulence [Mcw84]. This reflects similarities between 2D ideal fluids and 1D Vlasov plasmas. They are both 2D Hamiltonian systems, which conserve phase-space density. They both satisfy a circulation theorem [LB67]. Furthermore, the evolution of each system is constrained by two invariants: energy and enstrophy (mean square vorticity) in the fluid case, wave energy and mean square distribution function in the Vlasov case.

Based on this analogy, Diamond coined the term *phasestrophy* [DKL11, DII10], for phase-space enstrophy [2]. In angle-action formalism, the phasestrophy writes

$$\Psi \equiv \int \left\langle \tilde{f}^2 \right\rangle \mathrm{d}\boldsymbol{J}, \tag{2.39}$$

where $\tilde{f} \equiv f - \langle f \rangle$, angle brackets denote the average over all angles, and the integration is over all action space. The aim is to measure self-trapped PS structures.

Conservation of $\int f^2 \mathrm{d}\Gamma$ yields

$$\frac{\mathrm{d}}{\mathrm{d}t} \int \langle f^2 \rangle \mathrm{d}\boldsymbol{J} = \frac{\mathrm{d}}{\mathrm{d}t} \int \langle f \rangle^2 \mathrm{d}\boldsymbol{J} + \frac{\mathrm{d}\Psi}{\mathrm{d}t} = 0. \tag{2.40}$$

The evolution of phasestrophy follows

$$\frac{\mathrm{d}\Psi}{\mathrm{d}t} = -\int \frac{\partial \langle f \rangle^2}{\partial t} \mathrm{d}\boldsymbol{J} \tag{2.41}$$

$$= -2 \int \langle f \rangle \frac{\partial \langle f \rangle}{\partial t} \mathrm{d}\boldsymbol{J}, \tag{2.42}$$

which links phasestrophy and relaxation. Substituting Eq. (2.12) yields

$$\frac{\mathrm{d}\Psi}{\mathrm{d}t} = 2 \int \langle f \rangle \frac{\partial}{\partial \boldsymbol{J}} \cdot \boldsymbol{\Lambda} \, \mathrm{d}\boldsymbol{J}. \tag{2.43}$$

We recall that $\boldsymbol{\Lambda} = \left\langle \dot{\boldsymbol{J}} \, \delta f \right\rangle = \left\langle \dot{\boldsymbol{J}} \, \tilde{f} \right\rangle$ is the flux of phase-space density in the directions of the actions. Provided vanishing $\boldsymbol{\Lambda}\langle f \rangle$ or periodic boundary conditions in the actions, integration by part yields an exact expression of phasestrophy production,

$$\frac{\mathrm{d}\Psi}{\mathrm{d}t} = -2 \int \boldsymbol{\Lambda} \cdot \frac{\partial \langle f \rangle}{\partial \boldsymbol{J}} \, \mathrm{d}\boldsymbol{J}. \tag{2.44}$$

The same relations after the substitution $(\langle f \rangle, \tilde{f}) \to (f_{\mathrm{eq}}, \delta f)$, including in the definition of phasestrophy, are exactly satisfied as well.

Note that phasestrophy is also related to fluctuation entropy. Indeed, if fluctuations are small enough, we can use the relations

$$\langle f \log f \rangle = \langle f \rangle \log \langle f \rangle + \frac{\left\langle \tilde{f}^2 \right\rangle}{2\langle f \rangle} + O\left(\frac{\tilde{f}^3}{\langle f \rangle^2} \right) \tag{2.45}$$

$$= f_{\mathrm{eq}} \log f_{\mathrm{eq}} + \frac{\langle \delta f^2 \rangle}{2 f_{\mathrm{eq}}} + O\left(\frac{\delta f^3}{f_{\mathrm{eq}}^2} \right). \tag{2.46}$$

2.3.3 The Energy-Phasestrophy relation

In Ref. [LD13], we propose a link between phasestrophy production and wave power, which I summarize here.

The parallel between 2D ideal fluids and 1D Vlasov plasmas suggests that we can use common strategies, based on solution of the two coupled energy and enstrophy (fluid) or

2. In the neologism phasestrophy, 'phase' refers to phase-space, and 'strophy' is greek for 'rotation'. However, in some papers the 's' is missing, and the word 'phasetrophy' is used.

phasestrophy and wave energy (plasma) equations, respectively. In the case of the 2D Navier-Stokes equations, this lead to the theoretical prediction of the two inertial (or self-similar) ranges in the spectrum of steady-state turbulence [Kol41b, Kol41a, Kra67].

The expression of phasestrophy production Eq. (2.44) is straightforwardly generalized to include a collision operator, and specialized to 1D plasmas of length $L = 2\pi/k_1$ with periodic boundary conditions and electrostatic fluctuations. In this case, the angle action variables for each species s are $\alpha = k_1 x$ and $J = m_s v/k_1$. The perturbed hamiltonian is $\delta H = q_s \phi$. Therefore, $\Lambda_s = q_s E \tilde{f}_s / k_1$. Substituting into Eq. (2.44) yields

$$\frac{\mathrm{d}\Psi_s}{\mathrm{d}t} = -2\frac{q_s}{m_s}\int_{-\infty}^{\infty}\frac{\mathrm{d}\langle f_s\rangle}{\mathrm{d}v}\left\langle E\,\tilde{f}_s\right\rangle \mathrm{d}v - \gamma_\Psi^{\mathrm{col}}\,\Psi_s, \tag{2.47}$$

where $\gamma_\Psi^{\mathrm{col}}$ is the decay rate of phasestrophy due to collisions, which we write explicitly in chapter 4 (4.3.2).

The wave energy equation is

$$\frac{\mathrm{d}W}{\mathrm{d}t} = -2\sum_s u_s q_s \int \left\langle E\,\tilde{f}_s\right\rangle \mathrm{d}v, \tag{2.48}$$

where $W = n_0 q^2 \left\langle E^2\right\rangle/(m\omega_p^2)$ is the total wave energy, including sloshing energy. Here, u_s is roughly the mean velocity of dominant phase-space structures, and can be obtained from nonlinear calculation of particle orbits, and depends on the specific setup. We assume that $\langle f_s\rangle$ has a constant slope in the velocity-range spanned by evolving phase-space structures. Then, phasestrophy evolution is linked to the wave energy evolution, by

$$\frac{\mathrm{d}W}{\mathrm{d}t} + 2\gamma_d W = \sum_s \frac{m_s u_s}{\mathrm{d}_v\langle f_s\rangle}\left(\gamma_\Psi^{\mathrm{col}} + \frac{\mathrm{d}}{\mathrm{d}t}\right)\Psi_s. \tag{2.49}$$

Hereafter, we call this as the energy-phasestrophy relation. In parallel with quasi-geostrophic fluids, this relation is the kinetic counterpart of the Charney-Drazin theorem on the non-acceleration of zonal mean flows by steady conservative waves [CD61].

In this manuscript, we apply this relation to the Berk-Breizman model in subsection 4.3.2 by removing the subscript s and adding prescribed wave dissipation, and to current-driven ion-acoustic turbulence in section 5.3 by taking $\gamma_d = \nu_a = \nu_f = \nu_d = 0$.

Chapter 3

Subcritical instabilities

In neutral fluids and plasmas, the analysis of perturbations often starts with an inventory of linearly unstable modes. Then, the nonlinear steady-state is analyzed or predicted based on these linear modes. A crude analogy would be to base the study of a chair based on how it responds to infinitesimally small perturbations. One would conclude that the chair is stable to all frequencies, and cannot fall down. Of course, a chair falls down if subjected to finite-amplitude perturbations. Similarly, waves and wave-like structures in neutral fluids and plasmas can be triggered even though they are linearly stable. These subcritical instabilities are dormant unless their amplitude is pushed above some threshold. Investigating their onset conditions requires nonlinear calculations. Subcritical instabilities are ubiquitous in neutral fluids and plasmas. In plasmas, subcritical instabilities have been investigated based on analytical models and numerical simulations since the 1960s. More recently, they have been measured in laboratory and space plasmas, albeit not always directly. The topic could benefit from the much longer and richer history of subcritical instability and transition to subcritical turbulence in neutral fluids. In this chapter, which is based on a tutorial we published in Japanese only [LSS16], and our more recent review paper [LMSS18], we describe the fundamental aspects of subcritical instabilities in plasmas, based on systems of increasing complexity: from simple examples of a point-mass in a potential well or a box on a table; to turbulence and instabilities in neutral fluids; and finally to modern applications in magnetized toroidal fusion plasmas.

3.1 Introduction

Subcritical instabilities are nonlinear instabilities that occur even as the system is linearly stable, but with a threshold in the amplitude of initial perturbations. Subcritical instabilities stay dormant until they are brought over their threshold by some interaction, drive, forcing, or even thermal noise or other naturally occurring perturbations if the threshold is low enough. Subcritical instabilities are ubiquitous in neutral fluids and in plasmas. They are of great interest for their essential impact on the onset of turbulence, structure formation, anomalous resistivity, and potentially, turbulent transport. Indeed, the widespread use of linear theory, which subcritical instabilities circumvent, as foundation of nonlinear (or quasi-linear) theories is a major caveat in the conventional analysis of wave-like perturbations. The growth of subcritical instabilities is a nonlinear process, which is often independent of their linear decay rate. They open a new channel for tapping free energy.

The physical mechanisms of nonlinear growth are multiple, but subcritical instabilities share common features in terms of bifurcation, and in terms of their macroscopic impact, which are typically equivalent or larger than the impacts of linearly unstable perturbations. The growth mechanisms are well documented, and theories often yield accurate analytic formulas for their threshold in amplitude and for their nonlinear growth rate.

Direct measurements in neutral fluid experiments have confirmed the existence and implications of subcritical instabilities. In plasmas, fluid-like subcritical instabilities are well documented in laboratory experiments. However, high-temperature plasmas feature other

kinds of instabilities, which involve non-gaussian distribution functions. Direct measurements of these kinetic subcritical instabilities are more difficult, because they are often based on short-lived structures, with small-scales in both real space and velocity space (but which altogether yield macroscopic, long-lived impacts on magneto-hydrodynamics). The development of new techniques to obtain more accurate measurements of phase-space density are ongoing.

Subcritical instabilities can be approached from various standpoints. Large parts of the literature focus on the mechanisms by which a finite-amplitude seed perturbation can grow nonlinearly, or how the nonlinear structure sustains itself. Several scenarios for the onset of subcritical instabilities or the subcritical transition to turbulence have been uncovered. In some cases, infinitesimal perturbations or noise can grow transiently, either into a finite-amplitude seed, or directly into a self-sustained nonlinear structure. In other cases, large enough seeds can be formed by external forcing, or by an avalanche process originating from a linearly unstable region (which can be a region in spacetime). Dauchot and Manneville described the concept of subcritical instability from the point-of-view of local versus global analysis of stability [DP97]. Based on a simplified model of Navier-Stokes turbulence, they showed that stability conditions can only be determined from the knowledge of all reachable attraction basins rather than from the stability of the local basin. Yoshizawa, Itoh and Itoh described the topic of subcritical instabilities based on examples of plasma instability, as can be found in their textbook [YII02a]. Nonmodal stability theory, as reviewed by Schmid [Sch07], has been successfully applied to analyze nonlinear stability in a wide range of fluid and plasma contexts, including space-and-time-dependent flows in complex geometries.

Hereafter, let us describe basic concepts of subcritical instability, starting from the simplest example of a point mass in a potential well, then building up to increasingly complex physical contexts: the Kelvin-Helmholtz instability, quasi-2D and pipe flows, 1D plasma, drift-waves in magnetized plasmas, and finally strong electro-magnetic bursts driven by energetic particles in magnetized toroidal plasmas. We do not attempt any comprehensive review of the literature on subcritical instabilities and subcritical turbulence, but rather propose an introduction of the topic by selecting a few paradigmatic examples. The aims are two-fold: 1. to allow the reader to get clear physical pictures of some of the various mechanisms by which subcritical instability can occur, and 2. to point out interesting analogies between neutral fluids and plasmas, which may be exploited to push the research further.

3.2 Concepts of subcritical instability

Let us set up a simple model of Newtonian mechanics to illustrate by analogy the concept of subcritical instability.

Consider a point mass of radial coordinate r resting on a surface of altitude $\phi(r)$, or equivalently, a positively charged particle in an electric potential $\phi(r)$, where

$$\phi(r) \;=\; -ar^2 - br^4 + cr^6. \tag{3.1}$$

Here, a, b and c are constant input parameters which characterize the shape of the potential. Let us assume that the point mass or particle is initially at $r = 0$, and is ultimately bounded to a finite r region of space, which is imposed by the condition $c > 0$. In this section we choose arbitrarily $c = 0.1$. We consider two qualitatively different cases for b, namely $b = 1$ and $b = 0$. As we argue hereafter, these two cases represent systems which can ($b = 1$) or cannot ($b = 0$) feature subcritical instabilities.

Fig. 3.1(a) shows the potential ϕ for $a = 1.5$, $b = 0$ and $c = 0.1$, and a point mass or charged particle after it was perturbed by an external push towards positive r. This corresponds to the conventional, supercritical instability. We assume that there is some form of energy dissipation. Any initial perturbation in r will grow linearly at first, then r will oscillate around the stable equilibrium, before reaching the latter equilibrium in the time-asymptotic steady-state. In contrast, Fig. 3.1(b) shows the potential ϕ for $a = -2$, $b = 1$ and $c = 0.1$, which is linearly stable, but nonlinearly unstable. If the initial perturbation is small enough, the point mass or particle will oscillate around $r = 0$ with amplitude decreasing

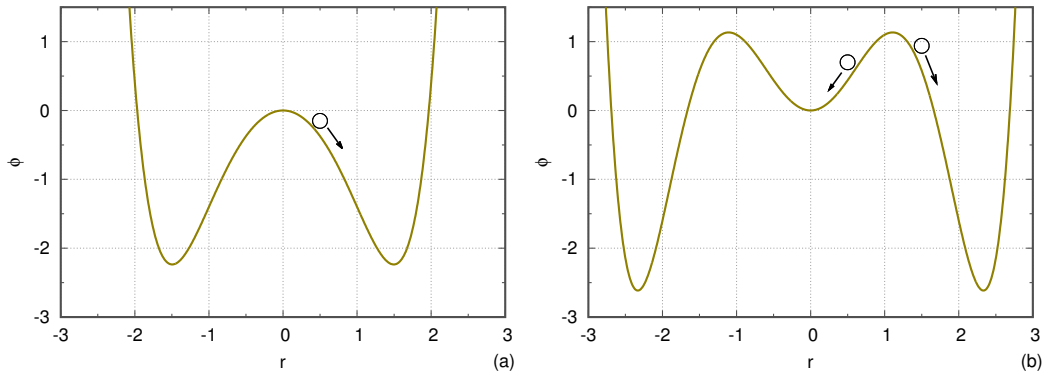

Figure 3.1 – Cartoon of the concept of supercritical and subcritical instabilities. The solid curve is a fixed potential. (**a**) Supercritical case, $a = 1.5$, $b = 0$ and $c = 0.1$. The equilibrium $r = 0$ is unstable. (**b**) Subcritical case, $a = -2$, $b = 1$ and $c = 0.1$. The equilibrium $r = 0$ is stable to small perturbations (circle and arrow at $r = 0.5$), but unstable to perturbations with an amplitude above a certain threshold (circle and arrow at $r = 1.5$).

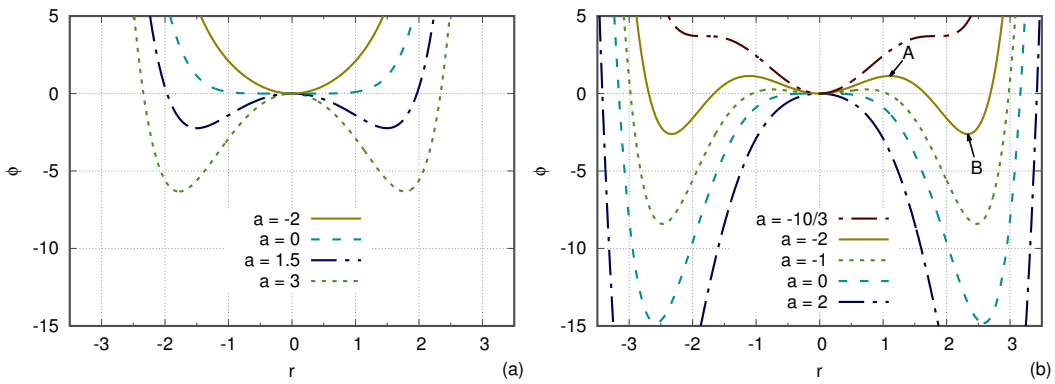

Figure 3.2 – Potential $\phi(r)$ for various values of a. We recall that a is proportional to the square of the linear growth rate. (**a**) Supercritical case, $b = 0$. (**b**) Subcritical case, $b = 1$. Two points are shown by arrows: point A is the potential barrier at $r = r_{\min}$, and point B is the saturated value for the subcritical instability, $r = r_{\max}$.

in time, until it rests back in its original location. If the push is large enough, on the contrary, the point mass or particle will overcome the potential barrier and reach an other potential well. Doing so, it will extract free energy that would not be available if it did not overcome the potential barrier. This illustrates qualitatively the basic concept of subcritical instability. Next, we perform a quantitative analysis.

Fig. 3.2(a) and (b) show the potential ϕ for the two cases $b = 0$ and $b = 1$, and for various values of a ($c = 0.1$ as before). In both cases, in the neighborhood of $r = 0$, the potential is strictly concave for any $a > 0$, and strictly convex for any $a < 0$. The equation of motion is

$$\ddot{r} \equiv \frac{d^2 r}{dt^2} = -K \frac{d\phi}{dr}, \tag{3.2}$$

where K is a positive constant. The linearized equation of motion is $\ddot{r} = 2aKr$. Therefore, a linear analysis informs us that the equilibrium $r = 0$ is stable for $a < 0$, unstable for $a > 0$, and marginal for $a = 0$. In other words, the linear instability threshold is simply $a = 0$. For $a > 0$, the linear growth rate is proportional to $\sqrt{a}$.

A nonlinear analysis, in contrast, yields a much different story. The equilibrium states are given by $\dot{r} = 0$ and r such that $d\phi/dr = 0$. The slope of the potential is

$$\frac{d\phi}{dr} = -2r\,(a + 2b\,r^2 - 3c\,r^4), \tag{3.3}$$

which cancels out for $r = 0$ and 0, 2 or 4 other real solutions, depending on the value of b

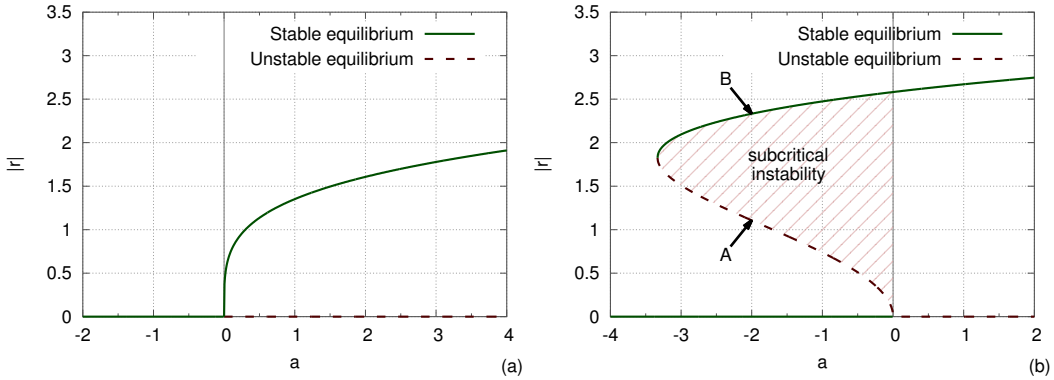

Figure 3.3 – Bifurcation diagram, which yields the nonlinear stability. The solid curves are the stable equilibria $|r| = 0$ and $|r| = r_{\max}$, which correspond to the saturation amplitude. The dashed curves are the unstable equilibria $|r| = 0$ and $|r| = r_{\min}$, which correspond to the threshold amplitude. (**a**) Supercritical system, $b = 0$. (**a**) Subcritical system, $b = 1$. The region of subcritical instability is shown by hashes. The same points A and B as in Fig. 3.2 are shown by arrows in this figure as well.

and $b^2 + 3ac$. Let us focus on the case $b \geq 0$.

1. If $b^2 + 3ac \leq 0$ there is no other real solution than $r = 0$.
2. If $0 < b^2 + 3ac < b^2$ (which is only relevant for $ac < 0$), there are four real solutions other than $r = 0$, which are $r = \pm r_{\min}$ and $r = \pm r_{\max}$, where

$$r_{\min} = \left(\frac{b - \sqrt{b^2 + 3ac}}{3c}\right)^{1/2} \quad \text{and} \quad r_{\max} = \left(\frac{b + \sqrt{b^2 + 3ac}}{3c}\right)^{1/2}. \tag{3.4}$$

   The second derivative of the potential at these solutions is, straightforwardly,

$$\phi''_{\min} = 8\left(a + b\, r_{\min}^2\right) \quad \text{and} \quad \phi''_{\max} = 8\left(a + b\, r_{\max}^2\right). \tag{3.5}$$

   Therefore, with our initial assumption of $c > 0$, $\phi''_{\min} < 0$ and $\phi''_{\max} > 0$. This proves that $r = \pm r_{\min}$ are unstable equilibria, while $r = \pm r_{\max}$ are stable equilibria, as can be seen from the plot of ϕ in Fig. 3.2(b).
3. Finally, if $b^2 + 3ac \geq b^2$, there are two real solutions other than $r = 0$, which are $r = \pm r_{\max}$.

Let us summarize how this translates in terms of stability for two qualitatively different systems: $b = 0$ and $b = 1$. For $b = 0$, if $a \leq 0$ the only equilibrium $r = 0$ is stable. If $a > 0$, the equilibrium $r = 0$ is unstable, and there are two attraction basins, $r = -r_{\max}$ and $r = r_{\max}$, which are stable. This corresponds to the conventional linear instability followed by nonlinear saturation, where, in the analogy, r would be the amplitude of fluctuation.

For $b = 1$, if $a > 0$, the situation is qualitatively similar to the case $b = 0$, $a > 0$. We recover the same two attraction basins, $r = \pm r_{\max}$, which are easily reached because ϕ is concave at $r = 0$. However, if $-1/(3c) < a < 0$ there are three stable equilibria, $r = -r_{\max}$, $r = 0$, and $r = r_{\max}$. Starting from the location $r = 0$, the point mass or the particle can reach one of the two other attraction basins, if it overcomes the potential barrier peaking at $\phi(r_{\min})$. This corresponds to the subcritical instability.

From the latter analysis, one can draw the conditions for instability in bifurcation diagrams such as Fig. 3.3(a) for the system with $b = 0$ and Fig. 3.3(b) for the system with $b = 1$. In terms of bifurcation theory, the system with $b = 0$ features a supercritical Hopf bifurcation, and the system with $b = 1$ features a subcritical Hopf bifurcation (at $a = 0$) as well as a fold bifurcation (at $a = -1/(3c)$). The unstable equilibria are also thresholds that must be reached to trigger the instability. The stable equilibria are also the saturated amplitudes. As we will see, the "finger" shape in Fig. 3.3(b) is typical of subcritical instabilities in neutral fluids and in plasmas. Note that while linear stability is given by a condition in a

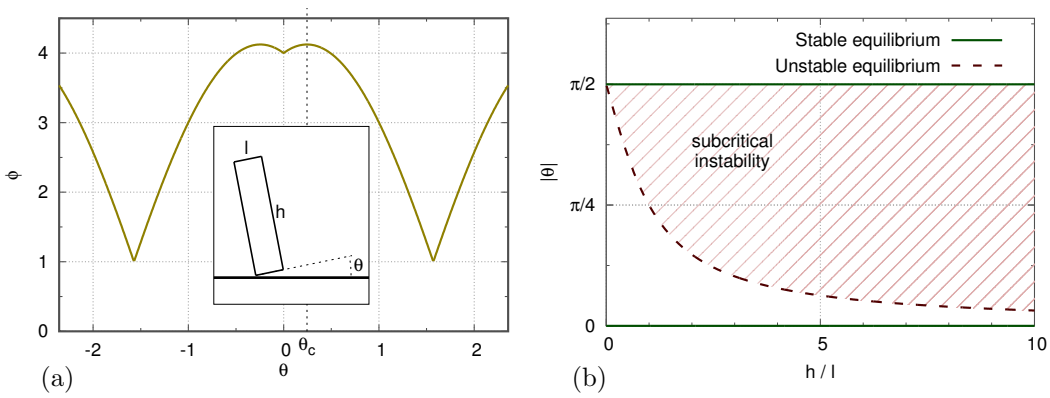

Figure 3.4 – Case of a box on a plane with height $h = 4\,l$. (a) Potential energy (normalized). Inset: cartoon of the setup, where the box is tilted by an angle θ. (b) Corresponding bifurcation diagram. The dashed curve is the unstable equilibrium $|\theta| = \tan^{-1}(l/h)$, which correspond to the threshold amplitude. The region of subcritical instability is shown by hashes: it spans the whole range of finite values of the control parameter h/l.

1D parameter space (a), nonlinear stability is given by a condition in a 2D parameter space (a, r).

These subcritical bifurcations have crucial implications, not only for linear theories, but also on nonlinear theories that are based on an expansion in the perturbation amplitude. Indeed, in the system $b = 0$ where subcritical instabilities are absent, an argument of near-marginality is often made: the system naturally remains near linear marginality $a = 0$, because if the conditions overcome linear marginality ($a > 0$), the instability will tend to counteract the source of instability, bringing the system back to $a = 0$. Now, in the system $b = 1$, the same argument does not stand, for two reasons: 1. near marginality $a = 0$, the perturbation has a finite amplitude $|r| = [2/(3c)]^{1/2}$; and 2. if the conditions overcome linear marginality, the instability will counteract the source, bringing a not only back to $a = 0$ but even to a finite negative value of the order of $a = -1/(3c)$, which may be far from marginal stability.

Finally, let us mention the existence of a third paradigm. A system can feature subcritical instabilities, even if there is no linear instabilities for any finite value of the control parameter. As an example, we can consider a solid box placed on a plane surface (an idealization of a cup on a table). The box has a square base of length l, and a height h. Fig. 3.4(a) shows the box tilted by an angle θ, and the potential energy, which is then proportional to $\sin\theta + h/l\cos\theta$. As the parameter h/l increases, the potential well at $\theta = 0$ becomes shallower and narrower, but never vanishes. Hence the equilibrium $\theta = 0$ is always linearly stable. However a subcritical instability can be triggered if the perturbation overcomes a threshold θ_c such that $\tan\theta_c = l/h$. Fig. 3.4(b) shows the resulting bifurcation diagram. Here there is no subcritical Hopf bifurcation (or one could argue that it has been pushed towards infinity), and the subcritical instability spans the whole parameter space.

3.3 Subcritical instabilities in neutral fluids

In fluid dynamics, the concept of subcritical instability is not to be confused with that of subcritical flow, which is defined as a flow with Froude number less than 1 [Cha99]. To my knowledge, subcritical flows and subcritical instabilities are unrelated. Subcritical turbulence, in particular in the presence of sheared flow, has a long history of experimental [Cou90, DW+28, Col65, TA92], numerical [LJ91], and theoretical research as summarized in [TTRD93]. As entry points, we refer to a textbook by Drazin and Reid [DR81], partial reviews of transition to turbulence by Grossman [Gro00] and Manneville [Man15], and a review of the history of this topic in chapter 2 of Borrero's PhD thesis [Bor14]. In this section, rather than attempting another review, we describe a few examples to introduce the reader to the relevant concepts, which find counterparts or analogies in plasma flows.

Firstly, the Kelvin-Helmholtz instability in 2D geometry (in a Hele-Shaw cell) provides a clear example of subcritical bifurcation. Secondly, the literature on Couette flow, Poiseuille flow, and flat plate laminar boundary layer, provides a relatively simple example of physical mechanisms of growth of a finite amplitude perturbation.

3.3.1 Experimental measurement of subcritical bifurcation

Meignin et al. observed and characterized with great clarity a subcritical instability in experiments of the Kelvin-Helmholtz instability in a Hele-Shaw cell [MGRQR03]. Fig. 3.5 describes the experimental setup. Two fluids (Nitrogen gas and oil here) are injected at the same pressure into a thin space between two parallel glass plates. The two fluids flow out at atmospheric pressure. Here, the gas to liquid density ratio is of the order of 10^{-3}. The gas velocity U_g is used as a control parameter, which corresponds to the drive of the instability. A perturbation is applied via a periodic modulation of the oil injection pressure (keeping the pressure of both fluids equal on average). This leads to an observed sine wave (at the inlet) of vertical amplitude A_0 ("forcing amplitude"). Fig. 3.6 shows the observation in three typical cases: damping (stable), marginal (steady), and growing (unstable).

For large enough values of gas velocity, they found a critical forcing amplitude below which the perturbation is damped, but above which the perturbation grows until it saturates to a larger value. This threshold in forcing amplitude is shown by open circles in Fig. 3.7. The saturation value is shown by filled circles. From this figure, one concludes that linear instability is given by a simple condition $U_g > U_{c,L}$ where $U_{c,L} \approx 4.63\text{m.s}^{-1}$. In contrast, nonlinear instability extends to a larger domain, given by two conditions, $U_g > U_{c,NL}$ where $U_{c,NL} \approx 4.2\text{m.s}^{-1}$, and $A_0 > A_{c,NL}(U_g)$. The unstable region is marked by up arrows in the figure. The part of the unstable region where $U_g < U_{c,L}$ is the region of subcritical instability. Note the striking similarity with Fig. 3.3(b). A similar diagram is found in a wide range of fluid applications, including increasingly complex systems such as the Taylor–Couette cell of polymer solutions [GS98]. A specific introduction for subcritical instabilities of visco-elastic polymers flows is available [MvS07].

In the Kelvin-Helmholtz case, as can be seen in Fig. 3.7, the subcritical region extends by 9% (in terms of U_g) into the linearly stable region. In the case of plane Poiseuille flow, the subcritical region extends by 50% in terms of the Reynolds number into the linearly stable region (linear threshold $R_c \approx 5772$, nonlinear threshold $R_{nl} \approx 2900$ [Man04]). In the case of hot plasmas, we will see that this extension can be even more dramatic.

The existence of a subcritical instability in the case of two layers of immiscible, inviscid and incompressible fluids in relative motion, which is an ideal limit of the latter experiment, was predicted qualitatively by Weissman [Wei79]. The key point is the existence of nonlinear solutions. In addition, he has shown that the nonlinear stability of an initial perturbation is sensitive to the form of the initial perturbation. We will be able to make many similar conclusions for hot plasmas.

Finally, subcritical turbulence can be strong enough to hide underlying linear instabilities. This is the case for Hagen-Poiseuille flow in slightly curved pipes [KBS+15].

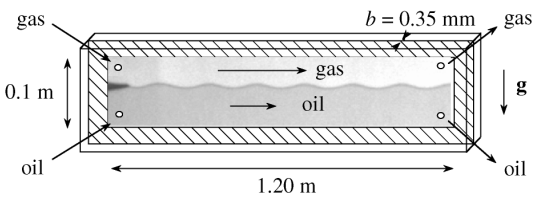

Figure 3.5 – Reproduced from [MGRQR03]. Sketch of the experimental setup to study the subcritical Kelvin-Helmholtz instability in a Hele-Shaw cell. Nitrogen gas and silicon oil are injected from the left into a thin cell between two parallel glass plates. Gravity is shown by an arrow marked $\boldsymbol{g}$. An initial sine perturbation of the interface is imposed at the end of a splitter tongue where fluids meet (left), and observed downstream (right).

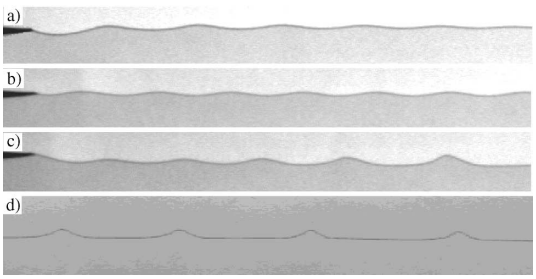

Figure 3.6 – Reproduced from [MGRQR03]. Experimental results are shown. As the wave propagates, its amplitude is either damped (a), or constant (b), or amplified (c), depending on the initial amplitude and on the injection velocity. When the wave is amplified, it eventually saturates to a cnoidal-like wave as shown in a picture taken far downstream (d).

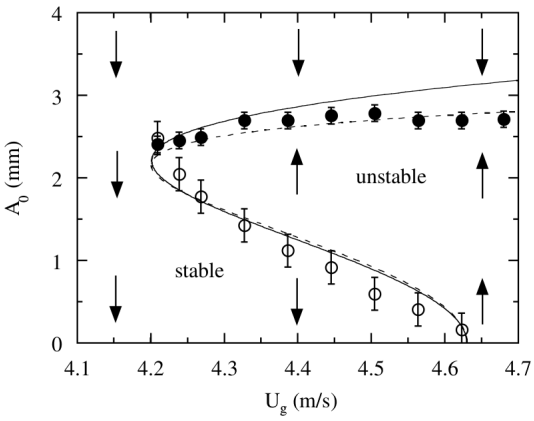

Figure 3.7 – Reproduced from [MGRQR03]. Nonlinear stability diagram in the space of forcing amplitude A_0 against gas velocity U_g (instability drive). Open circles show the amplitude threshold for subcritical instability. Filled circles show the saturation amplitude. The curves are fits of the experimental results by a reduced theoretical model. See the reference for details.

3.3.2 Physical mechanism of subcritical growth in neutral fluids

The physical mechanism of subcritical growth of a finite amplitude perturbation, can take various forms depending on the system.

Let us first focus on two classical flows: plane Couette flow, and plane Poiseuille flow. The setups are illustrated in Fig. 3.8. The plane Couette flow is the laminar flow of a viscous fluid between two parallel plates, one moving with respect to the other. The plane Poiseuille flow, on the other hand, can be seen as a limiting case of the plane Couette flow, where the boundary plates are not moving. The flow is then driven by a pressure gradient imposed between the inlet and the outlet.

In the case of planar Poiseuille flow, Henningson and Alfredsson proposed a mechanism called as "growth by destabilization" [HA87], based on a more general suggestion by Gad-el-Hak [GEHBR81]. In the growth by destabilization mechanism, a spot of finite amplitude fluctuations acts as a local obstruction, modifying the velocity profile in the vicinity of the spot. The modified profile is linearly unstable, and allows the perturbation to grow. The modified profile was later confirmed experimentally by Klingmann and Alfredsson in the

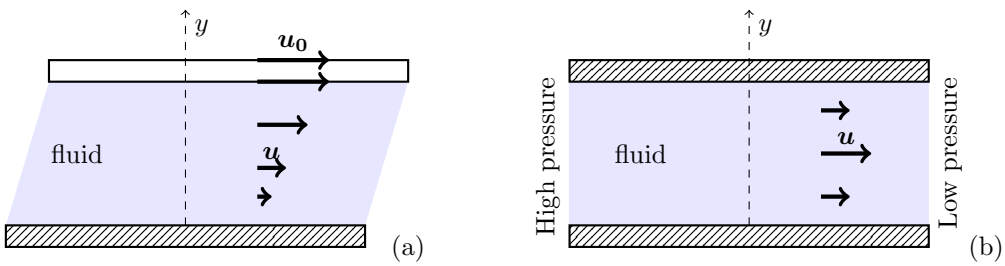

Figure 3.8 – (**a**) Cartoon of the plane Couette flow setup. A fluid is contained between two plates, both normal to the y-axis. The bottom plate is fixed, as illustrated by hashes. The upper plate is moving at a given velocity $\boldsymbol{u_0}$. (**b**) Cartoon of the plane Poiseuille flow setup. A fluid is contained between two plates, both normal to the y-axis, and both fixed. The pressure is higher at the inlet than at the outlet.

case of planar Poiseuille flow [KA90], as well as by Dauchot and Daviaud [DD95] in the case of the plane-parallel Couette flow, suggesting the validity of the mechanism of growth by destabilization.

To give an example of another mechanism, let us now focus on the flow in the laminar boundary layer near a flat plate. It was shown experimentally [SLC01] and explained theoretically [SdS03] how a convecting vortex moving at a fixed distance from the flat plate can drive instabilities in the free streaming flow, when its translational velocity is a fraction of the free-stream velocity [LSC04]. This instability can grow either upstream or downstream from the vortex, depending on the relative signs of vorticity between the mean field and the vortex structure. This suggests an other mechanism of subcritical instability. Suppose that in some region of a flow, a linear instability generates a vortex. The vortex, which is an extremely coherent structure, may then travel without much distortion to a linearly stable region of the flow and in turn drive instabilities by extracting further energy from the mean flow. This latter mechanism of vortex-induced subcritical instability will be particularly important in plasma, where we will meet a kinetic counter-part of fluid vortices.

In wall-bounded shear flows, subcritical transition to turbulence has been quite thoroughly investigated [HLJ93, Man08]. The whole process, called lift-up, is now fairly well understood, from the first local formation of finite-amplitude perturbation, to its evolution toward 3-dimensional structures, and the self-sustaining mechanism of these structures [Wal97, WW05]. Here, let us summarize the self-sustaining mechanism, assuming that the equilibrium fluid velocity is along the x axis, and is sheared in the y direction, $\boldsymbol{u} = u_x(y)\hat{\boldsymbol{x}}$. The mechanism involves three main elements. 1. stream-aligned rolls $\boldsymbol{\delta u} = u_y(y,z)\hat{\boldsymbol{y}} + u_z(y,z)\hat{\boldsymbol{z}}$ sustain perturbations in the z direction of the parallel (streamwise) fluid velocity, $\delta u_x(y,z)$, called as streaks. 2. The latter streaks are linearly instable and lead to a 3D perturbation of the form $\exp \imath\alpha x \boldsymbol{\delta u}(y,z)$. 3. In the nonlinear phase of this instability, the latter 3D perturbation self-interacts via convective acceleration, and transfer its energy to the original stream-aligned rolls, closing the cycle. A similar mechanism was later found in pipe flow [FE03, WK04, HvDW$^+$04].

It should be noted that subcritical transition to turbulence often feature co-existing laminar and turbulent regions. Localized turbulence may or may not expand globally depending on the parameters. Pomeau proposed the concept of spatio-temporal intermittency to interpret these observations [Pom86].

Subcritical instabilities are not limited to laboratory experiments. They have been proposed for shear instabilities of wave-driven, alongshore currents, first in an idealized situation [SVK97], and then for realistic configuration reproducing US coastlines, and including effects of eddy viscosity and bottom friction [DIC04].

3.4 Subcritical instabilities in plasmas

We propose to categorize subcritical instabilities in plasmas as either fluid or kinetic. On the one hand, in collisional plasmas, the particle distribution can be adequately described by fluid equations that give the evolution of its first few velocity moments. As expected, these fluid-like plasmas feature subcritical instabilities, which we refer to as fluid subcritical instabilities, with many similarities with the hydrodynamic instabilities discussed in the previous section. On the other hand, in hot plasmas, collisions can be so rare that the particle distribution readily explores the degrees of freedom in the energy (or velocity) space. This often leads to strong resonances between particles and waves, nonlinear particle trapping, and the spontaneous formation of non-wavelike fluctuations in the particle distributions. These nonlinear kinetic processes give birth to a whole different class of subcritical instabilities, which resemble fluid subcritical instabilities (in terms e.g. of stability diagram with a threshold that is sensitive to the form of the initial perturbation), but with physical mechanisms that involve and couple both the real space and the energy space. That said, hot plasmas still retain a fluid-like character at the lowest order. Therefore, we can expect various combinations of fluid and kinetic subcritical instabilities.

3.4.1 Fluid-like subcritical instabilities in plasmas

The linear theory of drift-waves is well-known. In the presence of magnetic shear, drift-waves are generally linearly unstable in toroidal geometry (thanks to the magnetic curvature), but they are linearly stable in slab geometry. In contrast, 2D fluid simulations of electrostatic drift-wave turbulence in sheared slab geometry, by Biskamp and Walter, showed that finite turbulence levels can be maintained even if the linear growth rates of modes are negative, due to a nonlinear suppression of shear damping [BW85]. The mechanism seems to involve bidirectional spectral energy transfer. Later, Scott found similar results for the collisional counterpart of the drift wave [Sco90]. Drake et al. clarified the nonlinear drive mechanism based on fluid simulations of a 3D model, still in sheared slab geometry [DZB95]. The persistence of turbulence results from a nonlinear amplification of radial flows. Note that this mechanism is self-consistently described by a fluid-like (MHD) model. Similarly with neutral fluids, subcritical turbulence can be strong enough to significantly affect the saturated state even in the presence of supercritical instabilities [BTF00, TBG06].

Highcock et al. developed further the theory of subcritical turbulence in the presence of shear flow, based on local gyrokinetic simulations, in the case of zero magnetic shear [HBS$^+$10, HBP$^+$11]. In that case, the plasma is linearly stable for any finite value of flow shear, but subcritical turbulence can be sustained except for a non-trivial region in parameter space. This regime of quenched turbulence was mapped based on ~ 1500 nonlinear simulations [HSC$^+$12]. It was shown that, though linear theory cannot predict nonlinear stability in general, in some limits it might help reduce the extent of the parameter space that needs to be scanned. Van Wyk et al. argued that subcritical Ion-Temperature-Gradient turbulence is experimentally-relevant for the MAST spherical Tokamak [VWHS$^+$16, vWHF$^+$17]. It is very important to note that this self-sustained turbulence requires an initial perturbation amplitude close to the nonlinear saturation amplitude.

On the other hand, Yagi et al. obtained subcritical instabilities from low initial amplitudes in fluid simulations [YII$^+$95]. They performed 2D simulations of electrostatic current-diffusive interchange turbulence, in a simplified geometry of sheared magnetic field with average bad curvature, including both ion and electron nonlinearities. They observed, not only self-sustained subcritical turbulence due to current diffusion, as predicted by analytic theory [IIF92], but also subcritical growth from initial amplitudes orders-of-magnitude lower than the nonlinear saturation level. Later, Itoh et al. developed an analytical theory for this subcritical instability, which is in comprehensive agreement with numerical simulations [IIYF96]. In particular, they recovered a subcritical bifurcation similar to that of Fig. 3.3.

Another typical example in toroidal devices, is the formation of self-sustaining magnetic islands (the neoclassical tearing mode) [CHK86]. The interested reader is encouraged to explore the relevant literature.

Subcritical instabilities are also found in astrophysical contexts. For example, in radially stratified disks with shear flow, incompressive short-wavelength perturbations can only be sustained nonlinearly [JG05].

Recently, nonlinear non-modal methods of analysis have been developed to predict turbulence, transport and turbulence onset in subcritical cases [FC15, PMT17]. In particular, a wave-like advecting solution was found as an attractor at the threshold amplitude, which promises to clarify the mechanism by which subcritical turbulence is sustained [MPT18].

3.4.2 Kinetic subcritical instabilities

Although fluid-like subcritical instabilities can include kinetic effects, in this section we address subcritical instabilities, which are essentially kinetic in the sense that their growth mechanism relies on nonlinear wave-particle interactions.

Overview

In simplified 1D geometry, many authors have investigated a situation such as the one described in Fig. 3.9, where Landau damping induced by one of the plasma species (electrons here) is competing with inverse Landau damping induced by an other species (ions here).

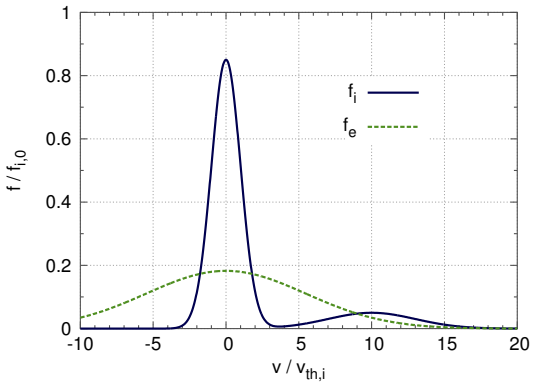

Figure 3.9 – Velocity distribution of ions (solid curve) and electrons (dotted curve) in a two-species plasma, with a population of supra-thermal particles, and equal bulk ion and electron temperatures. The ion/electron mass ratio is reduced to 30 for the sake of readability of the figure.

Based on quasi-linear theory, O'Neil demonstrated the existence of a kinetic subcritical instability of a spectrum of many modes [O'N67]. This is due to the flattening in the velocity distribution, which effectively mitigates Landau damping. He argued that in general, this subcritical instability is possible when the total resonant kinetic energy available for growth is less than the total resonant kinetic energy available for damping.

This theory discarded the role of nonlinear particle trapping, which was later found to be essential in many contexts, as discussed below. Here, by nonlinear particle trapping, we refer to the trapping of charged particles by their own electrostatic potential, which leads to a BGK-like island in phase-space, as introduced in chapter 1.

A BGK island can evolve into a phase-space hole in many situations [Sch86]. A phase-space hole is a BGK-like structure with a local depression of phase-space density within the vortex. It can be seen as a kinetic counterpart of the fluid vortex. Although, in contrast to a fluid vortex, which lives in real (configuration) space, the phase-space hole lives in the phase-space of particle distribution, that is real space and energy (or velocity) space.

Dupree predicted analytically that phase-space holes can grow nonlinearly, and drive subcritical instabilities [Dup78, Dup82, Dup83]. The mechanism is detailed in the next part, 3.4.2.

In part 4.3.2, we further develop the theory of subcritical instabilities in the conditions of Fig. 3.9, with an additional simplification of the model. In the Berk-Breizman model, the damping species is assumed to take only the role of a neutralizing background, and all damping processes are modeled by a linear external dissipation with a fixed rate [BB90a]. In this system, subcritical instabilities have been observed in numerical simulations [BBC$^+$99, LIG09, LIS$^+$10, LI12], and interpreted by analytical theory. Linear Landau damping generates a seed structure in phase-space, which can grow nonlinearly as a result of dissipation acting as a drag force (see next section). In part 4.3.2, based on the energy-phasestrophy relation, Eq. (2.49), we obtain the nonlinear growth rate, as well as the threshold of initial perturbation amplitude (by balancing the growth of a phase-space structure due to wave dissipation, and its decay due to collisions).

In toroidal geometry, we recently showed by analytic calculations the possibility of kinetic subcritical instabilities for the trapped ion mode [KID$^+$17]. As we discuss in chapter 6, the destabilizing role of electron dissipation is then essential. Similarly to the 1D systems discussed above, the mechanism is based on the dissipative nonlinear growth of a hole structure in phase-space [Dup82, TDH90]. The mechanism still works in the present of turbulent decorrelation of such structures [BDT88a, KID$^+$14a], so that this is relevant to the context of granulation [Dup72].

We also investigated another kind of subcritical instability, driven by a nonlinear reduction of damping as well, but due to nonlinear particle trapping in the situation of Fig. 3.9 for a single sine wave [NLG$^+$10]. We showed that this type of subcritical instability is in principle relevant for acoustic modes, such as beta Alfvén eigenmodes or geodesic acoustic modes, under standard tokamak conditions [NGG$^+$10]. However, the subcritical instabilities discussed in this manuscript are in the absence of reduction of damping.

Although these theories of kinetic subcritical instabilities predict essential impacts of subcritical instabilities on turbulence, transport, and mean flows, they do not yet provide

any unambiguous macroscopic signature, which could help discriminate these impacts from the similar impacts of linearly unstable modes. Moreover, there is no indication that the instability being subcritical is a key feature of the resulting turbulence, transport and flows. In subsection 3.4.3, we review the first experimental evidence of strong effect of kinetic subcritical instability, in a context where subcriticality does come with a key impact: abrupt growth. But let us first detail the physical mechanism of nonlinear growth of a phase-space hole, which is responsible for the most abrupt kinetic subcritical instabilities.

Nonlinear growth mechanism of a phase-space hole

Let us focus on a 1D plasma with ions and electrons, but unlike the situation of Fig. 3.9, here both ion and electron velocity distributions are Gaussian, and the electron distribution is shifted by a given mean velocity. This is the situation investigated in more details in chapter 5. Fig. 3.10 shows the initial, or equilibrium velocity distributions $f_{0,i}$ and $f_{0,e}$, as well as the distributions at some arbitrary time $t = t_1$ in the presence of a single electron hole. The electron hole can grow nonlinearly in this situation, where, in the vicinity of the hole, the electron velocity gradient is positive and the ion velocity gradient is negative. The impact on the ion distribution of the electron hole is represented as a barely visible flattening. Fig. 3.11 is a cartoon of the electron hole in phase-space. Trapped electrons form a vortex structure, with a deficit of phase-space density (in other words a negative perturbation of the distribution function, $\delta f < 0$) inside the eye-shaped separatrix. Therefore the electron density features a local deficit as well, which is consistent with the local bump of potential, which in turn is consistent with the trapping of electrons. Therefore the BGK-like vortex forms a self-consistent, self-sustained (in the absence of collisions) structure. Here, to simplify the discussion, the perturbation in the ion density is assumed to be negligible.

The nonlinear mechanism of growth of this electron hole can be understood based on the latter figures, 3.10 and 3.11.

Firstly, if the hole changes its mean velocity slowly enough, trapped electrons within the hole will move along with the hole. Detrapping is rare enough for slow variations of the velocity of the hole. Since the Vlasov equation states that the distribution function f is conserved along particle orbits, the value of f at the bottom of the hole will remain constant even as the hole accelerates or decelerates. Therefore, since the equilibrium electron distribution has a positive slope in the vicinity of the hole, the hole deepens if its mean velocity increases, as schematized in Fig. 3.10.

Secondly, in this configuration, there is a force, which does accelerate the hole, leading to its growth. Here the impact of electron hole on ions is essential. The ion trajectories are shown in the bottom of Fig. 3.11. The positive charge of the electron hole scatters ions in both directions away from the center of the hole. Due to the negative gradient of the ion velocity distribution, there is an imbalance between decelerated ions and accelerated ions, such that ions as a whole gain momentum. Electrons, on the contrary, lose momentum (ensuring total momentum conservation). The result for the electron hole, which has a negative mass, is to accelerate.

Let us give a rough estimate of the nonlinear growth rate, by noting u the velocity of

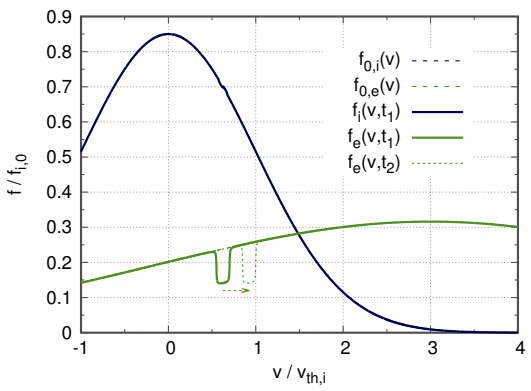

Figure 3.10 – Velocity distribution of ions and electrons in a two-species plasma, with a mean velocity drift. The equilibrium distributions are noted $f_{0,i}$ and $f_{0,e}$. The ion/electron mass ratio is reduced to 10 for the sake of readability of the figure. An electron hole is drawn schematically at some arbitrary time $t = t_1$. and the mechanism of its growth from $t = t_1$ to a later time t_2 is explained in the text as the result of a drag force due to the scattering of ions by the electron hole.

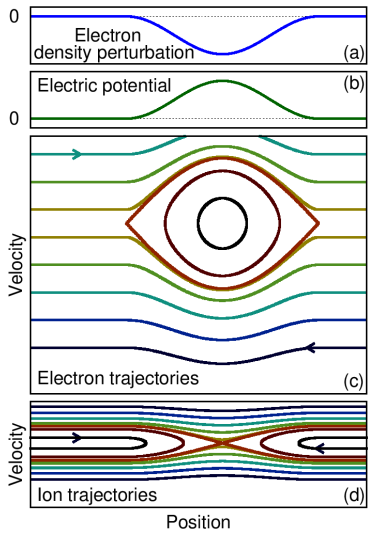

Figure 3.11 – Cartoon of an electron hole, in the reference frame of the hole. (a) Electron density perturbation. (b) Electric potential. (c) Electron trajectories. (d) Ion trajectories. Here the scales are consistent with a mass ratio $m_i/m_e = 10$.

the hole, h the hole depth ($h > 0$), Δv the width of the hole, ϕ_0 the amplitude of the trapping potential, and $f'_{0,s} = df_{0,s}/dv|_{v=u}$ the equilibrium velocity gradient for species s in the vicinity of the hole. A simple calculation of particle orbits based on energy conservation yields that Δv is proportional to $\sqrt{\phi_0}$. The positive charge of the electron hole scatters ions, which, because of the negative gradient of $f_{0,i}(v)$, leads to a positive force on ions, $F^{e\to i}$ proportional to $-\phi_0^2 f'_{0,i}$.The equal and opposite reaction is a drag force on electrons $F^{i\to e} = -F^{e\to i}$. As a result the electron hole accelerates at a rate $\dot{u} = F^{i\to e}/M_{hole}$, where M_{hole} is the negative mass of the hole, which is proportional to $-h\Delta v$. Since the trapped-electron distribution function remains constant, the hole deepens at a rate dh/dt proportional to $\dot{u} f'_{0,e}$. Finally, Poisson equation shows that ϕ_0 is roughly proportional to $h\Delta v$, therefore h is proportional to $\sqrt{\phi_0}$. Putting the above relations of proportionality together, we obtain a growth rate

$$\gamma \equiv (1/h)dh/dt = (1/\phi_0)d\phi_0/dt = -C f'_{0,e} f'_{0,i}\sqrt{\phi_0}, \tag{3.6}$$

where C is a factor which is roughly constant.

The full calculation is tedious, and takes into account additional effects such as potential screening, and the retroaction of the growth on the drag force [Dup83, Tet83]. However the final result is consistent with the above simplified mechanism.

This nonlinear growth of phase-space holes was confirmed by Berman et al. in numerical simulations of the ion-acoustic instability in 1D collisionless electron-ion plasmas with a velocity drift (but no supra-thermal population) [BTDBG82]. They performed Lagrangian (particle-in-cell) simulations with an initial sine perturbation. They found that a subcritical instability with a very small threshold in amplitude was developing, even for velocity drifts much below the linear threshold. Recently, we found by both Lagrangian and semi-Lagrangian simulations that these results were attributable to the spurious numerical noise due to the low number of particles that could reasonably be calculated given the computing resources of the '80s [LDK14a]. However, with modern computing [Les16], we still obtained unambiguous subcritical instabilities, given an initial sine perturbation with large initial amplitude ($e\phi_0/T \sim 1$), or, more importantly, given an initial BGK-like perturbation even with small initial amplitude ($e\phi_0/T \sim 10^{-2}$). We describe these findings in chapter 5.

For the origin of a large-enough initial perturbation, or initial BGK-like fluctuations, we have discussed three plausible scenarios [LDK14a]. The first scenario is a growth from e.g. thermal fluctuations, which is limited to an initial barely stable equilibrium. The second scenario is the growth of a hole, which would have been externally driven by the experimental setup or convected from a region of linear instability. The third scenario is the case of self-sustained turbulence, as plasma conditions go from linearly unstable to subcritical on a slow time-scale.

3.4.3 Hybrid Fluid-Kinetic subcritical instabilities

Despites decades of theoretical advances, experimental observations of kinetic subcritical instabilities have been lacking, probably in part because it is difficult to measure the velocity-space distribution in relevant conditions. However, we recently identified a good candidate experimentally [IIO+16] and interpreted it by theory as a subcritical instability driven by a combination of fluid and kinetic nonlinearities [LII+16b].

In the helical plasma of the Large Helical Device (LHD), bursts of geodesic acoustic mode driven by energetic particles (EGAM) are sometimes accompanied by a much more abrupt, large-amplitude burst of an other mode. The observation cannot be explained by conventional mechanisms such as nonlinear coupling of turbulence alone [DIIH05], or resonant interaction with energetic particles [Fu08]. In particular, the measurements point to a threshold in amplitude of the EGAM for the destabilization of the abrupt mode.

We proposed a theoretical interpretation based on a reduced 1D model, including both fluid and kinetic nonlinearities [LII+16b]. The model qualitatively recovers the experimental observations in terms of temporal evolution and phase relation, with input parameters consistent with the measured plasma parameters. Within the framework of this model, we found that the abrupt burst belongs to a new class of subcritical instability, which is hybrid between fluid and kinetic subcritical instabilities. In fact, we found two distinct regimes, depending mainly on collisionality [LII+16a]. For very low collisionality, nonlinear fluid coupling between modes provides a seed perturbation, which evolves due to particle trapping into a phase-space hole, then grows, dominated by kinetic nonlinearity. In contrast, for slightly higher collisionality, the subcritical instability requires both fluid and kinetic nonlinearities to continuously collaborate. The LHD observation was interpreted as a manifestation of the latter one. We describe these findings in chapter 4 (section 4.4).

In this context, it is the fact that the instability is subcritical, which yields such abrupt growth, with a growth-rate one order-of-magnitude above that of its supercritical counterpart.

3.5 Conclusions

Subcritical instabilities are ubiquitous in neutral fluids and in plasmas, and merit attention since the access to free energy, and the spectrum of turbulence, are ultimately nonlinear issues. Subcritical instabilities have common characteristics, such as a threshold in amplitude, and a growth rate that increases with increasing amplitude. However, they can originate from a wide variety of physical mechanisms.

In plasmas, subcritical instabilities are of great interest for their essential impact on the onset of turbulence [Lan46, IIK+16], structure formation [CH93], anomalous resistivity [LDK14a, LDK14b], and potentially, turbulent transport [KID+17].

To widen the scope, we invite the interested reader to look into the literature on subcritical instabilities in other areas, which we have not discussed in this chapter. Let us give a non-exhaustive list of examples:

— the follower-loaded double pendulum in vibrational mechanics [I+04],
— the dynamics of railway vehicles [XjTL15],
— acoustic waves [ADC05] and flame dynamics [EDB+18] in combustion chambers,
— spin-waves in magnetic nanocontact systems [CFLDA09],
— the zigzag transition for confined repelling particles in quasi-1D chemical physics [SDSGL13, DCSJ15].

Chapter 4

Energetic-particle-driven modes in 1D

Energetic Particles (EPs) in an ignited tokamak include α-particles and high-energy ions injected by heating devices. EPs drive Magneto-Hydrodynamic (MHD) macroscopic modes such as Alfvén Eigenmodes (AE) or geodesic acoustic modes (GAM). Examples include the Toroidal Alfvén Eigenmode (TAE) [CCC85], the Global Alfvén Eigenmode (GAE), the Beta-induced Alfvén Eigenmode (BAE), and the EP-driven GAM (EGAM). They transport EPs, and couple with background turbulence. They impact fuelling and the wall integrity, and ultimately the efficiency of a fusion reactor. Understanding the linear and nonlinear evolution of EP-driven modes is crucial to predict and control these impacts. Indeed, transport and loss of fast particles depend on both the nonlinear saturation amplitude and the kind of nonlinear behaviour.

In a toroidal device, the structure, linear frequency, and linear growth rate of an EP-driven mode are determined by 3D calculations. These linear properties evolve on a slow time scale of mean field evolution ($\sim$ 100ms). In contrast, nonlinear wave-particle interactions, which determine the saturated state in the single-mode limit, happen on a fast time scale ($\sim$ 1ms).

Near the resonant surface, it is possible to obtain a new set of variables in which these wave-particle interactions are treated perturbatively by a 1D Hamiltonian in two conjugated variables [BBP97a, BBP$^+$97c, WB98], if we assume an isolated single resonance, and by taking advantage of the timescale separation. This is done by a perturbative expansion of a gyrokinetic Hamiltonian around a resonant surface in phase-space, as we describe in section 4.1.

In this sense, the problem of EP-driven modes is homothetic to the well-known paradigm of a single mode bump-on-tail instability. The Berk-Breizman (BB) model [BBY93b, BBP96, BBP97a, BBP$^+$97c], which we describe in Sec. 4.2, is a generalization of the simple bump-on-tail Vlasov-Poisson model for a single mode, where we take into account two essential ingredients:

— a prescribed damping of the wave energy at a constant rate γ_d, with the aim of accounting for background dissipative mechanisms,

— a collision operator, with the aim of modeling Coulomb collisions as perceived by EPs near the resonant surface.

Hence, although the BB model describes wave-particle interactions between EPs and an electrostatic wave in a 1D plasma, it also provides a basis for estimating the nonlinear saturation amplitude, and the qualitative nonlinear behaviour of an isolated EP-driven mode in toroidal fusion plasmas. In the 2010's, observed quantitative similarities between BB nonlinear theory and both 3D simulations [WB98, PBG$^+$04] and experiments [FBB$^+$98, HFS00] already indicated the validity of this reduction of dimensionality. Since then, there is a growing body of evidence, some of which described in this chapter, which further confirms the usefulness of this approach, as a complementary approach to heavier 3D analysis. Although we focus on 3D EP-driven modes, the BB model is also applicable to the traveling wave

tube "quasilinear experiment" with a lossy helix [TDM87].

The apparent simplicity of the equation system of the BB model hides surprisingly rich physics. In the stable case, when the perturbation is small, linear theory predicts exponential decay of the wave amplitude, which in the absence of collisions and external damping is known as Landau damping [Lan46]. In the unstable case, on the contrary, linear theory predicts exponential growth of the wave amplitude. Then, trapping of resonant particles significantly modifies the distribution function and an island structure appears in phase-space. The following nonlinear saturation is determined by a competition among the drive by resonant particles, the external damping, the particle relaxation which tends to recover the initial positive slope in the distribution function, and particle trapping which tends to smooth it. As a result, the long-time state bifurcates in the parameter-space between three kinds of behaviours, namely steady-state, periodic, or chaotic responses [BBP96].

In addition, chaotic solutions can display rapid, significant, continuous shifting of the mode frequency. This is called as *chirping*. Chirping has been shown to correspond to the formation and nonlinear evolution of holes and clumps in the distribution function. Theory relates the time evolution of frequency shift with linear drive γ_L and damping rate γ_d, when holes and clumps evolves on a slow timescale compare to that of the bounce motion of particles trapped within [BBP97b].

Finally, nonlinear wave-particle interactions can drive a kinetic subcritical instabilities due to the growth of holes and clumps in the distribution function, as we mentioned in chapter 3 (see 3.4.2). We investigate their onset conditions in subsection 4.3.2.

In toroidal magnetic fusion experiments, chirping is an ubiquitous feature of EP-driven modes. For example, chirping TAEs with an extent of chirping of 10-30% (with respect to the linear mode frequency) have been observed in the plasma core region of tokamaks DIII-D [Hei95], JT-60 Upgrade (JT-60U) [KKK+99], the Small Tight Aspect Ratio Tokamak (START) [MGS+99], the Mega Amp Spherical Tokamak (MAST) [PBG+04], the National Spherical Torus Experiment (NSTX) [FBD+06], and in stellerators Compact Helical Stellerator (CHS) [TTT+99], and the Large Helical Device (LHD) [OYT+06]. In general, two branches coexist, with their frequency sweeping downwardly (down-chirping) for one, upwardly (up-chirping) for the other. Chirping TAEs have been reproduced in three-dimensional (3D) simulations with a drift-kinetic perturbative code [PBG+04], and with a hybrid MHD/drift-kinetic code [TSTI03]. In many experiments, chirping events are quasi-periodic, with a period in the order of the millisecond. Frequently, asymmetric chirping has been observed, with the amplitude of down-chirping branches significantly dominating up-chirping ones. Qualitatively similar chirping modes are spontaneously generated within the BB model.

In this chapter, I describe my main contributions to the nonlinear theory of the BB model, and its application to EP-driven modes in tokamaks and stellerators. Sec. 4.1 details how wave-particle interactions may be reduced to a 1D formalism. In Sec. 4.2, we recall the equations of the BB model, in both full-f and δf approaches, and describe our numerical simulation code. In Sec. 4.3, we focus on nonlinear theory in the case of a single mode, and in particular concerning subcritical instabilities and chirping. We apply the energy-phasestrophy relation to obtain analytical expressions for the subcritical threshold and for the nonlinear growth-rate in cases where a single phase-space structure dominates. We investigate chirping characteristics (velocity, lifetime, period), including the effects of collisions. We develop a simple semi-analytic model of hole/clump pairs in the presence of dynamical friction and velocity-diffusion, and apply it to clarify the mechanism of relaxation oscillations associated with chirping bursts. We describe and apply a method for estimating local linear drive, external damping rate and collision frequencies based on experimental observations of chirping EP-driven modes. In Sec. 4.4, we develop a model to explore how one linearly unstable mode may transfer its energy to another, stable mode, triggering a subcritical instability. The model expands the BB model to two interacting modes, by combining kinetic description and nonlinear fluid coupling. Finally, in Sec. 4.5, we discuss a few additional phenomena in the presence of many modes.

4.1 From 3D to 1D

Depending on the experimental conditions, EP-driven modes in toroidal fusion plasmas can be isolated in the sense that they are well localized radially, and they don't interact with other modes.

Let us take the example of a Toroidal Alfvén Eigenmode (TAE) composed of a number of $(n,\, m)$ modes, where n is the toroidal mode number and m is the poloidal mode number. If we consider only small toroidal mode numbers, then neighboring n and $n+1$ modes are isolated. Let us consider a single toroidal mode number n. On the one hand, since on a flux surface $r = r_m$ where the component m of the mode structure is approximately centered, the safety factor is $q(r_m) = (2m+1)/(2n)$, then we can estimate the distance $\Delta r = r_{m+1} - r_m$ between two neighboring m modes by writing $\Delta r\, q' \approx q(r_m) - q(r_{m+1})$, as

$$\Delta r \;\approx\; \frac{1}{nq'}. \tag{4.1}$$

On the other hand, the characteristic width of TAE modes δr is of the order of $\delta r \sim r_m^2/nqR_0$ [CCC85]. Hence, for typical parameters, $\delta r/\Delta r \sim (r_m/R_0)S \ll 1$, where $S \equiv rq'/q$ is the magnetic shear. Thus, TAEs have a two-scale radial structure, the larger scale corresponding to the envelope of the TAE. In our analysis, we assume that the number of m harmonics involved is small enough to consider resonances one by one, as isolated $(n,\, m)$ mode. The latter hypothesis is reasonable for sufficiently core-localized, low-n TAEs. We must keep in mind, though, that high-n TAEs are likely to be destabilized in future devices such as ITER, in which case it may be necessary to take into account multiple-wave resonances.

Therefore, let us consider the case of an isolated EP-driven mode, dominated by a single pair of toroidal and poloidal mode numbers. The resonance condition $\omega = \boldsymbol{n}\cdot\boldsymbol{\omega}_{\mathbf{eq}}$, as we recall from Eq. (2.9), defines a resonant phase-space surface $\boldsymbol{J} = \{\boldsymbol{J}_R$ such that $J_{R3} = G(J_{R1}, J_{R2})\}$, where G is a function whose expression depends on the eigenmode.

4.1.1 Reduction of the perturbed Hamiltonian

In Ref. [BBP95b] the perturbed Hamiltonian of an isolated shear Alfvén wave (in the zero beta limit) is put in the form

$$\delta H \;=\; V(\boldsymbol{J})\,\cos(\boldsymbol{n}\cdot\boldsymbol{\alpha} \,-\, \omega t). \tag{4.2}$$

In the appendix of Ref. [LII+16a], we describe a similar calculation for the case of an EGAM. To summarize, developing the perturbed 3D Hamiltonian δH for an EGAM, in the neighborhood of the flux surface of peak electric potential, yields, as a zeroth-order-in-$\partial H_{\mathrm{eq}}/\partial J_\theta$ approximation, and after substituting the resonance condition $\omega = m\omega_\theta$, a 1D Hamiltonian of the form of Eq. 4.2, with $\boldsymbol{n}\cdot\boldsymbol{\alpha} = m\theta$ and $\boldsymbol{n}\cdot\boldsymbol{J} = mJ_\theta$. Here, J_θ is the canonical poloidal angular momentum.

Both problems can then be reduced to one action and one angle [Lic69, GDPN+08], by performing a canonical transformation $\boldsymbol{J}\cdot\mathrm{d}\boldsymbol{\alpha} - H\mathrm{d}t = \boldsymbol{I}\cdot\mathrm{d}\boldsymbol{\xi} - H'\mathrm{d}t + \mathrm{d}S$ with the generating function

$$S \;=\; -\boldsymbol{I}\cdot\boldsymbol{\xi} \;+\; I_3(\boldsymbol{n}\cdot\boldsymbol{\alpha} \,-\, \omega t) \;+\; I_1\alpha_1 \;+\; I_2\alpha_2 \;+\; F(I_1, I_2)\alpha_3. \tag{4.3}$$

This procedure yields,

$$\begin{aligned} J_1 &= I_1 \,+\, n_1\, I_3 & \qquad \xi_1 &= \alpha_1 \,+\, \alpha_3\, \partial_{I_1} F \\ J_2 &= I_2 \,+\, n_2\, I_3 & \qquad \xi_2 &= \alpha_2 \,+\, \alpha_3\, \partial_{I_2} F \\ J_3 &= F(I_1, I_2) \,+\, n_3\, I_3 & \qquad \xi_3 &= \boldsymbol{n}\cdot\boldsymbol{\alpha} \,-\, \omega t, \end{aligned}$$

and $H \;=\; H' \,+\, \omega\, I_3$. Thus, near the resonant phase-space surface, $\boldsymbol{J} \;=\; \boldsymbol{J}_R \,+\, I_3\,\boldsymbol{n}$, and we can expand the new Hamiltonian around this surface,

$$\begin{aligned} H'(\boldsymbol{\xi}, \boldsymbol{I}) \;&=\; H_{\mathrm{eq}}(\boldsymbol{J}_R \,+\, I_3\,\boldsymbol{n}) \,+\, V(\boldsymbol{J}_R \,+\, I_3\,\boldsymbol{n})\cos\xi_3 \,-\, I_3\,\omega & (4.4) \\ &=\; H_{\mathrm{eq}}(\boldsymbol{J}_R) \,+\, I_3\,(\boldsymbol{n}\cdot\boldsymbol{\omega}_{\mathbf{eq}}(\boldsymbol{J}_R) \,-\, \omega) \,+\, \frac{1}{2} D\, I_3^2 \\ &\qquad\qquad + V(\boldsymbol{J}_R \,+\, I_3\,\boldsymbol{n})\cos\xi_3, & (4.5) \end{aligned}$$

with $D(\boldsymbol{J}_R) \equiv l_i l_j \partial_{J_i} \partial_{J_j} H_{\rm eq}(\boldsymbol{J}_R)$.

If the variations of $H(\boldsymbol{J})$ are small around $\boldsymbol{J}_R$, we can replace $V(\boldsymbol{J}_R + I_3\,\boldsymbol{n})$ by $V(\boldsymbol{J}_R)$ in the latter expression, and obtain the new Hamiltonian $H' = H_{\rm eq}(\boldsymbol{J}_R) + \delta H_{,\boldsymbol{J}_R}(\xi_3, I_3)$, with

$$\delta H_{,\boldsymbol{J}_R}(\xi, I) \;\equiv\; \frac{1}{2}\, D\, I^2 \;+\; V \cos\xi. \tag{4.6}$$

Thus, the problem of interactions between EPs and the EP-driven mode has been reduced to a 1D Hamiltonian problem for the angle-action variables $(\xi,\, I) \equiv (\xi_3,\, I_3)$.

4.1.2 Reduction of the collision operator

A first, simple model is obtained by reducing the effects of collisions to the recovery of an equilibrium energetic particle distribution, with a recovery rate $\nu_a(v)$. However, as we will see in subsection 4.3.6, this is insufficient to recover the qualitative behavior of EP-driven modes in general.

A more rigorous treatment of collision processes is obtained if we project a collision operator that describes Coulomb collisions perceived by energetic ions, on the resonant phase-space surface. We consider collisions on energetic particles by thermal electrons, main ions, and impurities, and describe them by a Fokker-Planck collision operator [HS02] that acts on the distribution $f(\boldsymbol{x}, \boldsymbol{v}, t)$ of energetic particles. The Fokker-Planck collision operator is based on the fact that, in a tokamak plasma, collisions are dominated by binary Coulomb collisions with small-angle deflection. This collision operator can be projected on the resonant flux surface of a given TAE [BBP97a, LBS09]. We consider a TAE with toroidal mode number n, resulting from the coupling of m and $m+1$ poloidal modes. We consider strongly co-passing beam particles that resonate with the TAE at a velocity $v \approx v_\parallel = v_A$, where v_A is the Alfvén velocity. In Ref. [LIS+10], we give the details of the procedure to project the collision operator in spherical coordinates onto the resonant flux surface. It involves a Jacobian

$$\mathcal{J} \;=\; \frac{m S m_b v_\parallel}{2 r^2 e_b B_0}, \tag{4.7}$$

where $S \equiv r q'/q$ is the magnetic shear. Here e_s and m_s are charge and mass of a species s, respectively, and b stands for beam particles.

This procedure yields

$$\left.\frac{df}{dt}\right|_{\rm coll.} \;=\; \nu_f^2\, \frac{\partial f}{\partial \Omega} \;+\; \nu_d^3\, \frac{\partial^2 f}{\partial \Omega^2}, \tag{4.8}$$

where $\Omega = \boldsymbol{n} \cdot \boldsymbol{\omega}_{\rm eq}$. Dynamical friction rate ν_f and collisional diffusion rate ν_d are obtained as

$$\nu_f^2 \;=\; v_\parallel\, \mathcal{J}\, \left(2\nu_\parallel \;+\; \nu_{\rm slow} \;-\; \nu_{\rm defl}\right), \tag{4.9}$$

$$\nu_d^3 \;=\; \frac{v^2}{2}\, \mathcal{J}^2\, \left(\nu_\parallel \cos\Theta \;+\; \nu_{\rm defl} \sin\Theta\right). \tag{4.10}$$

where ν_{defl}, ν_{slow} and $\nu_\parallel$ are pitch-angle scattering, slowing-down, and parallel velocity diffusion rates, respectively, $v_\parallel$ is the parallel velocity of energetic particles, and Θ is the angle of velocity with respect to magnetic field.

We assume Maxwellian background distributions, with same temperature T_0. Typical experiments satisfy the following ordering of thermal velocities, $v_{Ti} \ll v_A \ll v_{Te}$, while the beam energy E_b is much larger than T_0. With these assumptions, around the resonance,

$$\nu_f^2 \;=\; \frac{v_\parallel \mathcal{J}}{v^3} \sum_s \frac{n_s \gamma_{bs}}{m_s} \left[\operatorname{erf}\eta_s \;-\; \frac{2\eta_s}{\sqrt{\pi}}\, e^{-\eta_s^2}\right], \tag{4.11}$$

$$\nu_d^3 \;=\; \frac{\mathcal{J}^2}{2v^3} \sum_s \frac{n_s \gamma_{bs}}{2 m_b \eta_s^2} \left[\left((2\eta_s^2 - 1) v_\perp^2 + 2 v_\parallel^2\right) \operatorname{erf}\eta_s \;+\; \frac{2\eta_s}{\sqrt{\pi}}\, (v^2 - 3 v_\parallel^2)\, e^{-\eta_s^2}\right], \tag{4.12}$$

where $\eta_s \equiv v/v_{Ts}$, $v_\parallel = v_A$,

$$\gamma_{bs} = \frac{4\pi e_b^2 e_s^2 \log\Lambda}{m_b}, \tag{4.13}$$

and $\log\Lambda$ is the Coulomb logarithm.

The equivalent collision operator in the Berk-Breizman model is obtained by substituting $\Omega = kv$ in Eq. (4.8).

4.1.3 Reduction of the background damping mechanisms

Since the time-scale of fast-particle evolution is much faster than background thermal populations evolution, these two dynamics are decoupled. Hence we can reasonably treat the effects of background damping in an extrinsic way. We assume that all background damping mechanisms affect linearly the wave energy $\mathcal{W}$,

$$\frac{\mathrm{d}\mathcal{W}}{\mathrm{d}t} = -2\,\gamma_d\,\mathcal{W}(t). \tag{4.14}$$

Damping includes mechanisms such as radiative damping, whose strength depends on the frequency [MM92]. Hence, in a rigorous model, γ_d should be a function of ω. However, theory needs to be developed before this complex interplay can be taken into account. Thus, we limit our framework to cases where γ_d can be treated as a constant. This framework is consistent with a fixed mode frequency.

4.1.4 Limitations

Firstly, the mathematical reduction of dimensionality from 3D to 1D assumes an isolated single mode. Further, since it is based on a development in the neighbourhood of a fixed resonant phase-space surface, we must also assume a fixed mode structure, implying a fixed MHD equilibrium. Hence, the BB model with time-independent input parameters cannot reproduce the evolution of EP-driven modes on a timescale of MHD equilibrium evolution, which is of the order of the second on large devices. However, this model can still describe bifurcations on a shorter timescale where the linear growth rate can be treated as a linear function of time as in Ref. [FBB+98]. More advanced models update the mode structure as the frequency chirps, allowing the study of long-range chirping [MQBH20]. We must also require a low wave amplitude, such that the nonlinear redistribution of energetic particles does not significantly alter the mode structure and frequency. In practice, if the eigenfrequency of a low-amplitude EP-driven mode observed in experiments stays nearly constant during a certain time-window, we infer that the fixed-mode-structure assumption is satisfied for this time-window, since the linear frequency of such modes is very sensitive to equilibrium plasma parameters such as the q profile [SHC95, KKK+99].

In the case of chirping, which is the case we apply to experiments, a fixed mode structure requires that the frequencies associated with the sweeping holes and clumps do not approach the shear Alfvén continuum frequencies. Even when the latter condition is satisfied, it is sometimes argued that since the frequency is changed, so must be the mode structure. However, we must distinguish at least three classes of frequency sweeping, namely, slow frequency sweeping (slow-FS), fast frequency sweeping (fast-FS), and so-called abrupt large-amplitude events (ALE) [SKT+01], although it is not clear for the latter if the frequency does sweep. In the case of JT-60U shot number E32359, which we analyze in subsection 4.3.6, slow-FS have a timescale of $100 - 200$ ms, and their frequency is correlated with bulk equilibrium variations, therefore they are out of the scope of the above reduce model. Fast-FS have a timescale of $1 - 5$ ms, and the associated redistribution of energetic ions is relatively small [STI+02], therefore they are consistent with a fixed-mode-structure hypothesis. Although the occurrence of fast-FS and ALEs seems to be linked, ALEs are identified as Energetic Particle-driven Modes (EPMs) [BFV+07], have significantly larger amplitude and shorter timescale ($200 - 400$ μs), and induce significant loss of energetic ions, and are out of the scope of this work since we assume a weak drive and a constant density of energetic ions in the BB model.

Finally, modeling all background damping mechanisms as an extrinsic, fixed linear damping on the wave is a strong assumption, since a nonlinear evolution of γ_d has been shown to have significant effect on the behaviour of the wave [NLG+10, NGG+10]. A more robust validation of this assumption requires improved theoretical understanding of the damping mechanisms. We must assume that γ_d does not depend neither on the wave amplitude, nor on the energetic population. In the case of frequency sweeping, this assumption is clearly violated if the nonlinear modification of frequency is of the order of the linear frequency, especially if a chirping phase-space structure approaches the shear Alfvén wave continuum, where the damping rate depends largely on the frequency.

4.2 The Berk-Breizman model

Depending on the application, it is convenient to cast the BB model either in a self-consistent form (full-f) or in a perturbative form (δf).

4.2.1 Normalization

For concision, we normalize frequencies to the plasma frequency ω_p and lengths to the Debye length $\lambda_{\rm D} = v_{\rm th}/\omega_p$. Here $\omega_p^2 = n_0 e^2/(\epsilon_0 m)$, e, m, and n_0 are the charge, mass, and total density, respectively, of the evolving species, and $v_{\rm th}$ is a typical thermal velocity. We also normalize densities to n_0, energies to $m v_{\rm th}^2$, particle distributions to $n_0/v_{\rm th}$, and electric fields to $m v_{\rm th}^2/(e\lambda_{\rm D})$.

4.2.2 Full-f BB model

We consider a 1D plasma with a distribution function $f(x, v, t)$. In the initial condition, the velocity distribution,

$$f_0(v) \;\equiv\; \langle f\rangle|_{t=0} \;=\; f_0^M(v) + f_0^B(v), \tag{4.15}$$

where $\langle f\rangle$ is the spatial average of f, comprises a Maxwellian bulk and a Gaussian beam of high-energy particles,

$$f_0^M(v) \;=\; \frac{n_M}{v_{TM}\sqrt{2\pi}}\, e^{-\frac{1}{2}\left(\frac{v}{v_{TM}}\right)^2} \quad \text{and} \quad f_0^B(v) \;=\; \frac{n_B}{v_{TB}\sqrt{2\pi}}\, e^{-\frac{1}{2}\left(\frac{v-v_B}{v_{TB}}\right)^2}, \tag{4.16}$$

where n_M and n_B are bulk and beam densities, which verify $n_M + n_B = 1$, v_{TM} and v_{TB} are thermal velocities of bulk and beam particles, and v_B is the beam drift velocity. To ensure charge neutrality, we assume a fixed background population of the opposite charge with a density $n_0 = 1$. Fig. 4.1(a) illustrates two typical initial distribution functions.

The evolution of the distribution is given by the kinetic equation

$$\frac{\partial f}{\partial t} + v\,\frac{\partial f}{\partial x} + E\,\frac{\partial f}{\partial v} \;=\; \mathcal{C}(\delta f), \tag{4.17}$$

where E is the electric field, $\delta f \equiv f - f_0$, and $\mathcal{C}(\delta f)$ is a collision operator.

In this work, we consider either one of the following two collision models. On the one hand, a large part of existing theory for the BB-model deals with collisions in the form of a Krook operator [BGK54],

$$\mathcal{C}_{\rm K}(\delta f) \;=\; -\nu_a(v)\delta f, \tag{4.18}$$

which is a simple model for collisional processes that tend to recover the initial distribution at a rate ν_a, including both source and sink of energetic particles. If we assume cold and adiabatic bulk plasmas, $\nu_a(v)$ acts only on the beam. Reflecting this situation, we design the velocity dependency of ν_a such that it is constant in the beam region, and zero in the bulk region.

On the other hand, the one-dimensional projection of a Fokker-Plank operator, Eq. (4.8) includes a dynamical friction (drag) term and a velocity-space diffusion term,

$$\mathcal{C}_{\rm FP}(\delta f) \;=\; \frac{\nu_f^2(v)}{k}\frac{\partial \delta f}{\partial v} \;+\; \frac{\nu_d^3(v)}{k^2}\frac{\partial^2 \delta f}{\partial v^2}, \tag{4.19}$$

where k is the wave number for the resonance under investigation, and with similar velocity-dependence for ν_f and ν_d. In this sense, it is a more realistic collision operator than the Krook operator.

The electric field E is assumed to be a single harmonic wave, of wave number k, reflecting the situation of an isolated single EP-driven mode. The displacement current equation (DCE),

$$\frac{\partial E}{\partial t} \;=\; -\int v\delta f \mathrm{d}v \;-\; 2\,\gamma_d\,E, \tag{4.20}$$

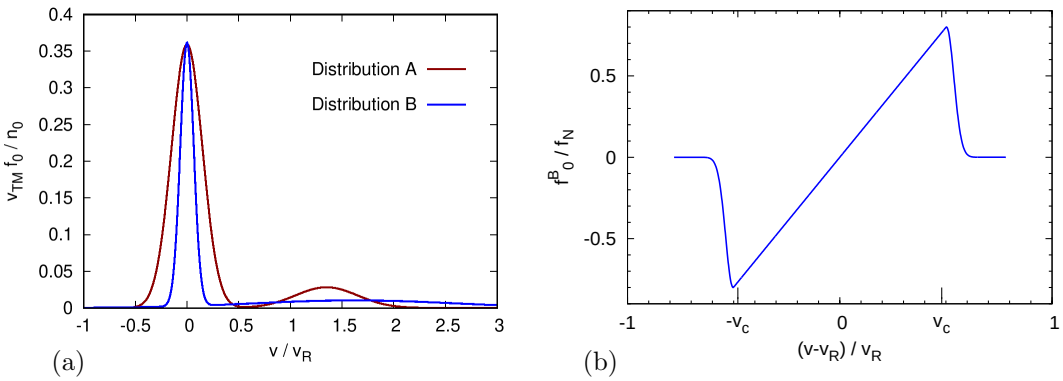

Figure 4.1 – Examples of initial distribution function. Here, velocity is re-normalized to the resonant velocity v_R. (a) Full-f case. (b) δf case, where $f_N \equiv \gamma_{L0}/(\sqrt{2\pi}v_R)$.

yields the time evolution of the wave. The crucial point in the BB model is to include external wave damping to model all linear dissipation mechanisms of the wave energy to the background plasma [BBY93b]. That is the role of the term proportional to γ_d in Eq. (4.20).

In the initial condition we apply a small perturbation, $f(x, v, t = 0) = f_0(v)(1+\epsilon \cos kx)$, and the initial electric field is given by solving Poisson's equation.

In the following, γ_L is defined as the linear growth rate for $\gamma_d = 0$ and no collisions. In the cold Maxwellian limit, $\gamma_L = \gamma_{L0}$, where γ_{L0} is a measure of the slope of initial distribution at resonant velocity,

$$\gamma_{L0} \equiv \frac{\pi}{2k^2} \left.\frac{\partial f_0}{\partial v}\right|_{v=v_R} . \tag{4.21}$$

In this limit, a simple relation, $\gamma = \gamma_L - \gamma_d$, stands. However, in general there is some discrepancy between γ and $\gamma_L - \gamma_d$.

The BB problem can be put in Hamiltonian form in a moving-frame coordinate set, (ξ, I), where $\xi \equiv kx - \omega t$ and $I \equiv (v - v_{\rm R})/k$. The Hamiltonian takes a standard form,

$$\delta H = \frac{k^2}{2} I^2 + \phi_0 \cos \xi, \tag{4.22}$$

which is shared with the effective Hamiltonian of an EP-driven mode, Eq. (4.6). Hence, the BB model is a simple 1D model that is homothetic to a whole class of instabilities, including EP-driven modes in toroidal fusion plasmas.

This model ensures conservation of total particle number $N(t) \equiv \int f \mathrm{d}x\mathrm{d}v$. It also satisfies a power balance equation,

$$\frac{\mathrm{d}\mathcal{E}}{\mathrm{d}t} + P_h + 4\gamma_d \mathcal{E} = 0, \tag{4.23}$$

where $\mathcal{E}(t) \equiv \int E^2/(2\epsilon_0)\mathrm{d}x$ is the electric field energy, $P_h(t) \equiv q \int vEf\mathrm{d}x\mathrm{d}v$ is the power transferred from the perturbed electric field to both bulk and beam particles (not including sloshing energy). Note that the power balance can be expressed in an equivalent, alternative way, if we consider waves as quasi-particles,

$$\frac{\mathrm{d}\mathcal{W}}{\mathrm{d}t} + P_h^{\rm R} + 2\gamma_d \mathcal{W} = 0, \tag{4.24}$$

where $\mathcal{W}$ is the total wave energy, and $P_h^{\rm R}$ is the resonant power transfer, To obtain this expression, we have separated the response of the particles into resonant and non-resonant pieces by decomposing the distribution as $f \equiv f^{\rm R} + f^{\rm NR}$ and the kinetic energy $\mathcal{T}$ accordingly, $\mathcal{T} \equiv \mathcal{T}^{\rm R} + \mathcal{T}^{\rm NR}$. The non-resonant part of the kinetic energy is the sloshing energy, which can be considered as part of the total wave energy. For non-resonant particles, the velocity

is oscillatory and we can replace the amplitude of its oscillation by the linear response, and we obtain $\mathcal{T}^{\mathrm{NR}} = \mathcal{E}$. The wave energy $\mathcal{W}$ is composed of the field energy $\mathcal{E}$ and the sloshing energy $\mathcal{T}^{\mathrm{NR}}$. While Eq. (4.23) shows the balance between the field and all the particles, Eq. (4.24) shows the balance between wave and resonant particles.

4.2.3 δf BB model

If the bulk particles interact adiabatically with the wave, their contribution to the Lagrangian can be expressed as part of the electric field. Then it is possible to adopt a perturbative approach, and to cast the BB model in a reduced form that describes the time evolution of beam particles only [BBP95a, CD93]. The evolution of the beam distribution, $f^B(x, v, t)$, is given by the kinetic equation

$$\frac{\partial f^B}{\partial t} + v\,\frac{\partial f^B}{\partial x} + \tilde{E}\,\frac{\partial f^B}{\partial v} = \mathcal{C}\left(\delta f^B\right), \tag{4.25}$$

where the pseudo-electric field $\tilde{E}$ is defined as

$$\tilde{E}(x,t) \equiv Q(t)\,\cos(\xi) - P(t)\,\sin(\xi), \tag{4.26}$$

where $\xi \equiv kx - \omega t$. Alternatively, we may use a complex representation,

$$\tilde{E}(x,t) \equiv Z(t)\,\exp \imath\xi + \text{c.c.}, \tag{4.27}$$

where the complex $Z = (Q + \imath P)/2$ encodes the information of amplitude and phase.

In this model, the real frequency of the wave ω is assumed constant (and since it is used to normalize time, $\omega = 1$ in normalized units). This restriction does not forbid nonlinear phenomena like frequency sweeping, since both amplitude and phase of the wave are time-dependent. Hereafter, we renormalize physical quantities for the δf model so that they do not depend on k. In practice, we choose $k = 1$. In the collision operators, ν_a, ν_f and ν_d are taken as constants, since, with the δf description, velocity dependency is not needed to avoid affecting bulk plasma with collisions.

Hereafter, we drop the subscript ^{B} in f^B for concision. The evolution of the pseudo-electric field is given by

$$\frac{\mathrm{d}Q}{\mathrm{d}t} = -\frac{1}{2\pi}\int f(x,v,t)\,\cos(\xi)\,\mathrm{d}x\,\mathrm{d}v - \gamma_d\,Q, \tag{4.28}$$

$$\frac{\mathrm{d}P}{\mathrm{d}t} = \frac{1}{2\pi}\int f(x,v,t)\,\sin(\xi)\,\mathrm{d}x\,\mathrm{d}v - \gamma_d\,P, \tag{4.29}$$

or, alternatively,

$$\frac{\mathrm{d}Z_1}{\mathrm{d}t} = -\frac{1}{2\pi}\int f(x,v,t)\,e^{-\imath\xi}\,\mathrm{d}x\,\mathrm{d}v - \gamma_d\,Z. \tag{4.30}$$

The initial values of Q and P (or Z) are given by solving Poisson's equation. Note that the latter equations, without factor 2 in front of γ_d, are consistent with Eq. (4.20).

In the collisionless case, the linear dispersion relation shows that $\omega = 1$ only if f_0 is symmetric around the resonant velocity, $v_R \equiv \omega/k$. Since we assumed $\omega = 1$ from the start, we consider only such distributions, for the model to be self-consistent. The velocity distribution of beam particles in the initial condition is shown in Fig. 4.1(b). A constant slope is imposed between $v = -v_c$ and $v = v_c$, where v_c is an arbitrary cut-off velocity. The zero average ensures that the plasma frequency is not perturbed by the beam density.

Since this type of initial distribution is characterized by its slope at resonant velocity, we use γ_{L0} as an input parameter of the BB model. In contrast, γ_L is calculated by solving the dissipation-less, collisionless linear dispersion relation,

$$\gamma_L = \frac{1}{2k}\int_\Gamma \frac{\partial_v f_0}{\gamma_L + \mathrm{i}\,(k\,v - 1)}\,\mathrm{d}v. \tag{4.31}$$

The discrepancy between γ_{L0} and γ_L comes from the finite extent of f_0. It is negligible for large enough v_c.

This model also conserves the total particle number. The power balance is slightly modified from Eq. 4.23, as

$$P_h \; + \; P_E \; + \; P_d \; = \; 0, \tag{4.32}$$

where P_h is the kinetic power transfer,

$$P_h \; \equiv \; \int v \, E \, f \, \mathrm{d}x \, \mathrm{d}v, \tag{4.33}$$

P_E is the electric field power transfer,

$$P_E \; \equiv \; \frac{2\pi}{k} \frac{\mathrm{d}}{\mathrm{d}t} \left(P\dot{Q} - Q\dot{P} \; + \; \frac{Q^2 + P^2}{2} \right), \tag{4.34}$$

and P_d is the power transfer due to external damping and collisions. In the Krook case,

$$P_d \; \equiv \; \frac{2\pi}{k} \left[(\gamma_d + \nu_a) \left(P\dot{Q} - Q\dot{P} \right) \; + \; \gamma_d \left(Q^2 + P^2 \right) \right], \tag{4.35}$$

while in the Fokker-Planck case, collisions do not contribute to this latter power transfer, thus P_d is obtained by substituting $\nu_a = 0$ in Eq. (4.35).

Compared to the full-f model, the δf model does not take into account effects of the time-evolution of bulk particles, which is a caveat when assessing limit of theory that breaks-up when phase-space structures approach the bulk, but it has an advantage in the application to experiment, where we assume fixed mode structure, hence fixed background plasma. Moreover, the velocity range required to simulate a similar resonant region can be significantly reduced with the δf model, saving computation time. In addition, the δf model assumes a constant total number of energetic particles.

4.2.4 The COBBLES code

We developed the kinetic code COBBLES based on the Constrained Interpolation Profile - Conservative Semi-Lagrangian (CIP-CSL) scheme [NTYT01] for solving the initial value BB problem. The acronym COBBLES stands for COnservative Berk-Breizman semi-Lagrangian Extended Solver. Here we present the main principles of our code.

Let us recall that the BB model is an extension of the Vlasov-Poisson system, which is recovered in the collisionless, closed system ($\gamma_d = 0$) limit. In a previous work [LIT07], we developed a 1D semi-Lagrangian Vlasov-Poisson code. Later, we extended this code to include distribution relaxation and extrinsic dissipation, and develop a δf version. We refer to these codes as full-f COBBLES and δf COBBLES, respectively.

In both codes we solve DCE instead of Poisson equation. Looking at the spatial average of Eq. (4.20),

$$\frac{\mathrm{d}\langle E \rangle}{\mathrm{d}t} \; = \; - \int v \left(\langle f \rangle - f_0 \right) \mathrm{d}v \; - \; 2 \, \gamma_d \langle E \rangle, \tag{4.36}$$

we see that a small deviation from a constant total momentum can be the source of a systematic error in the average electric field. Such deviation arises when Krook collisions are included, or can be caused by numerical error. To avoid this problem, we replace $\int v f_0 \mathrm{d}v$ by $\int v \langle f \rangle \mathrm{d}v$ in the DCE [Van02]. Then Eq. (4.36) is changed to $\mathrm{d}_t \langle E \rangle + 2\gamma_d \langle E \rangle = 0$, which ensures a zero average electric field, since $\langle E \rangle |_{t=0} = 0$.

Let us now describe the main points of our algorithm. All quantities like f are sampled on uniform Eulerian grids with N_x and N_v grid points in the x and v directions, respectively, within the computational domain $\{(x, v) \mid 0 \leq x < L, \; v_{\min} \leq v \leq v_{\max}\}$. Boundary conditions are periodic in x, and zero-flux at velocity boundaries. The time-step width is Δt. We use the Strang splitting [Str68] formula to obtain a second-order accuracy in time [VDR+03]. The DCE is solved by a forward Euler scheme. Collisional diffusion is solved by the Crank-Nicolson method [CN47]. The remaining problem is the advection of a 1D hyperbolic equation,

$$\partial_t F \; + \; u \, \partial_\lambda F \; = \; 0, \tag{4.37}$$

where u is constant in the λ direction, λ is a generalized advection coordinate, and F is a general function of λ and t.

In choosing the advection scheme, we focus on stability and convergence properties, which are estimated with severe benchmark parameters: full-f version, a cold bulk, a weak, warm beam, small collision frequencies, and near marginal stability. This is stringent because 1. the colder the bulk, the less grid points are available in the bulk, leading to artificial heating ; 2. the weak warm beam induces weaker linear instabilities, which produce narrower islands in phase space ; 3. collisions are too rare to significantly alleviate the problem of filamentation on the time-scale of the simulation ; 4. near marginal stability, the linear growth rate γ is very small and long-time computations ($t \sim 10^5$) are required. In Ref. [LIG09], we compared several advection schemes, and showed that the CIP-CSL scheme [NTYT01] features quick convergence without unfavorable numerical oscillations. Therefore, we use this scheme in all COBBLES simulations. The key idea of this scheme is that in addition to the distribution function, we advect its integrated value ρ to keep a flux balance between neighboring grids. As a result, the surface elements of phase-space density are locally conserved, up to the machine precision.

COBBLES is coded in Fortran 90 language. It is parallelized in a hybrid fashion, using MPI in the velocity direction and OpenMP. Differences between δf and full-f versions are in the initialization, which defines the distribution of EPs only instead of the full distribution, and in the DCE, which is replaced by Eqs. (4.28) and (4.29).

The COBBLES code in both full-f and δf versions was verified, validated, and benchmarked in the following ways.

— We compared linear growth rate and real frequency measured in COBBLES simulations with those obtained by solving the linear dispersion relation numerically. We found good agreement, with relative errors of the order of 0.1%.

— In subsection 4.3.1, we show that simulations recover nonlinear theory in the collisionless, $\gamma_d = 0$ limit, in terms of saturation level, relative oscillation amplitude, and the Bernstein-Greene-Kruskal (BGK) steady-state solution [BGK57].

— We regularly check conservation properties. The relative error in particle conservation is, as expected from a locally conservative scheme, of the order of machine precision. The accuracy of energy conservation (or rather, power balance), depends on the setup. Although the relative error is of the order of 10^{-5} (or less) for simulations of the BB model, it can reach the order of 10^{-3} in long-time simulations of ion-acoustic turbulence. Ref. [Les16] is dedicated to the study of entropy conservation and the interpretation of a lack thereof in particular cases.

— We reproduced a bifurcation diagram in (γ_d, ν_a) space, presented in Fig. 3. of Ref. [VDR+03].

— To verify our implementation of collision operator with drag and diffusion, we confirmed that a Gaussian perturbation in the velocity distribution follows the analytic solution of the diffusion equation in the absence of electric field and drag, and is simply advected at a rate $\dot{v} = \nu_f^2/k$ in the absence of electric field and diffusion. Additionally, in Ref. [LI12], we found a quantitative agreement between nonlinear steady-state solutions from δf-COBBLES and analytic predictions derived in Refs. [Lil09, LBS09].

To summarize, in the full-f case, the locally conservative implementation adopted in COBBLES is a key point for robust simulations in experimentally-relevant conditions, which are particularly stringent in a numerical point-of-view.

4.2.5 The PICKLES code

In order to discriminate between physical phenomena and numerical issues which may be due to either semi-Lagrangian or Lagrangian treatment, I developed a simple particle-in-cell code, PICKLES (Particle-In-Cell Kinetic Lazy Electrostatic Solver). It is based on a fourth-order Runge-Kutta method, and is parallelized via MPI. The PICKLES code takes the same input parameters as COBBLES, except for a number of marker-particles per species N_p instead of a number of grid points in velocity. It also provides most of the same outputs as COBBLES.

In addition, it can be switched between full-f and δf algorithms, which allow to further discriminate possible numerical issues due to either of these methods. We successfully benchmarked it against COBBLES in the limit of $N_p \to \infty$.

4.3 Single mode

We assume a single electrostatic wave, with a wave number k. The assumption that the electric field is sinusoidal corresponds to the situation of a single resonance, which is selected by the geometry in more complex systems.

4.3.1 Nonlinear analytic theory

Simple Vlasov-Poisson

Let us first consider the simpler collisionless Vlasov-Poisson model without external damping, corresponding to the BB model without any collision nor extrinsic dissipation. In the unstable case, linear growth goes on until a significant number of resonant particle trajectories are modified by electrostatic trapping. In the nonlinear phase, the distribution develops an island structure in phase-space, and becomes flat on average in the resonant velocity region [ZK62, ZK63]. The instability saturates and linear theory breaks down. As a measure of the electric field amplitude E_0, we use ω_b, the bounce frequency of particles that are deeply trapped in the electrostatic potential. It satisfies $\omega_b^2 \equiv kE_0$. O'Neil and Mazitov extended the theory of collisionless wave-particle interaction in the nonlinear phase [O'N65, Maz65]. They both obtained analytic estimates for the evolution of wave amplitude. Within the assumptions $\gamma_L/\omega_b \ll 1$ and $\omega/\omega_b \gg 1$, and in the small-time limit, $\omega_b t \ll 1$, the electric field amplitude is estimated in Ref. [O'N65] as

$$\frac{\omega_b(t)}{\omega_b(0)} = \exp \frac{\gamma_L}{\pi\omega_b} \int_0^1 \mathrm{d}\kappa \left(1 - \cos \frac{2\omega_b t}{\kappa}\right). \tag{4.38}$$

Fig. 4.2 shows the evolution of normalized bounce frequency ω_b/γ_L, along with snapshots of the distribution function, for initial distribution B. The nonlinear evolution of the wave is in qualitative agreement with the analytic calculation (4.38) in its validity limit (for the first few amplitude oscillations). Although we cannot quantitatively compare all the features of this analytic solution because of an ambiguity in the initial time in Eq.(4.38), we observe a good agreement for the amplitude oscillations frequency, and for the relative amplitude of these oscillations compared to the saturation level. Furthermore, the saturation level is close to the value $\omega_b/\gamma_L \sim 3.2$, which was numerically obtained in Refs. [CD93, OWM71] with the δf BB model. A surprising relationship with residual zonal flow is discussed in Ref. [GDE+16].

In the time-asymptotic limit, assuming some infinitesimal amount of collision, the steady-state solution of the Vlasov-Poisson system is a distribution given as a function of the energy only. This BGK solution is consistent with a non-zero electric field. Fig. 4.3 is a contour plot of the distribution function in the time-asymptotic limit of numerical simulation, on which several constant energy curves are superposed. We clearly observe an island structure, which

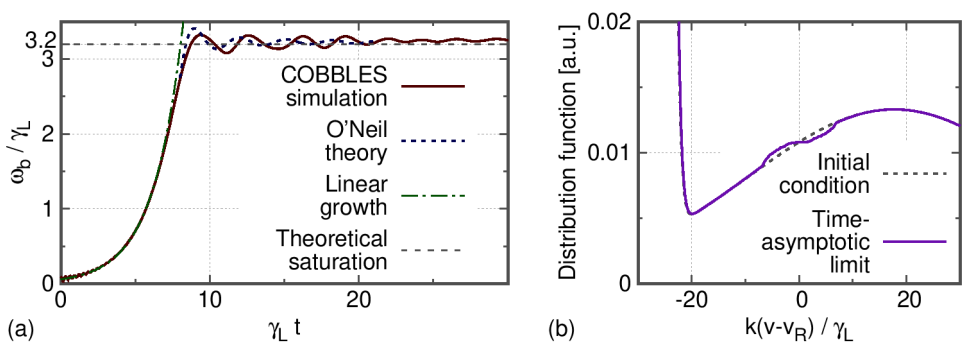

Figure 4.2 – Full-f COBBLES simulation with $\gamma_d = \nu_{a,f,d} = 0$, for initial distribution B, with $N_x \times N_v = 256 \times 2048$ grid points. (a) Nonlinear evolution of normalized bounce frequency. (b) Snapshots of distribution function.

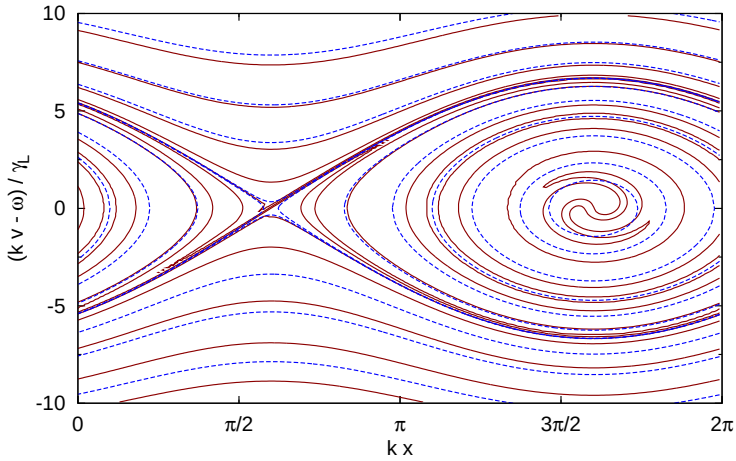

Figure 4.3 – Contour plot of the time-asymptotic distribution function (solid curves) and constant energy curves (dashed curves) for the simulation of Fig. 4.2.

agrees with the BGK solution. This island is topologically different from the initial condition, thus some collisions are needed to violate Liouville's theorem and obtain the BGK solution. In numerical simulations, finite numerical dissipation, which is due to interpolation on a discretized grid, smears out fine-scale structures near the separatrix, allowing a reconnection of contour lines of f.

BB model with Krook collisions

Theories have been developed by Berk, Breizman, and coworkers, to quantitavely predict nonlinear behaviors in various parameter regimes and to explain underlying mechanisms [BB90a, BB90b, BBP96, BBP97b, BBP98, BBC+99]. The nonlinear behavior of an instability is determined by a competition among the drive by resonant particles, the external damping, the particle relaxation which tends to recover the initial positive slope in the distribution function, and particle trapping that tends to smooth it. Chirping solutions arise in a low collision regime when hole and clump structures are formed in phase-space [BBP97a]. Let us review the analytic theory available for the (single-mode) BB model, which provides simple expressions for the following nonlinear features:

— saturation level in a parameter regime above marginal stability,
— saturation level and bifurcation criterion between steady-state and periodic solutions near marginal stability,
— time-evolution of the frequency of a chirping mode.

Steady-state above marginal stability ($\gamma_d \sim \nu_a \ll \gamma_L$)

When external damping and distribution relaxation are of the same order and both are small compared to the linear drive, the wave amplitude saturates to a steady-state in the time-asymptotic limit. To estimate a saturation level, the rate of annihilation of beam particles is assumed to be much smaller than the saturated bounce frequency, $\nu_a \ll \omega_b$ at $t \to \infty$. Further, the resonant region is assumed to be narrow compared to the resonant velocity, $4\,\omega_b/k \ll \omega/k$, so that the contribution to resonant power transfer comes from a narrow region around v_R. Under these assumptions, Berk and Breizman derived a relation yielding the saturation level [BB90a],

$$\omega_b \;=\; 1.96\,\frac{\nu_a}{\gamma_d}\,\gamma_L. \tag{4.39}$$

Thus, if we normalize all frequencies to the linear growth rate, then the saturation level depends only on the ratio of ν_a to γ_d.

Quantitative agreement was found between this prediction and numerical simulations with a δf particle code, in a region where $\gamma_d \sim \nu_a$ [BBP95a]. In Refs. [LIG09, Les11], we recovered similar results from both δf and full-f COBBLES simulations for a weak, warm-beam distribution - in fact the distribution B in Fig. 4.1(a) - as shown in Fig. 4.4. However, for a distribution with a slightly higher beam density, $n_B = 0.15$, and a slightly lower beam

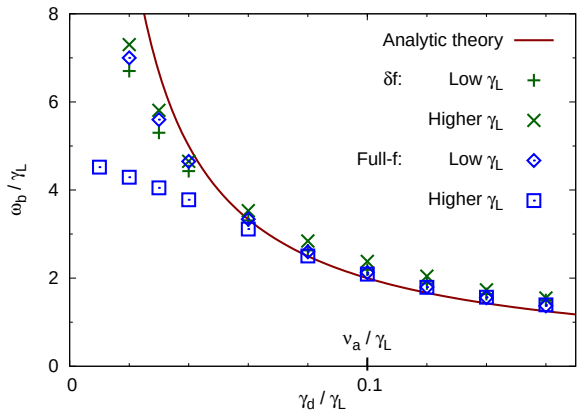

Figure 4.4 – Saturation level far above marginal stability. Here $\nu_a/\gamma_L = 0.1$. Results are shown for both distribution B (Low-γ_L case), and a distribution with higher beam density and lower beam temperature (Higher-γ_L case).

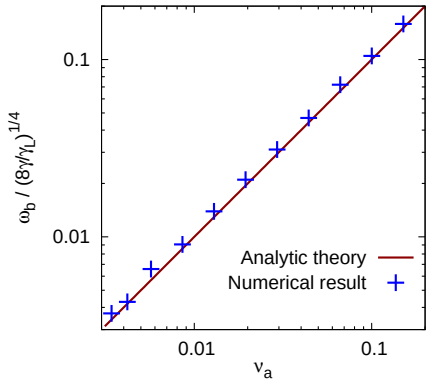

Figure 4.5 – Saturation level near marginal stability. Measured in full-f simulations for distribution B.

temperature, $v_B = 2.5$, giving $\gamma_L = 0.067$ instead of 0.032, and only for the full-f model, we observe a significant dependency of the saturation amplitude on the linear growth rate. For larger γ_L, there is significant discrepancy with theory in the low γ_d region, because the island width Δv becomes of the order of the resonant velocity ($\Delta v/v_R = 0.14\,\omega_b/\gamma_L$ in the low-γ_L case, and $\Delta v/v_R = 0.29\,\omega_b/\gamma_L$ in the higher-γ_L case). This reveals a limitation of δf model, which does not take into account the evolution of bulk plasma.

Near-marginal steady-state and periodicity ($\gamma \approx \gamma_L - \gamma_d \ll \gamma_L$)

When $\gamma \ll \gamma_L$, a reduced integral equation for the time evolution of electric field amplitude has been developed using an extension based on the closeness to marginal stability [BBP96]. Within the assumption $\omega_b/\gamma \ll 1$,

$$\frac{d\omega_b^2}{dt} = (\gamma_{L0} - \gamma_d)\,\omega_b^2 - \frac{\gamma_{L0}}{2}\int_{t/2}^{t} \mathrm{d}t_1 \int_{t-t_1}^{t_1} \mathrm{d}t_2 (t-t_1)^2 \; e^{-\nu_a(2t-t_1-t_2)}\,\omega_b^2(t_1)\,\omega_b^2(t_2)\,\omega_b^2(t+t_2-t_1). \quad (4.40)$$

This equation is consistent with steady, periodic, chaotic and explosive solutions. The latter are associated with chirping. Since this theory was developed using an extension based on the closeness to marginal stability, a common misconception is that chirping is only possible near marginal stability. But logically, this analytical theory does not preclude anything far from marginal stability. In fact, the BB model yields all steady, periodic, chaotic and chirping solutions both close and far from marginal stability. We have shown that chirping is found even when γ is as low as $0.2\gamma_{L0}$ [LIG09].

For a cold bulk, warm beam distribution, in the collisionless limit, as we approach marginal stability, the linear growth rate reduces to

$$\gamma \approx \gamma_{L0} - \gamma_d, \quad (4.41)$$

which agrees with the linear part of the latter integral equation (4.40). In Ref. [BBP96], the analytic treatment is carried on by normalizing time by $\gamma_{L0} - \gamma_d$. However, the linear growth rate is different with finite collisions. Then, as we get closer to the linear stability threshold, the relative error $|\gamma_{L0} - \gamma_d - \gamma|/(|\gamma_{L0} - \gamma_d| + |\gamma|)$ approaches unity. Moreover, depending on the initial velocity distribution, there can be significant discrepancy between γ_{L0} and γ_L. We infer that we can replace $\gamma_{L0} - \gamma_d$ by γ (which takes into account both collisions and effects of finite temperature bulk) in the integral equation (4.40) and use γ itself as the relevant choice of normalization parameter. This procedure yields a steady solution,

$$\omega_b^2 = 2\sqrt{2}\,\nu_a^2 \sqrt{\frac{\gamma}{\gamma_{L0}}}. \quad (4.42)$$

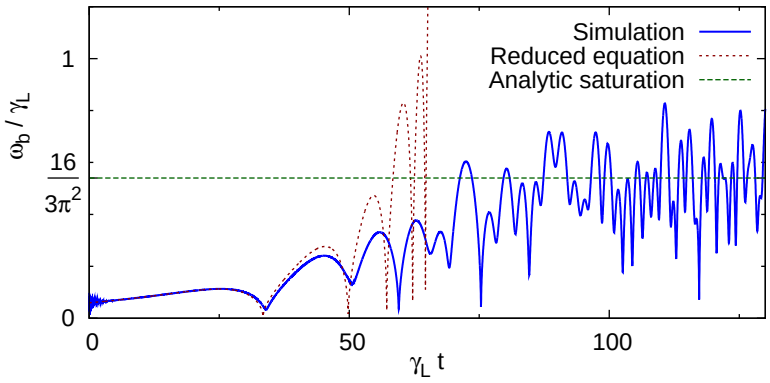

Figure 4.6 – Time evolution of the normalized field amplitude, obtained from full-f simulation and from the reduced equation (4.40), with initial distribution B, $\gamma_d = 0.035$, and $\nu_a = 10^{-4}$.

A series of simulations near marginal stability ($0.005 < \gamma/\gamma_L < 0.02$), for ν_a spanning 2 orders of magnitude, confirms the validity of the latter expression. Fig. 4.5 shows quantitative agreement with the saturation level of numerical solutions.

Moreover, nonlinear stability analysis reveals that the steady solution (4.42) is unstable when $\nu_a < \nu_{\rm cr}$, with

$$\nu_{\rm cr} = 4.4\gamma. \tag{4.43}$$

This criterion gives the bifurcation from steady-state to periodic solutions near marginal stability. In Ref. [Les11], we confirmed the qualitative agreement with simulations, although the initial perturbation amplitude must be low enough to avoid additional nonlinear effects. Quantitatively, $\nu_{\rm cr}/\gamma$ can range from 3 to 6.

Chirping

In the collisionless limit, when $\nu_a < \gamma \ll \gamma_L$, the integral equation (4.40) is consistent with explosive solutions that diverge in a finite time, which suggests that the mode energy is partitioned into several spectral components. The resulting sideband frequencies have been observed to shift both upwardly and downwardly [BBP+97c], the frequency shift $\delta\omega(t)$ increasing in time. These chirping solutions arise when hole and clump structures [BBP97a] are formed in phase-space. They belong to a chaotic regime, and each chirping event is slightly different.

Ref. [BBP97b] shows how one can isolate one spectral component and model it as a BGK-like structure to obtain the time-evolution of one chirping branch. This theory is based on the following assumptions:

— The resonant velocity of a hole/clump evolves slowly enough for trapped particle orbits to keep their coherency, $\dot{\delta\omega}/\omega_b^2$, $\ddot{\delta\omega}/\omega_b^3 \ll 1$;

— The width of a hole/clump evolves slowly enough for trapped particle orbits to keep their coherency, $\dot{\omega}_b/\omega_b^2 \ll 1$;

— Holes and clumps are narrow enough that they don't overlay each others, $\omega_b/\delta\omega \ll 1$.

Within the above assumptions, the perturbation of passing particle distribution is negligible, and a bounce-average treatment of trapped particle distribution yields the frequency shift, in the collisionless limit, as

$$\delta\omega(t) \;=\; \alpha\,\gamma_{L0}\,\sqrt{\gamma_d\,t}, \tag{4.44}$$

with $\alpha \approx 0.44$; and a saturation level as

$$\omega_b \;\approx\; 0.54\,\gamma_{L0}. \tag{4.45}$$

These analytic expressions have been found to agree with 1D δf particle simulations, [BBP97b], with both Krook and diffusion-only collision operators, with full-f COBBLES simulations, and with 3D simulations such as HAGIS [PBG+04]. To illustrate, Fig. 4.6 shows the time evolution of field amplitude, with initial distribution B, when $\gamma_d = 0.035$,

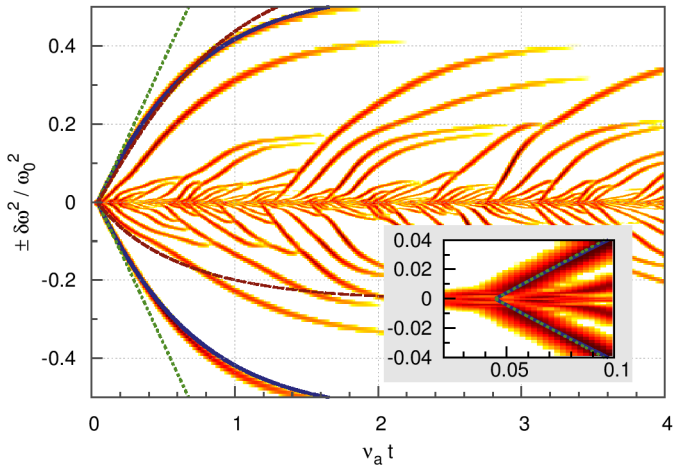

Figure 4.7 – Effect of finite Krook collisions on chirping velocity. Spectrogram of the electric field obtained in a δf-COBBLES simulation with $\gamma_{L0} = 0.05$, $\gamma_d = 0.045$, and $\nu_a = 4\times10^{-5}$. Logarithmic color code ranging from 1 (black) to 10^{-3} (white). Two dotted, straight lines correspond to Eq. (4.46). Two solid curves correspond to Eq. (4.47). We include a correction coefficient $\beta = 1.23$. Two dashed curves correspond to Ref. [NLB12]. Inset: zoom on the beginning of the first chirping event.

and $\nu_a = 10^{-4}$, so that $\gamma = 0.05\,\gamma_{L0}$. The simulation result agrees with a numerical solution of reduced equation (4.40), until the field amplitude approaches the applicability limit. After saturation, the solution is close to analytic prediction Eq. (4.45).

In Sec. 4.3.6, we consider frequency sweeping in a regime where $\dot{\delta\omega}/\omega_b^2 \approx 0.5$, which approaches the limit of validity of the above theory. Indeed, when $\dot{\delta\omega}/\omega_b^2 \approx 0.5$, $4\omega_b/\dot{\delta\omega} \approx 2\pi/\omega_b$, in other words a hole or a clump is shifted by its width in a bounce time of deeply trapped particles. In this regime, the previous analytic treatment is not relevant. However, numerical simulations show a similar square-root dependency of the frequency shift in time. We argue that $\dot{\delta\omega}/\omega_b^2$ can be seen as a measure of departure from hole/clump adiabaticity, and we introduce the effect of non-adiabaticity on chirping velocity as a correction parameter β,

$$\delta\omega(t) \;=\; \alpha\,\beta\,\gamma_{L0}\,\sqrt{\gamma_d\,t}. \tag{4.46}$$

One effect of the departure from adiabatic conditions is a collision-induced trapping of particles near the separatrix [EB02], which was observed to account for a 10% modification ($\beta = 1.1$). We analyzed the dependency of β on input parameters in Ref. [LIS+10].

Furthermore, the above theory is valid on a timescale smaller than a collision time. Fig. 4.7 shows the spectrogram of the electric field obtained in a δf-COBBLES simulation. Note that the vertical axis is the square of $\delta\omega$. It is clear from this figure that it is only for early times, $t \ll 1/\nu_a$, that the chirping branches follow the square-root law, which shows as straight lines on this figure. We test above and following theories on the first chirping branch, since after the first chirping burst, the velocity distribution is modified and the assumption of a constant velocity slope is broken. In Ref. [LDK14b] we extended the above theory to include the effects of Krook collisions, and explain deviations from the square-root

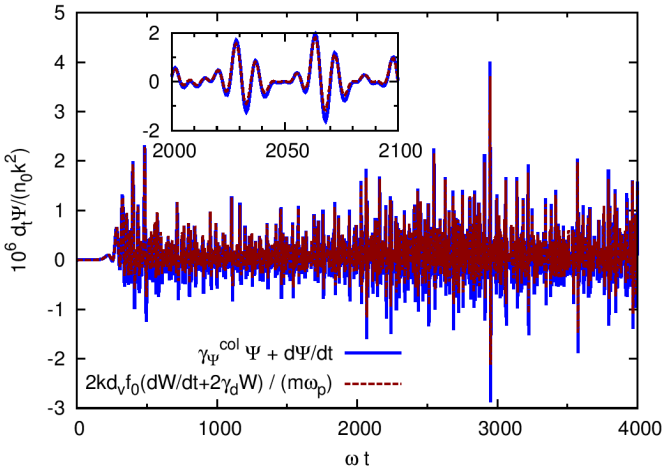

Figure 4.8 – Growth of phasestrophy and wave energy in the BB case. Inset: zoom on a smaller timescale. Simulation parameters are $\gamma_{L0}/\omega = 0.1$, $\gamma_d/\gamma_{L0} = 0.7$, $\nu_a/\gamma_{L0} = 10^{-3}$ and $\nu_f = \nu_d = 0$.

law Eq. (4.44) on a collision timescale. We obtained the following expressions,

$$\begin{aligned}\delta\omega(t) &= \pm\alpha\,\beta\,\gamma_{L0}\sqrt{\gamma_d t}\left[1 - \frac{1}{3}(\nu_a t) + \frac{7}{90}(\nu_a t)^2\right.\\ &\quad\left. - \frac{19}{1890}(\nu_a t)^3 + \frac{1507}{1701000}(\nu_a t)^4 + \ldots\right], \qquad (4.47)\\ \omega_b(t) &= \frac{16\gamma_{L0}}{3\pi^2}\left[1 - \frac{2}{3}(\nu_a t) + \frac{8}{45}(\nu_a t)^2\right.\\ &\quad\left. - \frac{8}{315}(\nu_a t)^3 + \frac{152}{42525}(\nu_a t)^4 + \ldots\right]. \qquad (4.48)\end{aligned}$$

Fig. 4.7 shows a good agreement between Eq. (4.47) and the observed bended chirping. Here, the value of $\beta = 1.23$ is obtained by linear fit of $\delta\omega^2(t)$ for $\delta\omega/\omega_0 < 10\%$. Note that Eqs. (4.44)-(4.45) are recovered in the collisionless, adiabatic ($\beta = 1$) limit. The effect of finite collision is to reduce the extent of chirping by bending shifting branches. This effect is not negligible since $\delta\omega$ is reduced by 27% after a collision time, which is of the order of chirping lifetime. The effects of drag and diffusion have been calculated in Ref. [LBS10].

4.3.2 Subcritical instability

In Ref. [LD13], which we summarize in this subsection, we apply the energy-phasestrophy relation to obtain analytical expressions for the subcritical threshold and for the nonlinear growth-rate in cases where a single phase-space structure dominates. The simulations here are δf-COBBLES simulations with $\gamma_{L0}/\omega = 0.1$.

Energy-phasestrophy relation

For the BB model, the energy-phasestrophy relation, Eq. (2.49), writes

$$\frac{\mathrm{d}W}{\mathrm{d}t} + 2\gamma_d W = \frac{m\omega_p}{2k\mathrm{d}_v f_0}\left(\gamma_\Psi^{\mathrm{col}} + \frac{\mathrm{d}}{\mathrm{d}t}\right)\Psi. \qquad (4.49)$$

Here, the decay rate $\gamma_\Psi^{\mathrm{col}}$ of phasestrophy due to collisions (combining both kinds of collision operators) is

$$\gamma_\Psi^{\mathrm{col}} = 2\nu_a + \frac{2}{\Psi_s}\frac{\nu_d^3}{k^2}\int_{-\infty}^{\infty}\left\langle\left(\frac{\partial\delta f_s}{\partial v}\right)^2\right\rangle \mathrm{d}v. \qquad (4.50)$$

Note that collisional drag ν_f does not appear in the latter expression. Fig. 4.8 shows good quantitative agreement between the lhs and the rhs of the energy-phasestrophy relation in a simulation.

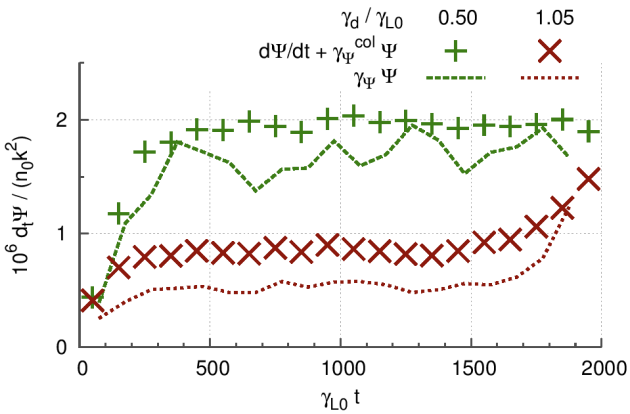

Figure 4.9 – Growth rate of the phasestrophy of one isolated hole. Simulation parameters are $\gamma_{L0}/\omega = 0.1$, $\nu_a = 0$, $\nu_f/\gamma_{L0} = 0.3$, $\nu_d/\gamma_{L0} = 0.17$, and two different values of γ_d, which are given in the legend. Points: phasestrophy growth measured in simulations, including contribution from collisions. Dashed curves: theory, Eq. (4.54).

Nonlinear growth rate

If we assume that the evolution of phasestrophy is dominated by that of an isolated phase-space structure, we can obtain an analytical expression for the nonlinear growth rate of the structure. We assume that δf is of the form $\delta f = \langle \delta f \rangle \left[1 + \cos(kx + \theta)\right]$, with a Gaussian velocity-profile,

$$\langle \delta f \rangle \;=\; h(t)\, \exp\left[-(v - v_0(t))^2/(2\Delta v(t)^2)\right]. \tag{4.51}$$

As we will confirm in subsection 4.3.5, this shape is a good approximation. It corresponds to a BGK mode, which was shown to be a state of maximum entropy subject to constant mass, momentum, and energy [Dup82]. To relate W back to Ψ, we use the Poisson equation, even though in the BB model it is only approximately satisfied,

$$W = \frac{1}{2}\frac{m\omega_p^2}{k^2 n_0}\left(\int \langle \delta f \rangle \,\mathrm{d}v\right)^2. \tag{4.52}$$

Thus the evolution of phasestrophy follows a simple expression,

$$\frac{\mathrm{d}\Psi}{\mathrm{d}t} \;=\; \left(\gamma_\Psi - \gamma_\Psi^{\mathrm{col}}\right)\,\Psi, \tag{4.53}$$

where γ_Ψ is the collisionless phase-space structure growth-rate,

$$\gamma_\Psi \;\approx\; \frac{16}{3\sqrt{\pi}}\,\frac{\Delta v}{v_R}\,\frac{\gamma_{L0}}{\omega_p}\,\gamma_d. \tag{4.54}$$

To be concise, in this expression for γ_Ψ we assumed $\Delta v\, \mathrm{d}_v f_0 \ll k n_0/\omega$ and $\dot{\Delta v} \ll \gamma_d \Delta v$, which are satisfied in our simulations. Eq. (4.54) is in qualitative agreement with the collisionless structure growth-rate estimated in Ref. [DKL15]. However, the method used in the reference assumes that $\partial E_0/\partial t \ll \gamma_d E_0$, which is only valid in the initial, linear phase, near marginal stability.

Fig. 4.9 shows the growth-rate of phasestrophy, averaged over a time window of duration $\gamma_{L0}\Delta t = 100$, where Δv in the expression of γ_Ψ is estimated by fitting a Gaussian to $\langle \delta f \rangle$ in the vicinity of the hole at each time-step. We observe quantitative agreement between our simulations and theory for the supercritical case ($\gamma_d/\gamma_{L0} = 0.5$), and qualitative agreement in the subcritical case ($\gamma_d/\gamma_{L0} = 1.05$). There is a 40% discrepancy in the subcritical case, which is due in part to the co-existence of a secondary hole with 20% as much phasestrophy as that of the main hole. This suggests that consideration of the primary-secondary hole interaction is necessary to improve the accuracy of the theory.

Eq. (4.54) shows that the growth of phase-space structures is independent of linear stability, since it is not related to the sign of the total linear growth rate $\gamma \approx \gamma_{L0} - \gamma_d$. Nonlinear growth requires a positive γ_d to enable momentum exchange, a positive slope for f_0 to provide free energy, and a seed structure with a width Δv large enough for γ_Ψ to overcome collisions. When the linear growth rate γ is negative, the seed structure is the hole (clump) corresponding to the $v > v_R$ ($v < v_R$) part of the plateau, which is formed by particles trapped in the finite initial electric field.

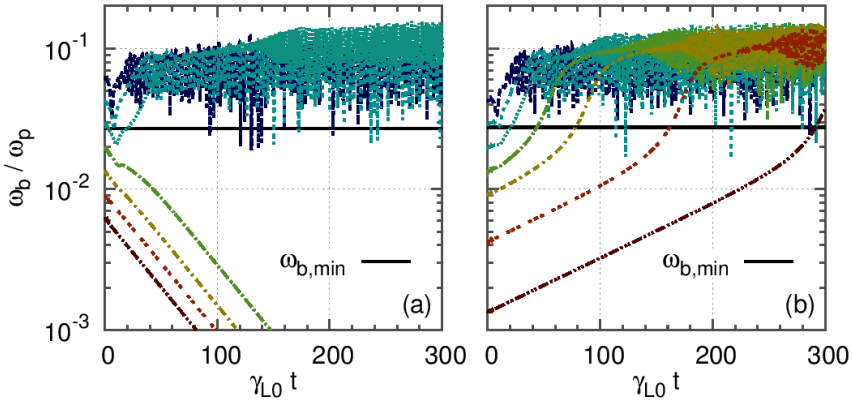

Figure 4.10 – Dashed curves: time-series of electric field amplitude for different initial amplitudes. (a) Subcritical case, $\gamma_d/\gamma_{L0} = 1.05$. (b) Supercritical case, $\gamma_d/\gamma_{L0} = 0.98$. The other simulation parameters are given in Fig. 4.9. Solid line: theoretical nonlinear instability threshold, Eq. (4.57).

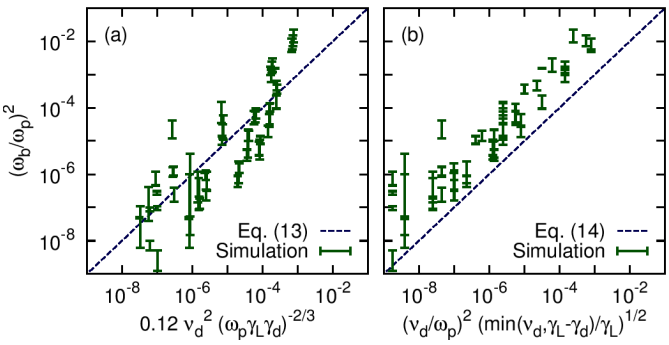

Figure 4.11 – Vertical bars: range of electric field amplitude between the highest stable and the lowest unstable simulation. Dotted line: theory described in (a) this paper; (b) Ref. [BBC+99].

Threshold in initial amplitude

The expression of collisional phasestrophy decay, Eq. (4.50), can be used to obtain the threshold of initial perturbation amplitude required to trigger the subcritical instability. If Krook-like collisions dominate in $\gamma_\Psi^{\rm col}$, the threshold width $\Delta v_{\rm min}$ of a seed structure is

$$\frac{\Delta v_{\rm min}}{v_R} \approx \frac{3\sqrt{\pi}}{8}\,\frac{\omega_p}{\gamma_{L0}}\,\frac{\nu_a}{\gamma_d}. \tag{4.55}$$

If Krook-like collisions are negligible, then $\gamma_\Psi^{\rm col} \sim \nu_d^3/(k\Delta v)^2$ and

$$\frac{\Delta v_{\rm min}}{v_R} \sim 0.7\left(\frac{\omega_p}{\gamma_{L0}}\,\frac{\omega_p}{\gamma_d}\right)^{1/3}\frac{\nu_d}{\omega_p}. \tag{4.56}$$

The width of the electrostatic potential well is $4\omega_b/k$, which is twice the width of a seed hole. Thus, the initial amplitude threshold $\omega_{b,\rm min}$ is of the order of

$$\left(\frac{\omega_{b,\rm min}}{\omega_p}\right)^2 \sim 0.12\left(\frac{\omega_p}{\gamma_{L0}}\,\frac{\omega_p}{\gamma_d}\right)^{2/3}\left(\frac{\nu_d}{\omega_p}\right)^2. \tag{4.57}$$

Fig. 4.10(a) shows time-series of electric field amplitude ω_b for different initial amplitudes, for the case $\gamma_d/\gamma_{L0} = 1.05$, which is a subcritical instability with $\gamma/\gamma_{L0} = -0.045$. The threshold between damped solutions and nonlinear instabilities is in agreement with Eq. (4.57).

We further investigate the validity of this scaling by performing a scan of $\gamma_{L0}/\omega_p = 0.02 - 0.50$, $\gamma_d/\gamma_{L0} = 1.01 - 1.20$ and $\nu_d/\gamma_{L0} = 2\times 10^{-3} - 10^{-1}$. For each case, a series of simulations with different initial amplitudes is performed, and we measure, after one island turnover, the amplitude of the highest stable solution and the amplitude of the lowest stable

solution. Fig. 4.11 shows the range of the instability threshold, and compares it against (a) our theory, and (b) the scaling obtained in Ref. [BBC+99] in the limit $\omega_b \ll \gamma_L$,

$$\omega_{b,\min}^2 \sim \nu_d^2 \max\left[\left(\frac{\nu_d}{\gamma_{L0}}\right)^{1/2}, \left(\frac{|\gamma_{L0}-\gamma_d|}{\gamma_{L0}}\right)^{1/2}\right]. \tag{4.58}$$

Note that the two theories are not incompatible. The observed error in Fig. 4.11(a) is expected since Eq. (4.57) corresponds to a single-hole limit. The picture of Landau damping seeding the structure is valid only if the plateau shrinks slowly enough, $|\dot{\omega_b}| \ll \omega_b^2$. This condition must be satisfied during at least one orbit, which gives an additional condition on the initial amplitude, namely $\omega_b \gg (\pi + 1/2)|\gamma|$.

In addition, our theory predicts the existence of a nonlinear instability for positive but small γ. For a plateau of width $2\Delta v$, $\Psi \sim \Delta v^3$ and the growth due to the linear instability is $\dot{\Delta v}/\Delta v = \gamma/2$. Then the nonlinear instability due to phasestrophy growth is stronger than the linear growth if $\gamma_\Psi - \gamma_\Psi^{\rm col} > (3/2)\gamma$. We discovered numerically the existence of such supercritical nonlinear instabilities for $0 < \gamma/\gamma_{L0} < 0.04$. Fig. 4.10(b) shows time-series of electric field amplitude ω_b for different initial amplitudes, for $\gamma_d/\gamma_{L0} = 0.98$, which is slightly above marginal stability with $\gamma/\gamma_{L0} = 0.018$. The threshold where the linear growth becomes nonlinear is in agreement with Eq. (4.57).

Summary

To summarize, the energy-phasestrophy relation can be applied in the BB case to obtain a simple expression for the growth rate of a single phase-space structure, $\gamma_\Psi \sim \gamma_d\gamma_{L0}\Delta v$ in the collisionless limit. This expression shows that dissipation drives a nonlinear instability of holes and clumps via momentum exchange, regardless of linear stability. This leads to faster-than-linear growth in barely unstable regimes, as well as to subcritical instabilities, subject to the presence of a finite seed structure. Simulations in both subcritical and supercritical regimes show a good agreement with analytic theory. These results were obtained in the single structure case. Although we expect similar physical processes in the presence of multiple holes and clumps, the theory should be revisited by taking into account multi-structure interactions. This will likely necessitate some form of turbulence closure theory.

4.3.3 Phenomenology

As we have seen in subsection 4.3.1, it has been predicted that three kinds of behaviours emerge from the BB model, namely steady-state, periodic, chaotic, and chirping responses. In fact, many qualitatively distinct nonlinear regimes have been observed in confinement fusion experiments in the presence of EPs [FBG+97], including a zoo of different kinds of chirping. Chirping modes are qualitatively diverse in terms of their intermittency [KKK+99, PBF+10, CDL+10], their monotonicity in frequency shift [BBB+06, NFA+08], their asymmetry [BBB+06, TOI+11], and whether frequency shifting branches end as a continuous mode [GS04] or not. In this subsection, which was published as Ref. [LI12], the goal is to define and categorize each nonlinear regime in a systematic manner. Such a categorization indicates how experimental input parameters may be adjusted to change the nonlinear behavior. For instance, since Alfvén avalanches are often associated with chirping bursts, rather than continuous modes, a good strategy would be to avoid chirping bursts.

When collisions are modeled by a simple Krook operator, a systematic categorization of these nonlinear regimes in the $(\gamma_d,\ \nu_a)$ parameter space for a fixed initial velocity distribution has been performed numerically [VDR+03, LIG09]. In the chirping cases, two branches coexist, with their frequency sweeping downwardly (down-chirping) for one, upwardly (up-chirping) for the other, as pairs of hole and clump in the distribution evolve [BBP97b, BBP98, BBC+99]. However, including dynamical friction (drag), and diffusion in the collision operator have a strong impact on the nonlinear behaviour, and is necessary to qualitatively reproduce experimental chirping AEs [LBS09, LIS+10]. Let us then focus on drag and diffusion.

We must keep in mind that, although the terms in ν_f and ν_d in the BB equations are referred to as drag and diffusion, they do not correspond to drag and diffusion in the sense

of a 3D Fokker-Planck collision operator, but rather to a projection of these operators on a resonant surface. In fact, as we have seen in subsection 4.1.2, ν_f includes contributions from the slowing down term, the pitch-angle scattering term and the parallel velocity diffusion, while ν_d includes contributions from the pitch-angle scattering term and the parallel velocity diffusion.

Here, we adopt the δf BB model. In this model, the linear frequency of the wave is imposed as $\omega_0 = \omega_p$. Even when chirping occurs, ω_0 does not change. Chirping (existence of a significant spectral component at finite $\delta\omega \equiv \omega - \omega_0$) is due to the nonlinear evolution of the amplitude and phase of the wave.

The initial velocity distribution is that shown in Fig. 4.1(b), with $\gamma_{L0} = 0.1$, which is experimentally relevant gorelenkov00,heidbrink03,nazikian08. The linear drive γ_L, which, we recall, is defined as the linear growth rate in the absence of damping and collision, is $\gamma_L/\omega_0 = 0.09$. This is consistent with energetic particle-driven experiments, where γ_L/ω_0 is estimated within the range $\sim 0.1\% - 30\%$. It is acknowledged that deviations from a constant-slope distribution are expected to affect the nonlinear behaviour. Thus, when discussing experiments, our analysis must be understood as an ideal case where the energetic-particle distribution can be modeled with a constant slope in a neighbourhood of the resonant velocity, where the size of this neighbourhood depends on the domain spanned by resonant wave-particle interactions and evolving phase-space structures.

Categorization

We consider five main categories for the time-evolution of the instability. The category is obtained by an analysis of $\omega_b(t)$ (which, we recall, measures the amplitude the electric potential), and a spectrogram $\mathcal{P}(\delta\omega, t)$ of $\tilde{E}(0, t)$. Since we want to categorize the time-asymptotic behaviour, we restrict our analysis to a time-interval that starts well after the end of the linear phase and the nonlinear saturation, ignoring some transient evolution. We detail in Ref. [LI12] how we define the categories shown in the following chart.

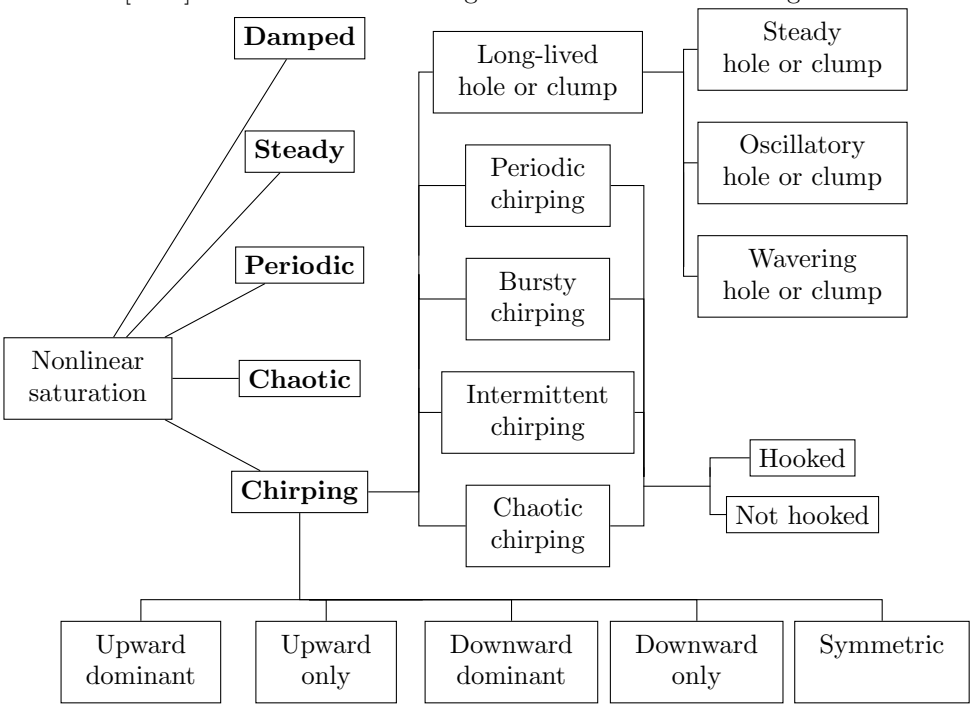

Typical nonlinear behaviour

For a typical example of each nonlinear regime, Figs. 4.12 to 4.15 show the time-evolution of the electric field amplitude. For each example, we also show the corresponding spectrogram.

Fig. 4.12 shows three nonlinear regimes, which do not feature frequency sweeping, namely

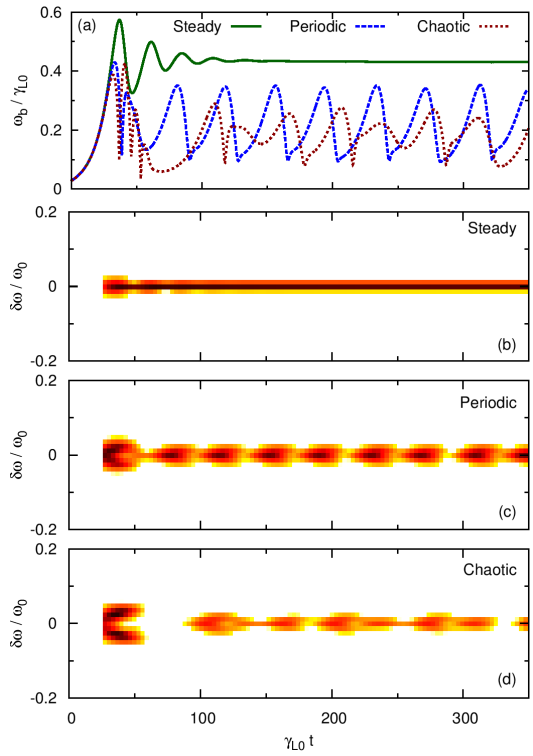

Figure 4.12 – (a) Time-series of electric field amplitude and (b,c,d) spectrograms for typical non-chirping solutions, with $\gamma_d/\gamma_{L0} = 0.8$, and $\nu_d/\nu_f = 5$. The value of ν_d/γ_{L0} is 0.50 for steady (b), 0.30 for periodic (c) and 0.23 for chaotic (d). Each simulation corresponds to a point in Fig. 4.16(a). Each spectrogram on this page and the next has a logarithmic color code, which spans 3 orders of magnitude.

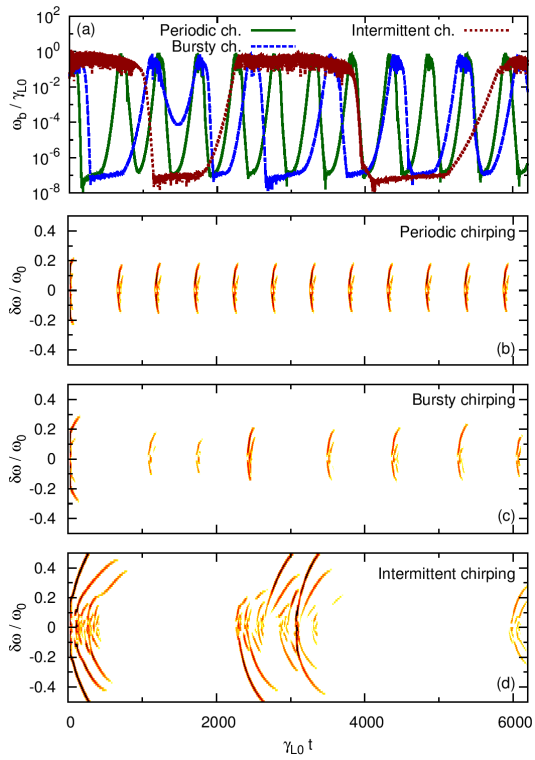

Figure 4.13 – (a) Time-series of electric field amplitude and (b,c,d) spectrograms for typical chirping solutions, with $\gamma_d/\gamma_{L0} = 0.5$, and $\nu_d/\nu_f = 5$. The value of ν_d/γ_{L0} is 0.14 for periodic chirping (b), 0.11 for bursty chirping (c) and 0.065 for intermittent chirping (d). Each simulation corresponds to a point in Fig. 4.16(a).

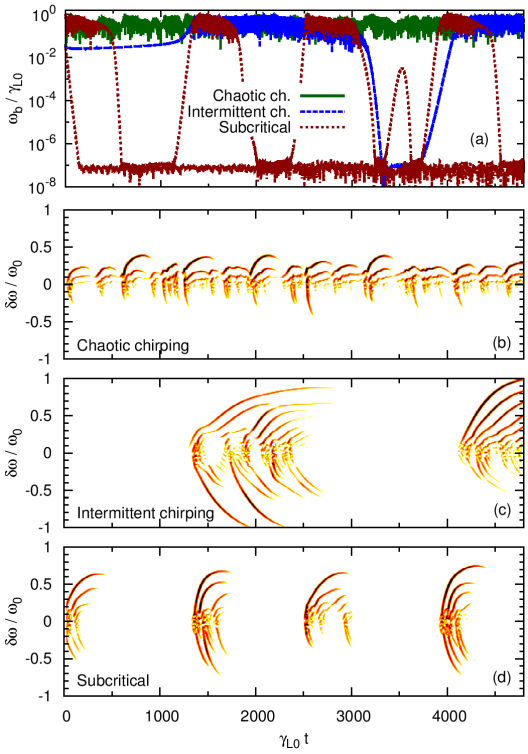

Figure 4.14 – (a) Time-series of electric field amplitude and (b,c,d) spectrograms for typical chirping solutions, with $\nu_f = \nu_d$. The parameters are $\gamma_d/\gamma_{L0} = 0.8$, $\nu_d/\gamma_{L0} = 0.13$ for chaotic chirping (b); $\gamma_d/\gamma_{L0} = 1.0$, $\nu_d/\gamma_{L0} = 0.05$ for intermittent chirping (c); and $\gamma_d/\gamma_{L0} = 1.2$, $\nu_d/\gamma_{L0} = 0.09$ for a subcritical case (d). In the subcritical case, we show the amplitude time-series for two choices of initial amplitude $\omega_b(0)/\gamma_{L0}$: 0.03, which yields a damped solution; and 1.0, which yields a nonlinear instability. Each simulation corresponds to a point in Fig. 4.16(b).

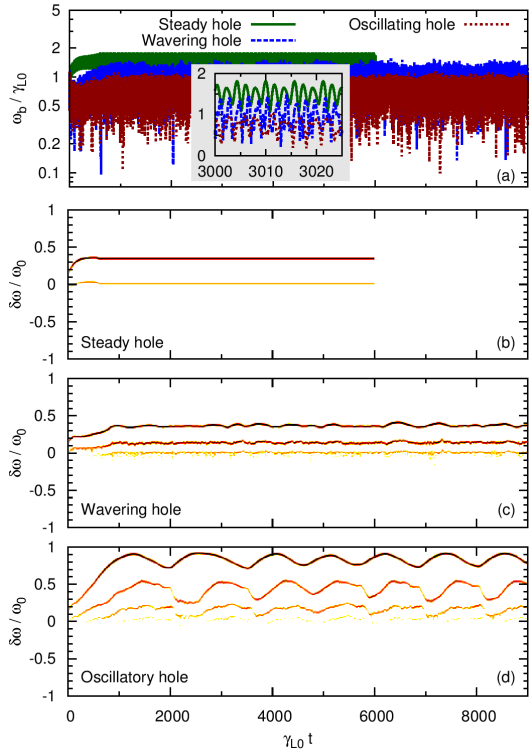

Figure 4.15 – (a) Time-series of electric field amplitude and (b,c,d) spectrograms for typical solutions with long-lived hole, with $\gamma_d/\gamma_{L0} = 0.5$. The parameters are $\nu_f/\gamma_{L0} = 0.36$, $\nu_d/\gamma_{L0} = 0.27$ for steady hole (b); $\nu_f/\gamma_{L0} = 0.16$, $\nu_d/\gamma_{L0} = 0.09$ for wavering hole (c); and $\nu_f/\gamma_{L0} = 0.16$, $\nu_d/\gamma_{L0} = 0.12$ for oscillatory hole (d). Inset: zoom over a few oscillation periods of the amplitude. Each simulation corresponds to a point in Fig. 4.16(d).

steady, periodic, and chaotic. These solutions were predicted and observed when collisions are modelled by a Krook operator, for sufficiently large collisions.

Fig. 4.13 shows three nonlinear regimes with frequency sweeping, namely periodic chirping, bursty chirping and intermittent chirping, which are not obtained in the Krook case. The electric field amplitude displays clear relaxation oscillations, with more or less regularity depending on the parameters. The periodic chirping regime is studied in more details in subsection 4.3.5.

Fig. 4.14(b) shows a fourth nonlinear regime with frequency sweeping, namely chaotic chirping. This is also an example of a solution with upward chirping dominant. In general, chaotic chirping corresponds to an uninterrupted generation of holes and clumps of various sizes, which yields a spectrogram with many minor and major chirping branches without clear quiescent phases. This latter behaviour is the only chirping behaviour that was obtained in the Krook case. There are also other kinds of chaotic chirping, not shown here, where the spectrogram features several behaviours alternating in time, for example bursty chirping and wavering hole.

For $\nu_f \sim \nu_d$, dynamical friction significantly modifies the shape of a chirping branch, up to a situation where the sweeping direction of a chirping hole is reversed at some point, as seen in Fig. 4.14(b), which is called as hooked chirping. For larger collision frequencies, the contradicting effects of drag and dissipation on a hole seem to balance, yielding long-lived holes with more or less stable frequency shift. Such situations have been observed and explained in Ref. [LBS09]. Fig. 4.15 shows three nonlinear regimes with long-lived holes. When several holes coexist, the categorization into steady, oscillatory or wavering hole is based on the hole with the largest frequency shift, which is observed to dominate the spectrogram. We observed that the number of holes is roughly increasing with decreasing collisionality.

The case of Fig. 4.14(d) is actually a subcritical instability, with $\gamma/\gamma_{L0} = -0.18$. The case of Fig. 4.14(c) is also a nonlinear instability, albeit not subcritical. In this case, the growth rate is very small, $\gamma/\gamma_{L0} = 1.5 \times 10^{-7}$, but after a finite time, wave amplitude grows explosively to a chirping state. The practical consequence is that the wave saturates to a high level $\omega_b \sim \gamma_L$ much sooner than what linear theory predicts ($\gamma_L t \sim 10^3$ instead of 10^8 in this case). For $\nu_f = \nu_d = 0.05\,\gamma_{L0}$, we observe such supercritical nonlinear instabilities when $\gamma/\gamma_{L0} < 0.04$. In a long-time point-of-view though, after nonlinear saturation, the chirping behaviour does not depend on the initial amplitude.

Small drag

To investigate the regime of small drag, we perform a series of 260 simulations where $\nu_d/\nu_f = 5$, which is relevant to present day tokamaks [LIS+10]. Fig. 4.16(a) shows the categorization of each simulation result in the $(\gamma_d,\ \nu_d)$ parameter space. Note the agreement between the linear stability threshold $\gamma = 0$ and the boundary between linearly stable and unstable simulations. This phase diagram is qualitatively similar to what was obtained with Krook collisions. We recover the same bifurcations from steady, to periodic, to chaotic, to chirping as the collision frequencies decrease. We don't observe chirping solutions for $\gamma_d/\gamma_{L0} < 0.1$. The main difference is that chirping solutions can be intermittent, bursty or periodic, whereas we only observed chaotic chirping in the Krook case. We observed that several holes and clumps with different amplitudes co-exist in the Krook case, while diffusion smooths out fine-scale structures, which explains isolated chirping events we observe in the drag-diffusion case. Nonlinear instabilities, including subcritical instabilities, are also found for collision frequencies slightly below the range of our diagram, $\nu_d/\gamma_{L0} < 0.04$. Based on the analysis described in subsection 4.3.6, TAEs in JT-60U discharge E32359 are roughly located at the point marked by the letter J in this diagram. In such case, the strategy to avoid chirping bursts would be to increase the ratio γ_d/γ_L, perhaps by decreasing the beam injection power, in order to bring the system closer to marginal stability. An other approach would be to increase effective collision frequencies, but the required increase may be too difficult to achieve.

Lilley showed that steady-state solutions are not possible for $\nu_d/\nu_f < 1.043$ [LBS09].

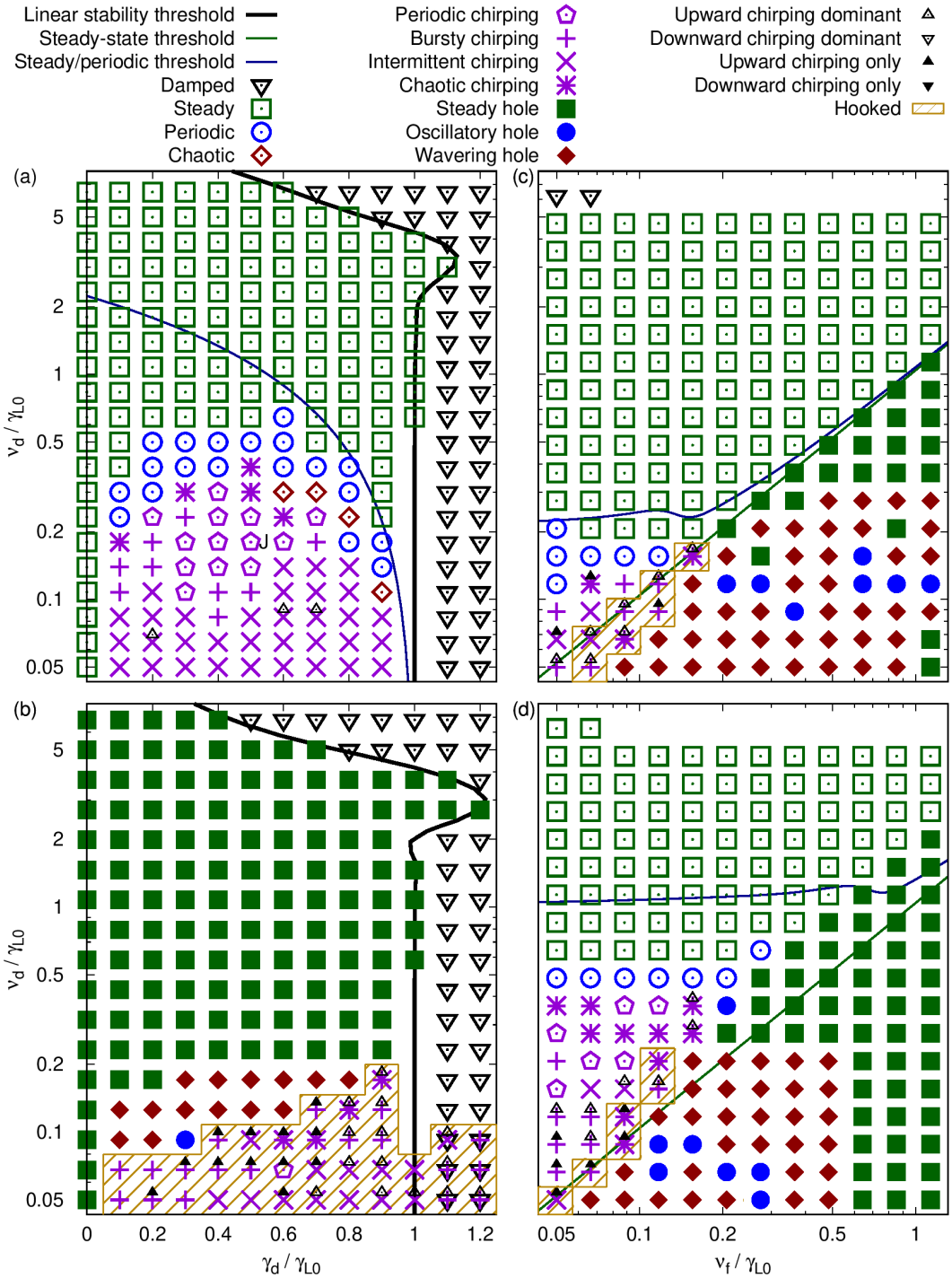

Figure 4.16 – Behaviour bifurcation diagrams for $\gamma_{L0} = 0.1$. (a) For $\nu_d/\nu_f = 5$. An absence of point signifies that longer, or better resolved simulations are necessary to categorize the time-asymptotic behaviour. The letter J indicates the JT-60U discharge E32359. (b) For $\nu_d/\nu_f = 1$. In the bottom right corner, superposed symbols show subcritical solutions for which the amplitude is damped when $\omega_b/\gamma_{L0} = 0.03$, but unstable when $\omega_b/\gamma_{L0} = 1$. (c) For $\gamma_d/\gamma_{L0} = 0.9$ (close to marginality). (d) For $\gamma_d/\gamma_{L0} = 0.5$ (far from marginality).

This steady-state threshold, as well as the steady/periodic threshold Eq. (4.43), are shown in the bifurcation diagrams, when relevant. There is qualitative agreement within the validity limit of each theory.

Large drag

To investigate the effect of large drag, we perform a series of 221 simulations where $\nu_d/\nu_f = 1$, which may be more relevant to ITER parameters [LBS09]. Fig. 4.16(b) shows the categorization of each simulation result in the $(\gamma_d,\ \nu_d)$ parameter space. This diagram is qualitatively different from what was obtained with Krook collisions. We don't observe any steady solution, which is consistent with the theoretical steady-state threshold. Neither do we observe periodic or chaotic solutions. Instead, long-lived holes fill the parameter space for large collision frequencies. For $\nu_f/\gamma_{L0} = \nu_d/\gamma_{L0} < 0.1$ and $\gamma_d > \gamma_{L0}$, we observe subcritical instabilities. We find only 1 periodic chirping solution, compared to 13 in the small drag case, which suggests that quasi-periodically bursting AEs, which are often observed in present tokamaks, may not or rarely be observed in ITER.

Since the initial distribution is symmetric around the resonant velocity, the drag term is the only term in the δf-BB model that is asymmetric around $\delta\omega = k(v - v_R) = 0$. This is consistent with the fact that we find only 3 upward chirping dominant solutions when $\nu_f = \nu_d/5$, whereas most solutions are upward chirping dominant or upward chirping only when $\nu_f = \nu_d$ (steady-hole solutions are trivially asymmetric). Drag has a counter-intuitive effect on chirping asymmetry. Since the effect of drag on any phase-space structure is to advect it from large to small velocities, one could imagine that the presence of drag would make down-chirping dominant. However, upward chirping dominates and a physical explanation is proposed in Ref. [LBS09].

Close to marginal stability

Let us investigate the barely unstable regime, which is relevant for theory and may be relevant for ITER in some cases [GBB05]. We perform a series of 204 simulations where $\gamma_d/\gamma_{L0} = 0.9$, which is near marginal stability in the sense that $\gamma/\gamma_L \approx 0.05$. Fig. 4.16(c) shows the categorization of each simulation result in the $(\nu_f,\ \nu_d)$ parameter space. The linear stability threshold is out of the range of this plot. As predicted by theory, steady-state solutions only exist above the steady-state threshold. Moreover, the boundary between steady and periodic solutions agree with the theoretical steady/periodic threshold.

Farther from marginal stability

To investigate the nonlinear behaviour relatively far from marginal stability (in an instantaneous point-of-view, not necessarily in a time-averaged point-of-view), we perform a series of 204 simulations where $\gamma_d/\gamma_{L0} = 0.5$, which is relevant for experiments [LIS$^+$10]. Fig. 4.16(d) shows the categorization of each simulation result in the $(\nu_f,\ \nu_d)$ parameter space. The linear stability threshold is out of the range of this plot. The agreement with the theoretical steady-state threshold and steady/periodic threshold is not as good as when $\gamma_d/\gamma_{L0} = 0.9$, which is expected since for $\gamma_d/\gamma_{L0} = 0.5$, $\gamma/\gamma_{L0} \approx 0.4$, whereas the assumption is $\gamma/\gamma_{L0} \ll 1$.

General remarks

In all cases, each category is relatively isolated in a well-defined region, rather than dispersed in the whole parameter space. Note also that the region of hooked chirping is contiguous to the region of long-lived hole.

All periodic chirping solutions satisfy our criteria for bursty chirping. In this sense, periodic chirping is a special case of bursty chirping. Periodic chirping solutions are restricted

to a region where $\gamma_d/\gamma_L = 0.2 - 0.7$, which is relatively far from marginal stability. This suggests that, in experiments that feature periodic chirping bursts, one must be careful in using the assumption $\gamma_d \approx \gamma_L$, which stems naively from self-organization arguments.

As a caveat, we don't observe neither long-lived clump or down-chirping dominant cases, which are often observed in the experiment.

Ultimately, nonlinear behaviour bifurcations may be used as a guide to mitigate energetic particle transport in magnetic fusion experiments. However, we must note the following caveats.

1. Although quantitative similarities between AE experiments and the BB model have been found, a one-to-one correspondence has not been established, leaving some uncertainty in any experimental analysis based on the BB model.
2. Processes that are not included in the BB model, such as turbulence-induced drag and diffusion, may change the qualitative picture, or yield new kinds of behaviour, such as long-lived clumps if some process brings an effect opposite to collisional drag.
3. Several resonances or several modes co-exist in most experiments, and can interact to produce other kinds of behaviour, such as avalanches.

4.3.4 Chirping lifetime

As illustrated in subsection 4.3.3, several holes and clumps with different amplitudes can co-exist. Here, we are interested in the nonlinear chirping characteristics, averaged over a significant number of chirping events. In particular, in our simulations, we observe that the first chirping event stands out from the statistics, with a larger extent of chirping – up to twice as much as any other one of the following series of repetitive chirping. The reason is explained in subsection 4.3.5. Here, the first chirping burst is ignored.

The resonant velocity of a hole (a clump) does not increase (decrease) indefinitely. We define the life-time τ of a chirping event as the time it takes to the corresponding power in the spectrogram to decay below a fraction e^{-2} of the maximum amplitude reached during this chirping event. The maximum life-time $\tau_{\max}$ is the maximum reached by τ during a time-series, ignoring the first chirping event and any minor event. It is reasonable to assume that the island structure is dissipated by collisional processes, in which case the maximum chirping life-time should be of the form

$$\tau_{\max} = \frac{\iota_a}{\nu_a}, \tag{4.59}$$

in the Krook case, and

$$\tau_{\max} = \iota_d \frac{\gamma_{L0}^2}{\nu_d^3}, \tag{4.60}$$

in the case with drag and diffusion, when $\nu_f \ll \nu_d$, where ι_a and ι_d are constant parameters. Therefore we define the effective collision frequency as $\nu_{\text{eff}} \equiv \nu_a$ in the Krook case and $\nu_{\text{eff}} \equiv \nu_d^3/\gamma_{L0}^2$ in the case with diffusion.

In Fig. 4.17, we plot the maximum lifetime measured in δf-COBBLES simulations where the ratio γ_d/γ_{L0} is chosen as 0.5 and 0.9, i.e. far from and close to marginal stability, respectively. A quantitative agreement is found with Eq. (4.59), with $\iota_a = 1.1$, for ν_a spanning 2 orders of magnitude. With the diffusive collision operator, the chirping lifetime agrees with Eq. (4.60) only for low collisionality. For high collisionality, we find that lifetime satisfies

$$\tau_{\max} = \iota_d \left(\frac{\gamma_{L0}}{\nu_d^3}\right)^{0.5}, \tag{4.61}$$

obtained by a linear fit with $\iota_d = 2.7$. Note that this is an improved fit compared to the one with the formula $\tau_{\max} = \iota_d \left(\gamma_{L0}^2/\nu_d^3\right)^{0.5}$ mistakenly given in Ref. [LIS+10]. This high collisionality regime is important because chirping observed in experiments has a life-time of the order of $\tau \sim 500$ (we recall that we normalize time with the linear frequency of the mode).

Note that Eq. (4.60) assumes that the initial width of holes and clumps is proportional to γ_{L0} only [BBP97b]. We suggest that diffusion affects the width of a hole or clump during the

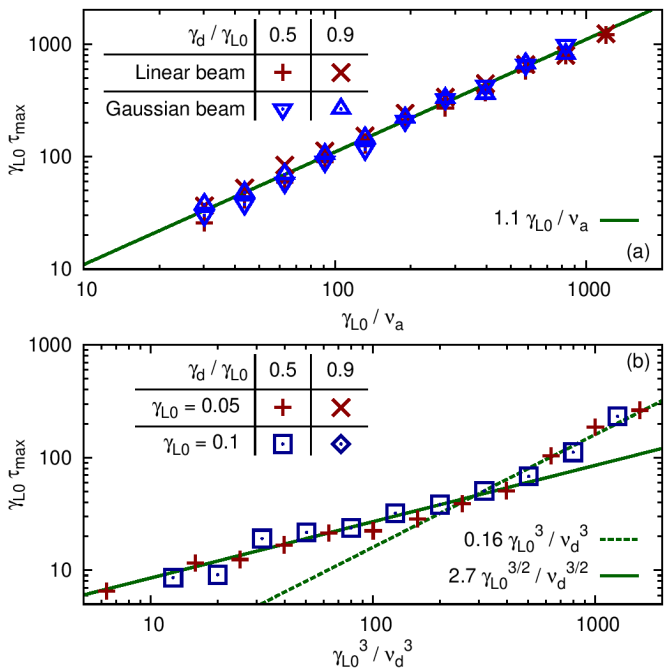

Figure 4.17 – Maximum lifetime of a hole or clump, for $\gamma_d/\gamma_{L0} = 0.5$ (far from marginal stability) and 0.9 (near marginal stability). (a) Krook collisions. The crosses correspond to the δf BB model ("Linear beam") and the triangles correspond to the full-f model ("Gaussian beam"). In both cases, $\gamma_{L0} = 0.05$. The solid line corresponds to Eq. (4.59). (b) Drag and diffusion (δf model only) with $\nu_f/\nu_d = 0.1$, for two different values of γ_{L0}. The dashed line corresponds to Eq. (4.60) with $\iota_d = 0.16$, the solid line to Eq. (4.61) with $\iota_d = 2.7$.

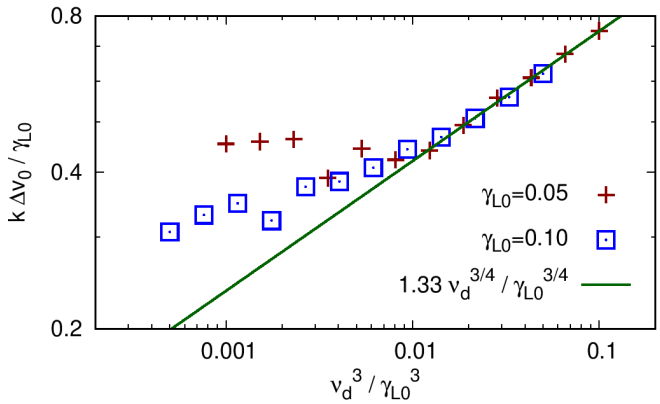

Figure 4.18 – Initial width of holes as a function of the effective collision frequency $\nu_{\text{eff}} \equiv \nu_d^3/\gamma_{L0}^2$. The simulation parameters are $\gamma_d/\gamma_{L0} = 0.5$, $\nu_d/\nu_f = 10$ and γ_{L0}/ω given in the legend. A dashed line shows a power law with exponent $-1/4$.

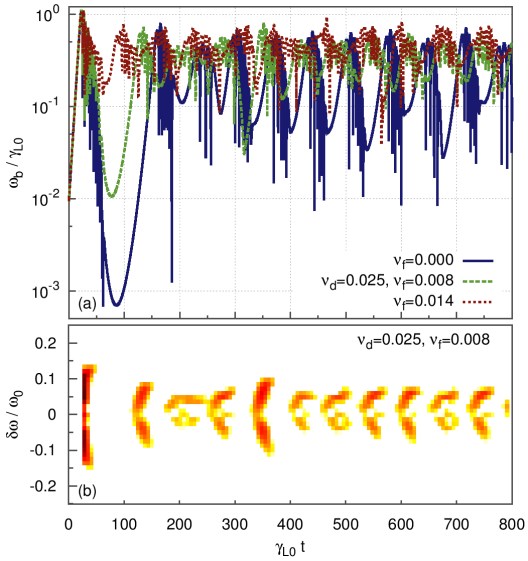

Figure 4.19 – Effect of drag in the periodic chirping regime. (a) Time-evolution of the electric field amplitude for $\nu_d = 0.025$ and ν_f shown in the legend. (b) Spectrogram of the electric field, for $\nu_f = 0.008$. Logarithmic color code ranging from 1 (black) to e^{-3} (white).

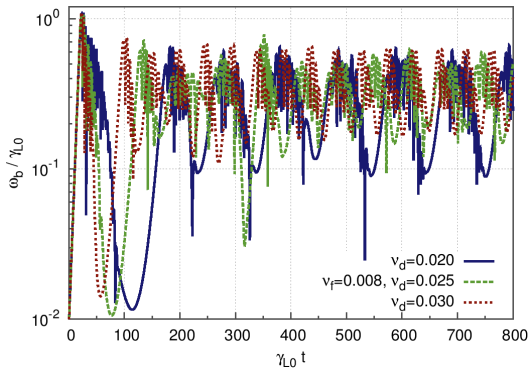

Figure 4.20 – Effect of diffusion in the periodic chirping regime. Time-evolution of the electric field amplitude for $\nu_f = 0.008$ and ν_d shown in the legend.

first phase of their evolution, namely drive by free-energy extraction, which in turn affects the decay by diffusion. Our simulation data support the latter claim. We measure the width of shifting holes (ignoring the first, exceptional burst) by fitting a Gaussian to $\langle \delta f \rangle$, and we keep only the minimum Δv_0 for each simulation. Fig. 4.18 shows that $k\Delta v_0/\gamma_{L0}$ is roughly constant for low collisionality, but is proportional to $(\nu_d/\gamma_{L0})^{3/4}$ for high collisionality, which is consistent with Eq. (4.61).

To investigate the impact of the shape of the fast particles distribution, we repeat the same analysis (in the Krook case) with an initial bump-on-tail distribution with a Gaussian beam (with the full-f version of COBBLES) instead of a constant gradient, or linear, beam. Fig. 4.17(a) shows that the agreement is kept, even if the shape of the distribution has a significant effect on the extent of chirping as can be seen for example in Fig. 12 of Ref. [LIG09].

4.3.5 Chirping period

As long as the background plasma parameters are not significantly changed, chirping events of EP-driven modes in most tokamak and stellerator experiments are quasi-periodic, with a quiescent phase between two chirping branches that lasts a few milliseconds. It should be noted that this statement does not seem to apply to DIII-D [Hei95]. As we have seen in subsection 4.3.3, this regime appears when the drag/diffusion collision operator is applied, for $\nu_f \ll \nu_d \ll \gamma_{L0}$ and $\gamma_d \approx \gamma_{L0}/2$. In this subsection, we focus on the chirping period Δt_{chirp}, which is defined as the average time between two bursts.

Throughout this section, δf-COBBLES simulations are performed with parameters $\gamma_{L0} = 0.1$, $\gamma_d = 0.05$, $N_x \times N_v = 128 \times 2048$ grid points, and time-step width $\Delta t = 0.05$. The collision frequencies vary, but we choose a reference case as $\nu_f = 0.008$ and $\nu_d = 0.025$. We recall that the electric field amplitude is measured by the bounce-frequency $\omega_b = (Q^2+P^2)^{1/4}$ of particles that are deeply trapped in the electrostatic potential.

Fig. 4.19 shows the time-evolution of electric field amplitude for three quasi-periodic chirping with three values of drag, as well as the spectrogram for the reference case, illus-

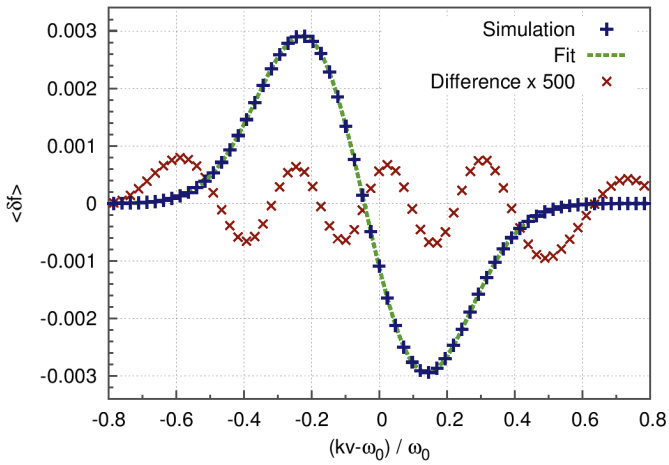

Figure 4.21 – Perturbed velocity distribution for $\nu_f = 0.008$, $\nu_d = 0.025$, at $\gamma_{L0}t = 100$, and fit, Eq. (4.62), with $l_c = 3.20 \times 10^{-3}$, $l_h = 3.23 \times 10^{-3}$, $v_c = 0.203$, $v_h = 0.115$, $\Delta v_c = 0.215$ and $\Delta v_h = 0.213$. The difference between the numerical distribution and the fit is amplified 500 times.

trating the quasi-periodic chirping regime. As ν_f increases, Δt_{chirp} decreases. Fig. 4.20 shows three values of ν_d. As ν_d increases, Δt_{chirp} decreases.

The dependency of chirping period on the model parameters (γ_{L0}, γ_d, ν_f and ν_d) is complex and lack theoretical analysis. In the following, we estimate the effects of ν_f and ν_d.

Gaussian model

Dupree showed that a phase-space density hole corresponds to a state of maximum entropy, and that this state is a BGK mode, with $\delta f \sim \exp -H/H_0$, where H is the energy in the rest-frame of the hole and H_0 is a constant [Dup82]. In the periodic chirping regime, the phase-space is dominated by a single hole and a single clump for most of the duration of a chirping burst (except at the very beginning of a burst), as hinted by the observation of a single downwardly shifting branch and a single upwardly shifting branch for each burst in Fig. 4.19(b). Then the spatial average of the perturbed distribution can be reasonably modeled by two Gaussian distributions,

$$\langle \delta f \rangle (v,t) \;=\; l_c \exp\left[-\left(\frac{v - v_R + v_c}{\Delta v_c}\right)^2\right] \;-\; l_h \exp\left[-\left(\frac{v - v_R - v_h}{\Delta v_h}\right)^2\right], \tag{4.62}$$

where l_c, l_h, v_c, v_h, Δv_c and Δv_h are positive functions of time, and the subscripts c and h denote the clump and the hole, respectively. Fig. 4.21 shows the perturbed velocity distribution for the reference case, at $\gamma_{L0}t = 100$, where $\omega_b/\gamma_{L0} \sim 0.1$. The model is a good fit for the simulation in this particular snapshot. The agreement is typically better for lower amplitudes or just before a burst ; worst for higher amplitudes or during and just after a burst.

When the field amplitude is small enough, the collision operator dominates over the nonlinear term $\tilde{E}\partial_v f$ in Eq. (4.25). Then the velocity distribution satisfies a Fokker-Planck equation,

$$\frac{\partial \langle \delta f \rangle}{\partial t} \;=\; F_v \frac{\partial \langle \delta f \rangle}{\partial v} \;+\; D_v \frac{\partial^2 \langle \delta f \rangle}{\partial v^2}, \tag{4.63}$$

where $F_v = \nu_f^2/k$, and $D_v = \nu_d^3/k^2$ The form of the hole/clump pair is unchanged, and the time-evolution is solved analytically,

$$l_c(t) = \frac{\Delta v_c(t_0)}{\Delta v_c(t)}\, l_c(t_0), \qquad l_h(t) = \frac{\Delta v_h(t_0)}{\Delta v_h(t)}\, l_h(t_0), \tag{4.64}$$

$$v_c(t) = v_c(t_0) + F_v\ (t - t_0)\,, \qquad v_h(t) = v_h(t_0) - F_v\ (t - t_0)\,, \tag{4.65}$$

$$\Delta v_c(t)^2 = 4D_v\ (t - t_0) + \Delta v_c(t_0)^2, \qquad \Delta v_h(t)^2 = 4D_v\ (t - t_0) + \Delta v_h(t_0)^2. \tag{4.66}$$

Fig. 4.22 shows the evolution of the hole/clump pair characteristics. We adopt a least-square fit of the hole/clump pair in the simulation at $t = t_0$. We arbitrarily choose $\gamma_{L0}t_0 = 100$, and confirm that the theory is in good agreement with simulation for $40 < \gamma_{L0}t <$

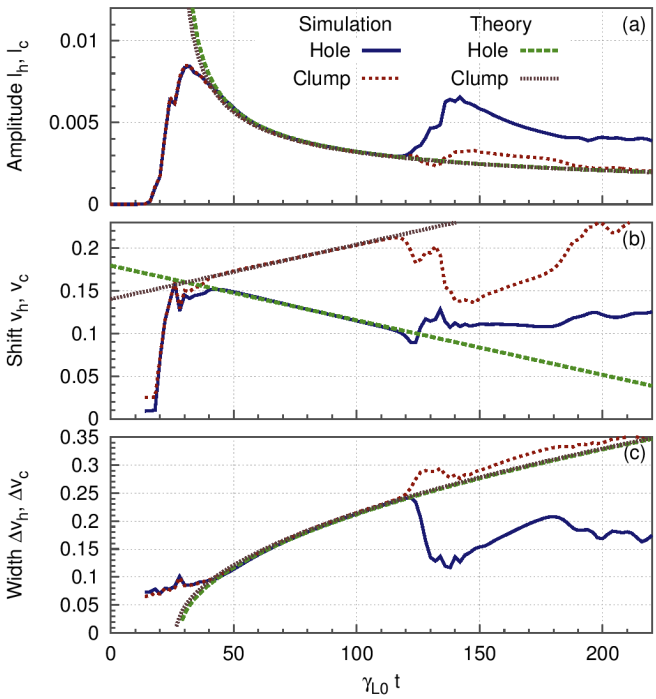

Figure 4.22 – Time-evolution of hole and clump characteristics, for our reference case ($\nu_f = 0.008$, $\nu_d = 0.025$). (a) Amplitude l_h and l_c. (b) Shift v_h and v_c. Note that increasing v_h means accelerating hole, while increasing v_c means decelerating clump. (c) Width Δv_h and Δv_c. The dashed curves correspond to Eqs. (4.64)-(4.66), with $\gamma_{L0} t_0 = 100$.

120. Similar results are found for various simulation parameters and various choices of t_0. Observed deviations from a Gaussian distribution do not have qualitative impacts on the evolution of amplitude, shift or width. This justifies that we use the Gaussian model to demonstrate following qualitative statements without lack of generality.

For the sake of explanations, we separate two phases. In the bursting phase, which immediately follows the amplitude saturation, the dynamics is dominated by the formation of holes and clumps. The hole (clump) is rapidly growing and rapidly accelerating (decelerating). Two examples for the reference case are $20 < \gamma_{L0} t < 30$ and $120 < \gamma_{L0} t < 140$. This phase appears as strong bursts of activity in the spectrogram, Fig. 4.19(b). In this phase, the term $\tilde{E}\,\partial_v f$ dominates over the collision operator, and the time-evolution of the amplitude depends mostly on γ_{L0} and γ_d.

In the quiescent phase, the dynamics is dominated by the evolution of one hole and one clump under the effect of dynamical drag and velocity-diffusion ($E_0 \ll \nu_f^2/k$, ν_d^3/k^2). Both hole and clump are slowly decaying and slowly decelerating (for finite ν_f). Two examples for the reference case are $40 < \gamma_{L0} t < 120$ and $140 < \gamma_{L0} t < 180$. This phase appears as a quiescent period in the spectrogram. Although we consider two phases for the sake of explanations, there is, in fact, no clear separation between these two phases. It should be kept in mind that velocity-diffusion is necessary for the quiescent phase to exist, as was shown in Ref. [LIS+10]. When the lifetime of holes and clumps exceeds the distribution recovery time, we leave the periodic chirping regime.

Quasi-linear growth rate

Let me define the quasi-linear growth rate as the rate obtained by replacing f_0 by $f_0 + \langle \delta f \rangle$ into the linearized model equations, where $\langle \delta f \rangle$ is given by our Gaussian model of hole/clump pair. As a preliminary step to the analysis below, we show that this quasi-linear growth rate reproduces the instantaneous growth rate of wave amplitude measured directly in simulations. To obtain the linear growth rate, we search for solutions of the form $\exp(pt)$, where $p \equiv \gamma - \imath\omega$. Writing $f_k(v,t) = f_p(v) e^{pt}$ the Fourier components of δf, and

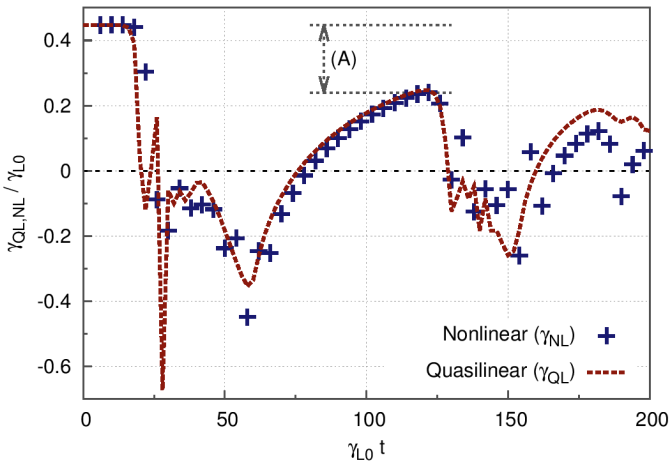

Figure 4.23 – Time-evolution of the growth rate in our reference case. Points: obtained from the time-series of electric field amplitude (Fig. 4.20, dashed curve). Dashed curve: obtained from the linearized equations and the Gaussian model for $\partial \langle f \rangle / \partial v$. In the absence of hole and clump, $\gamma/\gamma_{L0} = 0.4476$. (A) shows the discrepancy between the latter value and the maximum growth rate reached before the second burst.

$\exp(-\imath t)(Q + \imath P) = Z_p e^{pt}$, we obtain a linear equation system,

$$(p + \imath v) f_p + \frac{Z_p}{2} \frac{\partial f_0}{\partial v} = F_v \frac{\partial f_p}{\partial v} + D_v \frac{\partial^2 f_p}{\partial v^2}, \tag{4.67}$$

$$(p + \gamma_d + \imath) Z_p = -\int f_p \, \mathrm{d}v. \tag{4.68}$$

Discretizing the velocity space, the latter system can be put in the form of an eigenvalue problem. We solve it using Lapack library. For our reference case in the absence of holes and clumps ($l_c = l_h = 0$), we obtain $\omega = 1.000$ and $\gamma = 0.04476$. In the presence of holes and clumps, we denote the growth rate as γ_{QL}, indicating that we use the velocity distribution that results from nonlinear calculations.

From the amplitude time-series of the numerical simulation, we extract the instantaneous growth rate γ_{NL}, defined as $E(t_2) = E(t_1) \exp[\gamma_{NL}(t_2 - t_1)]$, where we choose arbitrarily $\gamma_{L0}(t_2 - t_1) = 4$. Fig. 4.23 shows that the quasi-linear growth rate obtained from the eigenvalue problem with the Gaussian model for hole and clump is in good agreement with the nonlinear growth rate extracted from the simulation. We could easily go one step further, and use the numerical velocity distribution itself, retrieved from numerical simulations, without modeling it. We would expect even better agreement between the quasi-linear and the nonlinear growth rate. However, the goal here is to clarify hole/clump dynamics. To reach this goal, it is necessary to keep models as simple and analytic as reasonably possible.

Here we make an important remark. Fig. 4.22(a) shows that the second burst occurs before the remnant hole-clump pair from the first burst is completely dissipated. Since the initial distribution function is not recovered, there is a discrepancy between the linear growth rate $\gamma = 0.04476$ and the maximum growth reached before the second burst at $\gamma_{L0}t = 122$, $\gamma_{NL} = 0.024$. This discrepancy is marked (A) in Fig. 4.23. In Alfvén waves experiments in magnetic confinement devices, the amplitude time-series of magnetic perturbation looks as though the linear growth rate γ can be extracted by fitting an exponential to the signal. Our analysis shows that this procedure, which is used in data analysis (e.g. [STI+02]), can lead to large error (50% in our case). In other words the growth is not linear in the case of quasi-periodic chirping bursts. For the same reason, successive chirping rates may not reflect the relaxed distribution – $f_0(v)$ in the collision operator $\mathcal{C}(f - f0)$ – but the instantaneous state of the relaxing distribution – $f(x, v, t)$. In addition, since the discrepancy (A) depends on the details of the velocity distribution, theory predicts the timing of the subsequent burst (e.g. at $\gamma_{L0}t \approx 125$), but only qualitatively.

Effect of drag

The effect of drag on chirping period is complex and depends on other parameters. Fig. 4.24 shows the period as a function of drag, for two fixed values of diffusion. The data points are shown only for simulations categorized as periodic chirping. We observe that,

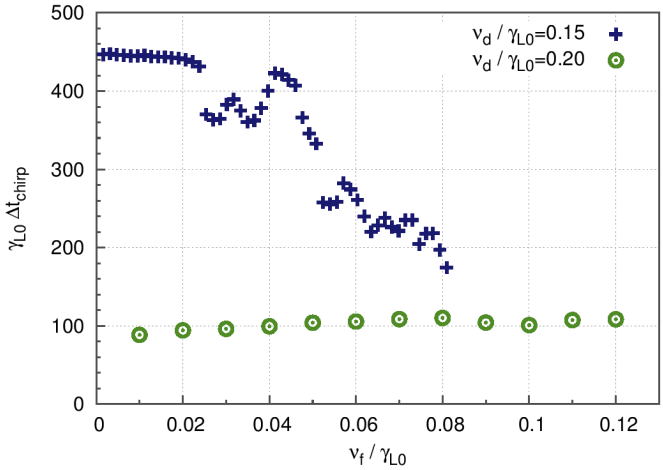

Figure 4.24 – Effect of drag on chirping period at fixed diffusion, for $\nu_d = 0.015$ and 0.020.

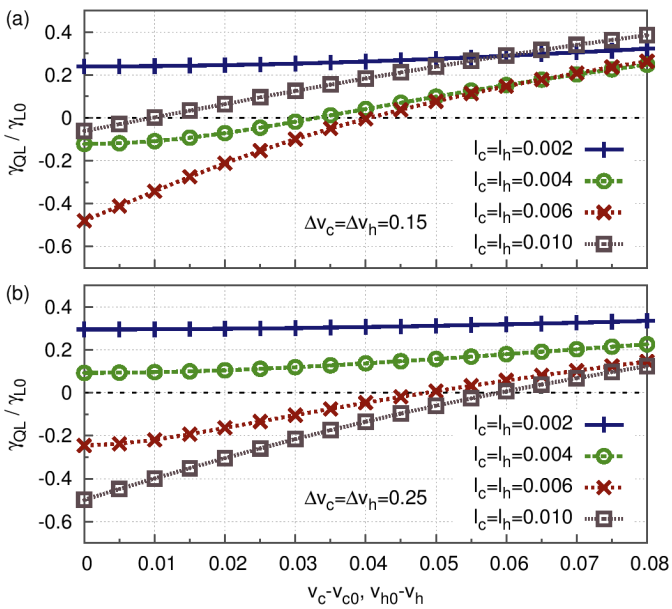

Figure 4.25 – Effect of hole/clump shift on quasilinear growth rate. (a) Small width $\Delta v_h = \Delta v_c = 0.15$. (b) Large width $\Delta v_h = \Delta v_c = 0.25$. In both cases we choose $v_{c0} = v_{h0} = 0.16$, where lines cross in Fig. 4.22(b).

when the period is large, the general trend is a decreasing period as drag increasing. The trend is reversed when the period is small.

To understand this complex behavior, we need to take into account the effect of drag on both bursting phase and quiescent phase. In the bursting phase, drag lengthens the lifetime of the hole by deepening it [LBS10]. On the one hand, when the bursting phase is significantly shorter than the whole period, this is not a significant effect, as can be seen in Fig. 4.19(a). Thus the effect of ν_f on chirping period is explained by the effect on the quiescent period. From Eqs. (4.64)-(4.66), it is clear that the only effect of drag during the quiescent period is to shift holes and clumps to smaller velocities. After one chirping burst, both hole and clump are roughly shifted by a same amount, here $v_{c0} = v_{h0} = 0.16$ at $\gamma_{L0}t = 30$, which is the extent of chirping. Fig. 4.25 shows the quasilinear growth rate against the shift $v_c - v_{c0} = v_{h0} - v_h$, for various hole/clump sizes and widths. We observe that in all these cases, the growth rate increases with shift. This clarifies the effect of drag on period: the larger the drag, the more rapidly the hole/clump pair is decelerated after a burst, the larger the nonlinear growth rate, thus the shorter the quiescent phase and the smaller the chirping period.

On the other hand, when the quiescent phase is much smaller than the whole period, the dominant effect is the lengthening of the bursting phase. In this case, which is less frequent, chirping period increases with increasing drag. This corresponds to the case $\nu_d/\gamma_{L0} = 0.2$ in Fig. 4.24.

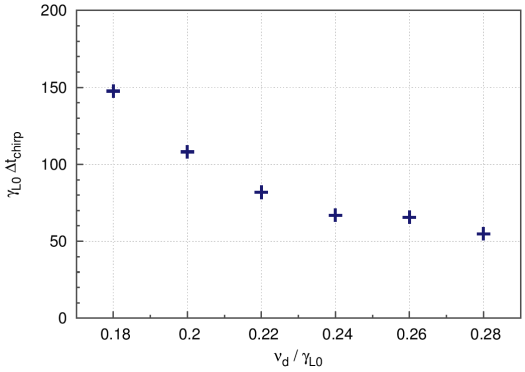

Figure 4.26 – Effect of diffusion on chirping period at fixed drag, $\nu_f = 0.005$.

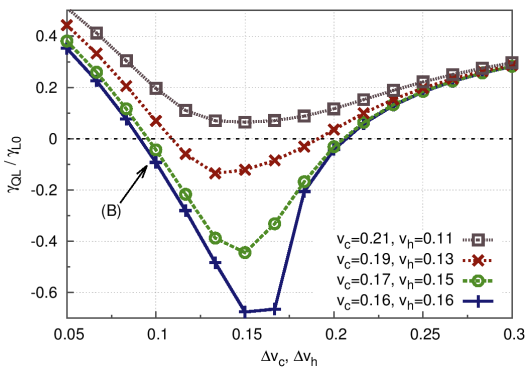

Figure 4.27 – Effect of diffusion on quasilinear growth rate. The product $l_{c,h}\Delta v_{c,h} = 8 \times 10^{-4}$ is kept constant.

Effect of diffusion

The effect of diffusion on chirping period is consistent with simple intuitive arguments. Fig. 4.26 shows that the period decreases as diffusion increases, for fixed drag. For large diffusion, the effect tends to saturate. Again, the data points are shown only for simulations categorized as periodic chirping.

As can be seen from Eq. (4.64), while the hole/clump amplitude is decreased and the width is increased by diffusion, the product $l_{c,h}\Delta v_{c,h}$ is conserved. Fig. 4.27 is a scan of the quasilinear growth rate for decreasing $l_{c,h}$ and increasing $\Delta v_{c,h}$, while $l_{c,h}\Delta v_{c,h} = 8\times10^{-4}$ is kept constant, for various shifts of the hole/clump pair. In all these cases, the rate decreases until $\Delta v_{c,h} \approx 0.15$, then increases. This clarifies the mechanism of relaxation oscillation of the wave amplitude. After a burst, the system is typically at the point marked (B) in Fig. 4.27 with a negative growth rate. As diffusion acts (as we move to the right in the figure), the growth rate must go through even more negative values before recovering toward the linear growth rate. The larger ν_d is, the quicker this process is, thus the smaller the chirping period.

In addition to the effect of ν_d on the quiescent period, increasing ν_d also decreases the duration of the bursting phase, by damping holes and clumps. This is an additional reason why Δt_{chirp} decreases with increasing ν_d.

Conclusion

To clarify the mechanism of relaxation oscillation, I showed that the period is mainly dictated by dynamical friction and velocity-space diffusion. Between two bursts, wave amplitude is low, and collisions dominate over the nonlinear term in the kinetic equation. By modeling a hole and a clump in the velocity distribution by two Gaussians, their dynamics is obtained as the analytic solution of a Fokker-Planck equation, given an initial fit of the structures just after a burst. There is good agreement between analytic prediction and numerical simulation for the hole/clump width, amplitude and shift. The instantaneous quasi-linear growth rate was then obtained numerically by solving a linear equation system. This procedure recovers time-evolution of amplitude growth and leads to a better qualitative understanding of the nonlinear evolution of wave amplitude between bursts. In addition, this theory explains why the growth rate of the first burst, which is equal to the linear growth rate, is different from (in the simulation, twice larger than) the instantaneous growth rate of subsequent bursts.

Let me mention a few caveats to this analysis. Firstly, collision frequencies are not the only factors that determine Δt_{chirp}. If linear drive is decreased, more time is required to recover a gradient steep enough to overcome damping, hence Δt_{chirp} increases. Secondly, the accuracy of our simple model of hole/clump pair as two Gaussians is degraded after the first burst, as remnants of holes and clumps from former bursts enter the picture. Thirdly, particle trapping and detrapping are not taken into account in my theory. However, the

agreement with simulations, where trapping and detrapping naturally occurs, shows that their effect on hole/clump amplitude, shift and width is not significant in the quiescent phase. Finally, additional effects, such as hole-hole or clump-clump interactions, and long-range chirping [Bre10], should be taken into account to improve the theory. However, these effects have limited impacts when the quiescent phase is larger than the bursting phase, or for the periodic chirping regime with small enough frequency shift. The latter regime is important since it was observed in tokamak experiments [KKK+99, PBG+04]. Hole-hole or clump-clump interactions can be neglected because one single hole and one single clump dominate during one chirping burst.

4.3.6 Analysis of experimental chirping modes

Here we describe a method for estimating local linear drive, external damping rate and collision frequencies based on experimental observations of chirping EP-driven modes. The method, which relies on the theoretical and semi-empirical laws for nonlinear chirping characteristics, consists of fitting procedures between the BB model and the experiment, in the quasi-periodic chirping regime. The uncertainty of this method is estimated by measuring the effects of small variations. The linear drive and the damping rate are estimated to within 5% and 10% accuracy, respectively. We apply this method to TAEs in JT-60U and in MAST (the method we apply to EGAMs on the LHD in 4.4.6 is related but different). In both cases, we find a relaxation oscillation with $\gamma_L \approx 2\gamma_d$, while the system is very close to marginal stability in a long time-averaged, or nonlinear point-of-view.

We have seen simple analytic expressions for the chirping velocity, Eq. (4.46), and for the chirping lifetime, Eqs. (4.60)-(4.61). Analytic theory does not provide a robust analytic expression for the chirping period in function of the input parameters. However, conceptually, there exists some relation with a subset of the input parameters. Thus, if we normalize time with the mode frequency, then chirping velocity, lifetime and period are dictated by the input parameters of the model, γ_{L0}, γ_d, and ν_a, or ν_f and ν_d. In the Krook case, we have a 3-variables, 3-equations system, which can be solved by a fitting procedure described in Ref. [LIS+10]. However the periodic regime with quiescent phases between bursts, observed in the experiments, is not recovered. Therefore we focus on the collision operator with drag and diffusion. In this case, there is one additional degree of freedom, hence the solution is not unique, but the boundaries of chirping regime limit the possible range of input parameters.

Motivation

Although considerable progress has been made in the theoretical understanding of the principal EP-driven instabilities [HF14], including with strong drive [CZ16], and the question of their stability in ITER [PCL+15], the estimation of the mode growth rate γ remains complex. Accurate estimations of the linear drive γ_L and the damping rate γ_d are needed, especially if the system is close to marginal stability, where γ is sensitive to small variations.

The linear drive γ_L depends on several factors such as the spatial and energy gradients of the EP distribution and the alignment between particle orbits and the eigenmode. It can be estimated either by linear stability codes, such as PENN [JAVV95], TASK/WM [FA03], NOVA-K [Che92], CASTOR-K [BBB+02], or LIGKA [LGKP07] ; or by gyro- or drift- kinetic perturbative nonlinear initial value codes, such as MEGA [TSW+95], FAC [CBB+97], HAGIS [PAC+98].

The global damping involves complicated mechanisms, which include continuum damping [ZC92], radiative damping [MM92], Landau damping with thermal species [BF92, ZCS96] and collisional damping [GS92]. A linear code benchmark shows that the typical accuracy is about 50% for γ_d [BFG+10]. Experimentally, γ_d can be estimated by active measurements of externally injected perturbations [FBB+95, FBB+00]. However, the applicability of this technique is limited to dedicated experiments. Moreover, the existence of subcritical AEs has not been ruled out. Therefore, nonlinear analysis is needed to assess the stability.

Methodology

We consider magnetic field perturbations measured by a Mirnov coil at the edge of a fusion plasma, for a time interval during which quasi-periodic, perturbative chirping is observed, and during which background plasma parameters are not significantly changed. One important assumption to reduce the problem to a one dimensional Hamiltonian is a fixed mode structure. This implies that we must assume that frequency shifting occurs well within the gap of the Alfvén continuum.

In the corresponding magnetic spectrogram, we extract the mode frequency f_{A}, the average chirping velocity, $d\delta\omega^2/dt$, the maximum chirping life-time, $\tau_{\max}$, and the average chirping period, $\Delta t_{\mathrm{chirp}}$. We aim at estimating the values of γ_{L0}, γ_d, ν_f and ν_d for which the δf BB model fits experimental observations.

Eq. (4.46) gives a relation between the linear drive and external damping,

$$\gamma_{L0}^2\,\gamma_d \;=\; \frac{1}{\alpha^2\beta^2}\,\frac{d\delta\omega^2}{dt}. \tag{4.69}$$

For frequency sweeping of the order of 10% of the linear frequency, it is reasonable to assume that the chirping lifetime is determined by collision processes, rather than by an evolution of continuum damping. Inverting Eq. (4.61) yields a relation between the linear drive and collisional diffusion,

$$\frac{\gamma_{L0}}{\nu_d^3} \;=\; \left(\frac{\tau_{\max}}{\iota_d}\right)^2. \tag{4.70}$$

Eqs. (4.69) and (4.70) form a system of two equations with four unknowns. The limited range of the quasi-periodic chirping regime yields a third constraint on the input parameters. Finally, we need a 2D scan in (ν_f, ν_d), where we search for solutions that fit the chirping period. In general, $\beta \neq 1$, and trial-and-errors are required to adjust chirping velocity to the experimental value.

Assumptions and caveats

Based on the above relations, it is possible to recover the input parameters of the BB model such that the nonlinear evolution fits the experiment in terms of chirping velocity, lifetime and period. In our analysis, we choose and fix the shape and extent of f_0, the approximation that f_0, γ_d, and collision frequencies are time-independent, and the approximation that collisions are velocity-independent. These choices are justified in the same way than we justify applying the BB model to TAEs: a posteriori, by checking that the fitted parameters agree with experimental values and independent calculations.

However, this method of analysis is subject to important caveats, in addition to the caveats which come with applying the BB model to EP-driven modes (described in subsection 4.1.4). Namely, we assume that the input parameters of the BB model that fit the experimental spectrogram are a good estimate of the local growth rate, damping rate, and collision frequencies. This is a strong assumption, which requires independent validation.

Overall, this method of analysis is suitable for weakly driven, isolated EP-driven chirping modes, as long as

— the extent of chirping is small enough ;
— phase-space structures are well confined within the continuum gap ;
— the redistribution of energetic population is negligible as far as wave dispersiveness and damping mechanisms are concerned ;
— we consider timescales much smaller than the equilibrium evolution timescale.

Application to JT-60U

In JT-60U, TAEs are destabilized by a negative ion based neutral beam (N-NB), which injects deuterons at $E_b = 360$ keV. A distinction is made between abrupt large-amplitude events (ALE) and fast frequency sweeping (fast-FS) [SKT+01]. Here, we focus on the latter phenomenon, which has a timescale of $1-5$ ms, and with which the associated redistribution of energetic ions is relatively small [STI+02]. ALEs are identified as energetic particle driven modes [BFV+07], have larger amplitude and shorter timescale (200-400 μs),

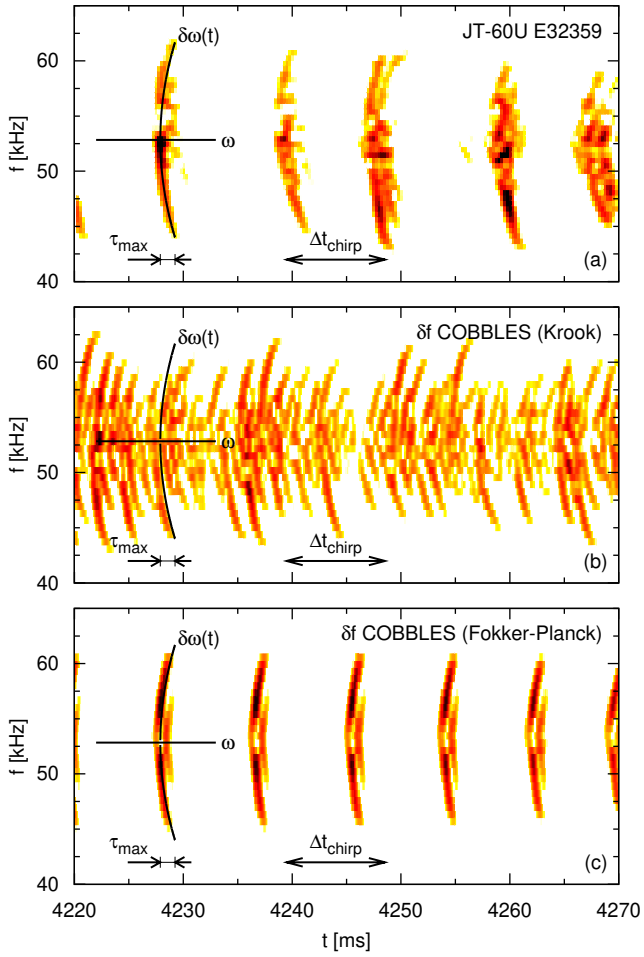

Figure 4.28 – (a) Spectrogram of magnetic fluctuations during fast-FS modes in the JT-60U discharge E32359, obtained with a moving Fourier window of size $2\,ms$. (b) and (c) Spectrogram of the electric field, where the kinetic parameters of the δf BB model were chosen to fit the magnetic spectrogram for JT-60U discharge E32359. The solid curve shows the analytic prediction for the chirping velocity. (b) Krook collisions, correction parameter $\beta = 0.65$. (c) Friction-diffusion collisions, correction parameter $\beta = 0.75$.

induce significant loss of energetic ions, and are out of the scope of this work since we assume a constant density of energetic ions. In the discharge E32359, around $t = 4.2$ s, chirping modes have been identified as $m/n = 2/1$ and $3/1$ TAEs [KKK+99]. Fig. 4.28(a) shows the corresponding spectrogram.

Let us apply our fitting procedure. We perform a first, rough scan in (ν_f, ν_d) parameter space, assuming $\beta = 1$. Measuring average chirping velocity in repetitive chirping solutions yields an estimation of the correction parameter, $\beta = 0.75$. We perform a second, more careful scan, which consists of a series of 4×8 simulations in the domain ($1.5\% \leq \nu_d \leq 2.2\%$, $1 \leq \nu_d/\nu_f \leq 8$), where γ_{L0} and γ_d are constrained by Eqs. (4.69) and (4.70). In this scan, we find only one repetitive chirping solution with a period in agreement with the experiment within 10% accuracy. The corresponding spectrogram is shown in Fig. 4.28(c). All chirping features measured in this simulation fit the experiment. The estimated linear parameters

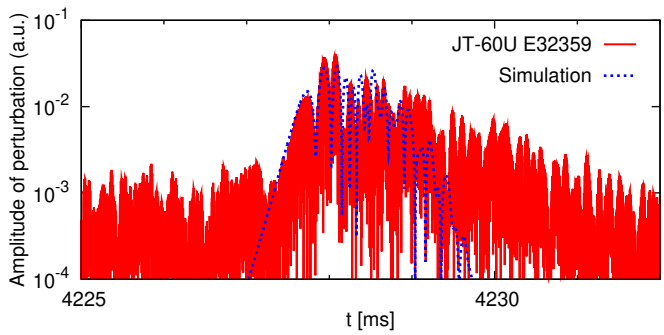

Figure 4.29 – Evolution of the amplitude of perturbations during a single chirping event. The signal is filtered between 40 and 65 kHz. In these arbitrary units, 10^{-3} roughly corresponds to a noise level. The parameters of the simulation are shown in Tab. 4.1.

Experiment	γ_{L0}	γ_L	γ_d	ν_f	ν_d	γ
JT-60U (E32359)	0.098	0.088	0.047	0.0042	0.017	0.046
MAST (#5568)	$0.112^{+5\%}_{-2\%}$	$0.099^{+4\%}_{-2\%}$	$0.050^{+9\%}_{-4\%}$	$0.0055^{+6\%}_{-9\%}$	$0.0228^{+3\%}_{-1\%}$	$0.055^{+2\%}_{-2\%}$

Table 4.1 – Frequencies and growth rates estimated from the magnetic spectrogram of chirping TAEs, in units of the mode frequency $\omega_{\rm A} = 2\pi f_{\rm A}$. In the last row, the percentages in subscript and superscript indicate the relative uncertainties.

are shown in the second row of Tab. 4.1, in units of the mode frequency $\omega_{\rm A} = 2\pi f_{\rm A}$. In theory, the solution is not unique, but the latter estimations are quite accurate because of the narrow range of periodic chirping regime.

We also included as Fig. 4.28(b) the simulation which is closest to the experiment in term of chirping quasi-period in the Krook case. We observe a series of minor chirping events in between, which are absent from the experimental spectrogram. The damping rate estimated from this analysis is $\gamma_d = 8.6\omega_{\rm A}$, which is inconsistent with the latter estimation with drag and diffusion processes. Since the latter shows much better agreement with the experiment, we imply that the Krook model is insufficient to describe nonlinear features related to repetition of chirping.

To validate this analysis (with drag and diffusion), we compare the amplitude of perturbations in Fig. 4.29. Since the growth rate of chirping structure is neither γ nor γ_L, and the decay rate not simply γ_d, but a function of several linear parameters, the agreement we obtain is not trivial (we measure a growth rate of 2.3%, and a decay rate of 0.3%). For further validation, let us estimate the values of ν_f and ν_d from plasma parameters.

Validation by comparing the collision frequencies

In the discharge E32359 around $t = 4.2$s, the resonant surface of the $m/n = 2/1$ and 3/1 TAE is located around $r = 0.7$m. The magnetic shear is estimated from the q profile [GBC+00], $S = 0.8$. The deuterium plasma has the following characteristics, $B_0 = 1.2$T, $R_0 = 3.3$m, and the tangential radius of the N-NB is $R_T = 2.6$m. At $r = 0.7$ m, $n_e = 1.4 \cdot 10^{-19}\mathrm{m}^{-3}$, and $T_0 = 0.75$keV. We take into account carbon impurities with $Z_{\rm eff} = 2.7$. Since the magnetic moment is an invariant of the motion of injected beam ions from deposition to resonant surface, we substitute $v_\perp^2 = v_b^2(1 - R_T^2/R_0^2)$, where v_b is the velocity of beam particles. With these equilibrium measurements, Eqs. (4.11-4.12) yield $\nu_f/\omega = 1.2\%$ and $\nu_d/\omega = 1.7\%$. Note that electrons account for 99% of ν_f^2, which reflects a high Alfvén velocity, while impurities account for 57% of ν_d^3, which is consistent with the fact that pitch-angle scattering is more effective with heavier particles. The value of ν_d estimated above quantitatively agrees with this independent estimation. However, with our fitting procedure, ν_f was underestimated by 64%. Though error bars in the experimental data may account for this discrepancy, it is also possible that our model misses some mechanism that would enhance the friction.

Application to MAST

The magnetic spectrogram for the MAST discharge #5568 between 64 and 73 ms is shown in Fig. 4.30(a). The frequency sweeping mode has been identified as a global $n = 1$ TAE, with a relative amplitude peaking at $\delta B/B_0 \approx 4 \times 10^{-4}$ [PBG+04], which is below a typical threshold of 10^{-3} for large fast particles losses induced by orbits stochastisation [SHWC92, BBY93a]. The extent of chirping is of the order of 15% of the linear mode frequency. The median frequency is constant, which suggests that the linear mode structure is not significantly changed during the time interval of interest. Although we do not have enough information to reconstruct the shear-Alfvén continuum, the small aspect ratio in MAST suggests a large gap [GS04]. These are indications that the BB model may be applied to this TAE.

We apply our fitting procedure. After three iterations of scans in the (ν_f, ν_d) parameter space, our final scan consists of a series of 4×8 simulations in the domain ($0.017 \leq \nu_d \leq 0.026$,

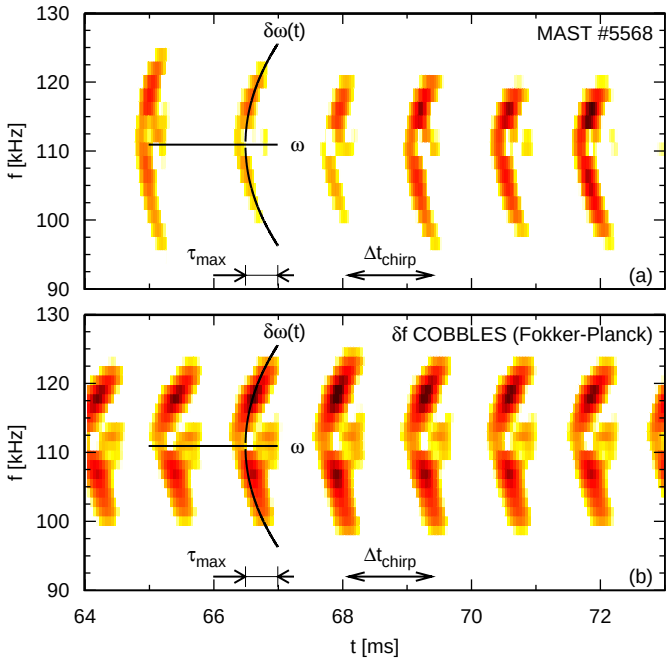

Figure 4.30 – (a) Spectrogram of magnetic fluctuations in the MAST discharge #5568, obtained with a moving Fourier window of size 2 ms. Logarithmic colour scale spanning 3 orders of magnitude. (b) Spectrogram of the electric field, obtained with a moving Fourier window of size 0.6 ms, where the input parameters of the δf BB model were chosen to fit (a). Solid curves show the analytic prediction for the chirping velocity and lifetime, with a non-adiabaticity correction parameter $\beta = 0.65$.

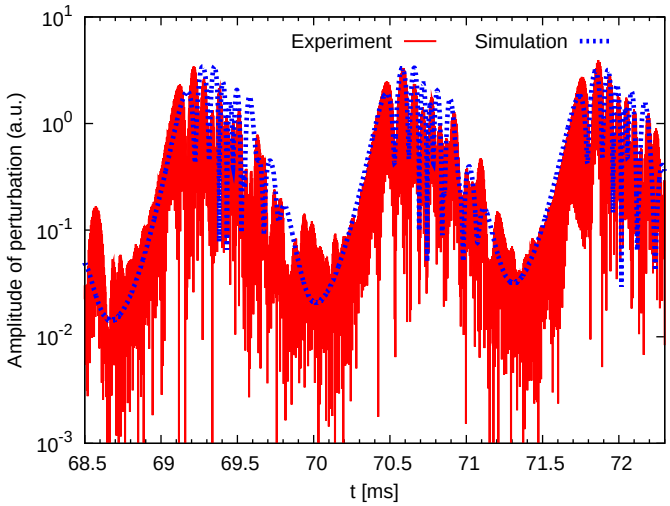

Figure 4.31 – Time-evolution of the perturbation. The signal is filtered between 90 and 130 kHz. The parameters of the simulation are shown in Tab. 4.1. For the simulation, to avoid hiding experimental data, we show the amplitude of perturbations (the envelope) instead of the perturbations themselves. Note the use of arbitrary units (we compare normalized quantities only).

$1 \leq \nu_d/\nu_f \leq 8$), where γ_{L0} and γ_d are constrained by Eqs. (4.69) and (4.70). We find only one repetitive chirping solution with a period in agreement with the experiment within 10% accuracy. The corresponding spectrogram is shown in Fig. 4.30(b). We verify that all chirping features measured in this simulation fit the experiment. The estimated linear parameters are shown in Tab. 4.1.

As a validation of our analysis, we compare the amplitude of perturbations in Fig. 4.31. As another validation, we measure a saturated bounce frequency of $\omega_b \approx 0.06$ in the simulation, which is in agreement with the value of 0.054 estimated in Ref. [PBG+04]. We note that the relationship with linear drive is also in agreement with the theoretical result $\omega_b \approx 0.54\gamma_{L0}$ [BBP97b].

An important result, which was also found in our analysis of JT-60U, is that $\gamma_L \approx 2\gamma_d$. This contradicts a naive assumption, $\gamma_L \approx \gamma_d$, or $\gamma \ll \gamma_L$. The latter assumption can be made from self-organization arguments, according to which nonlinear effects tend to keep a system close to its instability threshold. However, this physical picture should be understood in a long-time average point-of-view, whereas γ_L represents an instantaneous instability drive from the initial distribution. Fig. 4.32 shows the velocity distribution corresponding to the simulation shown in Fig. 4.31, averaged over 15 chirping bursts. This average distribution

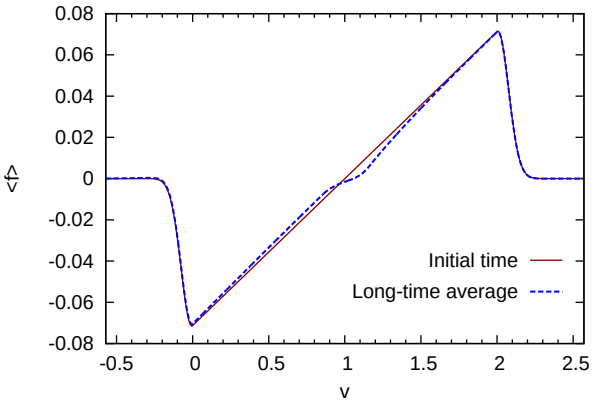

Figure 4.32 – Initial (solid line), and long-time averaged (dashed line) velocity distribution function, for the simulation shown in Fig. 4.31. Here, $\langle f \rangle$ is the average over 20ms of the velocity distribution.

yields a (quasi-)linear growth rate $\gamma = 0.003$, which is much smaller than γ_L. Therefore, in a long-time average point-of-view, the mode is close to marginal stability, but in an instantaneous point-of-view, $\gamma \sim \gamma_L$.

To quantify the accuracy of our fitting procedure, we make two scans, one on ν_f, and another on ν_d, in the neighbourhood of the solution for MAST. Based on the way the simulations deviate from the experimental data, we estimate errorbars for the estimations of input parameters, which are included in the last row of Tab. 4.1.

Discussion on the analysis of chirping modes

We described how to take advantage of measurements of fluctuations associated with EP-driven modes in the quasi-periodic chirping regime to estimate fundamental kinetic parameters of the local EP distribution. Since quantitative agreement with theory suggests the predictability of nonlinear chirping characteristics based on fundamental linear kinetic parameters, the latter may be estimated in the opposite way from chirping data in experiments. More precisely, chirping velocity and life-time yield two relations among γ_L, γ_d, and collision frequencies; and a fitting of Δt_{chirp} yields an estimation of remaining unknowns. Note that major advantages of this technique are 1. kinetic parameters in the core of the plasma estimated only from the spectrogram of magnetic fluctuations measured at the edge, without expensive kinetic MHD calculations nor detailed core diagnostics, and 2. unified treatments of supercritical and subcritical modes. We showed that drag and diffusion are essential to reproduce quiescent phases observed in experiments between chirping events.

We confronted this procedure by analyzing AEs on MAST and JT-60U. We found quantitative agreement with measured magnetic fluctuations for the growth and decay of chirping structures, with 3D calculations of the bounce-frequency, and qualitative agreement with collision frequencies estimated from experimental background measurements. In these estimations, impurities account for the main part of velocity diffusion. An effect of drag is to break the symmetry around the resonant velocity. The discrepancy between simulations and experiments in terms of asymmetry between up-shifting and down-shifting frequencies remains to be clarified. The shape of the energetic particle distribution has a significant effect on chirping asymmetry. In the present analysis, we chose a linear initial distribution. However it is unclear what shape of velocity distribution is relevant to the experiment.

Finally, an analytic theory for the chirping quasi-period, or an empirical formula, would allow real-time estimations of the kinetic parameters to replace this time-consuming fitting procedure.

4.4 Fluid coupling with another mode

We have seen in Sec. 4.3.2 that linearly stable modes can be destabilized (subcritically) by the presence of structures (holes and clumps) in phase-space. However, the nonlinear growth of these structures requires the presence of a seed structure with a relatively large threshold in amplitude. We demonstrate that, in the presence of another, linearly unstable (supercritical) mode, wave-wave coupling can provide a seed, which can lead to subcritical instability by either one of two mechanisms. Both mechanisms hinge on a collaboration between fluid nonlinearity and kinetic nonlinearity. If collisional velocity diffusion is low enough, the seed provided by the supercritical mode overcomes the threshold for nonlinear growth of phase-space structure. Then, the supercritical mode triggers the conventional subcritical instability. If collisional velocity diffusion is too large, the seed is significantly below the threshold, but can still grow by a sustained collaboration between fluid and kinetic nonlinearities. Both of these subcritical instabilities can be triggered, even when the frequency of the supercritical mode is rapidly sweeping. These results were obtained by modeling the subcritical mode kinetically, and the impact of the supercritical mode by simple wave-wave coupling equations. This model is applied to bursty onset of geodesic acoustic modes in a LHD experiment. The model recovers several key features such as relative amplitude, timescales, and phase relations. It suggests that the strongest bursts are subcritical instabilities, with sustained collaboration between fluid and kinetic nonlinearities.

4.4.1 Introduction

As we reviewed in chapter 3, the subcritical bifurcation in hot plasmas can originate either from fluid nonlinearities (or nonlinearities in real space), or a kinetic nonlinearities (or nonlinearities in the phase-space of particle distribution).

However, such subcritical growth requires a large-amplitude seed perturbation. Several scenarios could provide the seed for kinetic nonlinear growth of a linearly stable mode:

1. the presence of large thermal noise or an external source of wave excitation,
2. a hysteresic path from supercritical to subcritical regime, or
3. a transfer of energy from another, linearly unstable mode.

Previous works on kinetic subcritical instabilities, including the theory presented in subsection 4.3.2, assumed some initial, relatively large amplitude (at least, compared to thermal noise) perturbation [BBC+99, LIG09] for the subcritical mode, corresponding to scenario 1. The hysteretic behavior, corresponding to scenario 2, was obtained in COBBLES simulation, although this work remains unpublished. As for the work on ion-acoustic turbulence we describe in section 5.3, it corresponds to an artificial scenario, where a seed phase-space hole is imposed at $t = 0$.

In Ref. [LII+16b], we developed a model to explore the scenario 3. The model combines the kinetic description of a linearly stable (subcritical) mode with the nonlinear fluid coupling with a prescribed linearly unstable (supercritical) mode. It is an extension of the Berk-Breizman (BB) model [BBP95a] to two interacting modes. The model suggests that the supercritical mode can provide a seed for the nonlinear growth of the subcritical mode. Hereafter, we investigate two interesting regimes. In a first regime, of *successive fluid then kinetic growth*, the dormant subcritical mode is first triggered by fluid coupling to the supercritical mode, which allows it to reach amplitudes of the same order of magnitude as the supercritical mode. This amplitude is above the threshold for the conventional kinetic subcritical instability, Eq. (4.57), therefore the amplitude can keep growing by momentum exchange between the wave and phase-space structure(s). In a second regime, of *collaborative fluid-kinetic growth*, the subcritical growth is due to an uninterrupted collaboration between fluid and kinetic nonlinearities. This is a new kind of instability mechanism, where fluid and kinetic nonlinearities have similar (in amplitude) contributions to the mode growth. Contrarily to the mechanism developed in earlier theories, the growth occurs much below the amplitude threshold, and without chirping.

As shown in Ref. [LII+16b], the model qualitatively reproduces an experimental observation, and interprets it as a subcritical instability with essential roles of both fluid and

kinetic nonlinearities. In the latter reference, we analyzed an intriguing observation in the helical plasma of the LHD, which was described first in Ref. [IIO+16]. Bursts of EGAM, with dynamical evolution of frequency (chirping) are routinely observed, with a 10 ms duration [IOS+15]. Surprisingly, such a primary EGAM burst is sometimes accompanied by a secondary, stronger burst. The secondary burst has a 1 ms duration, and a peak amplitude that significantly exceeds that of the primary burst. Since the existence of the secondary burst appears to be tied to the primary burst, we call the primary (weaker, and chirping) burst as *mother mode*, and the secondary burst as *daughter mode*. The mother EGAM chirps from 50 kHz to 90 kHz. When it approaches 80 kHz, the daughter mode abruptly appears at ~ 40 kHz, with a growth rate one order-of-magnitude larger than the mother's. The amplitude increase of the daughter is so large (compared to the amplitude decrease of the mother) that it clearly violates the Manley-Rowe relations [MR56]. This suggests that the daughter is not excited by e.g. simple parametric coupling. In subsection 4.4.6, we summarize the relevant experimental conditions, and apply our model to a typical daughter burst as shown in Fig. 4.37. Our analysis suggests that the daughter mode is a subcritical instability, which is dormant until the mother excites it into the regime of collaborative fluid-kinetic growth. This was first reported in Ref. [LII+16b], and here we expand on the latter analysis of LHD experiment. We further discuss the applicability of the model to this experiment, and several caveats.

The main point of this section, though, is to provide more theoretical basis for the reduced model (subsection 4.4.2), explore different regimes (subsections 4.4.3 and 4.4.4), and clarify the underlying physics based on the behavior in simpler limits (subsection 4.4.5).

4.4.2 Expanding the Berk-Breizman model

In this work, we consider the interaction of two modes. To treat the present problem, we split the electric field E between the two waves, $E = E_1 + E_2$, and introduce a hybrid model. The subcritical (daughter) mode, E_1, is treated by the kinetic 1D model, and the supercritical (mother) mode, E_2, is treated as a simple medium for nonlinear energy transfer. For E_2, we prescribe the initial amplitude $Z_{2,0}$ and time-evolution of frequency $\omega_2(t)$. We assume that the impact of the mother on the particles near the resonant location of the daughter is negligible. This is a strong assumption, because there is a near-integer frequency ratio at the time of daughter burst. We encourage direct tests of this assumption by first-principles calculations. The interaction between the two waves is modeled by the equations for period doubling.

In our model, as for the δf-BB model, the linear frequency of the wave E_1 is fixed. Even when chirping occurs, ω_1 does not change. Chirping, when it occurs, is due to the nonlinear evolution of the amplitude and phase of E_1, rather than the evolution of ω_1.

The evolution of the energetic particle distribution, $f(x, v, t)$, in the neighbourhood of the resonance of the daughter mode E_1, is given by the same kinetic equation as in the BB model, Eq. (4.25), which we recall here with adapted notations:

$$\frac{\partial f}{\partial t} + v\frac{\partial f}{\partial x} + \frac{qE_1}{m}\frac{\partial f}{\partial v} = \frac{\nu_f^2}{k_1}\frac{\partial \delta f}{\partial v} + \frac{\nu_d^3}{k_1^2}\frac{\partial^2 \delta f}{\partial v^2}. \tag{4.71}$$

The evolution of the two parts of electric field is given by

$$\frac{\mathrm{d}Z_1}{\mathrm{d}t} = -\frac{m\omega_1^3}{4\pi q^2 n_0}\int f(x,v,t)\, e^{-i(k_1 x - \omega_1 t)}\,\mathrm{d}x\,\mathrm{d}v \;-\; \gamma_d\, Z_1 \;-\; \imath\frac{V}{\omega_1} Z_2 Z_1^* e^{-\imath\theta t}, \tag{4.72}$$

$$\frac{\mathrm{d}Z_2}{\mathrm{d}t} = -\imath\frac{V}{\omega_2} Z_1^2 e^{\imath\theta t}, \tag{4.73}$$

where $E_j \equiv Z_j \exp\left[\imath(k_j x - \omega_j t)\right] + c.c.$, and n_0 is the total density.

Note that we recover Eq. (4.30) in the limit of no wave coupling ($V = 0$). The perturbed current is obtained by assuming that energetic particles interact with a mode only if their velocity v_i is close enough to the mode's phase velocity $v_\phi = \omega_1/k_1$. Terms of the order of $(\omega_b/\omega_1)^2(v_i - v_\phi)/v_\phi$ are neglected.

Parameter	Description	Value	Range	Independent estimat.
γ_{L0}/ω_1	Linear drive of daughter	0.03	$0.01 - 0.08$	0.1 is supercrit. [WT13]
γ_d/γ_{L0}	L. dissipation of daughter	1.03	$1.01 - 1.7$	$\gamma_L \approx \gamma_d$ hypothesis
ν_f/γ_{L0}	Collisional friction	0.067	$0.003 - 0.3$	Fokker-Planck, 0.068
ν_d/γ_{L0}	Collisional diffusion	0.53	$0.3 - 1.5$	Fokker-Planck, 0.44
VZ_0/ω_1^2	Fluid coupling coefficient	50	$40 - 80$	$\sim 10^{-2} - 10^2$ [IHI+05]
$Z_{\text{noise}}/Z_{2,0}$	Noise amplitude	0.06	$10^{-4} - 0.3$	Input from
$10^3 Z_{2,0}/Z_0$	Initial mother's amplitude	1	$0.6 - 2.0$	experimental
$\omega_1^{-2}\mathrm{d}\omega_2/\mathrm{d}t$	Mother's chirping rate	5.10^{-4}	$10^{-4} - 10^{-3}$	data

Table 4.2 – Input parameters of the model. Here, Z_0 is an arbitrary normalizing factor.

We note that in this model, we split the electric field into two parts, and assume that there is one class of particles (distribution f) which does not interact with one of the two parts of the electric field. We consider the system composed of the two waves and the latter class of particles.

Novelty of the model

Eqs. (4.72) and (4.73) both include a term that describes energy exchange between mother and daughter. The nonlinear interaction between GAMs (zonal flows) has been studied. The dominant interaction originates either from second-order coupling between vorticity and parallel velocity, as well as vorticity and density [SIN+09], or via higher-order modulation mechanisms of background turbulence [HB01, IHI+05], when the conventional $\boldsymbol{v} \cdot \boldsymbol{\nabla} \boldsymbol{v}$ nonlinearity is not efficient.

In both cases, the coupling takes a standard form, which depends on the coupling constant V, and the frequency mismatch $\theta \equiv \omega_2(t) - 2\omega_1$. This choice is guided by the experimental observation on the LHD [IIO+16], where a ~ 40 kHz daughter mode abruptly grows when the mother mode approaches ~ 80 kHz. This is not accidental because 1. this ratio of ~ 2 is observed in all bursts and in different plasma shots ; and 2. the dynamics of period doubling has been demonstrated experimentally in the reference.

In this model, the linear frequency of the mode, ω_1 is fixed, but the frequency of E_1 can evolve nonlinearly due to the time-evolution of Z_1. In contrast, ω_2 is a prescribed function of time, which is a model for the nonlinear chirping of mode 2.

Eq. (4.73) does not include any dissipative term (no γ_d) nor driving term, because we assume a balance between external drive and external damping for simplicity. This assumption is consistent with the experiment we analyze in Sec. 4.4.6, given the timescale separation between evolutions of mother and daughter. Indeed, in the experiment, the timescale of evolution of the mother (~ 10 ms) is much slower than this of the daughter (< 1 ms), as long as the daughter's amplitude is less than half that of the mother's.

We extended δf-COBBLES to solve the initial-value model described above. Here all simulations are done with a grid $N_x \times N_v = 128 \times 2048$ and a time-step width is $\Delta t = 0.05\,\omega_1^{-1}$. To simulate thermal noise, we add to Z_1 a noise term $Z_{\text{noise}} e^{\imath \phi_r}$, where ϕ_r is a phase that is randomized at each time step. This is an important component of the modeling, since in our simulations, mode 1 is linearly damped and the quasi-resonance condition $|\theta| \ll \omega_1$ is only satisfied for a limited period of time. Without the noise, the amplitude of mode 1 would quickly decay to values orders-of-magnitudes below thermal noise, effectively disabling fluid coupling.

The input parameters of the model are summarized in Table 4.2, first and second columns. The third column gives reference values that are used in most simulations, apart from exceptions as mentioned later. The choice of reference values, and the meaning of the fourth and fifth columns, correspond to the LHD experiment, as will be explained in subsection 4.4.6.

Throughout this section, the frequency of the mother mode, ω_2, is chosen as a linear function of time, $\omega_2(t) = 1.5\omega_1 + (d\omega_2/dt)t$. The model is consistent with other kinds of slowly-evolving ω_2, but we impose this prescription in order to reduce the number of input

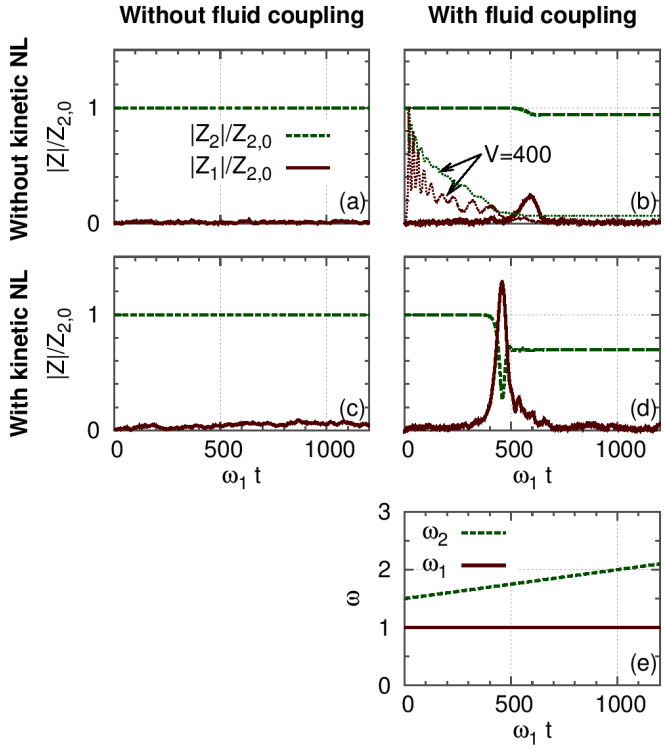

Figure 4.33 – Time evolution of the amplitudes of modes 1 and 2 in simulations of the full model (d), without fluid nonlinearity ($V = 0$) for (a) and (c), and without kinetic nonlinearity (no term in $\int f$ in Eq. (4.72)) for (a) and (b). The input parameters are given in Table 4.2. Thin dotted curves indicated by arrows in (b): case with increased coupling coefficient, $V = 400\,\omega_1^2/Z_0$.

parameters. The choice of constant slope can be seen as a first-order approximation based on the time-scale separation between the mother and the daughter, since we investigate the abrupt growth of the daughter rather than the slow evolution of the mother. The initial frequency mismatch $\theta(0) = -0.5\omega_1$ is arbitrary, but we have checked that the results do not depend on $\theta(0)$ (we have checked the range $\theta(0)/\omega_1 = -1.0$ to -0.4).

The extension of this model to three interacting modes is straightforward. However, a strong phase relationship between mode 1 and mode 2 in the experiment [IIO+16], suggests that the mechanism of energy exchange can be modeled by 2-waves coupling, without introducing additional input parameters associated with a 3-waves model. In our simulations, the time-evolution of mode 1 is similar whether we adopt the 2-waves model or 3-waves model. Therefore, for the sake of clarity, we do not discuss the 3-waves model any further in this manuscript.

4.4.3 Fluid and kinetic nonlinearities

Equation (4.72) contains two nonlinear terms, which we refer to as kinetic nonlinearity (the term proportional to $\int f e^{-\imath(k_1 x - \omega_1 t)}$), and fluid nonlinearity (the term proportional to $V Z_2 Z_1^* e^{-\imath\theta t}$). Figure 4.33 summarizes the main message of this section. It shows the time evolution of a subcritical mode 1 and a supercritical, chirping mode 2, obtained with the same input parameters, as listed in Table 4.2 (third column), with the following exceptions. The fluid nonlinearity is artificially disabled in the left column of the figure, and the kinetic nonlinearity is disabled in the top row of the figure. This figure shows that the fluid nonlinearity (b), and the kinetic nonlinearity (c), can work in collaboration (d) to drive a subcritical instability to relatively large amplitude. Figure 4.33(e) illustrates the fixed frequency ω_1 and the prescribed time-evolution of ω_2.

Let us make clear, that the message is not that fluid nonlinearity alone cannot drive a subcritical instability to relatively large amplitude. In fact, Fig. 4.33(b) includes, as dotted curves, a simulation with increased coupling coefficient, $V = 400\,\omega_1^2/Z_0$. In this case, mode 1 reaches an amplitude similar to the initial amplitude of mode 2. However, it does so at the expense of an increased depletion of the energy of mode 1, and with a qualitatively different evolution, in terms of e.g. the timing of the growth phase. The latter timing, in particular, is crucial to interpret experiments. The message is, rather, that the presence of

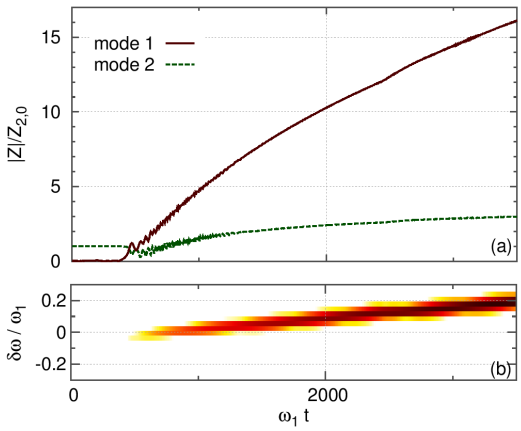

Figure 4.34 – Time-evolution of modes 1 and 2 (a), and spectrogram of the total field (b), in a simulation in the regime of successive fluid then kinetic growth. Input parameters are $\gamma_{L0} = 0.03\omega_1$, $\gamma_d = 0.031\omega_1$, $\nu_f = 1.3\gamma_{L0}$, $\nu_d = 0.53\gamma_{L0}$, $V = 60\omega_1^2/Z_0$, $Z_{\text{noise}} = 0.06Z_{2,0}$, $Z_{2,0} = 10^{-3}Z_0$, and $\mathrm{d}\omega_2/\mathrm{d}t = 5 \times 10^{-4}\omega_1^2$ (same as Fig. 4.37, except for an order-of-magnitude larger ν_f).

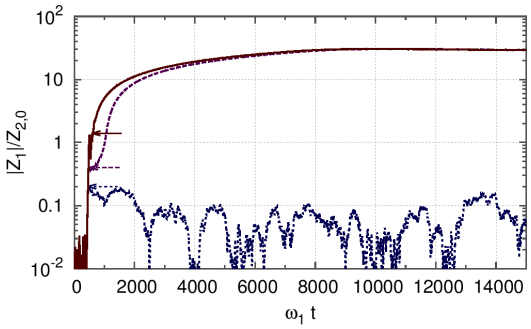

Figure 4.35 – Time-evolution of the amplitude of mode 1 for the same parameters as Fig. 4.34, but where the fluid nonlinearity is switched-off at a time marked by an arrow for each simulation.

kinetic nonlinearity, everything else being equal, can significantly enhance the subcritical growth of a mode coupled to a supercritical mode.

4.4.4 Phenomenology

We are interested in a parameter range where the daughter mode is significantly destabilized, with important contributions from both fluid and kinetic nonlinearities. In this parameter range, we can discriminate two interesting regimes (perhaps non-exhaustively).

1. In one regime, the daughter growth is first triggered by wave-wave fluid coupling to the mother mode, which allows it to reach amplitudes of the same order of magnitude as the mother. This amplitude is above the threshold for the conventional kinetic subcritical instability, therefore the amplitude can keep growing by momentum exchange between the wave and phase-space structure(s). In this case, the daughter mode chirps significantly, and its amplitude can grow one or more order(s)-of-magnitude above the mother.
2. In another regime, the daughter growth is due to an uninterrupted collaboration between fluid and kinetic nonlinearities. This is a new kind of instability mechanism, where fluid and kinetic nonlinearities have similar (in amplitude) contributions to the mode's growth. In this case, the daughter mode is not, or very weakly chirping, and its amplitude stays within the same order-of-magnitude as the mother. In subsection 4.4.6, we interpret an experimental observation of EGAM in the LHD as an example of this subcritical instability.

Let us now describe the evidences that support the previous claims.

Successive fluid then kinetic growth

When, typically, $\nu_f \sim \nu_d$, subcritical instabilities can arise, even in the single-mode limit, if the initial amplitude is large enough [LI12]. In previous works [BBC+99, LIG09, LD13], the kinetic subcritical instability was due to the growth of phase-space structures, and thus linked to chirping. In this case, we predicted that coupling to an unstable mode could provide the seed perturbation required for subcritical growth [LDK14a]. This is indeed what we observe with the present two-modes model.

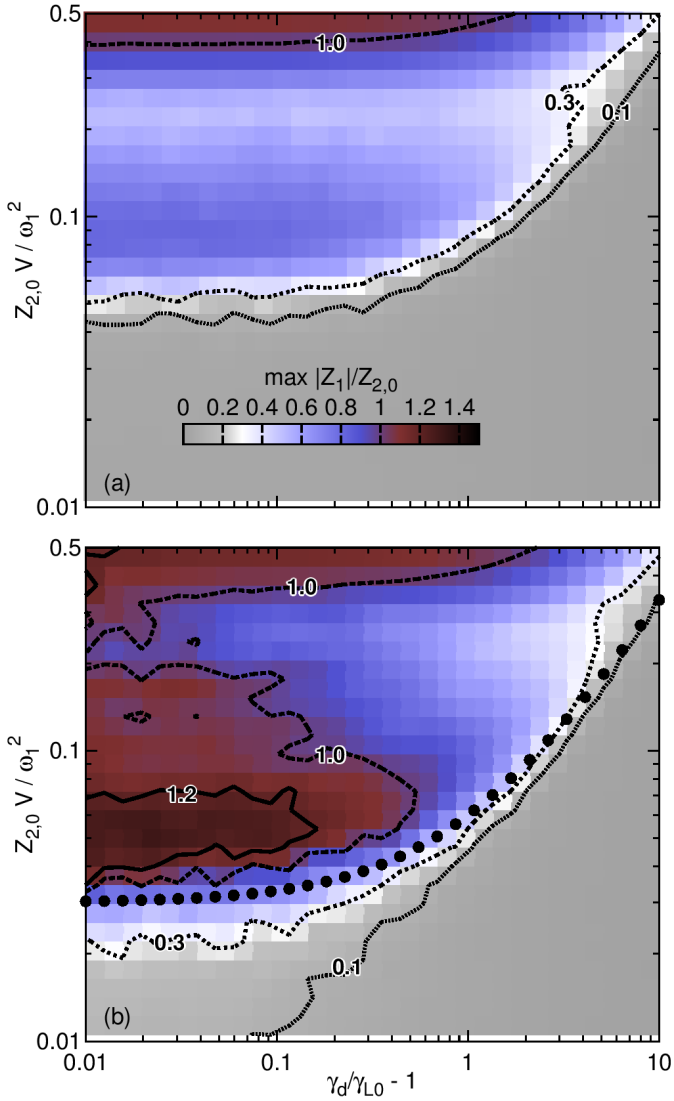

Figure 4.36 – Nonlinear stability diagram for the daughter mode without (a) and with (b) the kinetic nonlinearity. Peak amplitude of the daughter mode as a function of both the distance from linear stability, and the coupling coefficient. The white area corresponds to the stability threshold in a sense, which is explained in the main text. Plain circles in (b) show the threshold derived in Ref. [IIK+16].

Fig. 4.34 shows a typical simulation in this regime. We observe a subcritical instability of mode 1, and the amplitude grows to values much larger than the initial amplitude of mode 2. Meanwhile, as can be seen in the spectrogram (b), the frequency of mode 1 chirps significantly. When $\delta\omega/\omega_1 \approx 20\%$, we stop the simulation, because an assumption of the model breaks down. Namely, in the simulation, the phase-shift θ is calculated by assuming that ω_1 stays nearly constant.

Once fluid nonlinearity pushes the daughter amplitude to a large enough level, the subcritical instability is readily interpreted by the mechanism developed in Ref. [LD13]. Namely, the electric field of the daughter traps particles in a phase-space vortex, which is large enough to grow nonlinearly by climbing the positive velocity gradient of particle distribution.

This interpretation is further supported by the following numerical experiment. We switch off the fluid nonlinearity when the amplitude reaches a preset value. Fig. 4.35 shows the time evolution of three simulations with the same input parameters, except for a different preset amplitude of switch-off. When the switch-off amplitude is larger than $|Z_1|/Z_{2,0} \approx 0.3$, the growth of mode 1 continues to much larger levels. This shows that the fluid nonlinearity is not necessary after an initial part of the growth phase. This, along with previous knowledge, indicates that fluid and kinetic nonlinearities can act in a successive manner to yield a subcritical instability.

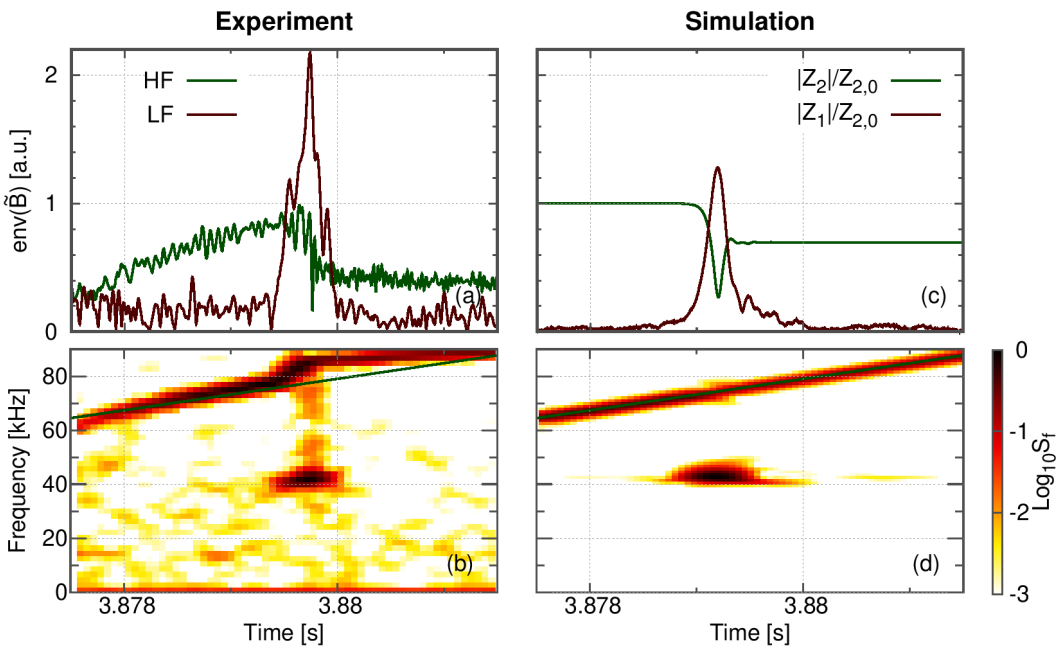

Figure 4.37 – Comparison of the evolution of perturbation between the experiment and the simulation. (a) Time evolution of magnetic perturbation, filtered into low (LF) and high frequency (HF) components. Here, "env" refers to the envelope. (b) Spectrogram of magnetic perturbation. (c) Time evolution of the amplitudes of modes 1 and 2 in the simulation. (d) Spectrogram of the total field. Superimposed curve in (b) and (d): $\omega_2(t)$ used as input in the model.

Collaborative fluid/kinetic nonlinearity

When, typically, $\nu_f \ll \nu_d$, the single-mode model features no subcritical instability, even for large initial amplitude of perturbation [LI12]. In the two-modes case, significant subcritical instability requires a combination of fluid and kinetic nonlinearities. This new hybrid fluid-kinetic subcritical instability is illustrated in Fig. 4.36, which compares the stability of the daughter without (a) and with (b) the kinetic term in Eq.(4.72). In this figure, the stability of the daughter, for a fixed chirping rate, is represented in a two-dimensional parameter space ($\gamma_d - \gamma_{L0}$, V). Here, $\gamma_d - \gamma_{L0}$ is used as a measure of distance from linear marginal stability. Fig. 4.36 shows in color code the peak amplitude of the daughter mode, in this parameter space. Each point is the result of an ensemble average over 8 simulations with identical input parameters (the statistical variations are due to the random noise). We observe that the unstable region ($\max|Z_1|/Z_{2,0} \sim 1$) is significantly extended to lower V in the parameter space of ($\gamma_d - \gamma_{L0}$, V). In Ref. [IIK+16], a threshold condition has been derived analytically for the onset of abrupt daughter growth, as $Z_{2,0}V/\omega_1 > \gamma_d$. It is shown by a series of circles in Fig. 4.36 (b). There is a good qualitative agreement with the stability threshold in the simulations, especially near linear marginality.

Fig. 4.37(c) shows a typical simulation of the collaborative fluid/kinetic subcritical instability. We will describe in subsection 4.4.6 how this particular simulation is related to the LHD experiment shown in Fig. 4.37(a).

Fig. 4.38 shows snapshots of the perturbed distribution function, at the time of maximum growthrate (a), at the time of peak amplitude (b), and at the time of maximum decay (c) of the daughter mode. We observe that mode 1 is not significantly chirping during its growth, and only slightly chirping (by less than 10%) during its decay. Indeed, the perturbation of particle distribution at the time of peak amplitude (b) is centered around the resonant velocity, and apparently corresponds to a non-chirping BGK. We then observe accelerating holes and decelerating bumps, but only later, during the decay of daughter amplitude (c). Therefore, the usual mechanism of kinetic subcritical growth, namely the acceleration of

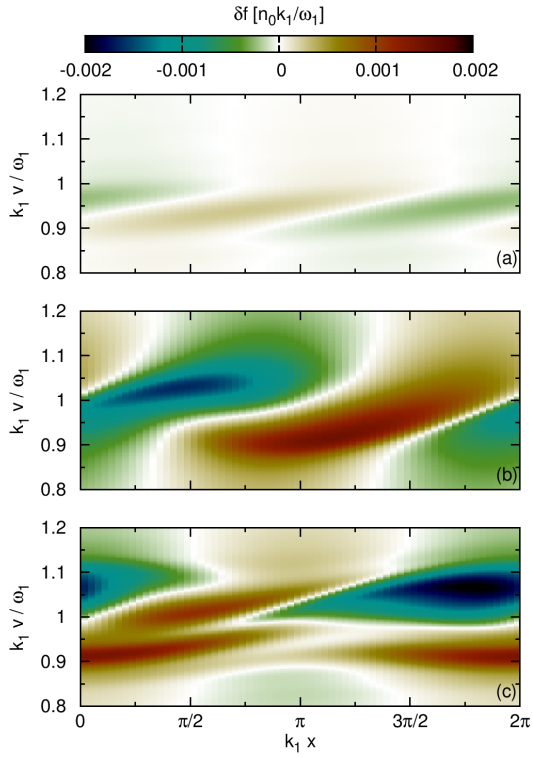

Figure 4.38 – Snapshots of the perturbed particle distribution function in phase-space, at three consecutive times of the daughter mode's evolution: (a) time of maximum growth-rate, (b) time of peak amplitude, and (c) time of maximum decay.

phase-space hole(s), is not responsible for the instability in this regime.

We can make a stronger statement, namely, that it is the sustained collaboration between fluid and kinetic nonlinearities that enable the subcritical growth in this regime. Indeed, in contrast with the results of Fig. 4.35 in the previous regime, $|Z_1|$ quickly decays back to noise level if we artificially disable the fluid nonlinearity at any point during the simulation.

Let us give more details about the mechanism of hybrid fluid-kinetic nonlinearity. It is convenient to describe the three terms in the r.h.s. of Eq. 4.72 as kinetic term (with the integral), dissipative term (with γ_d), and coupling term (with V), respectively. The time evolution of the real part of these three terms is shown in Fig. 4.39(b), for a simulation with the same input parameters as the simulation in Fig. 4.37(c). During daughter growth, the dissipative and coupling terms are nearly locked in phase, with an opposite sign for the amplitude. We have indeed verified directly in our simulation that the phase difference between dissipation and coupling terms stays between 1.2π and 1.3π during the growth. Therefore, the coupling acts as an effective reduction of dissipation. The kinetic term is in phase with the dissipative term. In amplitude, all three terms are comparable, as shown in Fig. 4.39(c). Therefore, the sum of three terms approximately results in a real, positive growth rate $\sim \gamma_d \sim \gamma_{L0}$. This can also be seen by defining an effective damping rate,

$$\gamma_{d,\mathrm{eff}} \;=\; \gamma_d \;+\; \mathrm{Re}\left[\imath(V/\omega_1)Z_2 Z_1^* Z_1^{-1} e^{-\imath\theta t}\right]. \tag{4.74}$$

The time evolution of $\gamma_{d,\mathrm{eff}}$ is shown in Fig. 4.39(d). The main growth occurs when $\gamma_{d,\mathrm{eff}}$ stays below γ_{L0}.

4.4.5 Fluid limit

Here, we consider two simpler limits. I In the kinetic limit, the fluid nonlinearity (the term proportional to $VZ_2Z_1^*e^{-\imath\theta t}$) is neglected. This yields the single-mode BB model as studied in section 4.3. Here, we focus on the fluid limit, where the kinetic nonlinearity (the term proportional to $\int f e^{-\imath(k_1 x-\omega_1 t)}$) is neglected. In this case, Eq. (4.71) can be ignored.

The theory in the dissipation-less ($\gamma_d = 0$) and chirp-less ($\mathrm{d}\theta/\mathrm{d}t = 0$) limit, is very well understood. Here, we investigate the coupled evolution of two modes in the presence of both finite dissipation, and finite chirping. We choose $\gamma_d = 0.031\omega_1$, $\mathrm{d}\theta/\mathrm{d}t = 5\times 10^{-4}\omega_1^2$,

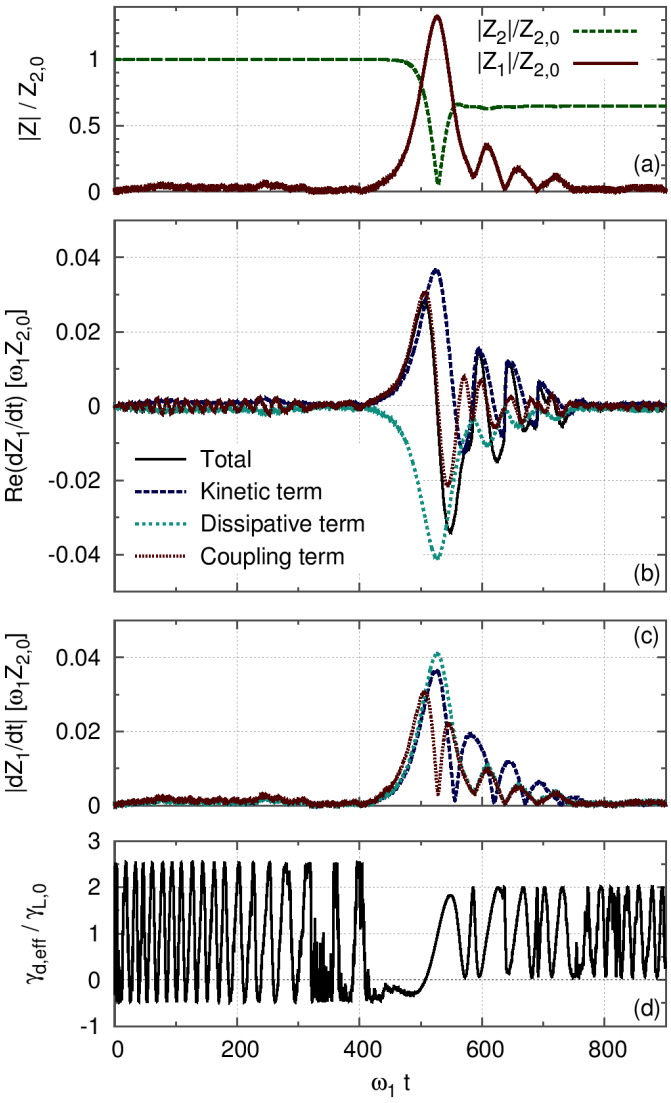

Figure 4.39 – Collaboration of fluid and kinetic nonlinearities. (a) Time evolution of the amplitudes of the two modes. Time evolution of the real part (b) and the absolute value (c) of the three terms in the r.h.s. of Eq. (4.72). (d) Time evolution of the effective damping rate, $\gamma_{d,\mathrm{eff}}$, normalized to γ_{L0}.

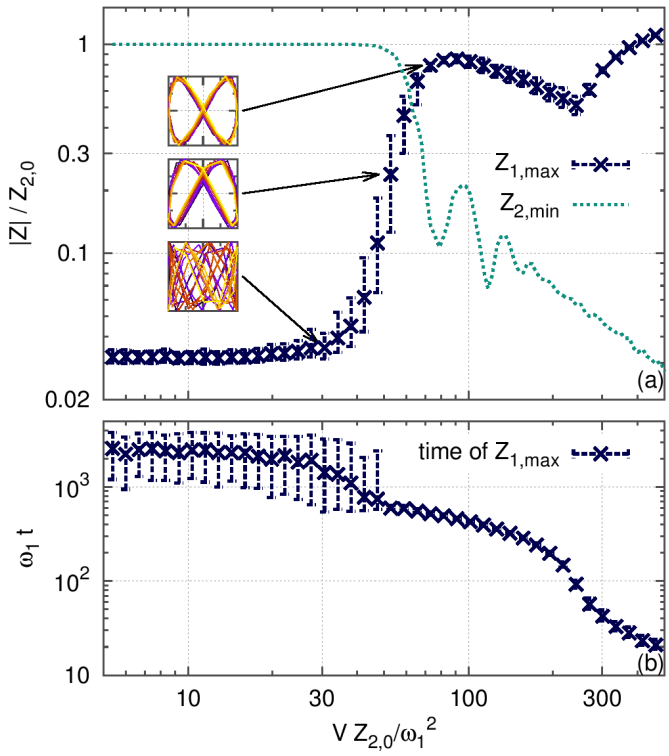

Figure 4.40 – Impact of the coupling coefficient V in the fluid limit. (a) Maximum amplitude of daughter mode, and minimum amplitude of mother mode. (b) . Error bars correspond to the top of lower quartile, and bottom of upper quartile, of 128 ensembles. Insets: Lissajous diagrams for (Z_1, Z_2), at $V = 34$, 53 and 73 $\omega_1^2/Z_{2,0}$

and noise level $Z_{\text{noise}}/Z_{2,0} = 0.03$, because these values are used later in modeling the experiment. Fig. 4.33(b) is an example of such a situation, with $V = 50\,\omega_1^2/Z_{2,0}$. Fig. 4.40 shows the impact of the remaining free parameter, i.e. the coupling coefficient V. There are two striking features, which contrast with the dissipation-less chirp-less case.

— There is a sharp transition between stability ($Z_{1,\max} \sim Z_{\text{noise}}$) and instability ($Z_{1,\max} \sim Z_{2,0}$).

— The relation between peak amplitude and coupling constant is non monotonous.

Fig. 4.40(a) includes Lissajous diagrams (Re $\tilde{Z}_1/|Z_1|$ against Re $\tilde{Z}_2/|Z_2|$, where $\tilde{Z}_j \equiv Z_j e^{-\imath\omega_j t}$) for three values of V, just below, at, and just above, the threshold value. Phase-locking occurs at and above the threshold. This suggests that the sharpness of the transition may be linked to a synchronization phenomenon.

The frequency ratio at the onset of daughter burst can be quite far from 2. For $V = 53$, where phase-locking is observed, $\omega_2/\omega_1 = 1.77$ at the time of maximum growth. Therefore, note that phase-locking does not necessarily implies a ratio of 2.

Note that for large values, $V > 400\,\omega_1^2/Z_{2,0}$, the daughter amplitude can become larger than the mother amplitude, without the help of the kinetic nonlinearity. However, in this case, the mother amplitude drops to 3% of its initial amplitude. This drop, and the timing with respect to the prescribed evolution of ω_2 (see Fig. 4.33(b), dotted curves), are inconsistent with the experiment we interpret in subsection 4.4.6.

Note that, since the peak amplitude is sensitive to V, one can loosely define the unstable region as a regime where the daughter reaches amplitudes comparable or much greater than the mother ($\max|Z_1|/Z_{2,0} \sim 1$), and the stable region as the counterpart ($\max|Z_1|/Z_{2,0} \ll 1$). In this sense, the white region in Fig. 4.36, where $\max|Z_1|/Z_{2,0} \approx 0.3$, corresponds to the stability threshold.

4.4.6 Application to EGAMs on the LHD

Bursts of Energetic particle-driven Geodesic Acoustic Mode (EGAM) with dynamical evolution of frequency (chirping) are routinely observed in tokamaks and stellerators. Suprisingly, as was reported in Ref. [IIO+16], an EGAM burst, with a 10 ms duration, is sometimes accompanied by a stronger burst, with a 1 ms duration, and up to twice the amplitude of the weaker burst. In Ref. [LII+16b], we have used the above model to analyze this obser-

	1D	3D
Angle	$kx - \omega t$	$\theta - \omega t$
Action	$m_i \frac{v - v^R}{k}$	$I \sim m_i \frac{v_\parallel - v_\parallel^R}{k_\parallel}$
Effective mass	$\frac{k^2}{m_i}$	$D \approx \frac{k_\parallel^2}{m_i}$
Electric potential	$\hat{\phi}$	$\hat{\phi}_1$
Electric field	E	E_θ

Table 4.3 – Analogies between a single wave in a 1D plasma, and a single EGAM in a 3D toroidal plasma.

vation. In this subsection, we provide more details on the latter analysis. We justify our assumption of fixed spatial profile of the daughter during its growth, based on experimental measurements. We discuss the role of the GAM continuum, and of the weak broadband signal, which is observed at the time of daughter growth. To allow quantitative analysis, we introduce scalar measures of the main properties of the daughter burst. These scalar measures are used to analyze the robustness of the modeling with respect to input parameters. Furthermore, observed correlations between these scalar measures provide readily-testable predictions.

Table 4.3 summarizes the analogy between the BB model and a 3D model of interactions between EPs and an EGAM.

Modeling the experiment

We concentrate on the LHD experiment, shot #119729, at $t \approx 3.88$ s. The local plasma parameters around the radial location of mode 1 ($r_1 \approx 0.06$m) are $B_0 \approx 1.375$T, $T_i \approx 0.5-1$ keV, $T_e \approx 4$ keV, $n_e \approx 10^{18}\mathrm{m}^{-3}$, and $q \approx 2.5$. The ion species is hydrogen. The energetic particles originate from tangential NBI with $E_b = 175$keV, and tangential major radius $R_T = 3.7$m. The major radius of magnetic axis is $R_0 = 3.75$m.

The density of energetic particles has not been measured in this experiment, but we may estimate the ratio between fast ions pressure β_h and thermal plasma pressure β or thermal ion pressure β_i, to help situate the experimental conditions in terms of dimensionless parameters (although this is not used in any of the calculations in this subsection). The density of energetic particles can be estimated [IOS+15] from the absorbed NBI power $P_\mathrm{NBI} = 140$kW as $n_\mathrm{NBI} \approx 2 \times 10^{16}\mathrm{m}^{-3}$, if we assume that the particle confinement time of the injected fast ions is ≈ 0.1s. Then, $\beta_\mathrm{h}/\beta \approx 0.7 - 0.8$, and $\beta_\mathrm{h}/\beta_i \approx 3.5 - 7$.

Fig. 4.37 shows the time evolution of the magnetic perturbations (a), and its spectrogram (b). In Fig. 4.37(a), the signal from the Mirnov coil has been filtered into a low frequency (LF, $f = 30 - 50$ kHz) component for the daughter mode, and a high frequency (HF, $f = 60 - 95$ kHz) component for the mother mode. From experimental measurements [IIO+16], the electric potential of the daughter mode is located in the core region, with a rather broad structure, $\Delta r/a \sim 0.5$, centered around $r/a \approx 0-0.1$. The spatial configuration agrees with this of a GAM. The toroidal mode number is $n = 0$. The poloidal mode number is dominantly $m = 0$ for the electric potential fluctuation, and $m = 1$ for the density fluctuation (up-down anti-symmetric).

Since the spatial 3D structures of mother and daughter are very similar [IIO+16], we ignore the radial inhomogeneity, and study the ratio between mother and daughter amplitudes of magnetic perturbation. As measured by heavy-ion beam probe, the profile of electric potential (normalized by the peak amplitude) in the core is unchanged during the rapid growth of daughter mode in experiments. As for the outer region, the profile is inferred from the ratio between measured electric potential and amplitude of magnetic field perturbations. The latter ratio for the daughter is unchanged during the growth in experiments. These indicate that the spatial profile of the mode is nearly unchanged during the growth. This is consistent with our simple 1D model with constant input parameters. To relate the electric field in the simulation with the Mirnov coil signal, we assume a linear relationship between

$|\tilde{\phi}|$ and $|\tilde{B}|$, which is consistent with experiment [IOS+15].

The dynamical change of frequency of the mother mode (mode 2), around the time of the burst of the daughter mode (mode 1), is modeled as a linear increase, with $\mathrm{d}\omega_2/\mathrm{d}t = 5 \times 10^{-4}\omega_1^2$, where $\omega_1 = 2\pi f_1$ and $f_1 = 43$ kHz. Here, f_1 is obtained from reading the frequency of the peak in the spectrum of measured magnetic fluctuations at the time of maximum amplitude of the daughter.

We use four scalar measures to objectively characterize the evolution of the daughter:

1. the maximum instantaneous growth rate γ,
2. the normalized peak amplitude, $A \equiv \max |Z_1|/Z_{2,0}$,
3. a scalar τ that measures the duration of daughter burst, and
4. the ratio $R^\omega \equiv \omega_2(t_{\mathrm{growth}})/\omega_1$ between mother and daughter frequencies at the time t_{growth} of largest growth of the daughter.

Here, the duration τ of the daughter burst is defined as

$$\tau \equiv \frac{1}{Z_{2,0}} \int |Z_1| S(|Z_1|) \mathrm{d}t, \tag{4.75}$$

where $S(|Z_1|) = 1$ if $|Z_1| > Z_{\mathrm{noise}}$, 0 else. For the experiment, we measure growth rate $\gamma = 1.2 \times 10^4$ s^{-1}, amplitude $A = 2.17$, duration $\tau = 0.6$ ms, and frequency ratio $R^\omega = 1.9$. Note that R^ω is slightly below the perfect frequency matching condition $R^\omega = 2$.

We scanned the parameter space (γ_{L0}, γ_d, ν_f, ν_d, V). We identified a finite region of the parameter space where γ, A, τ and R^ω in the simulation are in reasonable agreement with the experimental values. The experimental observation could also be reproduced by a wider range of input parameters (Z_{noise}, $Z_{2,0}$, and $\mathrm{d}\theta/\mathrm{d}t$). Fig. 4.37(c) shows the time evolution of the amplitudes $|Z_1|$ and $|Z_2|$ in the simulation, and the corresponding spectrogram of the total field (d). In Figure 4.37, time is scaled from normalized units to seconds by the coefficient ω_1, and shifted in such a way that simulation and experiment are synchronized on the instant where $\omega_2(t)/\omega_1 = 1.5$, which we choose arbitrarily as the beginning of the simulation, as explained in subsection 4.4.2. For example, the beginning of the simulation here is at $t = 3.8775$s. Table 4.2 lists each input parameter (first and second columns), and its value used in the simulation of Fig. 4.37(c) (third column). In this simulation, we measure growthrate $\gamma = 1.4 \times 10^4$ s^{-1}, amplitude $A = 1.34$, duration $\tau = 0.6$ ms, and frequency ratio $R^\omega = 1.8$. In addition to these four scalars, the simulation agrees qualitatively with the experiment in the sense that the daughter mode is only very slightly chirping ($\delta\omega/\omega_1 < 10\%$, as measured by tracking perturbations in the particle distribution), even though strongly chirping daughter mode is allowed in the model (self-consistently, albeit not consistently with physical assumptions). The lack of chirping of the daughter mode validates, a posteriori, our assumption of fixed ω_1 in the frequency mismatch θ used for computing the wave-wave coupling terms.

Furthermore, the mother/daughter phase locking, which was discovered in Ref. [IIO+16], is qualitatively captured by numerical simulations. Fig. 4.41 shows the Lissajous curve during growth and decay phases, for the experiment (a,b) and for the simulation (c,d). The mother/daughter phase relation locks itself during the growth phase and the decay phase of the daughter.

Therefore, we have shown that our model is able to qualitatively reproduce the nonlinear evolution of the daughter, in terms of amplitudes, timescales, and phase locking. We do not pretend to recover quantitatively from first principles the features of the daughter, neither to reproduce the combined evolution of both mother and daughter, but rather suggest the combined fluid-kinetic subcritical instability as a candidate mechanism for the strongest EGAM bursts in the LHD.

In our analysis, we have prescribed the time evolution of mother frequency $\omega_2(t)$ with constant chirping rate. As a caveat, this prescribed evolution ends when $|Z_1| \sim |Z_2|$. Indeed, in the experiment, the ratio ω_2/ω_1 increases very rapidly, but almost linearly, from 1.9 to 2.0, within a 0.2ms span during the daughter growth. The model, by its design, is unable to recover this apparent synchronization mechanism. However, the ratio of 2.0 is not reached before the very end of daughter growth. This indicates that the synchronization may not

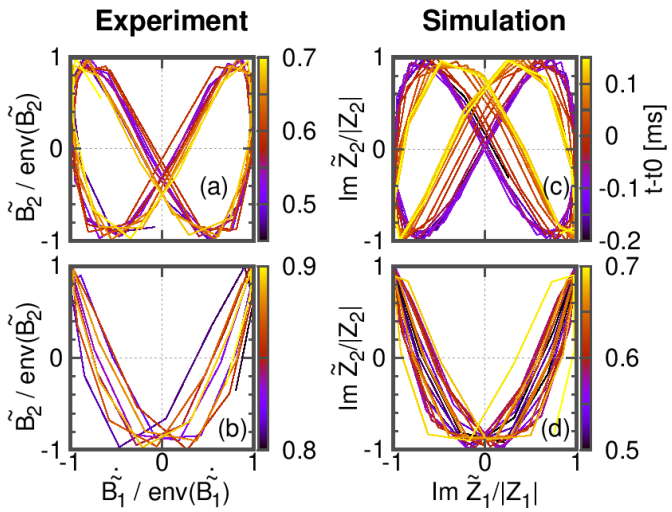

Figure 4.41 – Lissajous figure during the growth (a), and the decay (b) of daughter mode in the experiment, and (c-d) in the simulation. For the simulation, $\tilde{Z}_i \equiv Z_i e^{-\imath\omega_i t}$. Colorbars show the time shifted by $t_0 = 3.879$s.

be a key aspect of the instability mechanism, although it may be a key aspect of the full dynamics of coupled modes. We can speculate that, although a ratio of 2.0 may be key in a quasi-stationary state, here the resonance condition may be broadened due the large growth rate of the daughter. Indeed, the daughter growth rate is $\gamma_1/\omega_1 \sim 1/20$, therefore a ratio $\omega_2/\omega_1 \sim 1.9$ (neglecting the broadening of the mother) could allow the resonance between mother and daughter. In other words, given the observed phase-locking during the growth phase, it appears that the rapid time evolution of Z_1 overcomes the finite frequency mismatch $\theta = \omega_2 - 2\omega_1$ in $Z_1^* e^{-\imath\theta t}$.

The role of the GAM continuum merits to be discussed. Unfortunately, there are large uncertainties in the measurements of T_i (measured by a neutral particle analyzer, integrated over a line of sight) and T_e (the uncertainty is of the order of 100% because of the very low density). Here T_e is important because $T_e \gg T_i$ in this experiment. Therefore, an accurate calculation of the GAM continuum, or even of the local GAM frequency, is left as an open issue. However, a rough estimation with rotational transform $\iota(r) = 0.35 + 0.85(r/a)^3$, and temperature profiles peaking at $r = 0$ below 1keV for T_i (measurements indicate a $0.5-1$keV range), and around 4keV for T_e, suggests that both daughter and mother may probably be above the GAM continuum.

In addition to the mother and the daugther, a weak, broad ($30-160$ kHz) signal appears in the spectrogram at $3.87955-3.87985$s, which corresponds to the time of daughter growth. It appears to result from a parametric coupling of both mother and daughter with another mode, with a frequency in the range $10-15$ kHz, which is present even before the mother is destabilized. Parametric coupling is speculated based on the relationship between frequencies of peaks, observed in the spectrum of $\tilde{B}$ at $t = 3.8797$s. By design, this additional physics is not captured by the present model. Its impact on mother and daughter may be negligible, since the amplitude of this mode is one order-of-magnitude below the amplitude of the daughter.

Reproducing the self-consistent coupled evolution of both mother and daughter is a relevant challenge that we leave for future work. This would require either solving a more advanced model, with two kinetic equations and two field equations, after obtaining the coupling term between Z_1 and Z_2 from 3D kinetic equations ; or another approach altogether, such as full 3D gyrokinetic simulation. Here we focused on the instability mechanism of the daughter mode.

Impact of input parameters

The model includes a priori 8 input parameters (assuming that the chirping rate $\mathrm{d}\theta/\mathrm{d}t$ for the mother mode around the onset of daughter is a constant). In Ref. [LII+16a], we have conducted a sensitivity analysis, where we varied each input parameter, and measured the impact on the time evolution of the daughter mode. The fourth column (*Range*) of Table 4.2 lists for each parameter the range (everything else being equal) where the simulation is

in qualitative agreement with the experiment. Note that the evolution of the daughter is mostly sensitive to γ_{L0}, ν_d, V, $Z_{2,0}$ and $\mathrm{d}\omega_2/\mathrm{d}t$.

The fifth column of Table 4.2 lists estimations from independent methods when available. Two of the five sensitive parameters, $Z_{2,0}$, $\mathrm{d}\omega_2/\mathrm{d}t$, as well as Z_{noise}, are input from experimental data. Another sensitive parameter, ν_d, as well as not-so-sensitive ν_f, are obtained from the local plasma parameters measured in the experiment. In addition to the parameters given above, we assume a magnetic shear $S = 0.2$, and carbon impurities with $T_C = T_i$ and $Z_{\mathrm{eff}} = 2$. We obtain $\nu_f/\gamma_{L0} \approx 0.068$ and $\nu_d/\gamma_{L0} \approx 0.44$, which are 1% and 17%, respectively, below the parameters of the simulation shown in Fig. 4.37(c).

There remain two parameters with significant impacts: 1. the slope of energetic particle distribution, parametrized by γ_{L0}, and 2. the coupling coefficient V. For 1., it was shown that the order of magnitude $\gamma_{L0}/\omega_1 \sim 0.1$ is relevant for linearly unstable EGAMs on similar LHD plasmas [WT13], which suggests that 0.03 is relevant for linearly stable EGAMs. For 2., substituting the parameters of the experiment into Eq. (35) of Ref. [IHI+05] yields an estimate $Z_0 V/\omega_1^2 \sim 10^{-2} - 10^2$ which is sensitive to the radial wave number of the GAM, but not inconsistent with our simulation. Thus, V is a key parameter, with a finite range that reproduces the experiment, but with poor theoretical guide. Therefore, quantitative deduction of V from first principles is encouraged.

Predictions

The model provides the following predictions, which are open to future experimental test.

1. The ratio between the mother and the daughter mode can become much larger, $|Z_1|/|Z_2| \gg 1$, and the daughter mode exhibit strong chirping, $\Delta\omega_1 \sim \omega_1$, if the regime of successive fluid-kinetic subcritical instability is reached.
2. Since the best limit for driving a subcritical instability is $\mathrm{d}\omega_2/\mathrm{d}t \to 0$, and in this case, we observed no nonlinear instability for $\gamma_d > 2\gamma_{L0}$, we predict that there won't appear any subcritical instability with $\gamma_d \gg \gamma_{L0}$.
3. In Ref. [LII+16a], we show significant correlations between growth rate and peak amplitude, between frequency ratio and peak amplitude, and between frequency ratio and burst duration. It remains to be tested whether experiments recover similar correlations.
4. An analytic formulation for the onset condition of the subcritical instability for this model was developed in Ref. [IIK+16]. This theory also explains the observed period doubling phenomenon.

4.4.7 Summary

We have developed a reduced model for energetic particle-driven, nonlinear excitation of subcritical instabilities in toroidal plasma. The model combines a 1D kinetic equation with equations for period doubling. The kinetic equation approximately describes wave-particle interactions between fast ions and a single MHD mode in a toroidal plasma, such as an EGAM, or a toroidal Alfvén eigenmode.

Two regimes have been investigated. In a first regime, of successive fluid then kinetic growth, the dormant subcritical mode is first triggered by fluid coupling to the supercritical mode, which allows it to reach amplitudes of the same order of magnitude as the supercritical mode. This amplitude is above the threshold for the conventional kinetic subcritical instability [BBC+99, LD13]. Then, the amplitude can keep growing by momentum exchange between the wave and phase-space structure(s), accompanied by significant chirping. In a second regime, of collaborative fluid-kinetic growth, the subcritical growth is due to an uninterrupted collaboration between fluid and kinetic nonlinearities. This is a new kind of instability mechanism, where fluid and kinetic nonlinearities have similar (in amplitude) contributions to the mode growth. Contrarily to the mechanism developed in earlier theories [BBC+99, LD13], the growth occurs much below the amplitude threshold, and without chirping. Typically, the ratio ν_f/ν_d selects one or the other regime. The first regime is

obtained for $\nu_f/\nu_d \sim 1$ and above. In this case, the amplitude of the subcritical mode can grow orders-of-magnitude above the amplitude of the supercritical mode.

We have shown that the model can reproduce key aspects of the experimental observation of Ref. [IIO+16]. It interprets the daughter mode as a manifestation of the collaborative fluid-kinetic subcritical instability. In contrast with previously-known kinetic subcritical instabilities, the amplitude stays below the kinetic threshold, and chirping seems to be limited by a quasi-phase-matching condition with the mother mode. These results imply a new channel of mode excitation, which modifies the flow of energy in the system.

4.5 Many modes

4.5.1 Vlasov-Poisson limit

When many electrostatic waves are excited, the amplitude of each wave grows exponentially until nonlinear saturation occurs, and each wave develops an island structure in phase-space. If the width of each island is much smaller than the distance between the phase velocities of two neighbouring waves, we may treat the problem as a superposition of the former single wave-particle problem. However, if island structures overlap each others, particle trajectories are not integrable. We consider a situation where there exists a velocity interval within which the phase velocities of many waves are close enough and their islands overlap. This corresponds to the Chirikov resonance-overlap criterion [Chi60]

We perform a full-f COBBLES simulation, without collisions nor external damping, with $n_B = 0.05n_0$, $v_{TM} = v_{TB} = 4.0v_{\rm th}$, $v_B = 16.0v_{\rm th}$, $v_{\rm max} = -v_{\rm min} = 30v_{\rm th}$, $L = 512\lambda_D$, $N_x \times N_v = 512 \times 64$. The initial perturbation is a sum of 10 waves with wave numbers $k_n \equiv nk_1$, where $k_1 = 2\pi/L$, and a random phase for each wave n. Fig. 4.42(a) shows the position and width of each island, and trajectories in the velocity direction of three test particles evolving within the resonant region. We observe overlapping of islands, and resonant particles seem to undergo Brownian motion in the velocity direction. We also observe a flattening of the velocity distribution in the resonant region (not shown here).

These observations suggest that this simulation is in a regime where quasilinear theory as reviewed in chapter 2 (2.2.4). Here the angle action variables are $\alpha = k_1 x$ and $J = mv/k_1$. The equilibrium hamiltonian is $H_{\rm eq} = k_1^2 J^2/(2m)$, and the perturbed one is $\delta H = q\phi$. The equilibrium frequency is $\omega_{\rm eq} = k_1 v$, and so the resonant frequency is simply $\omega_{R,n} = k_n v$. Substituting into Eq. (2.25) yields

$$\frac{\partial \langle f \rangle}{\partial t} = D^{\rm QL} \frac{\partial^2 \langle f \rangle}{\partial v^2}. \tag{4.76}$$

The quasi-linear diffusion coefficient $D^{\rm QL}$ can be estimated as

$$D^{\rm QL} = \frac{q^2}{m^2} \frac{\pi}{\Delta v_R} \sum_n \frac{|\hat{E}_n|^2}{k_n}, \tag{4.77}$$

where Δv_R is the width of the whole resonant region.

Another way of estimating the diffusion coefficient involves the variance of the displacement in velocity of a large number of test particles. For any time interval Δt larger than the correlation time, but smaller than the distribution relaxation time, this coefficient $D^{\rm P}$

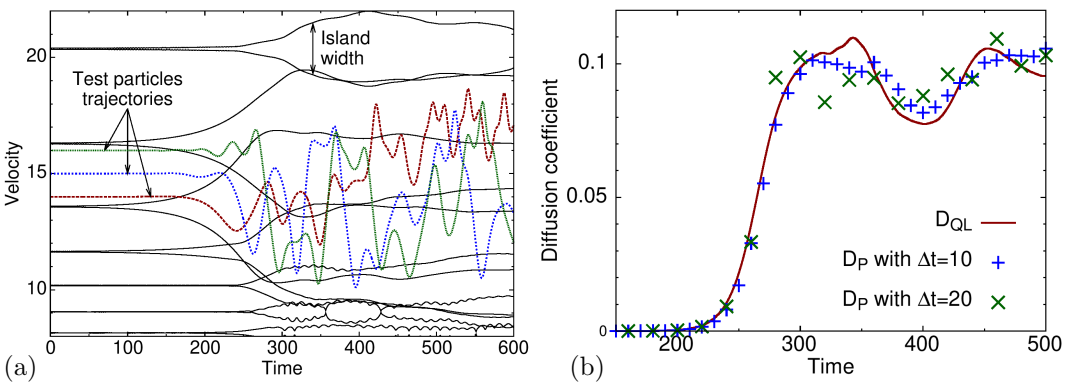

Figure 4.42 – Many waves in the Vlasov-Poisson model. (a) Evolution and overlapping of multiple islands. Dashed and dotted lines are trajectories of three test-particles. (b) Time-evolution of the quasi-linear diffusion coefficient estimated by quasi-linear theory (solid line), and by following test particles trajectories (pluses and crosses).

is given by

$$D^{\mathrm{P}} \;=\; \frac{\left\langle \left[v(t_0+\Delta t)-v(t_0)\right]^2 \right\rangle}{2\Delta t}, \tag{4.78}$$

where angle brackets represent an ensemble average.

In our simulation, we estimate D_{P} by following the trajectories of 3×10^5 test particles, which are initialized with an uniform distribution over the resonant region, and a random position. Fig. 4.42(b) shows that D^{QL} matches D^{P} in simulation, even as we double Δt.

We note that, although conventional quasilinear theory assumes that many waves are overlapping, Berk recently discussed how to modify the expressions to expand their validity all the way to the regime of isolated multiple waves [Ber12].

4.5.2 Secondary bump-on-tail instability

As we described in subsection 4.3.1, both bump-on-tail instability and BB instability can saturate to a steady-state with a flattening of the velocity distribution, due to the formation of a PS island near the resonant velocity.

In the context of the BB model, that is in the presence of finite dissipation, a mechanism of formation of hole/clump pair was proposed, as a dissipative instability of negative-energy modes, driven by strong velocity-gradients at the edges of the plateau formed by a primary PS island [LN14]. In the latter work, the plateau is modeled as a simple band in v. In other words, the x-dependency of δf is ignored.

Here we treat a related problem in the 2D phase-space (x, v). We investigate the possibility of secondary instabilities of separate modes driven by gradients of the distribution function nearby the separatrix of the saturated PS island of a primary mode. Note that this question is also related to the stability of BGK modes [GIB+88, GS95b, MB00, Bal12].

Model

We cast the full-f BB model in a many-waves form by relaxing the assumption of a single sine wave in the electric field, which can be written as

$$E(x,t) \;=\; \sum_k \left[E_k(t)e^{\imath kx} \;+\; c.c.\right]. \tag{4.79}$$

The initial velocity distribution f_0 is of the form given in Eqs. (4.15)-(4.16), with a maxwellian bulk and a gaussian beam. The kinetic equation is unchanged from Eq. (4.17). The collision operator is

$$\mathcal{C}_{\mathrm{FP}} \;=\; \frac{\nu_f^2}{k_1}\frac{\partial}{\partial v} \;+\; \frac{\nu_d^3}{k_1^2}\frac{\partial^2}{\partial v^2}, \tag{4.80}$$

which does not depend on the many k_n, but only on the length $L = 2\pi/k_1$ of the periodic simulation box.

The displacement current equation is written in Fourier space,

$$\frac{\partial E_k}{\partial t} \;=\; -4\pi q \int v f_k \mathrm{d}v \;-\; 2\gamma_d(k)E_k, \tag{4.81}$$

for $k \neq 0$. In the limit of $\gamma_d = 0$, it is equivalent to Poisson's equation. The average electric field, E_0, is zero at all times. We emphasize here that, contrary to the BB model described in Sec. 4.2, we allow the wave damping rate γ_d to depend on the wave-number. We readily extended the COBBLES code to enable this possibility.

In the initial condition we apply small perturbations,

$$f(x,v,t=0) \;=\; f_0(v)\left[1+\sum_k \epsilon_k \cos\left(kx+\phi_k\right)\right], \tag{4.82}$$

where each ϕ_k is a random phase.

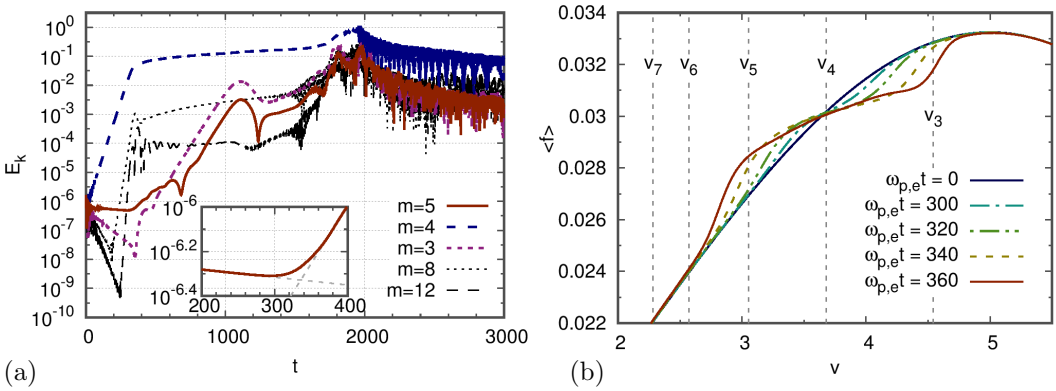

Figure 4.43 – Simulation with $n_M = 0.9n_0$. (a) Time-evolution of the amplitudes of Fourier modes $k = nk_1$ of electric field. Inset: zoom near the time of reversal of evolution of mode $n = 5$. In the inset, the two dashed lines correspond to growth rates $\gamma_{5,L} = -0.0008\omega_{pe}$ and $\gamma_{5,\text{sec}} = 0.012\omega_{pe}$. (b) Spatial average of the distribution function. Vertical lines indicate the phase velocities $v_n = \omega_{n,L0}/k_n$ of modes $k_n = nk_1$.

Numerical experiment setup

The parameters for the initial bump-on-tail distribution are $n_M = 0.9n_0$, $v_{TM} = 0.2v_{\text{th}}$, $n_B = 0.1n_0$, $v_{TB} = v_{\text{th}}$, and $v_B = 5v_{\text{th}}$. We choose a relatively large system size, with $k_1 = 0.006\lambda_D^{-1}$. The collision frequencies are $\nu_f = 0$, and $\nu_d = 10^{-2}\omega_{pe}$. The dissipation is arbitrarily set-up such that only one mode, namely mode $n = 4$, is linearly unstable for $f = f_0$. We choose $\gamma_d(k_4) = 0$, and $\gamma_d(k) = 0.038\omega_{pe}$ for $k \neq k_4$.

For the simulation presented here, $v_{\min} = -8v_{\text{th}}$, $v_{\max} = 18v_{\text{th}}$, $N_x \times N_v = 256 \times 2048$, and a time-step width $\Delta t = 0.05\omega_{pe}$.

Results

We define $\omega_{n,L0}$ and $\gamma_{n,L0}$ as the linear frequency and growth rate of the mode of wavenumber $k_n = nk_1$ in the absence of dissipation and collision. Note that $\gamma_{n,L0}$ is proportional to the slope of f_0 at the resonant velocity $v_n = \omega_{n,L0}/k_n$,

$$\gamma_{n,L0} = \frac{\pi}{2} \left.\frac{\partial f_0}{\partial v}\right|_{v=v_n}. \tag{4.83}$$

We define the full linear growth rate $\gamma_{n,L}$ as the linear growth rate including the effects of collisions and dissipation. In the collisionless limit, when $\gamma_{n,L} \ll \omega_{n,L0}$, the full linear growth rate reduces to $\gamma_{n,L} = \gamma_{n,L0} - \gamma_d(k_n)$. With the parameters listed above, $\gamma_{4,L} = 0.034\omega_{pe}$, and $\gamma_{n,L} < 0$ for all $n \neq 4$. In particular, $\gamma_{3,L} = -0.009\omega_{pe}$ and $\gamma_{5,L} = -0.0008\omega_{pe}$.

Fig. 4.43(a) shows the time evolution of the amplitudes of modes $n = 3$, 4, 5, 8, and 12, which are the dominant modes for the time interval $t < 1000$ (normalizing time with ω_{pe}). Fig. 4.43(b) shows snapshots of the velocity distribution near the phase velocities of modes $n = 3$, 4 and 5. We observe that mode $n = 4$ growths linearly until $t \approx 300$, after which it saturates, consistently with BB theory for a single mode. By comparing with a control simulation, where all other ($n \neq 4$) modes are artificially filtered-out, we observed that the time-evolution of both amplitude and velocity distribution are not significantly impacted by the presence of other modes until $t \sim 1000$.

The novelty concerns the neighboring modes. Modes $n = 5$ and $n = 3$ decay linearly consistently with linear theory, until $t \approx 280$ and $t \approx 320$, respectively, after which their evolution reverses and they grow. This timing of reversal coincides with the time when the steep slopes at the boundaries of the BGK island formed by mode $n = 4$ reaches the phase velocities of modes $n = 3$ and $n = 5$. Our hypothesis is that these two modes grow due to a secondary instability driven by steep velocity-gradient at the edges of the PS island formed by the primary mode $n = 4$.

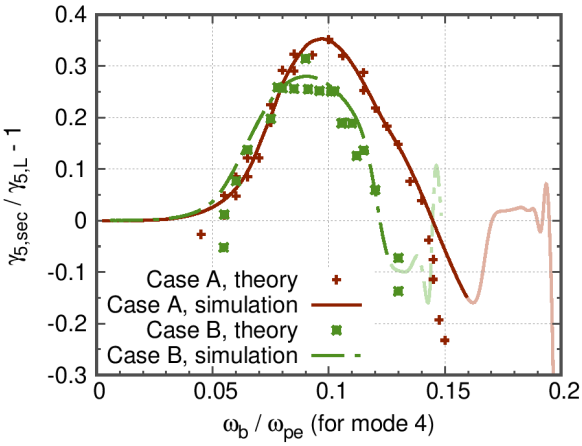

Figure 4.44 – Instantaneous growth rate of the secondary instability, versus the bounce frequency of the primary mode. Case A: $n_M = 0.95n_0$, $\gamma_{d,0} = 0.02\omega_{pe}$; Case B: $n_M = 0.97n_0$, $\gamma_{d,0} = 0.01\omega_{pe}$. In both cases, $v_{TM} = 0.2v_{\rm th}$, $v_{TB} = 3.0v_{\rm th}$, $v_B = 5.0v_{\rm th}$, $n_B = n_0 - n_M$, $\nu_f = 0$, and $\nu_d = 0.01\omega_{pe}$. For each curve, the semi-transparent part corresponds to later times, where nonlinear interactions between modes appear to strongly influence the secondary mode.

In Ref. [DGLW19], we solve a Fokker-Planck equation to obtain the primary equilibrium island, before deriving the dispersion relation for the secondary mode including the primary island. The growth rate can then be obtained numerically by solving the analytic dispersion relation. Based on this theory, we show that the onset of secondary modes is sensitive to the detailed structure of the primary island, which itself depends on collisional drag and diffusion. Note that this calculation applies to large primary island widths as well.

As can be seen in Fig. 4.43(a), the growth rate of $n = 5$ varies continuously around $t = 300$. We infer that this is due to the evolution of the primary equilibrium. Indeed, during the saturation phase, the primary mode slowly evolves, as can be seen in Fig. 4.43(a). Let us measure, at each time t, the instantaneous growth rate of the secondary instability $\gamma_{5,\rm sec}(t)$, as well as the instantaneous bounce frequency $\omega_b(t)$ which measures the amplitude of the primary mode. Fig. 4.44 shows the result of this procedure, which was repeated for various initial parameters (given in the legend). For each case, we emphasize the part of the curve where nonlinear interactions between modes appear to be negligible, since these interactions are outside of the scope of the present paper.

We observe that the general shape of the curve is similar for both cases. This is true as well for three other cases not shown here. It corresponds to what one can expect by examining Fig. 4.43(b): as ω_b, which also measures the width of the primary island, increases, the velocity slope at $v = v_5$ increases, before reaching a maximum, and finally decreasing below its initial value. Initially, the velocity slope at $v = v_5$ is unperturbed by the primary island, so $\gamma_{5,\rm sec} = \gamma_{5,L}$. The maximum (for both velocity slope at $v = v_5$ and the secondary growth rate) is reached for an island width $2\omega_b/k_4$ roughly equal to $v_4 - v_5$, which yields $\omega_b/\omega_{pe} \approx (1 - k_4/k_5)/2 = 0.1$, consistently with the simulation results (the exact value depends on the precise shape of the island). Then, as the velocity slope decreases below its initial value, $\gamma_{5,\rm sec} - \gamma_{5,L}$ becomes negative, as observed in Fig. 4.44.

Fig. 4.43(a) includes the amplitudes of modes 8 and 12. Since they are harmonics of the dominant mode $n = 4$, and since the growth rate of $n = 8$ is double that of $n = 4$, we interpret their growth as the result of fluid-like mode-mode coupling (probably in the class of modular-parametric instabilities), rather than the result of kinetic interactions between particles and waves.

Finally, we can take advantage of the variation of secondary growth rate with evolving primary equilibrium, to compare the simulation results with our analytic theory. Fig. 4.44 includes the growth rates calculated by solving numerically the analytic dispersion relation for the secondary mode including the primary island, for various values of primary island width. We observe quantitative agreement in the relevant range of moderate island widths, $\omega_b \sim \omega_L$.

Chapter 5

Ion-acoustic turbulence in 1D

Ion-acoustic turbulence is a central paradigm of plasma physics and controlled fusion. When ion and electron temperatures are similar, linear theory predicts that ion-acoustic waves are stable (except if the velocity drift between electrons and ions is at least of the order of the electron thermal velocity), due to strong ion Landau damping [Bun59]. As a consequence, ion-acoustic turbulence does not receive much attention in the context of magnetically confined fusion plasma. However, as we have seen in chapter 3, stability is a nonlinear issue, since the growth process of structures in phase-space can circumvent linear theory. Furthermore, ion-acoustic waves constitute the basis for dominant fluctuations in confined plasmas. Indeed, drift-waves arise from the ion-acoustic branch, modified by inhomogeneities and geometry effects. In particular, collisionless trapped-ion and trapped-electron modes are driven by wave-particle resonance, in the same way that the current-driven ion-acoustic is. Therefore, the understanding of phase-space structures and their impact on ion-acoustic turbulence is an important step towards the advance of the nonlinear kinetic theory of collisionless plasmas.

PS holes are of particular interest [RB67, SMPR79, Sch79, Dup82, BTD85, Sch86, BBP97b, LBS10, NLB12]. There are strong similarities between PS holes in the BB model and those in ion-acoustic turbulence.

1. They are non-wave-like fluctuations.
2. They are spontaneously formed by nonlinear wave-particle resonant interactions, and trap particles.
3. Like fluid vortices, they are not attached to a wave or a mode. The mean velocity of the structure can evolve away from the resonance, and grow by climbing up the gradient of a particle velocity distribution.
4. They exchange momentum and energy via channels which differ from those of familiar linear wave-particle resonance, and so can tap free energy when wave excitation cannot [Sch79, Dup82], leading to subcritical instabilities.
5. They can modify the saturation amplitude, yield amplitude oscillations or chaos, shift the frequency of oscillations.

They impact not only energetic particle-driven phenomena in space and magnetic fusion plasmas [ES06], but also collisionless magnetic reconnection [DSC$^+$03], collisionless shock waves [Sak72], alpha-channeling [MP94] and drift-waves [TDH90]. PS holes can drive anomalous transport [BDT88b, HCH$^+$94], drive anomalous resistivity [Dup70], and couple with zonal flows [KD11]. Multiple structures can coexist and interact, leading to rich nonlinear phenomena, which we refer to as phase-space turbulence.

In this chapter, we consider the ion-acoustic instability in one-dimensional (1D), collisionless electron-ion plasmas with a velocity drift, in other words Current-Driven Ion-Acoustic (CDIA) turbulence. Ion-acoustic waves are longitudinal electrostatic waves, which are commonly observed in space and laboratory plasmas. Theory and experiments indicate that ion-acoustic waves are key agents of magnetic reconnection (via anomalous resistivity) [CE77], turbulent heating [MSS70], particle acceleration [WHT05], and play important roles in the context of laser-plasma interaction [Kru88].

5.1 Model

5.1.1 Model description

The model describes the collisionless evolution of a two-species, 1D electrostatic plasma. In addition to academic and paradigmatic interests, a 1D model is relevant to plasmas immersed in a strong, relatively homogeneous magnetic field [OVNG01]. The evolution of each particle distribution, $f_s(x, v, t)$, where $s = i, e$, is given by the Vlasov equation,

$$\frac{\partial f_s}{\partial t} + v\,\frac{\partial f_s}{\partial x} + \frac{q_s E}{m_s}\,\frac{\partial f_s}{\partial v} = 0, \tag{5.1}$$

where q_s and m_s are the particle charge and mass, respectively. The evolution of the electric field E satisfies a current equation,

$$\frac{\partial E}{\partial t} = -\sum_s \frac{m_s \omega_{p_s}^2}{n_0 q_s} \int v f_s(x, v, t)\,\mathrm{d}v, \tag{5.2}$$

where $\omega_{p,s}$ is the plasma frequency and n_0 is the spatially-averaged plasma density. The initial electric field is given by solving Poisson's equation. We denote $\tilde{f}_s \equiv f_s - \langle f_s \rangle$. We remind that $\langle f_s \rangle$ is the spatial average of f_s, and that $\delta f_s \equiv f_s - f_{0,s}$ which is different from $\tilde{f}_s$ in general. The initial velocity distribution for each species is a Gaussian, $f_{0,s}(v) = n_0/[(2\pi)^{1/2} v_{T,s}] \exp[-(v - v_{0,s})^2/2v_{T,s}^2]$. The initial velocity drift is denoted as $v_d \equiv v_{0,e} - v_{0,i}$.

In a 1D periodic system, a spatially uniform current drives a uniform electric field, which oscillates at a frequency $\omega_u = \omega_{p,e}(1+m_e/m_i)^{1/2}$. This rapid oscillation of both the uniform electric field and the uniform current is of little interest here [OMMK96]. Numerically, the average part of E is set to zero, following common practice [BTD85, WHF02, PWHF03].

5.1.2 Numerical simulations

All simulations in this chapter are done with the full-f COBBLES code, which we readily extended to treat two species kinetically. Hereafter, we adopt the physical parameters of Refs. [BTDBG82, BTD85]. The mass ratio is $m_i/m_e = 4$ (small mass ratio improves numerical tractability and the readability of phase-space contour plots). The system size is $L = 2\pi/k_1$, where $k_1 = 0.2\lambda_D^{-1}$. We choose $v_{0,i} = 0$ without loss of generality. The ion and electron temperatures are equal, $T_i = T_e$. Boundary conditions are periodic in real space. The cut-off velocities are $v_{\min,s} = v_{0,s} - 7v_{T,s}$ and $v_{\max,s} = v_{0,s} + 7v_{T,s}$.

All simulations are performed with at least $N_x \times N_v = 768 \times 1024$ grid points, and a time-step width at most $\Delta t = 0.1\omega_{p,e}^{-1}$. The grid cell size in real space is $\Delta x = 0.04\lambda_D$. Although the length-scales of interest are larger than the Debye length, such a small cell size is necessary to reduce numerical artifacts.

5.2 Energy-phasestrophy relation

We can apply the energy-phasestrophy equation, Eq. (2.49),

$$\frac{\mathrm{d}W}{\mathrm{d}t} = \sum_s \frac{m_s u_s}{\mathrm{d}_v f_{0,s}} \frac{\mathrm{d}\Psi_s}{\mathrm{d}t}. \tag{5.3}$$

Fig. 5.1 shows the lhs ("wave energy growth") and the rhs ("phasestrophy growth") in a COBBLES simulation of CDIA turbulence. In the rhs, we approximate u_s as the velocity of maximum overlap between $f_{0,i}$ and $f_{0,e}$, $u_s = 1.42v_{T,i}$. For $\omega_{pe}t < 1000$, structures are not localized around $v = u_s$, which accounts for the discrepancy. For later times, we observe qualitative agreement (and quantitative agreement in a moving-average point-of-view). Since phasestrophy is directly related to the perturbed momentum in the collisionless limit, $\Psi_s = -2\mathrm{d}_v f_{0,s} \int v \langle \delta f_s \rangle\,\mathrm{d}v$, phasestrophy growth implies an exchange of momentum, between structures and waves, or between species.

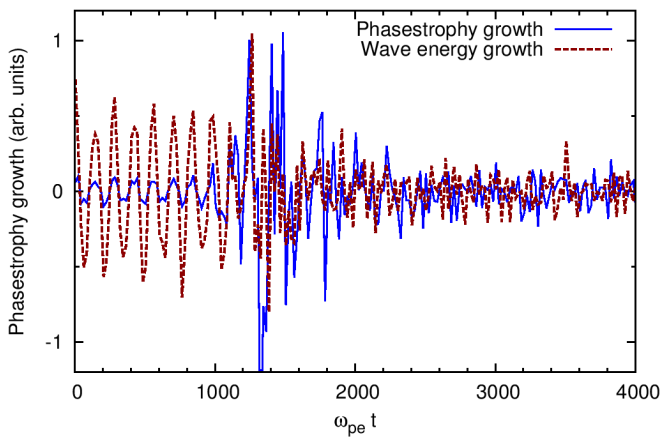

Figure 5.1 – Growth of phasestrophy and wave energy in a subcritical CDIA case.

Here the initial velocity drift is $v_d = 3v_{T,i}$, which is below the linear CDIA stability threshold of $3.92v_{T,i}$. Therefore the case shown here is subcritical. The nonlinear threshold for this subcritical instability depends on the kind of initial perturbations, as we describe in the next section.

5.3 Subcritical CDIA turbulence

Linear instability requires that the velocity drift v_d exceed some finite threshold $v_{d,\mathrm{cr}}$. However, nonlinear theory [BTDBG81, Dup83] predicts that phase-space density holes can grow nonlinearly, even for infinitely small drifts. In such plasmas, electron and ion structures behave like macroparticles and scatter each other, leading to dynamical friction (in addition to the usual quasilinear diffusion), which drives anomalous resistivity [Dup70]. From a momentum point-of-view, phase-space holes grow by exchanging their momentum with other species or with the wave pseudo-momentum [DKL15]. From an energetics point of view, growing structures continuously emit undamped waves by the Cherenkov process, leading to the growth of total wave energy [Dup70, LD13]. Holes can also be thought of as quasi-particle modes of zero or negative energy [Sch79]. The hole growth-rate was obtained far from [Dup83] and close to [Dup86] linear marginal stability. In the 1980's, particle simulations of the nonlinear electron-ion instability, with mass ratio $m_i/m_e = 4$ and temperature ratio $T_i/T_e = 1$, were performed [BTDBG82, BTD85]. To the credit of the authors, these simulations were performed three decades ago, when computing power was roughly 7 orders of magnitude lower than today. These simulations agree qualitatively with the theory, and nonlinear growth was observed for $v_d > 0.4v_{d,\mathrm{cr}}$, that is, far from linear marginal stability. Electron holes were reported to grow in a similar way from either a seed phase-space hole, or from random fluctuations, even with low-amplitude initial fluctuations ($e\phi/T \ll 10^{-2}$).

However, we demonstrated, based on PICKLES simulations, that these earlier particle simulations almost certainly suffered from numerical issues, such as noise associated with a small number of particles, leading to spurious conclusions [LDK14a]. In particular, nonlinear growth is found to be much more sensitive to initial conditions than suggested in references [BTDBG82, BTD85]. We observe that subcritical instabilities are absent when the initial perturbation consists of an ensemble of sine waves with random phases, except close to linear marginal stability ($v_d > 0.9v_{d,\mathrm{cr}}$) and for large initial amplitudes ($e\phi/T \sim 1$).

In contrast, a seed local negative perturbation (hole-like) in the electron phase-space can grow nonlinearly, even far below marginal stability ($v_d = 0.38v_{d,\mathrm{cr}}$) and for small initial amplitudes ($e\phi/T \sim 10^{-3}$). Depending on the initial conditions, a growing hole may keep most of the phase-space relatively intact (local hole growth), or, on the contrary, may lead to a turbulent state with significant potential energy $e\phi$, particle redistribution, heating and anomalous resistivity (global subcritical instability). Such system-wide effects are observed for $v_d = 0.76v_{d,\mathrm{cr}}$. However, the effects of the seed phase-space perturbation are indirect. A multitude of small holes emerge from the wake of the evolving seed perturbation. It is this

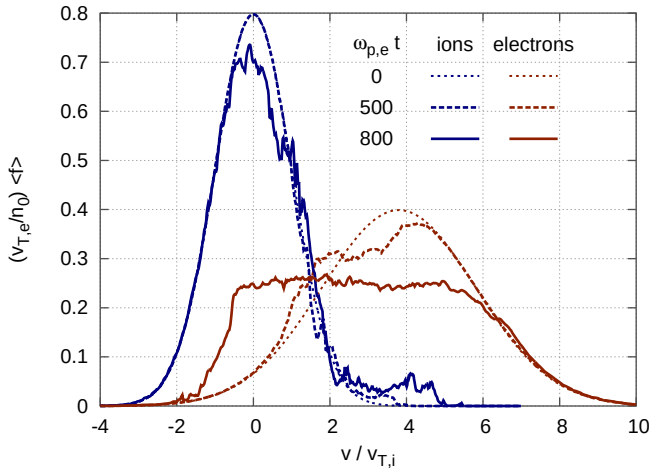

Figure 5.2 – Snapshots of the velocity distributions in a subcritical case. Simulation parameters are $v_d/v_{T,i} = 3.8$, $e\phi/T \approx 0.2$, and $N_x \times N_v = 768 \times 8192$.

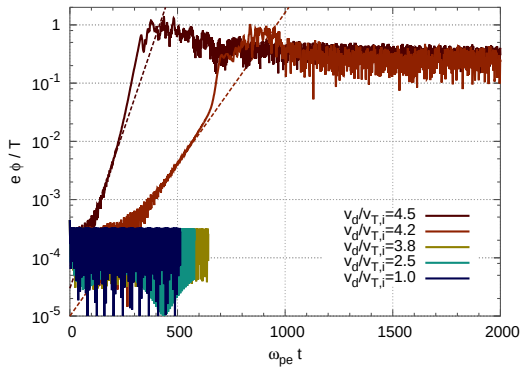

Figure 5.3 – Time-evolution of the normalized potential energy for small, incoherent initial perturbation, $e\phi/T \approx 2\times10^{-4}$. Linear theory is shown as dashed lines.

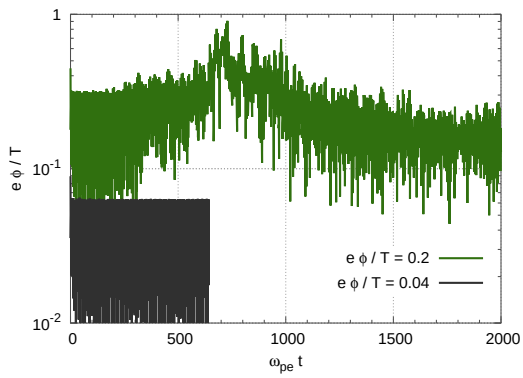

Figure 5.4 – Time-evolution of the normalized potential energy for $v_d/v_{T,i} = 3.8$ and various levels of incoherent initial perturbation.

phase-space turbulence that drives the subcritical instability. In other words, phase-space turbulence, rather than turbulence in the sense of a spectrum of incoherent waves, leads to substantial nonlinear growth (in general).

The main point of this section is to study how nonlinear stability depends on the type of initial perturbations. We focus on three types:

1. an ensemble of waves,
2. a single PS hole,
3. an ensemble of many PS structures.

5.3.1 Ensemble of waves

We run a series of COBBLES simulations for different values of initial drift. The linear stability threshold of the ion-acoustic mode is $v_d = v_{d,\mathrm{cr}}$, with $v_{d,\mathrm{cr}}/v_{T,i} = 3.92$. The initial velocity distributions are shown in Fig. 5.2 for $v_d/v_{T,i} = 3.8$. The initial perturbation is an ensemble of waves in the electron distribution,

$$f_e|_{t=0} = \left[1 + \sum_{n=1}^{n_{\max}} \frac{k_n}{k_1}\epsilon\cos(k_n x + \phi_n)\right] f_{0,e}(v), \tag{5.4}$$

where $k_n = nk_1$, $n_{\max} = 20$ ($k_{\max} = 4.0\lambda_D^{-1}$), ϕ_n are random phases, and ϵ controls the initial electric field amplitude. We measure the electric field energy by the mean square potential, $\phi = \left\langle\varphi^2\right\rangle^{1/2}$. We define the potential energy as $e\phi$.

		$v_d/v_{d,\mathrm{cr}}$ ($v_d/v_{T,i}$)					
		0 (0)	0.38 (1.5)	0.63 (2.5)	0.76 (3.0)	0.89 (3.5)	0.97 (3.8)
$e\phi/T$	1	W↓, H↓	W↓, H∼	W↓, H↑	W↓, H↑	W↑, H↑	W↑, H↑
	10^{-1}	W↓, H↓	W↓, H∼	W↓, H↑	W↓, H↑	W↓, H↑	W↑, H↑
	10^{-2}	W↓, H↓	W↓, H∼	W↓, H↑	W↓, H↑	W↓, H↑	W↓, H↑
	10^{-3}	W↓, H↓	W↓, H∼	W↓, H↑	W↓, H↑	W↓, H↑	W↓, H↑

Table 5.1 – Nonlinear stability. W↓ and W↑ mean decay and growth, respectively, of an initial ensemble of wave. H↓, H∼ and H↑ mean hole decay, local hole growth and global subcritical instability driven by an initial hole-like phase-space perturbation.

Fig. 5.3 shows the time-evolution of potential energy, normalized to thermal energy, $e\phi/T$, for three linearly stable cases, and two linearly unstable cases. For all stable cases, we hide data for times longer than half a numerical recurrence time, $T_{\mathrm{R}}/2 = \pi N_v/(10k_{\max}v_{T,e})$. The oscillations for $v_d/v_{T,i} < 4$ are due to the beating of waves with opposite phase velocities. We observe that the solutions are consistent with linear theory. Note that for drift velocities of 4.2 and 4.5, the growth rate increases before saturation. This is in contrast with the conventional wave saturation, where the growth rate decreases in time. This is the same phenomenon as the faster-than-linear growth in the barely unstable regime of the BB model, which we described in chapter 4 (4.3.2). It is due to the same mechanism: above a threshold amplitude, the nonlinear growth rate overcomes the linear growth rate.

The important conclusion here, is that we observe no subcritical instability. This is in contradiction with Ref. [BTDBG82], where subcritical instabilities are reported for the same parameters and $v_d/v_{T,i} \geq 1.5$, even for low-amplitude initial fluctuations with $e\phi/T \ll 10^{-2}$. We scanned the parameter space of velocity drift and initial amplitude, and concluded that subcritical instabilities emerge only when the drift is very close to linear marginal stability, and the initial perturbation is relatively large. Fig. 5.4 shows the time-evolution of normalized potential energy, for $v_d/v_{T,i} = 3.8$, which is only 3% below marginal stability, and for large initial amplitude. We do observe a subcritical instability when the initial amplitude is $e\phi/T \approx 0.2$, but not below. For $v_d/v_{T,i} = 0.5$, 1.5, 2.5 or 3.0, we did not obtain any subcritical instability even for initial amplitudes as high as $e\phi/T \approx 2$. These results are summarized in Table 5.1, which shows whether an incoherent ensemble of waves is nonlinearly stable (W↓) or unstable (W↑). From this table, we conclude that the nonlinear stability threshold is approximately $v_d/v_{T,i} = 3.5$ ($v_d/v_{d,\mathrm{cr}} = 0.89$).

Subcritical instabilities are in many aspects qualitatively similar to linearly unstable cases. The saturation level of potential energy is similar, we observe wide particle redistribution in phase-space, especially of the electrons, turbulent heating, and significant anomalous resistivity. Fig. 5.2 includes snapshots of ion and electron velocity distributions after the nonlinear growth for the subcritical simulation ($v_d/v_{T,i} = 3.8$) with high initial amplitude ($e\phi/T \approx 0.2$). At saturation, the electron distribution is flattened over a large range, $-1 < v/v_{T,i} < 6$. The ion distribution develops a plateau around $v/v_{T,i} = 4$, which is due to accumulating ion phase-space vortices.

Phase-space redistribution is associated with anomalous resistivity. We define the anomalous resistivity η as

$$n_0 q_i^2 \left(p_i - p_e\right) \eta = q_i \left\langle E \right\rangle - \left(\frac{1}{m_i} + \frac{1}{m_e}\right)^{-1} \frac{\mathrm{d}\left(p_i - p_e\right)}{\mathrm{d}t}, \tag{5.5}$$

where $\langle E \rangle$ is the spatial average of the electric field (here it is zero), and $p_s \equiv \int v f_s \mathrm{d}x\mathrm{d}v$ is the momentum of species s. Note that this corresponds to a standard definition of anomalous resistivity, $\eta = E/J$, where $J = e(u_i - u_e)$ is the current, and u_s is the fluid velocity of species s. Combining the electron and ion equations of motion in the collisionless limit yields $\mathrm{d}(u_i - u_e)/\mathrm{d}t = (m_i^{-1} + m_e^{-1})eE$. Accordingly, in our code, we estimate anomalous resistivity as $\eta = -m_i m_e/(m_i + m_e)\mathrm{d}log(u_i - u_e)/\mathrm{d}t$. For typical tokamak plasma conditions, $n_0 = 10^{19} m^{-3}$ and $T_i = T_e = 1keV$, the ion-electron collision frequency is of the order of

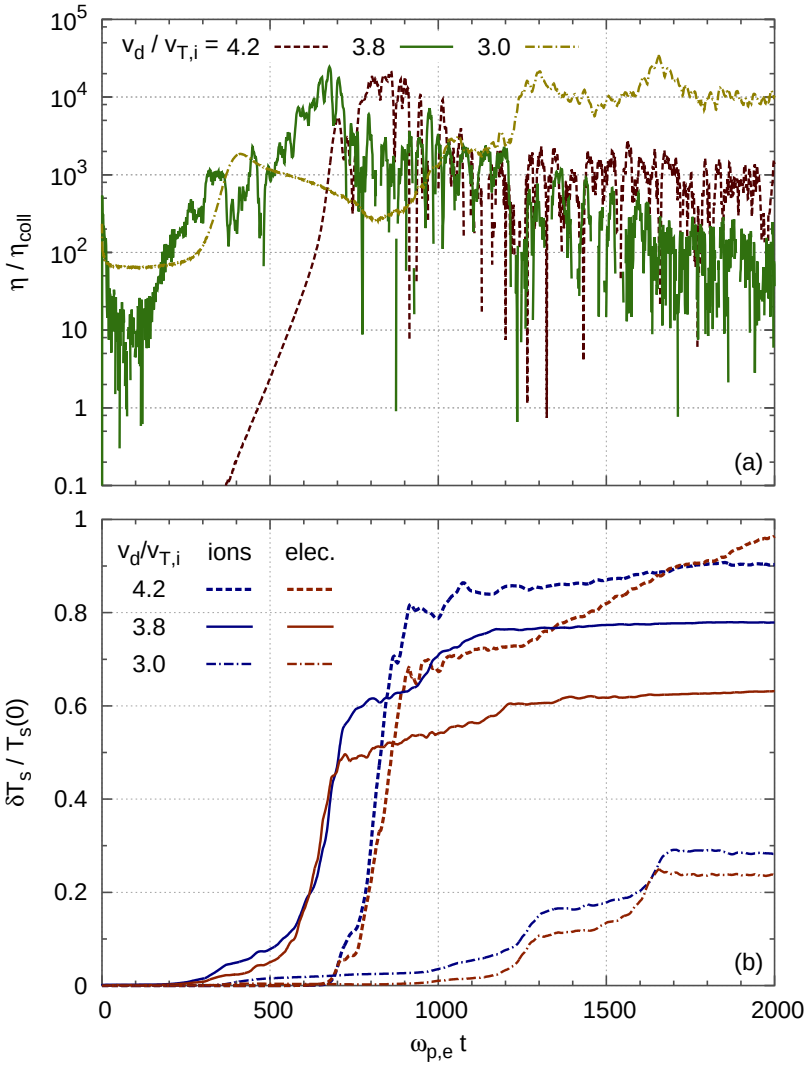

Figure 5.5 – Time-evolution of (a) anomalous resistivity, normalized to $\eta_{\rm coll} = 10^{-7} m_e \omega_{p,e}/(n_0 q_i^2)$, and (b) mean thermal energy perturbation. Three cases are shown, the simulation of Fig. 5.2 ($v_d/v_{T,i} = 3.8$, solid curves), a linearly unstable case ($v_d/v_{T,i} = 4.2$, dashed curves), and the reference case S of Fig. 5.12 ($v_d/v_{T,i} = 3.0$, chained curves).

$\nu_{ei} \sim 10^{-7}\omega_{p,e}$ (with real mass ratio). Fig. 5.5(a) shows the moving average (over $\delta t = 16\omega_{p,e}^{-1}$) of $\eta/\eta_{\rm coll}$ where $\eta_{\rm coll} = m_e\nu_{ei}/(n_0 q_i^2)$ is a typical value of the collisional resistivity. The maximum anomalous resistivity is 4 orders of magnitude higher than typical collisional resistivity, for both subcritical and supercritical cases.

In addition, ion-acoustic waves cause both ion and electron heating. We define the mean thermal energy $T_s \equiv (m_s/2n_0)\int(v-p_s)^2 f_s \mathrm{d}x\mathrm{d}v$. It reduces to the temperature for spatially uniform, Boltzmann distributions. Fig. 5.5(b) shows the moving average of the mean thermal energy perturbation $\delta T_s = T_s(t) - T_s(0)$. Both ion and electron thermal energies roughly double, for both subcritical and supercritical cases. These results indicate that the saturated level of turbulence, the anomalous resistivity, the turbulent heating, etc. are not directly affected by linear stability. In other words, essential nonlinear phenomena do not undergo any bifurcation at the linear stability threshold.

5.3.2 Single seed PS structure

We have shown that subcritical instabilities can grow from an ensemble of waves, but only close to linear marginality and when the initial amplitude is large. However, it is possible to drive subcritical instabilities from much smaller initial amplitude, and even far from marginal stability, by preparing a self-trapped structure at $t = 0$.

Hereafter, we study the evolution of a local, negative phase-space density perturbation (hole-like) in the electron distribution, and drop the subscript e in $\tilde{f}_{h,e}$. The initial electron distribution is

$$f_e|_{t=0} \;=\; f_{0,e}(v) \;-\; \tilde{f}_h \exp\left[-\frac{1}{2}\left(\frac{v-v_h}{\Delta v_h}\right)^2\right]\left[\frac{H(x)-\Delta x_h/L}{2}\right], \tag{5.6}$$

where $\tilde{f}_h(t)$ is the hole-like perturbation amplitude, $v_h(t)$ is its velocity, Δx_h and $\Delta v_h(t)$ are its width and velocity-width, and

$$H(x) = 1 + \cos\left[2\pi\,\frac{x-L/2}{\Delta x_h}\right] \tag{5.7}$$

if $|x - L/2| < \Delta x_h/2$, otherwise $H(x) = 0$. The initial depth $\tilde{f}_h(0)$ is chosen to satisfy the trapping condition [Dup82],

$$\tilde{f}_h = \frac{n_0\Delta v_h}{6\omega_{p,e}^2\lambda^2}\left[(1+2\lambda/\Delta x_h)\left(1-e^{-\Delta x_h/\lambda}\right)-2\right]^{-1}, \tag{5.8}$$

where λ is the shielding length, which is such that $(k\lambda)^{-2}$ is the real part of the linear susceptibility. The shape of this artificial hole-like seed is arbitrary and does not correspond to maximum entropy.

Let us study in details the evolution of one case, which we label as S. It will serve here as an example of a subcritical instability. The parameters for S are $v_d/v_{T,i} = 3.0$, $v_h(0)/v_{T,i} = 0.8$, $\Delta v_h/v_{T,i} = 0.2$, and $\Delta x_h/\lambda_D = 2$. Figs. 5.6 and 5.7 show snapshots of both ion and electron distribution functions in the reference case S. A video, which shows the evolution of the distribution functions, their spatial averages, the normalized potential energy, and the spectrum of potential, is available at `https://iopscience.iop.org/0741-3335/56/7/075005/media/PPCF484789_movie1.avi`. Fig.5.8 shows the evolution of the depth, velocity and velocity-width of the deepest hole. The reader should keep in mind that $\tilde{f}_h$ is defined as the depth of the deepest negative phase-space density perturbation at each instant. In other words, we do not track one single structure throughout its evolution, but rather switch to whichever structure is the deepest. Such switching is taking place between $\omega_{p,e}t = 1000$ and 3000, where the instantaneous maximum depth alternates between different holes. In these figures, we observe two distinct phases. In the first phase, from $\omega_{p,e}t = 0$ to 700, the initial artificial seed dominates the phase-space. In the second phase, after 700, many structures coexist and interact. Hereafter, we focus on the evolution of a single hole-like perturbation in the first phase. The impacts of many phase-space structures (phase-space turbulence) in the second phase is discussed in subsection 5.3.3.

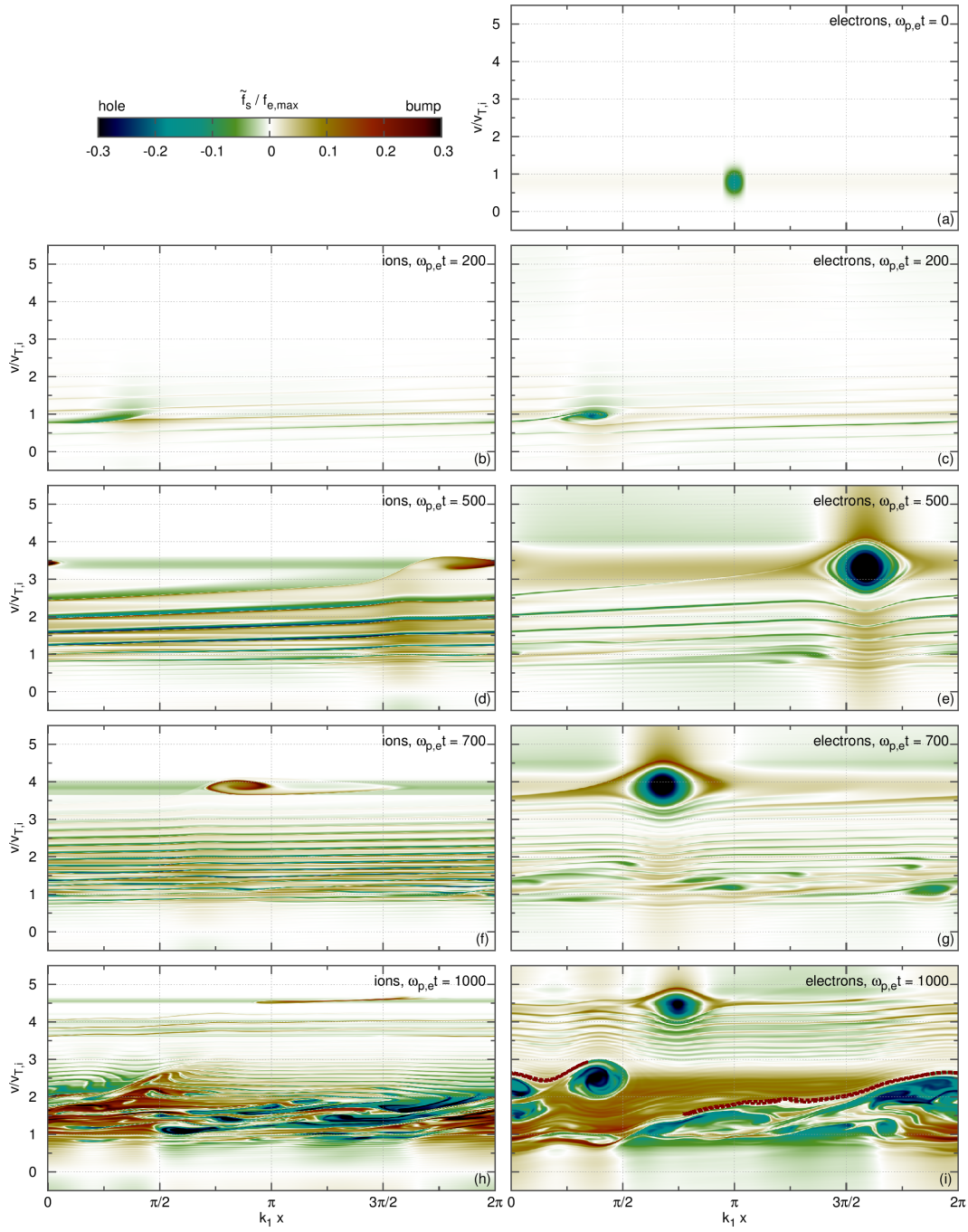

Figure 5.6 – Snapshots of ion (left) and electron (right) perturbed distribution in the reference simulation S ($v_d/v_{T,i} = 3.0$, $v_h(0)/v_{T,i} = 0.8$, $\Delta v_h/v_{T,i} = 0.2$, and $\Delta x_h/\lambda_D = 2$). Values of $\omega_{p,e}t$ from top to bottom are 0, 200, 500, 700 and 1000. A contour of constant f_e is dashed in (i).

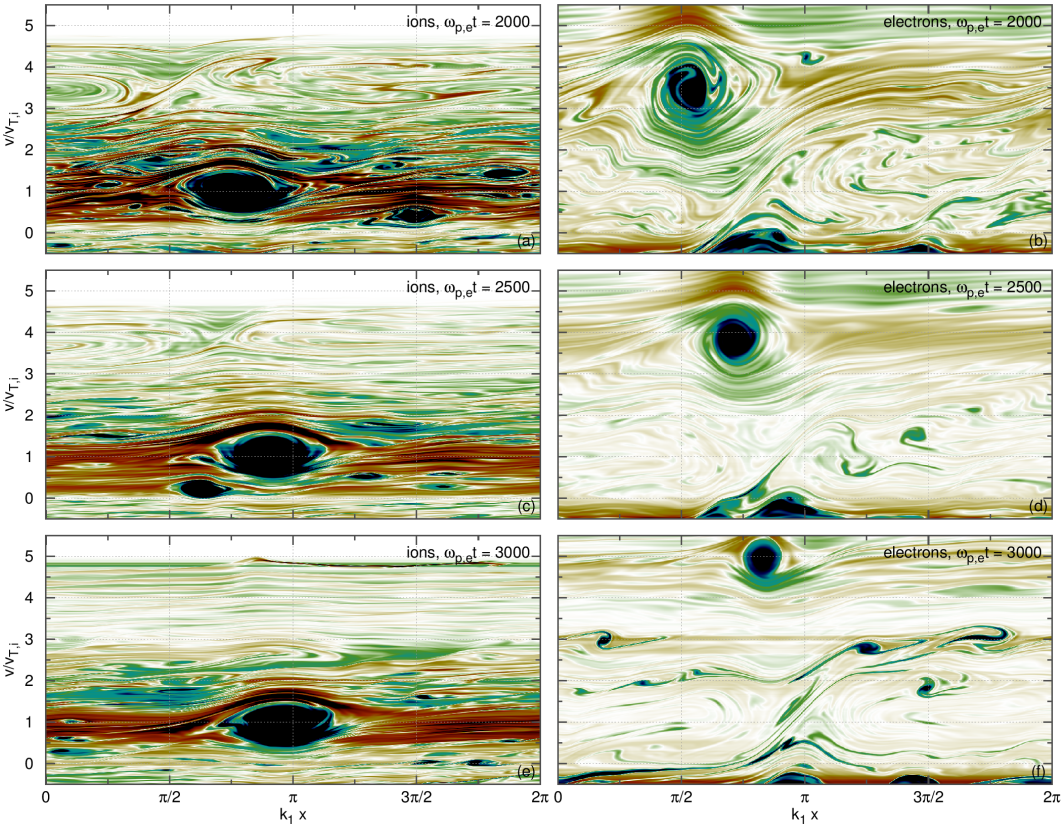

Figure 5.7 – Same as Fig. 5.6, but for later times. Values of $\omega_{p,e}t$ from top to bottom are 2000, 2500, and 3000.

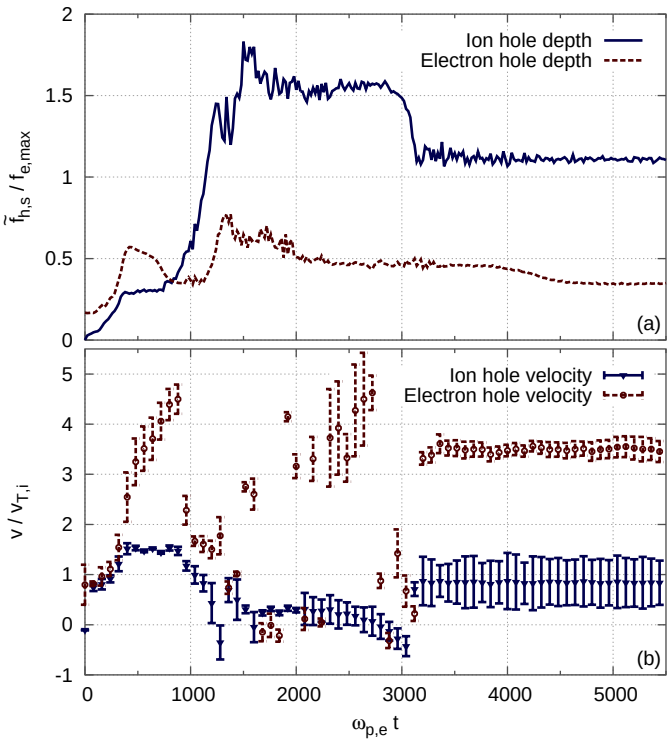

Figure 5.8 – Time-evolution of the depth (a) and velocity (b) of the deepest negative phase-space density perturbation in the reference case S. The velocity width is shown by error bars at $\pm\Delta v_h$.

We remind that, since phase-space density is conserved along particle trajectories, the center of a hole, where particles are deeply trapped, and which therefore follows particle orbits, must conserve f. Therefore, an isolated hole can grow (decay) by climbing (descending) a velocity gradient. When the gradient is positive (negative), it must accelerate (decelerate) to grow and decelerate (accelerate) to decay. In Fig.5.8, we observe that the artificial electron seed initially grows, from $\omega_{p,e}t = 0$ to 400, by climbing the positive velocity gradient, thereby accelerating from $v_h/v_{T,i} = 0.8$ to 3.0. The growth stops when the structure reaches the top of the electron distribution ($v_h = v_d$). Then, from $\omega_{p,e}t = 0$ to 400, it decays by descending the velocity gradient, while still accelerating. It decays until it reaches a velocity v such that $f_{0,e}(v) \approx f_{0,e}(v_h(0)) - \tilde{f}_h(0)$. Before this final velocity is reached, however, the diagnostic switches to other holes, which are then deeper than the initial seed. It is these new holes that drive the nonlinear instability at later times. This process is described in the next subsection, 5.3.3.

Whether an artificial hole-like seed initially grows or not depends on both its characteristics and the plasma drift velocity. Fig. 5.9 shows the evolution of an electron hole-like seed, initially located in the region of strong overlap between ion and electron distributions, for various initial conditions. The ratio $\Delta x_h/\Delta v_h = 20/\omega_{p,e}$ is arbitrary. For $v_d = 0$ [Fig. 5.9(a)], we observe that all seeds (for the shapes and sizes we tested, as listed in the legend of Fig. 5.9) are damped. This is expected since in this configuration, there is no free-energy. Note that in this configuration, an isolated hole must accelerate (descend the velocity gradient) to decay. Trapped particles accelerate with the hole. Thus, a phase-space structure can drive transient velocity-space particle transport, even as it decays.

For $v_d/v_{T,i} = 3.0$ [Fig. 5.9(c)], which is relatively close to linear threshold ($v_d = 0.76v_{d,\mathrm{cr}}$), all seeds (for the shapes and sizes we tested) initially grow. The evolution is similar to the reference case S. For $v_d/v_{T,i} = 2.5$, results are qualitatively similar and are not shown here.

For an intermediate value of drift, $v_d/v_{T,i} = 1.5$ [Fig. 5.9(b)], which is far from the linear threshold ($v_d = 0.38v_{d,\mathrm{cr}}$), the hole growth and subsequent decay depends on its size and location. When they are located in the velocity-region of strong overlap between ion and electrons, holes seem to grow more easily. This is consistent with the underlying growth mechanism (local momentum exchange between ions, electrons and waves) and with the predicted theoretical growth rate of an isolated hole. The hole growth is expected to be of the order of $-v_{T,e}^2\, v_{T,i}^2 \partial_v f_{e,0}(v_h)\, \partial_v f_{i,0}(v_h)\omega_b$, where ω_b is the bounce frequency of a particle deeply trapped in the hole [Dup83]. However, in all cases, the hole eventually decays and no other phase-space structure is generated. Whether a hole with a different shape can or cannot trigger phase-space turbulence remains an open question, since we have studied only six cases.

In [Fig. 5.9(b)], we observe that holes initially decay for a while before starting to grow. The reason may be that the shape of the artifical initial seed is not optimal for growth. This hypothesis is supported by the following analysis. Fig. 5.10 compares two cases, where $\Delta v_h(0)$ is fixed to $0.2v_{T,i}$, but $\Delta x_h(0)$ differs. If $\Delta x_h(0)/\lambda_D = 2$, which corresponds to a ratio $\Delta x_h(0)/\Delta v_h(0) = 20\omega_{p,e}^{-1}$, the ratio $\Delta x_h(t)/\Delta v_h(t)$ executes damped oscillations around a value of $200\omega_{p,e}^{-1}$, until it stabilizes. Then the hole starts its nonlinear growth. If $\Delta x_h(0)/\lambda_D = 5$, which corresponds to a ratio $\Delta x_h(0)/\Delta v_h(0) \approx 50\omega_{p,e}^{-1}$, the hole starts to grow almost straightaway, suggesting that its shape is closer to the optimal shape for nonlinear growth.

5.3.3 Ensemble of many PS structures

For a velocity drift $v_d/v_{T,i} = 1.5$, we mentioned that, although an artificial seed hole initially grows, it eventually decays and no other phase-space structure is generated. In such cases, we observe that the electric potential does not increase. The velocity redistribution is negligible ($\langle \delta f_s \rangle / f_{s,0} < 10\%$), the mean thermal energies are constants ($\delta T_s/T_s < 0.1\%$), and the anomalous resistivity is small ($\eta/\eta_{\mathrm{coll}} < 500$). Thus, the nonlinear growth of one isolated hole is observed without system-wide instability. We refer to this situation as *local hole growth*.

This local hole growth is in contrast with the *global subcritical instability* observed e.g. for the reference case S. Fig. 5.11(a) shows snapshots of the velocity distributions in the latter

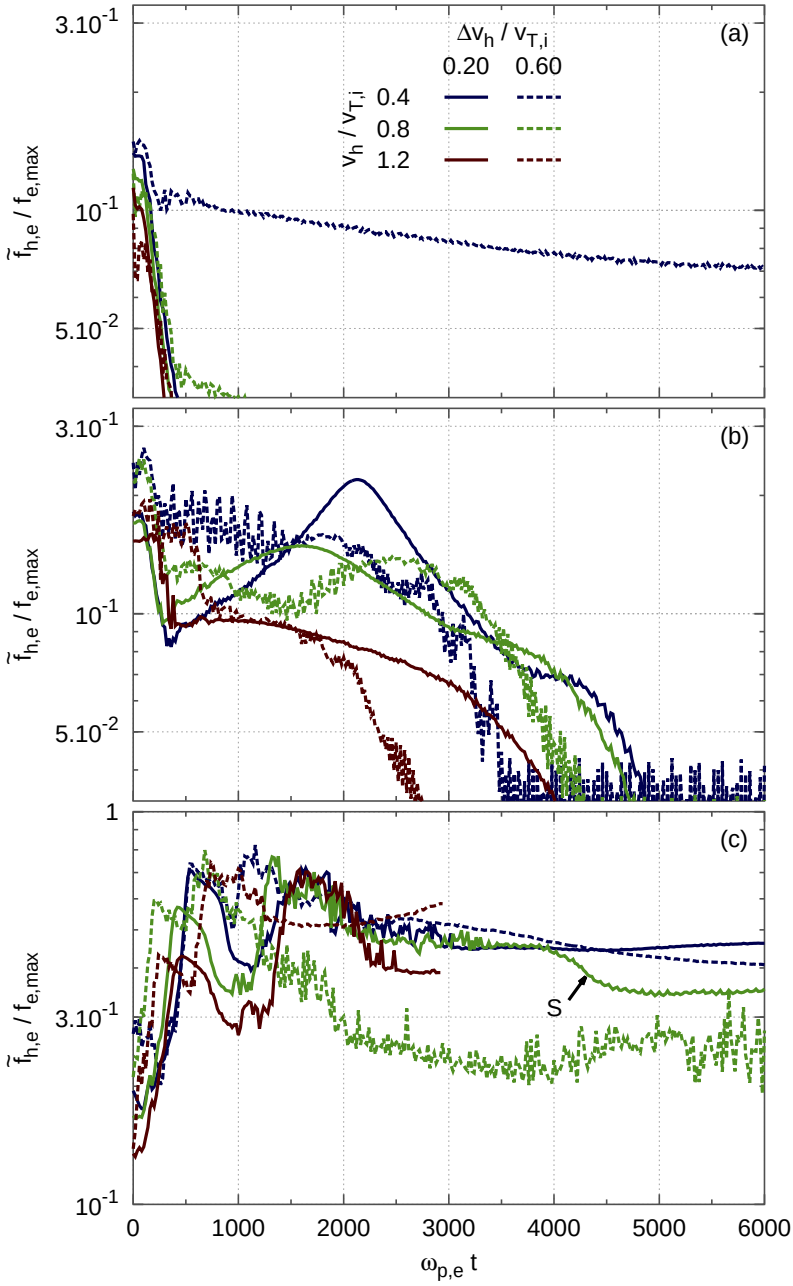

Figure 5.9 – Time-evolution of the depth of the deepest electron phase-space perturbation ($\tilde{f}_{h,e}$) with an initial electron seed with $\Delta x_h/\Delta v_h = 20/\omega_{p,e}$. The initial drift $v_d/v_{T,i}$ is (a) 0.0, (b) 1.5, and (c) 3.0. The reference simulation is marked by S in (c).

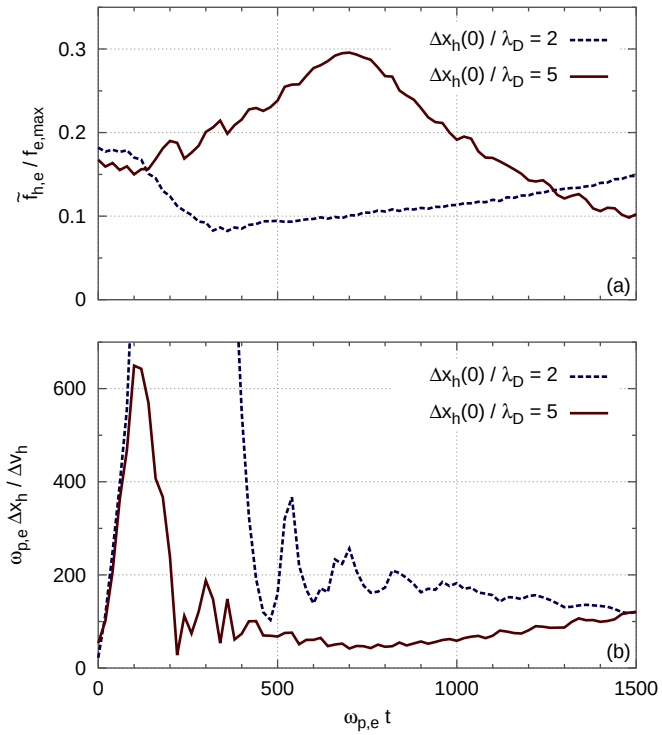

Figure 5.10 – Time-evolution of (a) the height of the largest electron hole and (b) the ratio $\Delta x_h/\Delta v_h$ with an initial electron hole with $\Delta v_h(0)/v_{T,i} = 0.2$, for $v_d/v_{T,i} = 1.5$ and $v_h(0)/v_{T,i} = 0.4$.

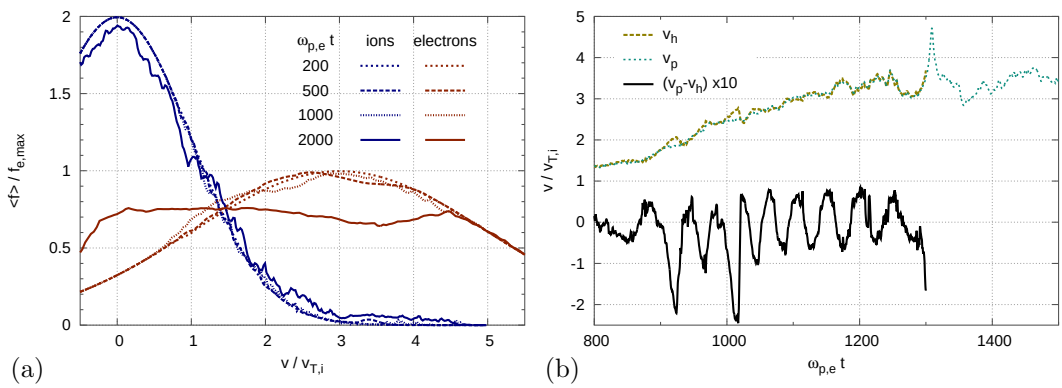

Figure 5.11 – Evolution of the reference simulation S. (a) Snapshots of velocity distributions. (b) Time-evolution of the velocity v_p of a test particle (electron) trapped in a hole with central velocity $v_h(t)$.

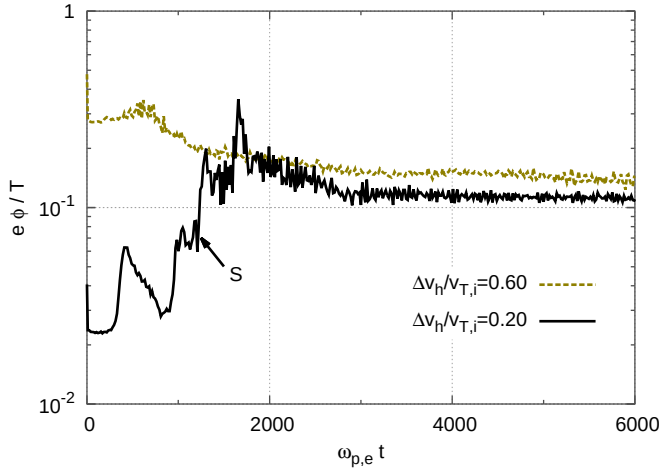

Figure 5.12 – Time-evolution of the normalized potential energy with an initial electron hole, for $v_d/v_{T,i} = 3.0$, $v_h/v_{T,i} = 0.8$, $\Delta x_h/\Delta v_h = 20/\omega_{p,e}$ and varying hole velocity-width. The reference simulation is marked by S.

case. We observe wide particle redistribution between $t = 1000\omega_{p,e}^{-1}$ and $t = 2000\omega_{p,e}^{-1}$, which is after the initial hole has decayed, and during the growth of the new holes. We can check that particles are indeed trapped into the self-emerging structures. Fig. 5.11(b) shows the velocity v_p of a test electron, which is deeply trapped by a hole formed around $t = 800\omega_{p,e}^{-1}$. The central velocity of the hole v_h is estimated by tracking the local minimum of f. The velocity of the test electron in the framework of the hole, $v_p - v_h$, is shown to oscillate around zero, which indicate that particles follow trapped orbits in phase-space, in the reference-frame of the structure. The bounce-frequency is measured from the time-trace of $v_p - v_h$ as $\omega_b \approx 0.15\omega_{p,e}$. An other way to estimate the bounce-frequency is to measure the local maximum φ_0 of the electric potential, and the spatial extent Δx_h of the negative perturbation. The bounce frequency is then given by $\omega_b^2 = |q_e|k_h^2\varphi_0/m_e$, with $k_h = 2\pi/\Delta x_h$. This method also yields $\omega_b \approx 0.15\omega_{p,e}$ for the same hole. The oscillation is quasi-periodic from $t_1 = 850\omega_{p,e}^{-1}$ to $t_2 = 1280\omega_{p,e}^{-1}$. At t_2, the hole appears to be sheared by the tidal forces exerted by a neighboring, larger hole. The lifetime of the hole is thus estimated as $\tau_c = t_2 - t_1 = 430$. The Kubo number in the region of phase-space within this hole is $K = \omega_b\tau_c/(2\pi) \approx 10$. Repeating this analysis for other holes among the largest ones, we found Kubo numbers in the range $K \approx 3 - 20$. This confirms that the simulation is in a regime of large Kubo number. The merging of holes reduces their lifetime. However, merging is rare enough that particles bounce many times during the life of most large holes.

Fig. 5.12 shows the moving average (over $\delta t = 16\omega_{p,e}^{-1}$) of the potential energy time-series in three cases, including the reference case S, for $v_h/v_{T,i} = 0.8$. We observe that the potential energy grows to $e\phi/T \sim 0.3$, which is of the same order as the saturated potential in linearly unstable cases. In the reference case S, we see a clear difference between the first phase ($t = 0 - 700$) and the second phase ($t = 700 - 2000$). In the first phase, a single hole develops [as seen in Fig. 5.6(c) ,(e) and (g)], and although the field energy grows, it is only transiently. The field energy then decays back to a value close to the initial perturbation. In the second phase, where multiple holes develop [as seen in Fig. 5.6(i) and (b)], the field energy grows to $e\phi/T \sim 0.3$ before relaxing to $e\phi/T \sim 0.1$, thereby driving a global subcritical instability. Therefore, for a given initial field energy, phase-space turbulence (multiple interacting holes) is more efficient than a single hole to drive the instability.

Fig. 5.5 includes the time-evolution of anomalous resistivity and perturbed mean thermal energies for the reference case S. We observe large anomalous resistivity and turbulent heating, qualitatively similar to the cases with an initial ensemble of waves. These subcritical instabilities occur relatively far from marginal stability, even when the initial potential energy is as low as $e\phi/T \sim 10^{-2}$. *This is in sharp contrast with the case where the initial perturbation is a collection of waves. In other words, phase-space structures, even with non-optimal shapes, are much more efficient than coherent waves for driving nonlinear instabilities.*

5.3.4 Partial summary

To summarize, we observe that many holes, even small, but when scattered in phase-space, can drive global subcritical instabilities. In contrast, one single hole, even a large one, can evolve while leaving most of the phase-space intact, without system-wide instability (without significant potential energy growth, redistribution, heating or anomalous resistivity). One single hole can drive instabilities indirectly though, by triggering the formation of many smaller holes in its wake. This process is detailed as follows. As can be seen in Fig. 5.6, as the initial, artificial hole accelerates within the region $v_h < v_d$, its depth increases (along with its width in velocity). This increase in depth is due to the trapping of additional particles. This leaves a trail of negative phase-space density perturbations in the region $v_h < v_d$ [See Fig. 5.6(c) or (e)]. Then, as the hole enters the region $v_h > v_d$, its width in velocity decreases, and de-trapping occurs. This, in turn, leaves a trail of positive phase-space density perturbation in the region $v_h > v_d$ [See Fig. 5.6(g)]. In analogy to self-gravitating matter organizing into hierarchical structures via the mechanism of Jeans collapse, negative phase-space density perturbations have a natural propensity to coallesce [RB67, BNR70]. The negative trail bunches into a collection of small holes, scattered in phase-space [See Fig. 5.6(g) and (i)]. The turbulent interaction of these many holes (phase-space turbulence), is shown in Fig. 5.7. From our analysis, we conclude that phase-space turbulence is a very efficient source of particle-transport in velocity space (or redistribution), turbulent heating and anomalous resistivity.

The above nonlinear stability analysis of phase-space holes is summarized in Table 5.1, which shows whether a hole decays (W↓), grows but then decays without triggering system-wide electron redistribution (local growth, W∼) or grows and trigger such redistribution (global subcritical instability, W↑). From this table, we conclude that the nonlinear stability threshold with an initial hole in terms of $v_d/v_{T,i}$ is between 1.5 and 2.5.

To study the effect of larger wave-lengths, we ran many of the simulations above with a quadrupled system size, allowing wave-numbers as small as $0.05\lambda_D^{-1}$. We did not find any qualitative difference in the results.

5.3.5 Discussions

We now turn to discussions of experimental scenarios, the effect of collisions, of a magnetic field and of the mass ratio. The purpose of this section is not only to clarify caveats, but also to stimulate further studies, and is more of a speculative flavor.

Experimental scenarios

Our numerical analysis clarify the process of phase-space structures formation. If the system is linearly unstable, a turbulent state can be reached, in which particles are randomly scattered, leading to fine-grain structures that act as seeds. If the system is linearly stable, we can speculate that at least four routes to instability are possible.

1. The first route was demonstrated in Fig. 5.4. It corresponds to the growth from random fluctuations. This route is limited to an initial barely stable equilibrium and requires large amplitude perturbations. The initial perturbation (e.g. thermal noise) can be seen as an ensemble of waves, which will trap particles and form seed structures that can grow nonlinearly.
2. The second route was demonstrated in Fig. 5.9(c). It corresponds to the growth of a single hole. Such holes may be externally driven by the experimental setup or by physical processes that are not included in this model. As we have seen, a single hole may or may not lead to phase-space turbulence.
3. We speculate the existence of a third route, which would be a transition from supercritical to subcritical instability on a fluid time-scale. Fluid parameters of the background plasma such as fluid velocities or temperatures may evolve, on a slow time-scale, due to processes that are not included in this model, such as an applied electric field, external heating, or other magneto-hydrodynamic instabilities. This may lead to a transition from a linearly unstable system to a linearly stable state.

Scenario	Linearly stable	Seed PS structure(s)	Requires high-amplitude IP	Sensitive to details of IP
Supercritical instability	No	Trapping islands	No	No
Marginal stability	Barely	Thermal noise	Yes	Yes
External drive	Yes	Externally-driven hole	Yes	No
Fluid transition	Yes	Pre-existing structures	No	No
Kinetic transition	Yes	Pre-existing structures	No	No

Table 5.2 – Scenarios that may lead to a turbulent state with phase-space granulation. Here, IP is short for initial perturbation, and transition refers to transition from supercritical to subcritical conditions.

Phase-space turbulence that originates from linearly-driven seeds should be able to survive this transition.

4. We demonstrated the viability of a fourth scenario relying on a transition from supercritical to metastable (subcritical steady-state) on a kinetic time-scale [NLG+10, NGG+10]. As the wave grows linearly, the ion resonance width increases. Eventually, trapped ions absorb wave energy at a rate for which the total nonlinear growth rate vanishes. Such process can result in a metastable steady-state, where phase-space structures may be continuously created and dissipated.

These scenarios are summarized in Table 5.2.

Effect of collisions

This work is concerned with collisionless plasma, but as we have seen in chapter 4, even small collisions can have qualitative effects on the nonlinear evolution of wave-particle interactions. If a collision operator is introduced, we expect to find regimes of intermittent, rather than transient, turbulence. This is a speculation, based on the effects of collisions on phase-space structures in the BB model.

Effect of the mass ratio

Phase-space holes with small mass ratio are relevant for pair plasmas [ES05] such as electron-positron plasmas [GS95a] and paired fullerene-ion plasmas [OH03], with applications in semiconductors and space. However, the small mass ratio $m_i/m_e = 4$ adopted in this work brings the question of applicability of our findings to the most common hydrogen-ion plasma. In the case of an electron-oxygen-ion plasma with mass ratio $m_i/m_e = 29500$, a single electron hole remains stationary for a hundred $\omega_{p,e}^{-1}$, until an ion density cavity is formed [ES04]. Whether phase-space turbulence and subcritical instabilities develop or not on a ion kinetic timescale ($\omega_{p,i}^{-1}$) in large mass-ratio plasma remains an open question. Moreover for larger mass ratio, the phase-space turbulence will probably not affect the ion distribution and its mean thermal energy.

Effect of a magnetic field

While in this work we focused on current-driven ion-acoustic instability in unmagnetized plasmas, similar scenarios can be developed for magnetized plasmas. Formation of a single phase-space structure is reported in Ref. [TDH90]. In that paper, it was shown that a drift-hole extracts free energy more efficiently than linear waves do. The turbulent case with many structures is discussed in Ref. [BDT88b]. In this work it was shown that in trapped-ion resonance driven, ion temperature gradient instability, transport is determined, not

by quasi-linear turbulent diffusion, but rather by dynamical frictions exerted on turbulent trapped-ion granulations. More recently, it was shown that both a coherent drift-hole and an ensemble of granulations can interact with zonal flows [KD11, KD12, KID$^+$14b]. The impact of zonal flows on transport driven by trapped ion granulations was formulated as a part of dynamical friction [KDW$^+$13]. In magnetized space plasmas, phase-space turbulence and jets are promising candidates mediators of magnetic reconnection via anomalous resistivity.

5.4 Phase-space jets

As we have seen, in the presence of wave dissipation (γ_d in the BB model, ion Landau damping in the present CDIA model), phase-space structures spontaneously emerge in nonlinear Vlasov dynamics. These structures include well-known self-trapped vortices (holes). In Ref. [LDK14b], which we summarize here, we reported the existence of another kind of phase-space structures: elongated filaments, resembling jets. Jets are highly anisotropic, and connect low and high velocity regions over a range larger than the electron thermal velocity. These jets are formed by straining due to interacting holes. Therefore, jets are not independent objects. They are tied to the formation and dynamics of holes. This process is similar to the formation of a bridge of material between two colliding galaxies. Indeed, there is a duality between gravitating matter and negative electron phase-space perturbations [BNR70]. Though less coherent than holes, jets survive long enough for particles to scatter between low and high phase-space density regions. Jets are found to contribute significantly to electron redistribution, velocity-space transport and anomalous resistivity.

We find that time-scales of holes and jets are ordered as follows: jet lifetime $\sim$ particle travel time on a jet $\sim$ hole trapping time $\ll$ hole lifetime. The lengthscale of jets is of the order of 10 Debye length. The velocity extents are ordered as follows: jet-driven convective acceleration $\lesssim$ hole size $\lesssim$ particle mean-free-path on a jet $\sim$ jet size $\sim$ electron thermal velocity. Jets and holes are associated with fundamentally different transport processes. Hole-driven transport is essentially convective, since trapped particles accelerate along with the hole. Jet-driven transport is essentially stochastic, since particles may accelerate or decelerate along the jet. In terms of magnitude, holes and jets each account for roughly half of the total particle flux.

5.4.1 Small mass ratio

In this section, we analyze a numerical experiment with a mass ratio of $m_i/m_e = 4$. The main reason for describing first the case of a small mass ratio, is that it drastically improves the readability of phase-space contour plots. The analysis is repeated in the next section for a mass ratio of $m_i/m_e = 1836$. Most findings are valid for both mass ratios.

In this subsection, we further analyze the linearly unstable case shown in Fig. 5.5. Let us recall the simulation parameters. The system size is $L = 2\pi/k_1$, where $k_1 = 0.2\lambda_D^{-1}$. The initial drift is $v_d = 4.2v_{T,i} = 2.1v_{T,e}$. Note that, although in the last section, velocities are given relative to $v_{T,i}$, in this section we give them relative to $v_{T,e}$, since PS jets appear to scale with electronic plasma parameters. The number of grid points is $N_x \times N_v = 1024 \times 2048$, and the time-step width is at most $\Delta t = 0.016\omega_{p,e}^{-1}$. In fact, for historical reasons, we actually performed the same simulation again, but with much lower initial amplitude of fluctuations, which yields a shift by $\delta t = 390\omega_{p,e}^{-1}$ of the nonlinear saturation compared with Fig. 5.5.

Fig. 5.13(a) shows snapshots of the velocity distribution before, during and after particle redistribution. Electrons loose momentum, which reduces the driving current. Ion redistribution is much weaker. Note that an electron hole at $v/v_{T,e} \approx 2.2$ survives for a long time. It is unfaltering even at the end of the simulation ($\omega_{p,e}t = 10000$). This is reminiscent of the weakly dissipative coherent trapped-particle state [SK96]. Here dissipation is due to numerical discretization. Fig. 5.13(b) shows the evolution, after the linear growth phase, of the mean square potential, $\phi = \left\langle \varphi^2 \right\rangle^{1/2}$, and anomalous resistivity η. Anomalous resistivity, or equivalently, redistribution of electrons and velocity-space particle transport, is strongest around $t \approx 1150 - 1400$ (in units of $\omega_{p,e}$), which is when coherent structures dominate the phase-space evolution.

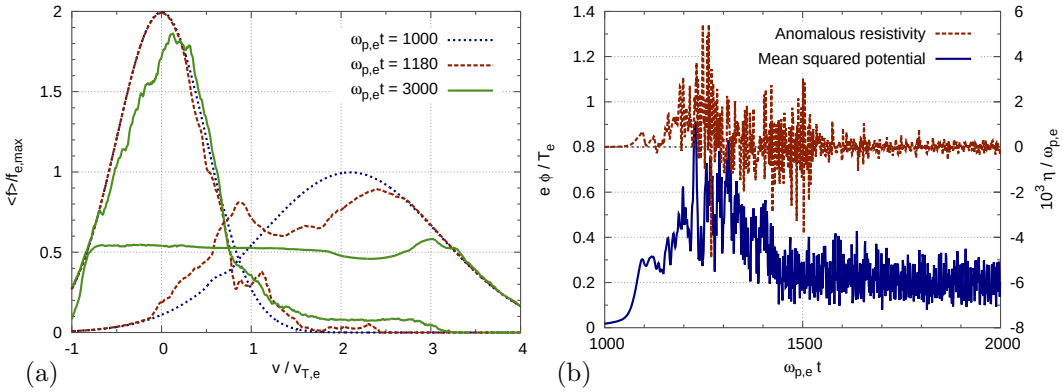

Figure 5.13 – CDIA simulation with mass ratio $m_i/m_e = 4$, system size $L = 10\pi\lambda_D$ and initial drift $v_d = 4.2v_{T,i} = 2.1v_{T,e}$. (a) Snapshots of the ion (left) and electron (right) velocity distributions. (b) Time-evolution of the mean square potential (left axis) and anomalous resistivity (right axis).

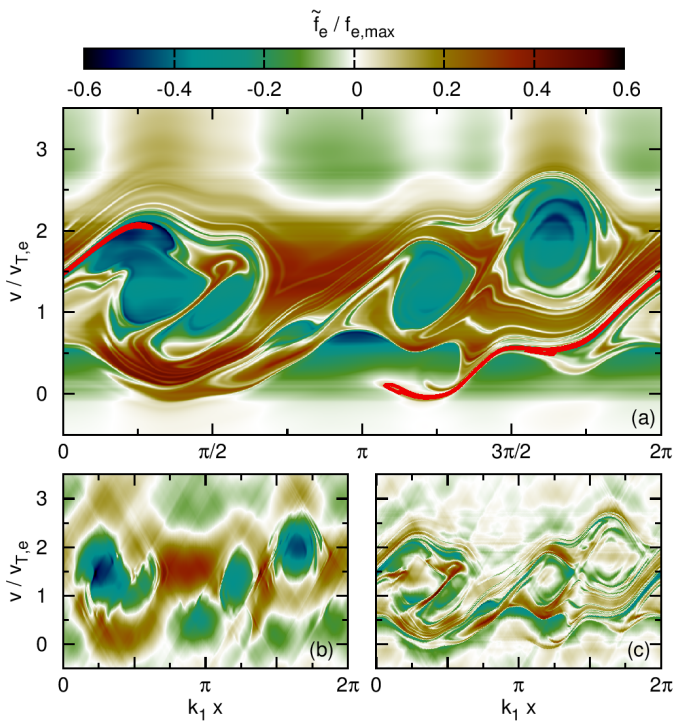

Figure 5.14 – (a) Snapshot at $\omega_{p,e}t = 1180$ of the perturbed electron distribution $\tilde{f}_e$, normalized to $f_{e,\max} = f_e(v_{0,e})$. Solid curve: contour of constant $f_e/f_{e,max} = 0.375$. (b) Low-pass filtered $\tilde{f}_{e,\text{holes}}$. (c) High-pass filtered $\tilde{f}_{e,\text{jets}}$. The mass ratio is $m_i/m_e = 4$. The system size is $10\pi\lambda_D$.

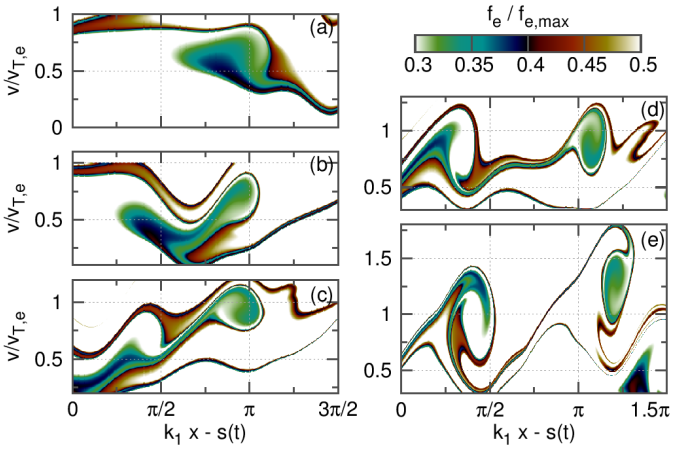

Figure 5.15 – Jet formation. Snapshots at $\omega_{p,e}t = 1100$ (a), 1120 (b), 1140 (c), 1150 (d) and 1160 (e) of the electron distribution f_e (mass ratio $m_i/m_e = 4$). The horizontal coordinate is shifted by $s(t) = 0.05\pi(\omega_{p,e}t - 1090)$, in order to compensate for free-streaming.

Fig. 5.14(a) is a snapshot at $t = 1180$ of the perturbed electron distribution (we recall that $\tilde{f}_e \equiv f_e - \langle f_e \rangle$). As we already described in section 5.3, we observe in the nonlinear phase that PS holes spontaneously form in the region of strong overlap between ion and electron distributions. The holes accelerate and grow by climbing the velocity gradient in the electron distribution. Particles that are trapped inside a hole are convected along with it, leading to velocity-space transport. All of the above physics was already documented in the literature.

However, holes are not the only entities which populate the phase-space of particle distributions. We also observe elongated structures, such as the one highlighted in Fig. 5.14(a) by a curve of constant phase-space density. Since f_s is constant along particle orbits, this curve represents an instantaneous electron trajectory. We also found similar structures in the subcritical case described in section 5.3, as highlighted by a dashed red contour in Fig. 5.6(i). We refer to these structures as *jets* when they satisfy the three following characteristic properties:

P1. their anisotropy is much higher than that of holes,

P2. they connect low and high velocity regions, separated by $\Delta v_{\text{jet}} \sim v_{T,e}$,

P3. their lifetime τ_{jet} is of the same order or higher than the average time τ_{travel} it takes a particle to change its velocity by $v_{T,e}$.

Based on these properties, jets have the potential to cause significant particle transport, since they provide a fast track for particles to commute between low and high phase-space density regions. Reporting the formation, and discussing the role of jets are the objects of this section.

The formation process is due mainly to straining between two holes with different velocities. This is illustrated in Fig. 5.15, which shows snapshots of the electron distribution function in phase-space, cropped to a small window which follows the birth process. At $t \approx 1100$ [Fig. 5.15(a)], a blob of negative phase-space density perturbation is extracted from the low-velocity region, attracted by a large hole at higher velocity (not shown in this figure). Since the large hole is traveling faster, the blob does not have time to connect to it. It does however form a hole by itself at about $t \approx 1120$ [Fig. 5.15(b)], probably because its dimensions approximately satisfy the self-trapping condition [Dup82]. At $t \approx 1140$ [Fig. 5.15(c)], a second hole is extracted from the blob, and the bridge between the two holes becomes thiner and thiner. At $t \approx 1150$ [Fig. 5.15(d)], the two holes are drifting apart. The resulting straining of the bridge is at the heart of the jet formation process. At $t \approx 1150$ [Fig. 5.15(e)], the bridge has become a jet, satisfying properties P1 (anisotropic) and P2 (extending from $v = 0.3v_{T,e}$ to $v = 1.8v_{T,e}$). It is obvious that any slowly (adiabatically) moving hole forces the ambient passing particles to flow around the hole when the particles come to the separatrix. What is surprising, is that this process leads in this case to structures one order of magnitude longer (both in space and in velocity) than the holes.

We turn to analyzing whether such a structure satisfies property P3 (lifetime $\gtrsim$ travel time). Fig. 5.16 shows a series of snapshots of another typical phase-space jet, namely the one shown by a solid curve in Fig. 5.14(a). Again, properties P1 and P2 are satisfied.

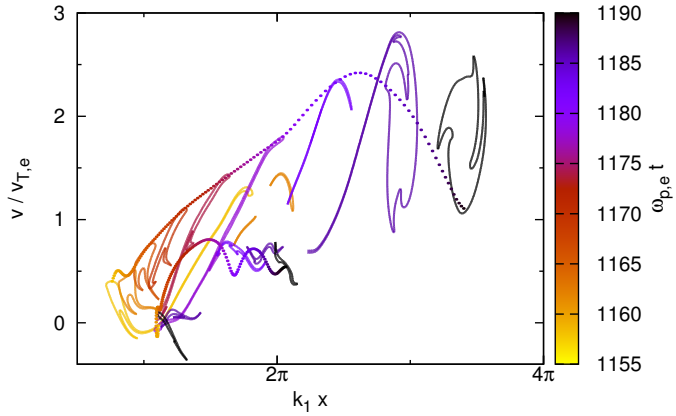

Figure 5.16 – Time-evolution of a jet. Solid: constant $f_e/f_{e,max} = 0.375$ contours. Dashed: orbits of two test particles. The mass ratio is $m_i/m_e = 4$.

From $t \approx 1160$, the jet grows by straining between a blob of negative phase-space density perturbation in the low-velocity region and a large hole at higher velocity. At $t \approx 1185$, the jet winds around the large hole. At $t \approx 1190$, the jet finally splits into several parts. More precisely, the jet becomes so thin at some locations that it cannot be resolved by the discretized grid in our simulation. In physical experiments, collisions fill the coarse-graining role of a discretized grid. From the jet's formation to its splitting, the jet's lifetime is $\tau_{\text{jet}} \approx 30$. Other jets have shorter (≈ 10) or longer (≈ 50) lifetimes. This is comparable to the average time it takes a particle to change its velocity by $v_{T,e}$, which can be estimated as $\tau_{\text{travel}} \sim v_{T,e}/(eE/m) \sim (k_1 v_{T,e} e\phi/T_e)^{-1} \sim 25$. Thus property P3 is also satisfied. For comparison, a typical hole trapping time is $\tau_{\text{tr}} = 2\pi/\omega_b \sim 50$, and a typical hole lifetime is $\tau_{\text{hole}} \sim 500$ or more (and the Kubo number is $K \sim 10$ or more). To summarize, the ordering of time scales is $\tau_{\text{jet}} \sim \tau_{\text{travel}} \sim \tau_{\text{tr}} \ll \tau_{\text{hole}}$.

Particles can ride a jet from low to high velocity, or in the opposite direction. Either collisions (here, small numerical collisions are present) or jet splitting make the process irreversible. This yields net velocity-space transport. Fig. 5.16 includes the orbits of two test particles, which are injected at $t = 1158$ on the contour of the jet. We estimate a mean free path in velocity space $\Delta v_{\text{m.f.p.}}$ as the average cumulative change of velocity of 600 such particles during the lifetime of the jet (from $t_1 = 1158$ to $t_2 = 1190$), i.e.

$$\Delta v_{\text{m.f.p.}} = \left\langle \int_{t_1}^{t_2} |\dot{v}_i(t)| \, \mathrm{d}t \right\rangle, \tag{5.9}$$

where $i = 1 \ldots 600$ is an index of test particles. This procedure yields $\Delta v_{\text{m.f.p.}}/v_{T,e} = 2.17$ for this one jet, which indicates that a jet can drive significant stochastic transport. The average non-cumulative change of velocity ($\Delta v_{\text{conv.}} = \langle v_i(t_2) - v_i(t_1) \rangle$) is $\Delta v_{\text{conv.}}/v_{T,e} = 0.48$ for this one jet, which indicates that a jet can also drive convective transport, albeit to a smaller extent. Other jets may convect particles in the opposite direction ($\Delta v_{\text{conv.}} < 0$). To summarize, the ordering of velocity extents is $|\Delta v_{\text{conv.}}| \lesssim \Delta v_{\text{hole}} \lesssim \Delta v_{\text{m.f.p.}} \sim \Delta v_{\text{jet}} \sim v_{T,e}$.

To quantify jet-driven transport, we split the distribution function into two parts, one containing mainly holes, the other one containing mainly jets. The hole part and jet part are shown in Fig. 5.14(b) and (c), respectively. The jet part is obtained by applying a filter in two-dimensional Fourier space (k_x, k_v), where the wave numbers satisfy $k_v/k_x > R$ and $k_v > k_h$. Here, R and k_h are thresholds, which are empirically adjusted to $R = 3$ and $v_{T,e} k_h = 5$. The remaining part ($k_v/k_x \leq R$ or $k_v \leq k_h$) is mainly composed of holes. We loosely refer to it as the hole part. We measure velocity-space transport of electron by the flux $\Gamma_v(v,t)$, where

$$\frac{\partial \langle f_e \rangle}{\partial t} + \frac{\partial \Gamma_v}{\partial v} = 0. \tag{5.10}$$

Fig. 5.17 shows the particle flux at $t = 1180$. Redistribution, or anomalous resistivity, is driven by a negative (positive) flux in the $v/v_{T,e} > 1$ (< 1) region. Our main observation is that the contributions of jet part and hole part are of the same order. Jets can either enhance or mitigate redistribution, depending on velocity and time. The oscillations in the hole-part and the jet-part for $v/v_{T,e} < 0$ and $v/v_{T,e} > 2.5$ are an artifact of velocity-space

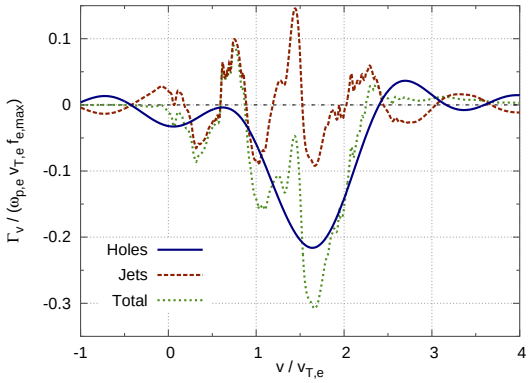

Figure 5.17 – Velocity-direction particle flux at $\omega_{p,e}t = 1180$ (mass ratio $m_i/m_e = 4$).

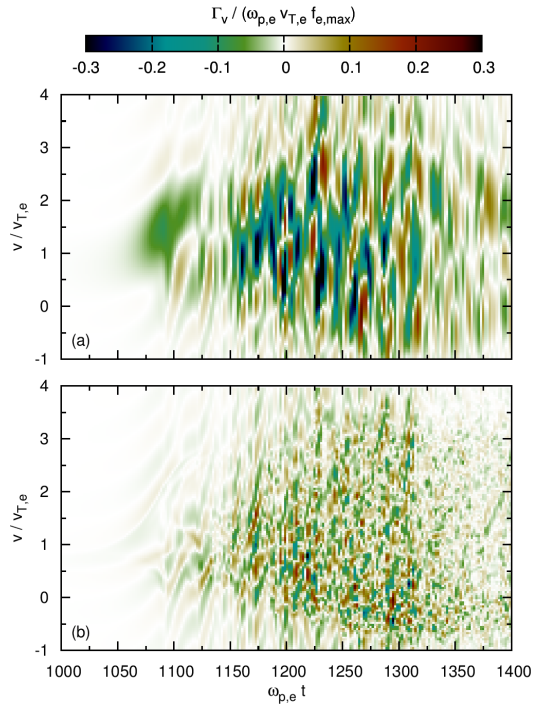

Figure 5.18 – Time-evolution of the particle flux (mass ratio $m_i/m_e = 4$). Contribution from (a) holes, (b) jets.

Fourier transformation. We observe that the hole-driven flux is mostly negative, while the jet-driven flux oscillates around zero. This reinforces the intuitive idea that jet transport is essentially stochastic, while hole transport is essentially convective.

Fig. 5.18 shows the time-evolution of hole-part and jet-part of the particle flux. This figure shows that the above observation is not a particular case for $t = 1180$. Jet-driven flux is of the same order as hole-driven flux (though slightly smaller) throughout the whole phase of electron redistribution. In the quasi-steady state ($t > 1700$), jets vanish. The electron phase-space is dominated by a single vortex, which results from the merging of the many structures seen in Fig. 5.14(a).

Globally, jets enhance anomalous resistivity, since they facilitate scattering in velocity-space. However, locally in velocity-time space, jets can mitigate anomalous resistivity. This is the case when holes form a negative gradient in the velocity distribution. As can be seen in Fig. 5.13(a), at $t = 1180$, the gradient is globally positive, but locally negative (around $v = v_{T,e}$ for example). Thus, flattening the distribution at this location means increasing the electron momentum, which mitigates anomalous resistivity. In an averaged-time viewpoint, though, jets enhance anomalous resistivity.

5.4.2 Large mass ratio

In this section, we repeat the above analysis with a mass ratio of $m_i/m_e = 1836$. The system size is $L = 2\pi/k_1$, where $k_1 = 0.05\lambda_D^{-1}$. The initial drift is $v_d = 80v_{T,i} \approx 1.87v_{T,e}$. The resolution is $N_x \times N_v = 2048 \times 4096$, and $\Delta t \leq 0.016\omega_{p,e}^{-1}$.

Fig. 5.19(a) shows snapshots of the velocity distribution before, during and after particle redistribution. As expected, ion redistribution is negligible. Fig. 5.19(b) shows the evolution, after the linear growth phase, of mean square potential, and anomalous resistivity.

Fig. 5.20(a) is a snapshot at $t = 2800$ of the perturbed electron distribution. The contour of a jet is overlapped. Because of the large mass ratio, the electrons are easily trapped, and the holes take up most of the electron distribution phase-space. As a consequence, the jets are completely wound around holes, which makes them more difficult to distinguish on a phase-space contour plot. However, our Fourier filter succeeds in extracting them. The hole

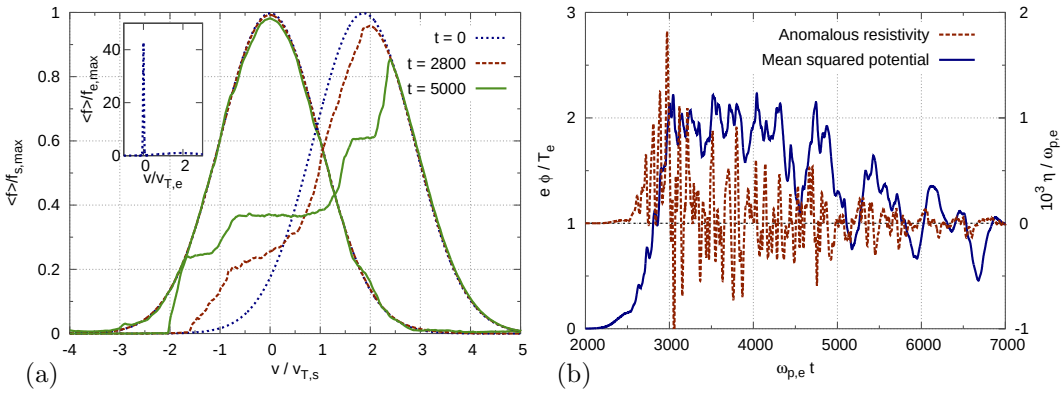

Figure 5.19 – CDIA simulation with mass ratio $m_i/m_e = 1836$ and system size $L = 40\pi\lambda_D$. (a) Snapshots of the ion (left) and electron (right) velocity distributions. Note that ion and electron distributions are not on a same scale. The inset shows them on a same scale. (b) Time-evolution of the mean square potential (left axis) and anomalous resistivity (right axis).

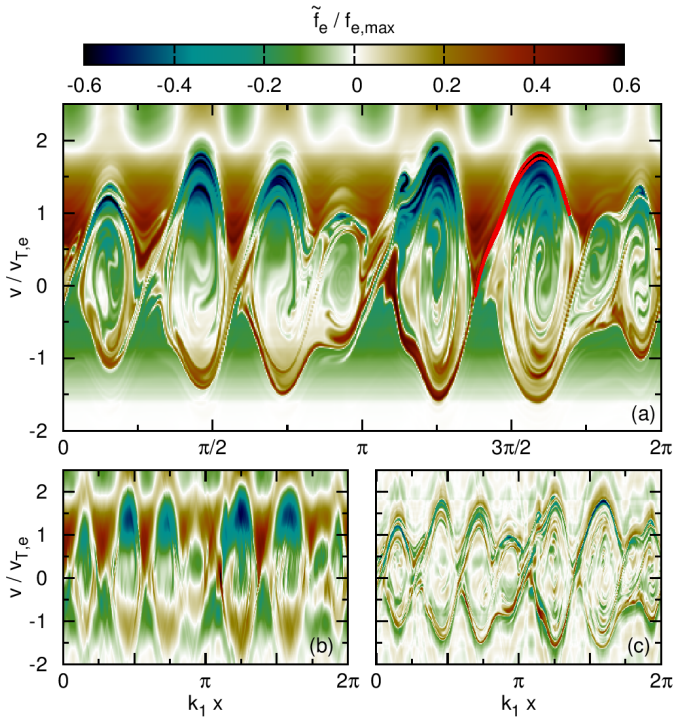

Figure 5.20 – (a) Snapshot at $\omega_{p,e}t = 2800$ of the perturbed electron distribution $\tilde{f}_e$, normalized to $f_{e,\max} = f_e(v_{0,e})$. Solid curve: contour of constant $f_e/f_{e,max} = 0.08$. (b) Low-pass filtered $\tilde{f}_{e,\text{holes}}$. (c) High-pass filtered $\tilde{f}_{e,\text{jets}}$. The mass ratio is $m_i/m_e = 1836$. The system size is $40\pi\lambda_D$.

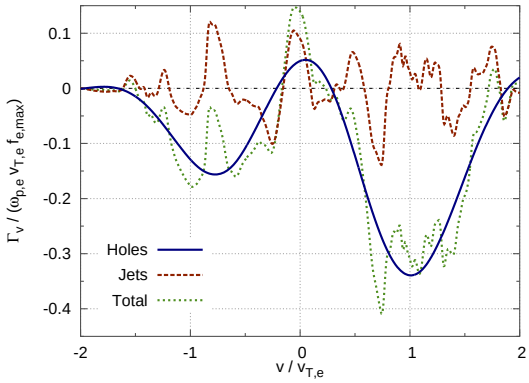

Figure 5.21 – Velocity-direction particle flux at $\omega_{p,e}t = 2800$ (mass ratio $m_i/m_e = 1836$).

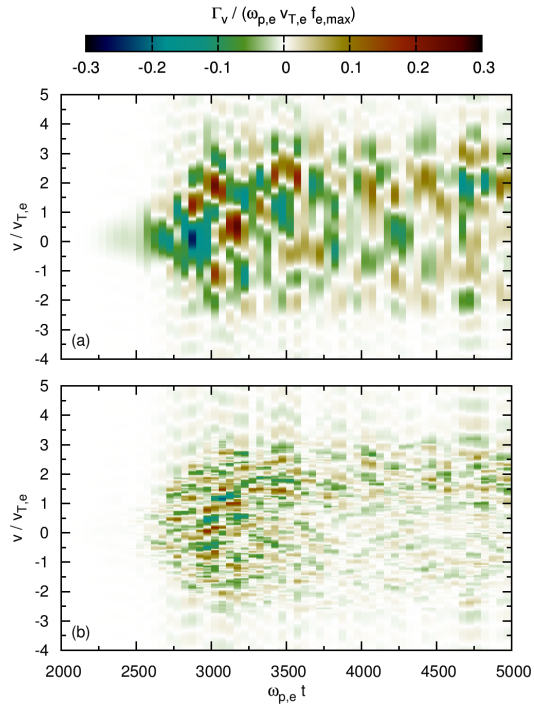

Figure 5.22 – Time-evolution of particle flux (mass ratio $m_i/m_e = 1836$). Contribution from (a) holes, (b) jets.

part and jet part are shown in Fig. 5.20(b) and (c), respectively.

Fig. 5.21 shows the particle flux at $t = 2800$, which roughly corresponds to the peak of electric field amplitude. Again, jet-driven flux is of the same order as hole-driven flux. Jets can either enhance or mitigate redistribution, depending on velocity and time. Hole-driven flux is mostly negative, while the jet-driven flux oscillates around zero.

Fig. 5.22 shows the time-evolution of hole-part and jet-part of the particle flux. This figure shows that the above observation is not a particular case for $t = 2800$. Jet-driven flux is of the same order as hole-driven flux (though slightly smaller) throughout the whole phase of electron redistribution.

5.4.3 Large system size

A caveat in the above analysis is that the system size is relatively small: comparable to the wavelength of the most unstable wave. For too small system size, quasilinear relaxation is effectively suppressed. Therefore a question remains: for larger systems, are phase-space jets still relevant or does quasilinear relaxation precede and preclude the formation of such structures? To address this issue, we have performed a series of simulations with increasing system sizes (and increasing number of grid points N_x).

Fig. 5.23 shows the time-evolution of electric field amplitude for system size $L = 2\pi/k_1$, where $\lambda_D k_1$ takes three different values, 0.2, 0.05, and 0.01. We observe that in all 3 cases, relaxation occurs on a similar timescale. Furthermore, the peak amplitude and the saturated amplitude are similar for 0.05 and 0.01. However, there is a significant difference between 0.2 and 0.05. We conclude that the large system size limit corresponds to $\lambda_D k_1 < 0.05$.

We have repeated the analysis of Section 5.4.1, for $k_1 = 0.01\lambda_D^{-1}$, with $N_x \times N_v = 8192 \times 2048$ grid points. We have found qualitatively similar conclusions: phase-space jets are present, and account for roughly half of the total particle flux. Fig. 5.24 is a snapshot at $t = 800$ of the perturbed electron distribution. We observe that jets have spatial scales of the order of 10 Debye lengths. Comparison with figures 5.14, 5.20, 5.26 and 5.28, suggests that this is true regardless of the mass ratio, system size or whether the system is driven or decaying.

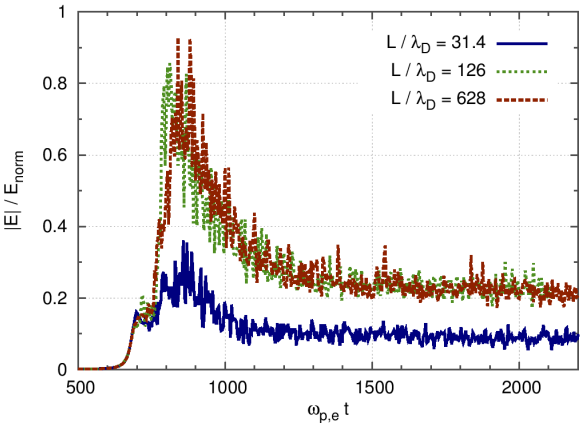

Figure 5.23 – Time-evolution of electric field amplitude, normalized by $E_{\text{norm}} = m_e v_{T,e} \omega_{p,e}/e$ for different system sizes, which are indicated in the legend. Mass ratio is $m_i/m_e = 4$. Initial drift is $v_d = 2.1 v_{T,e}$.

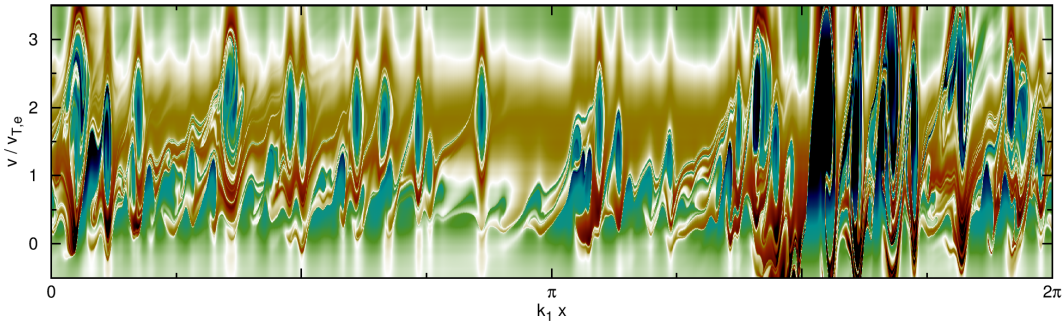

Figure 5.24 – Snapshot at $\omega_{p,e}t = 800$ of the perturbed electron distribution $\tilde{f}_e$, normalized to $f_{e,\max} = f_e(v_{0,e})$. The system size is $200\pi\lambda_D$.

5.4.4 Driven system

An other caveat in the above analysis is that we have studied an initial value problem. An other question remains: are phase-space jets (and holes) still relevant when an external drive supplies free energy continuously? To address this issue, we have studied an other set of simulations, where the initial velocity drift between ion and electron is zero ($v_d = 0$), and the system is driven by a constant and uniform external electric field E_{ext}.

Fig. 5.25 shows the time-evolution of mean square potential and anomalous resistivity in a system driven by an external electric field $E_{\text{ext}} = 10^{-4} E_{\text{norm}}$, where $E_{\text{norm}} = m_e v_{T,e} \omega_{p,e}/e$. We observe that the peak amplitude, peak anomalous resistivity, and timescale of relaxation are comparable to the case with initial drift and no drive. Further in time, as the constant electric field continues to provide free energy in the form of a current, more relaxation events occur, such as for $\omega_{p,e}t \approx 10500$. We repeat our analysis of phase-space structures and their

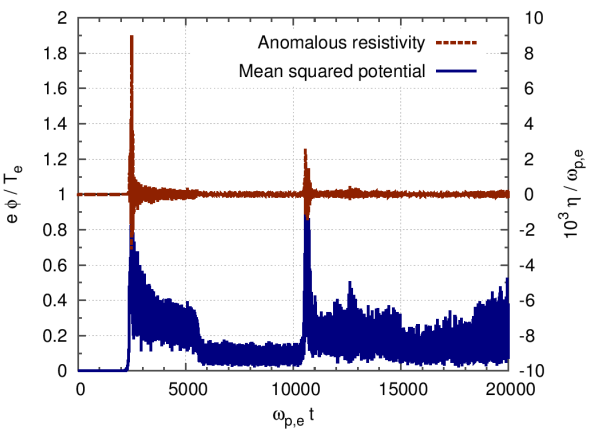

Figure 5.25 – Time-evolution of the mean square potential (left axis) and anomalous resistivity (right axis), in a system driven by an external electric field. The mass ratio is $m_i/m_e = 4$.

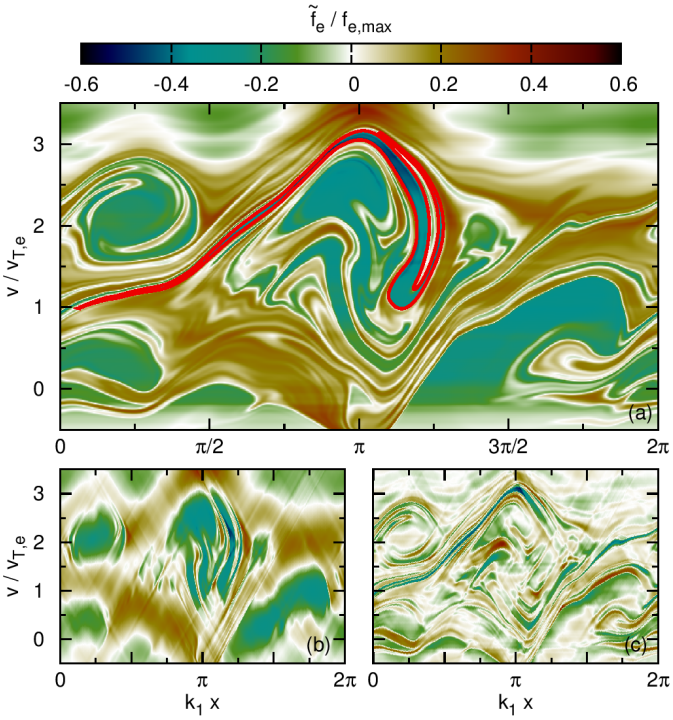

Figure 5.26 – (a) Snapshot at $\omega_{p,e}t = 2480$ of the perturbed electron distribution $\tilde{f}_e$, normalized to $f_{e,\max} = f_e(v_{0,e})$, for a driven system. Solid curve: contour of constant $f_e/f_{e,max} = 0.5$. (b) Low-pass filtered $\tilde{f}_{e,\text{holes}}$. (c) High-pass filtered $\tilde{f}_{e,\text{jets}}$. The mass ratio is $m_i/m_e = 4$.

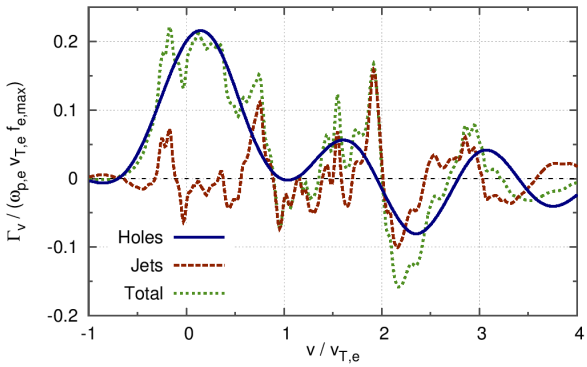

Figure 5.27 – Velocity-direction particle flux at $\omega_{p,e}t = 2480$ (mass ratio $m_i/m_e = 4$, driven system).

impact on particle flux for the first and the second relaxation events, which appears to be the largest one, and which occur at $\omega_{p,e}t \approx 2480$ and 10560, respectively.

Let us repeat our analysis of phase-space structures and their impact on particle flux for this driven case. Fig. 5.26(a) is a snapshot of the perturbed electron distribution at $\omega_{p,e}t = 2480$, which roughly corresponds to the peak of electric field amplitude. The contour of a jet is overlapped. The hole part and jet part are shown in Fig. 5.26(b) and (c), respectively. Fig. 5.27 shows the particle flux at $\omega_{p,e}t = 2480$. Similar figures, Fig. 5.28 and Fig. 5.29, are provided for the second redistribution event at $\omega_{p,e}t = 10560$. Again, for both relaxation events, jet-driven flux is of the same order as hole-driven flux.

We measure the dominant mode frequency as $\omega_{IA} = 0.123\omega_{p,e}$. Therefore, the second peak corresponds to $\omega_{IA}t = 1295$. On longer timescales, the jets are not expected to play any significant role, except during transient redistribution bursts. Fig. 5.30 is a snapshot of the perturbed electron distribution at $\omega_{p,e}t = 20000$ ($\omega_{IA}t = 2450$), which corresponds to a quiescent period between bursts. We observe that the jets are absent except for faint remnants. The phase-space dynamics is dominated by holes, which are much more robust. However, the anomalous resistivity during these quiescent periods is negligible (compared to during bursts), so this does not undermines out conclusion that jets contribute to about half of anomalous resistivity.

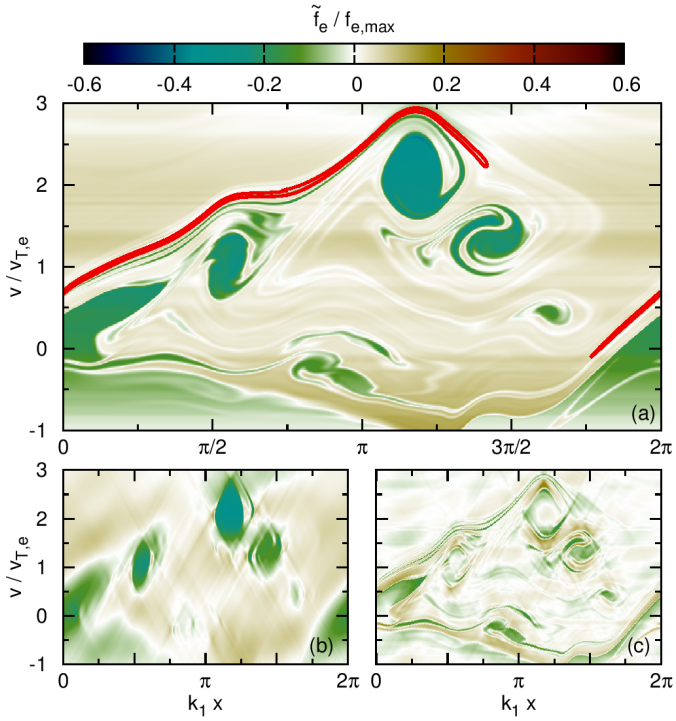

Figure 5.28 – Snapshot at $\omega_{p,e}t = 10560$ of the perturbed electron distribution $\tilde{f}_e$, normalized to $f_{e,\max} = f_e(v_{0,e})$, for a driven system. The mass ratio is $m_i/m_e = 4$.

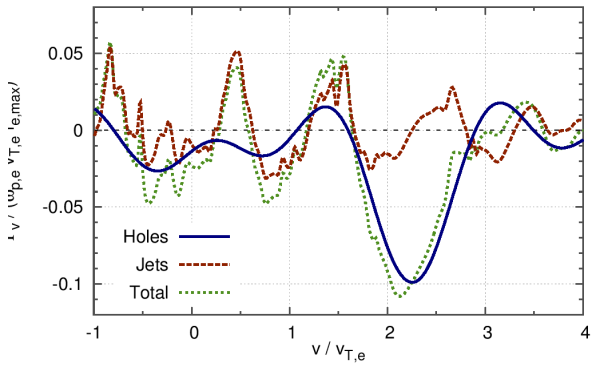

Figure 5.29 – Velocity-direction particle flux at $\omega_{p,e}t = 10560$ (mass ratio $m_i/m_e = 4$, driven system).

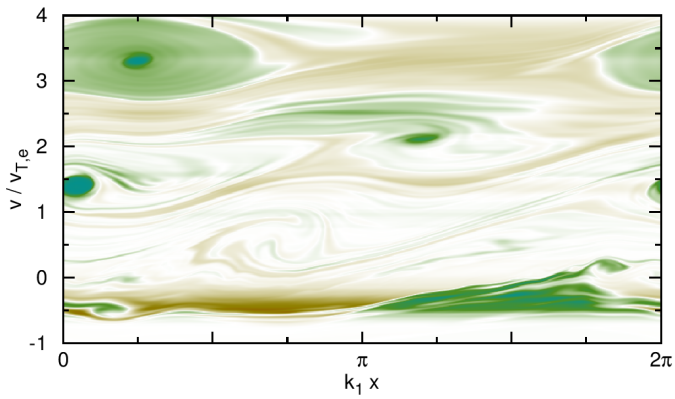

Figure 5.30 – Snapshot at $\omega_{p,e}t = 20000$ of the perturbed electron distribution $\tilde{f}_e$, normalized to $f_{e,\max} = f_e(v_{0,e})$, for a driven system.

5.4.5 Conclusion

In summary, velocity-space redistribution and anomalous resistivity are due to phase-space turbulence, which includes not only holes, but also phase-space jets. The latter are highly anisotropic structures, with an extent in velocity of the order of the electron thermal velocity. Compared to phase-space holes, which are very robust structures, jets are relatively transient objects. However, we showed that jets survive long enough for particles to scatter between low and high phase-space density regions, and drive significant particle redistribution. Jets and holes are associated with fundamentally different transport processes. Hole-driven transport is essentially convective, since trapped particles accelerate along with the hole. Jet-driven transport is essentially stochastic, since particles may accelerate or decelerate along the jet. These conclusions stand for both initial value and driven systems. When the mass ratio is high, ion relaxation is negligible, and jets are completely wound around holes. Since jets emerge from holes, jets are expected to play an important role in the $K \gg 1$ (strong wave-particle interactions) regime, or in other words, when the collision mean-free-path is much larger than the wavelengths of unstable modes.

Although we treated in this work the example of the ion-acoustic wave in 1D plasma with $T_i = T_e$, we have carried additional simulations with other parameters, other models, and other waves. Based on these, we expect qualitatively similar conclusions for many regimes of strong wave-particle interactions in dissipative collisionless or quasi-collisionless plasmas.

Chapter 6

Trapped-particle-driven 2D turbulence

In this chapter, we focus on turbulence in the core of axi-symmetric tokamaks. Let us focus on electrostatic turbulence, which makes numerical and analytical investigations much more tractable than with electromagnetic fluctuations, and is relevant for strongly magnetized tokamaks.

Unlike the problems treated in chapters 4 and 5, this kind of turbulence is not unidimensional. Though, strictly speaking, these fluctuations are inherently 3D, measurements and modeling both show that their typical parallel wavenumber is much smaller than their perpendicular one, $k_\parallel \ll k_\perp$ (parallel and perpendicular refer to the local direction of the equilibrium magnetic field). Therefore, depending on the problem at hand, it can be reasonable to neglect 3D effects and model this turbulence locally in 2D, in the radial and poloidal directions [Ken08]. Indeed, to the lowest order, the fluctuations induce an $\boldsymbol{E} \times \boldsymbol{B}$ drift, and thus vorticity in the local perpendicular plane.

A second important difference with the two previous chapters, where equilibrium density and temperature were constants, is the essential role of inhomogeneities of plasma profiles. In the presence of a radial pressure gradient, a phase shift between pressure and electric field fluctuations can drive instabilities called as drift-waves. Turbulence then develops by nonlinear self-advection of the $\boldsymbol{E} \times \boldsymbol{B}$ flow and coupling between modes. Drift-wave turbulence efficiently transports particles and heat radially.

Observed dominant fluctuations cover a wide range of scales, from the electron gyroradius to a few ion gyroradii, in terms of perpendicular wavelength. These fluctuations are considered microscopic, and altogether form electrostatic micro-turbulence. Density fluctuations are of the order of one to a few percents in the core of tokamaks.

The equilibrium magnetic field is inhomogeneous as well. Magnetic field lines are curved, and the amplitude of the field weakens toward the outside of the torus. As a consequence, an important fraction of the charged particles are trapped by the inhomogeneity of the equilibrium magnetic field [1]. Fig. 6.1 shows the equilibrium motion of a typical magnetically-trapped particle. It is a combination of three quasi-periodic motions, over three different timescales: the fast cyclotron motion (not represented in the figure), a bounce motion in the poloidal direction drawing a banana shaped figure, and a slow precession in the toroidal direction.

Pressure-gradient-driven drift-waves include Ion-Temperature-Gradient (ITG) or Electron-Temperature-Gradient (ETG), as well as collisionless trapped-particle-modes [KP71], which are excited by resonances with the precession of trapped particles. Trapped-particle-modes are further categorized as Trapped-Ion-Modes (TIM) or Trapped-Electron-Modes (TEM), depending on whether they are excited by trapped ions or trapped electrons. In modern tokamaks, radial transport is typically dominated by coupled ITG/TEM turbulence.

1. The physics of magnetic trapping is unrelated to the physics of electrostatic trapping, which is at the origin of PS vortices. Magnetic trapping is an effect of the equilibrium field on equilibrium particle motion; while electrostatic trapping of particles is a nonlinear effect of the fluctuations on the perturbed particle motion.

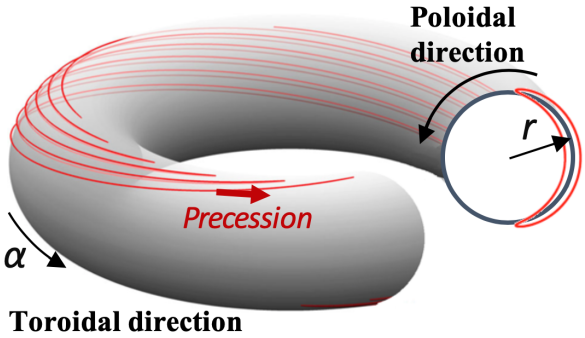

Figure 6.1 – Trajectory of a particle trapped by an inhomogenous magnetic field in a torus, and (rhs) projection on a poloidal cross-section.

In the gyrokinetic model, the fast cyclotron motion around the equilibrium magnetic field is averaged out. This procedure reduces the dimensionality: the dynamics is then described in a 4D phase-space, parametrized by one adiabatic invariant. The dimensionality of the problem is thus 5D. For the kinetic description of magnetically trapped particles, dimensionality can be reduced further by averaging out, not only the cyclotron motion, but the poloidal bounce-motion as well. The bounce-averaged (implicitly, gyro-averaged as well) dynamics can be described in a reduced 2D phase-space, parameterized by the energy and the pitch-angle [GD90, FH99]. The dimensionality of the problem is thus reduced to 4D. Finally, for particles which are most deeply trapped by the magnetic field inhomogeneity have, the pitch-angle takes a single value ($\pi/2$). The bounce-averaged dynamics of deeply trapped particles can then be described in a 2D phase-space (the precession angle α, and an action ψ which plays the role of a radial coordinate), parametrized by the energy invariant E. The dimensionality of the problem is thus reduced to 3D.

The main point of our approach is to focusing on a paradigmatic problem of interactions between trapped particles and TIM or TEM (or both) turbulence, taking advantage of this reduced dimensionality. This is much more tractable than the conventional gyrokinetic modeling of coupled ITG and TEM (and ETG possibly) turbulence. It can be described as halfway between a reduced model and a first-principle model. Although this reduced approach precludes direct quantitative applicability to tokamaks, we can use it as a prototype of wave-particle resonance-driven inhomogeneous plasma turbulence to explore general trends and clarify the mechanisms underlying the already complex nonlinear dynamics.

We adopt a self-consistent bounce-averaged gyrokinetic model for trapped particle precession resonance-driven turbulence, which was developed by Depret [DGBG00], Sarazin [SGF+05] and Darmet [DGS+08], based on the Tagger-Pellat-Diamond-Biglari model [TLP77, BDT88a]. This reduced model relies on the following assumptions:

— The frequencies of the dominant modes are much lower than the bounce frequencies of trapped particles for all species..
— The equilibrium configuration is that of a large aspect ratio tokamak.
— The plasma is strongly magnetized, so that trapped ion precession resonance-driven modes are mostly electrostatic.

In section 6.1, we describe the bounce-averaged gyrokinetic model, discuss the above assumptions, introduce the numerical simulation code TERESA, and describe our recent contributions to its development. In section 6.2, we develop the linear theory of this model, and investigate the impacts of electron dissipation on frequency, growth rate, and the energy-structure of the linear modes. In section 6.3, we investigate the impact of sub-resolution of the resonance in the energy space on the field amplitude in a simulation with a single mode. Finally, in section 6.4, we summarize our contribution to topics of turbulent transport: impacts of electron dissipation, the energy-space structure of transport, statistics of test particle trajectories, control of zonal flow by heating, and trapped impurity transport.

6.1 Model

6.1.1 Bounce-averaged gyrokinetics

The equilibrium motion for each species s in a tokamak can be described by three action-angle couples [Kau72]:

1. A first couple corresponds to gyration. The angle α_1 is the gyrophase, and the corresponding action is $J_1 = -m_s\mu/q_s$, where μ is the magnetic moment. The frequency is the cyclotron frequency $\omega_{c,s}$.
2. A second couple corresponds to the poloidal motion. The angle α_2 is roughly the poloidal angle for passing particles, and describes the bounce (banana) motion for trapped particles (this is analogous to a simple pendulum). The corresponding action can be approximated as $J_2 = (2\pi)^{-1} \oint m_s v_{G\|} \mathrm{d}s + \delta_{\text{pass.}} q_s \psi_T$, where $v_{G\|}$ is the parallel velocity of the guiding-center, s is an arc length along the magnetic field line, $\delta_{\text{pass.}}$ is 1 for passing particles, 0 for trapped particles, and ψ_T is the toroidal flux. The frequency is the mean poloidal frequency for passing particles, and the bounce frequency $\omega_{b,s}$ for trapped particles.
3. A third couple corresponds to the toroidal motion. The angle α_3 is roughly the toroidal angle for passing particles, and the bounce-averaged toroidal angle for trapped particles. The corresponding action is the canonical toroidal angular momentum $J_3 = P_\varphi$. For trapped particles, J_3 can be approximated as $J_3 = q_s\psi$, where ψ is the poloidal magnetic flux at the cusps of the bounce motion. The frequency is the mean toroidal frequency for passing particles, and the toroidal precession frequency $\omega_{d,s}$ for trapped particles.

We aim at modeling low-frequency (toroidal precession time-scale, $\omega \sim \omega_d \ll \omega_b \ll \omega_c$) turbulence in the core of a tokamak plasma of major radius R_0, composed of electrons, deuterium, and possibly impurities. In bounce-averaged gyrokinetics [GD90, FH99], the dynamics of trapped particles is described in the phase-space of toroidal precession angle $\alpha \equiv \alpha_3$ and toroidal angular momentum $J_3 = q_s\psi$, which plays the role of radial coordinate. The Hamiltonian for each particle is defined up to a constant. In this manuscript we choose

$$H \;=\; (1 + e\Omega_d\psi)E \;+\; q_s J_{0,s}\phi, \tag{6.1}$$

where e is the elementary charge, $\Omega_d = (eR_0^2 B_\theta)^{-1}$, B_θ is the poloidal magnetic field, E is the equilibrium energy, and $J_{0,s}(E)$ is an operator which performs two successive averages: a gyro-average (on a cyclotron motion), and a bounce-average (on a banana orbit).

The bounce-averaged gyrokinetic distribution f_s of trapped particles (or 'banana centers') satisfies a kinetic equation for each species s,

$$\frac{\partial f_s}{\partial t} \;+ [J_{0,s}\phi,\, f_s]_{\alpha,\psi} \;+ \omega_{d,s}\frac{\partial f_s}{\partial \alpha} \;=\; 0. \tag{6.2}$$

Here, $\omega_{d,s} = E\Omega_d/Z_s$ is the energy-dependent precession frequency, and Z_s is the charge number of species s. The radial dependencies are neglected in this operator.

Self-consistency is ensured by a quasi-neutrality constraint, including a polarization term $\bar{\Delta}_s\phi$, which involves a non-isotropic Laplacian operator,

$$\bar{\Delta}_s \;\equiv\; \left(\frac{q_0\rho_{c,s}}{L_\psi}\right)^2 \frac{\partial^2}{\partial\alpha^2} \;+\; \delta_{b,s}^2 \frac{\partial^2}{\partial\psi^2}. \tag{6.3}$$

Here, L_ψ is the radial length of the simulation domain, $\rho_{c,s}$ is the Larmor radius, and $\delta_{b,s}$ is the banana width, all in units of ψ, and q_0 is a typical value of safety factor.

The quasi-neutrality equation reads

$$\sum_s \frac{eZ_s^2 n_{eq,s}}{T_{eq,s}} \left[\frac{1-f_t}{f_t}\left(\phi - \epsilon_{\phi,s}\langle\phi\rangle\right) - \bar{\Delta}_s\phi\right] \;= 4\pi\sqrt{2}\sum_s \frac{Z_s}{m_s^{3/2}} \int_0^\infty J_{0,s} f_s E^{1/2} \mathrm{d}E, \tag{6.4}$$

where f_t is the fraction of trapped particles. The average $\langle\phi\rangle$ is an average on the angle α.

In this reduced model, passing particles are treated quasi-adiabatically. The free parameters $\epsilon_{\phi,s}$ controls the response of passing particles to electric perturbations. Typically, we impose $\epsilon_{\phi,e} = 1$ for passing electrons, consistently with their lack of response to the zonal potential in the limit of electron gyroradius much smaller than the characteristic radial variation of zonal flows [GIVW10]. For passing deuterium and impurities, which do respond to zonal flows, we impose $\epsilon_{\phi,s} = 0$.

This reduced model relies on the following assumptions:

— The mode frequency is much lower than the bounce frequencies of trapped particles for all species s, such as electrons ($s = e$) and deuterium ($s = D$). However, we note that this assumption breaks down for heavy impurities since their bounce frequency decreases with the square root of their mass number. Therefore, the results we describe in subsection 6.4.5 for tungsten can only be taken as qualitative trends, representative of cases with lower-mass impurities (and/or larger system sizes since $\omega/\omega_{b,s}$ is proportional to ρ^*).

— The equilibrium configuration is that of a large aspect ratio tokamak. However, the inverse aspect ratio ϵ must not be so small that the fraction $f_p \sim \sqrt{\epsilon}$ of trapped particles is negligible.

— Resonant interactions are dominated by strongly trapped particles. In this case we can focus on a single value of the pitch-angle.

— The mode frequency is much lower than the passing particles transit frequency.

— The plasma is at low-β, for which trapped particles precession resonance-driven modes are mostly electrostatic.

6.1.2 The TERESA code

A semi-Lagrangian simulation code, TERESA, has been developed based on the bounce-averaged gyrokinetic model, making efficient use of parallel computing [CMGGL13, CMGS$^+$14, DGR$^+$14]. The 3 dimensions of distribution functions are discretized, with numbers of grid points denoted as N_α, N_ψ and N_E. A range of energies from 0 to $20T_s$ is typically required for convergence. The energy grid is finer close to $E = 0$ and coarser for higher E allowing greater precision for low E (In fact the grid is uniform in $\sqrt{E}$).

Boundary conditions

In this manuscript, unless stated otherwise, TERESA simulations are performed with thermal baths at both outside boundary $\psi = 0$ and inside boundary $\psi = L_\psi$, and without any source nor sink. Note that in our model, ψ is not the conventional poloidal magnetic flux which is roughly proportional to $-r^2$, but a shifted version of it, such that the magnetic axis $r = 0$ corresponds to $\psi = L_\psi$, and the outer radial boundary corresponds to $\psi = 0$. Artificial dissipation is imposed in buffer regions $\psi < 0.15\, L_\psi$ and $\psi > 0.85\, L_\psi$ to smooth out the transition between turbulent fluctuations ϕ, and the constraint $\phi = 0$ at $\psi = 0$ and $\psi = L_\psi$.

Equilibrium distribution

The equilibrium distribution functions are chosen as

$$f_{\mathrm{eq},s}(\psi, E) \;=\; \frac{n_{\mathrm{eq},s}}{(2\pi T_{\mathrm{eq},s}/m_s)^{3/2}} \exp\left(-\frac{E}{T_{\mathrm{eq},s}}\right). \tag{6.5}$$

This is an approximation of a 2D Maxwellian where the radial dependency of the equilibrium Hamiltonian is neglected. This implies that curvature pinch is neglected, and that global effects due to the radial dependency of the precession frequency are neglected. This can be useful to discriminate thermo-diffusion from curvature pinch.

The initial radial density and temperature profiles for $0.2 < \psi/L_\psi < 0.8$ are linear in ψ,

$$n_{\mathrm{eq},s}(\psi) \;=\; n_{0,s}\left(1 + \kappa_{n,s}\,\frac{\psi}{L_\psi}\right), \tag{6.6}$$

$$T_{\mathrm{eq},s}(\psi) \;=\; T_{0,s}\left(1+\kappa_{T,s}\,\frac{\psi}{L_\psi}\right), \tag{6.7}$$

where the equilibrium densities at $\psi = 0$, $n_{0,s}$, are such that $\sum_s Z_s n_{0,s} = 0$, and where $\kappa_{n,s}$ and $\kappa_{T,s}$ are input parameters, which measure the equilibrium radial gradients in terms of ψ (therefore, positive $\kappa_{n,T}$ correspond to typical negative gradients in r). For $\psi/L_\psi < 0.2$ or > 0.8, the equilibrium gradients are gradually diminished toward zero at the boundaries $\psi = 0$ and $\psi = L_\psi$. This is done to avoid instabilities at these boundaries, consistently with our boundary condition $\phi = 0$.

The density and temperature ratios between species are noted as $C_s = n_{0,s}/n_{0,e}$, and $\tau_s = T_{0,i}/T_{0,s}$.

Note that in section 6.2, we adopt a first-order Taylor expansion in ψ of Eq. (6.5), as in Refs. [DGBG00, DGR$^+$14, DGR$^+$15, LCMD$^+$17],

$$f_{\mathrm{eq,s}}(\psi, E) \;=\; [1+(\kappa_{T,s}(E-3/2)+\kappa_{n,s})\psi]\exp\left(-\frac{E}{T_{0,s}}\right). \tag{6.8}$$

6.1.3 Recent developments

Let me summarize my main contributions to the recent developments of the TERESA code.

Normalization

In the code, the variables were normalized assuming that density and temperature profiles are homothetic. In 2019 I modified the normalization to extend the validity to non-homothetic profiles.

Curvature pinch

The equilibrium distributions given in Eq. (6.5) and Eq. (6.8) artificially disable curvature pinch. We recently implemented the possibility of equilibrium distribution function

$$f_{\mathrm{eq},s}(\psi, E) \;=\; \frac{n_{\mathrm{eq},s}}{(2\pi T_{\mathrm{eq},s}/m_s)^{3/2}}\,\exp\left(-\frac{H_{\mathrm{eq}}}{T_{\mathrm{eq},s}}\right), \tag{6.9}$$

which is a 2D Maxwellian taking into account the radial dependency of the equilibrium Hamiltonian, thus recovering curvature pinch.

Linear version

I developed a linear version of the TERESA code, which I verified in two ways: 1. against numerical solutions of the analytic dispersion relation, which was obtained in the limit of vanishing gradients, and 2. against single-mode simulations with the nonlinear version of TERESA.

Quasi-adiabatic response

To simplify analytic calculations, one may focus on TIMs, assume that electrons respond quasi-adiabatically to perturbations, and reserve the kinetic treatment to one species of ions only. In this context, electron dissipation is an essential ingredient: it destabilizes a range of modes, often called as electron roots, which propagate in the electron diamagnetic direction [KP71], and it drives radial particle transport. Therefore, we applied an electron dissipation model to the TERESA code.

To be consistent with the idea of a minimum model, we model electron dissipation as a simple nonadiabatic modification of the Boltzmann response [Man77, KP71, TRC86, Jar89]. It is expressed as a phase-shift between electron density and perturbed electric potential, $\hat{n_e}/n_0 = (1+\imath n\delta)e\hat{\phi}/T_e$ (in Fourier space), where n is the mode number in precession angle, and δ is an input, constant parameter.

In the literature, several ways have been adopted to model electron dissipation:

1. solving a kinetic equations for trapped electrons as well, and include a collision operator,
2. constant phase-shift implemented by a term of the form $\imath\delta$ in Poisson equation,
3. an *ad hoc* model with an arbitrary cut-off for high mode numbers [CD92].

Our choice corresponds to the approach number 2. In Eq. (6.4), we make the substitution

$$\phi - \epsilon_{\phi,s}\langle\phi\rangle \qquad \rightarrow \qquad \phi - \epsilon_{\phi,s}\langle\phi\rangle + \mathcal{F}^{-1}(\imath\delta_n\hat{\phi}_n) \tag{6.10}$$

where $\mathcal{F}^{-1}$ is the inverse Fourier transform operator, and $\hat{\phi}_n$ is the n-th component of the Fourier decomposition in α of ϕ. Electron dissipation is modeled by a phase-shift between ϕ and density perturbation, $\delta_n \equiv n\delta$, where δ is a constant, real, input parameter. This approximation stems from the linearized drift-kinetic equation for electrons. Here we have assumed $\nu_{e,i}/\epsilon_0 < \omega \sim \omega_* < \nu_{i,i}/\epsilon_0$, where ω_* is a diamagnetic drift frequency, and $\nu_{e,i}$ and $\nu_{i,i}$ are ion-electron and ion-ion collision frequencies. In this regime, δ can be approximated as $\delta \approx \epsilon_0^{3/2}\omega_{*e}\eta_e/\nu_{ei}$, where $\eta_e = d\ln T_e/d\ln n_e$ is the ratio between gradients in equilibrium electron density and temperature profiles.

The advantages of method 2 are a. decreased computation cost, b. analytical tractability, and c. consistency with the idea of a minimalist kinetic model with necessary ingredients only. A strong analogy can be made between the phase-shift δ in trapped-ion turbulence and the wave dissipation rate γ_d in the Berk-Breizman model [DKL15]. Both are minimalist models for investigating fundamental physical mechanisms introduced by dissipation in resonance-driven instabilities.

We have implemented the $\imath\delta_n$ term in the TERESA code, and verified our implementation in Ref. [LCMD$^+$17]. As a first verification, we confirmed the expected relationship between density and potential perturbations during the linear phase for unstable modes. As further verification, we showed that the simulations quantitatively recover solutions of the linear dispersion relation. Note that in the latter reference, we derived an analytic, explicit expression for the linear frequency and growth rate of the ion root ($\mathrm{Re}(\omega) > 0$), including the dissipation term, in the limit of small growth rate $\gamma/\omega \ll 1$.

Impacts of electron dissipation on the linear properties of TIM are described in subsection 6.2.1, and impacts on TIM turbulence and transport are described in subsection 6.4.1.

One must keep in mind the limitations of this simple electron dissipation model. As was pointed out by Crotinger and Dupree, the $\imath\delta$ approximation misses the effect of spectral broadening in regimes of strong turbulence, and does not give the correct response to a coherent structure [CD92]. Therefore, in the long term, numerical studies of granulation will require more advanced models.

Test particles

Although TERESA solves the distribution function f and the electric potential ϕ, it does not yield individual particle trajectories. Particle, momentum and energy fluxes can be obtained from f and ϕ, but discriminating the various transport processes (e.g. diffusion, advection, trapping, ballistic, super-diffusion, sub-diffusion) typically requires convoluted methods such as dedicated dynamical synthetic experiments (otherwise, a simple flux-gradient plot often yields an indecipherable cloud of points). Using statistics on particle trajectories, the analysis can be done locally in space, within a short timespan, and without ambiguity.

Test particles are particles advected by the electrostatic field, but which do not affect it. They can thus be used as markers in the turbulent plasma, representing exactly the motion of a single particle belonging to f. In 2018, we developed, parallelized, integrated and verified a test particle module. The test particle trajectories are computed directly in the TERESA code, thus allowing the same order of accuracy as the solving of f and ϕ. This was an important task in the research program of my first PhD student, Julien Médina.

Each test particle follows the Vlasov characteristics in phase-space,

$$\dot{\alpha} = \frac{E\Omega_d}{Z_s} + \frac{\partial(J_0\phi)}{\partial\psi}, \tag{6.11}$$

$$\dot{\psi} = -\frac{\partial(J_0\phi)}{\partial\alpha}. \tag{6.12}$$

These equations are solved using Runge-Kutta 4 algorithm. We verified the accuracy of the trajectory solver, using an analytic electric potential. With the self-consistent potential, we confirmed the balance of individual particle energy,

$$\left.\frac{\mathrm{d}H}{\mathrm{d}t}\right|_{\text{traj.}} = \frac{\partial H}{\partial t} + \frac{\partial H}{\partial \alpha}\frac{\mathrm{d}\alpha}{\mathrm{d}t} + \frac{\partial H}{\partial \psi}\frac{\mathrm{d}\psi}{\mathrm{d}t} = \frac{\partial H}{\partial t}. \tag{6.13}$$

In subsection 6.4.3 we exploit this new module using one million test particles on each energy grid point ($\sim 10^8$ test particles in total), in a turbulent simulation, to gain insight on the properties of transport phenomena.

6.1.4 Caveats

As mentionned in the introduction, the bounce-averaged gyrokinetic model is not to be readily applied to the quantitative interpretation or prediction of modern tokamak experiments, which couple the electromagnetic dynamics of both trapped and passing particles, both ions and electrons, including supra-thermal particles (EPs). However, it can be used to perform numerical analysis of resonance-driven drift-wave turbulence, as an isolated building block of a complex system of coupled blocks (for the purpose of improved understanding), with a great accuracy in all variables (including energy), at reasonable computing cost. It can provides some basis on the way to numerical investigation of nonlinear phenomena that involve strong wave-particle resonances and require a high accuracy in velocity-space.

6.2 Linear instabilities

6.2.1 Impact of electron dissipation

In this part, we analyze the frequency and growth rate of both ion and electron roots of TIM in the presence of electron dissipation, as well as the linear structure in energy space.

We can summarize the results as follows. In the limit of zero equilibrium density gradient, the growth rate decreases monotonously with δ. On the other hand, it peaks at $\delta \approx 0.02$ when the density gradient is comparable to the temperature gradient. When the density gradient exceeds the temperature gradient, the most unstable mode propagates in the electron diamagnetic direction for $\delta < 0.02$. The results are in qualitative agreement with analytic theories of trapped-ion modes in the literature [KP71, TLP77].

For a phase-shift $\delta_n = 0.02n$ between the n-th toroidal component of electron density and electric potential perturbations, a strong peak is found at the resonant energy, with a narrow width at half maximum $\Delta E = 0.2\,T_0$. This linear energy-space structure is stronger with increasing electron dissipation. Accurately resolving this narrow peak in numerical simulation of the initial-value problem, yields a stringent lower bound on the number of grid points in the energy space. A 10% (1%) accuracy requires 256 (1024) grid points in the energy direction, which is significantly higher than typical number of grid points in e.g. parallel velocity in conventional gyrokinetic simulations.

Dispersion relation

We treat only hydrogen ions kinetically, therefore we drop the species subscript when it is not ambiguous. Electrons are a neutralizing background, and their dissipation is taken into account via the ansatz Eq. (6.10). We neglect the radial dependency of Ω_d. For concision, we work with normalized units. In particular, energies are normalized to $T_i = T_{0,i}$, and distributions are normalized to $n_i m_i^{3/2}/(2\pi T_i^{3/2})$.

Linearizing the model equations, we obtain the dispersion relation $D(x) = 0$, where $x = \omega/(n\Omega_d)$, and

$$D(x) \;=\; C_r + \imath C_1 \delta_n + \frac{2}{\sqrt{\pi}} \int \frac{\sqrt{E}}{E-x} \frac{\partial f_{eq}}{\partial \psi} J_0^2(E) \mathrm{d}E, \tag{6.14}$$

In the latter expression, the integral is on a Landau path, and we define

$$C_r = C_1 + C_2 \left(n^2 q_0^2 \rho_c^2 / a^2 + k_r^2 \delta_b^2 \right), \tag{6.15}$$

$C_1 = \tau_e C_2 / f_p$ (we recall that $\tau_e = T_{0,i}/T_{0,e}$, and that f_p is the fraction of trapped particles), and $C_2 = a/R_0$. In the $\delta \to 0$ limit, Eq. (6.14) is in agreement with Ref. [DGBG00]. In this case, the marginal solution is $\omega = 3n\omega_0/2$, where ω_0 is the precession frequency of thermal ions.

Substituting the equilibrium distribution function, Eq. (6.8), yields

$$D(x) \;=\; C_r + \imath C_1 \delta_n - \kappa_T I_r - \frac{2}{\sqrt{\pi}} \left[\kappa_n + \kappa_T (x - \frac{3}{2}) \right] \int \frac{\sqrt{E} e^{-E}}{E-x} J_0^2 \mathrm{d}E, \tag{6.16}$$

where

$$I_r = \frac{2}{\sqrt{\pi}} \int_0^\infty \sqrt{E} e^{-E} J_0^2(E) \mathrm{d}E. \tag{6.17}$$

In the limit of small density gradient ($\kappa_n \to 0$), the latter dispersion relation yields a branch with positive real frequency, which corresponds to propagation in the ion diamagnetic direction. It is often called as the ion root. In the opposite limit of small temperature gradient ($\kappa_T \to 0$), the latter dispersion relation yields a root with negative real frequency, which corresponds to propagation in the electron diamagnetic direction. However, it can not be unstable unless electron dissipation is finite $\delta > 0$. It is often called as the dissipative electron root. This is consistent with previous works [KP71]. Let us then analyse the impact of electron dissipation on linear frequency and growth rate in various regimes.

	C_1	C_2	$q_0\rho_c/a$	δ_b/a	κ_T	κ_n	ϵ_ϕ
Case 1	0.1	0.1	0.01	0.1	0.15	0	1
Case 2	0.1	0.1	0.01	0.1	0.1	0.2	1
Case 3	0.1	0.1	0.01	0.1	0.15	0.15	1

Table 6.1 – Input parameters. Here $C_1 = aT_i(1-f_p)/(f_pR_0T_e)$, and $C_2 = a/R_0$.

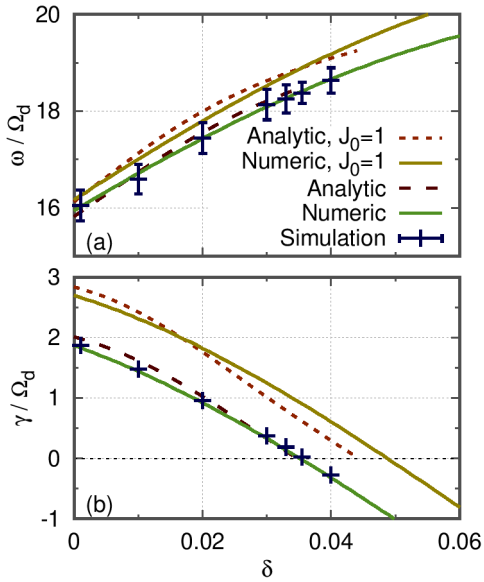

Figure 6.2 – Linear frequency (a) and growth rate (b) as a function of electron dissipation, for Case 1 (flat density profile), for a given mode ($n = 10$, $k = \pi/L_\psi$). The legend is shared. 'Analytic', 'Numeric' and 'Simulation' refer to the analytic approximate solution of the dispersion relation, the numerical solution of the dispersion relation, and TERESA simulation.

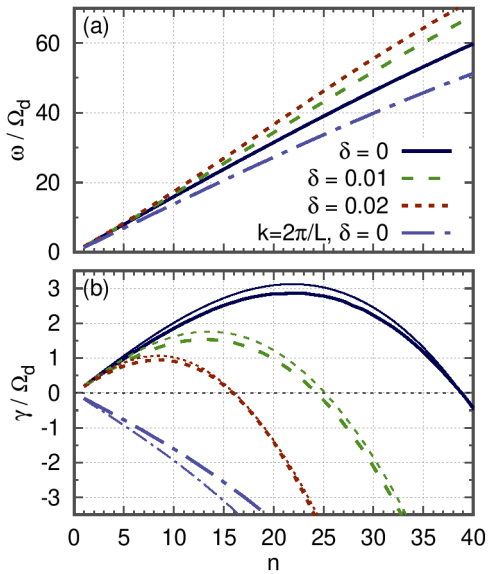

Figure 6.3 – Linear frequency (a) and growth rate (b) as a function of the toroidal mode number, for Case 1 (flat density profile). The radial mode number is $k = \pi/L_\psi$ except for one curve for $k = 2\pi/L_\psi$. The legend is shared. Thin curves correspond to the analytic approximate solution.

Ion root

Let us consider a flat density profile, $\kappa_n = 0$, and explore the ion root of the trapped-ion-mode. The input parameters of the model are shown as *Case 1* in Table 6.1.

The result from TERESA simulations, as well as the numerical solution of the dispersion relation are shown in Fig. 6.2 against the electron dissipation rate δ. Furthermore, in the appendix of Ref. [LCMD+17], we solve the dispersion relation for the ion root, perturbatively, up to the second order in $(\omega - 3n\omega_0/2)$. The solution is included in Fig. 6.2. We observe a quantitative agreement between analytic and numerical solution of the dispersion relation, as well as with the numerical simulation, for both the real frequency and the growth rate. The goal of Fig. 6.2 is only to provide a test for 1. our implementation of electron dissipation in TERESA, 2. our numerical dispersion relation solver, and 3. our analytic theory.

Hereafter, let us apply the numerical solver of the dispersion relation, alone, to explore the impact of electron dissipation on the various instabilities.

Fig. 6.3 shows the frequency (a) and linear growth rate (b) of modes with different wavelength. Most strikingly, electron dissipation significantly mitigates the global instability for values $\delta \sim 0.01$ (although the $n = 1$ mode is not stabilized unless $\delta > 0.37$). In addition, increasing electron dissipation significantly decreases the wavelength of the most unstable mode. The impact of dissipation (for reasonable values $\delta \ll 1$) on the real frequency is negligible, for each mode taken separately.

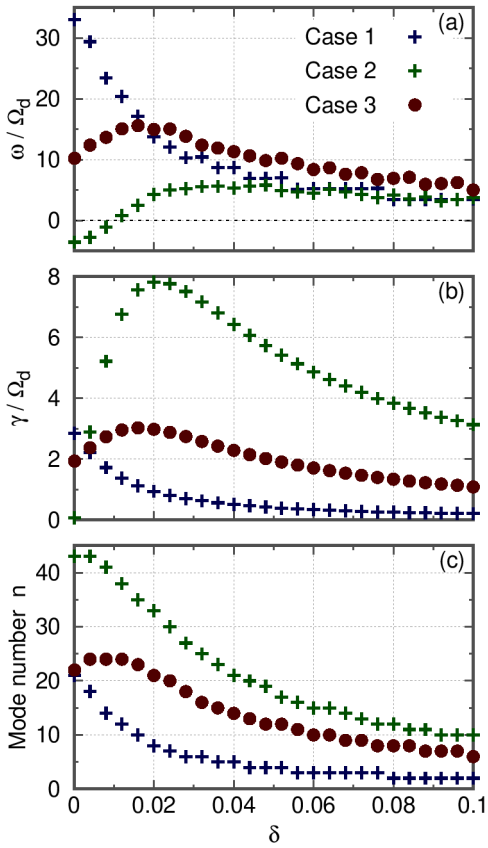

Figure 6.4 – Linear frequency (a), growth rate (b) and mode number (c) of the most unstable mode, as a function of electron dissipation.

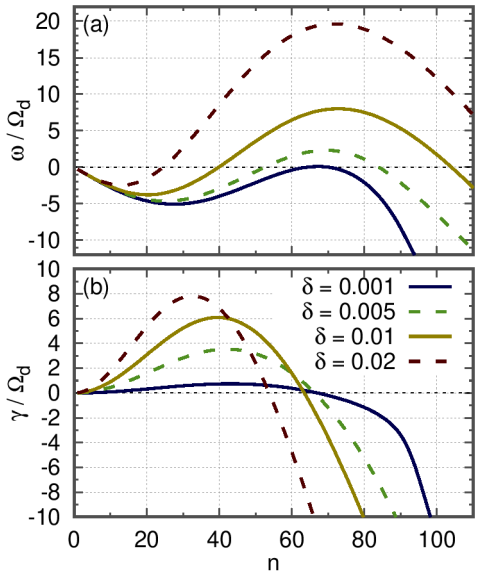

Figure 6.5 – Linear frequency (a) and growth rate (b) as a function of the toroidal mode number, for Case 2 (higher density gradient). The radial mode number is $k = \pi/L_\psi$.

We include in Fig. 6.3 the linear solution for $k = 2\pi$, to illustrate the fact that modes with radial mode numbers $k/\pi > 1$ are much more stable than modes with $k = \pi$. We also include the analytic approximate solution, to demonstrate that it is valid for many mode numbers.

Fig. 6.4 (case 1) summarizes the impact of electron dissipation on the most unstable mode. From this point of view, the real frequency (of the most unstable mode) significantly decreases with electron dissipation, even though the frequency for a given m slightly increases. The reason is that the mode number of the most unstable mode significantly decreases with increasing electron dissipation. The propagation stays in the ion diamagnetic direction ($\omega > 0$). The growth rate decreases monotonically as dissipation increases. The impact of dissipation on all frequency, growth rate and mode number, is almost linear for $\delta < 0.01$. The growth rate in the adiabatic electron limit ($\delta = 0$) is $\gamma \approx 3\omega_d$

Electron root

Let us consider a case where the equilibrium density gradient is larger than the temperature gradient, and explore the electron root of the trapped-ion-mode. The input parameters of the model are shown as *Case 2* in Table 6.1.

The numerical solution of the dispersion relation is shown in Fig. 6.4 against electron dissipation rate δ. In this regime, the growth rate is zero for $\delta = 0$, but positive for finite δ. It peaks to $\gamma \approx 8\omega_d$ at $\delta \approx 0.02$. For $\delta < 0.01$, the most unstable mode, which has a relatively high mode number $m > 40$, propagates in the electron diamagnetic direction ($\omega < 0$), and growth rate is an increasing function of δ. On the contrary, for $\delta > 0.02$,

the most unstable mode propagates in the ion diamagnetic direction, and growth rate is a decreasing function of δ, which appears to saturate to a finite value for large δ.

Fig. 6.5 shows in more details how frequency and growth rate depend on δ, for finite but small δ, not only for the most unstable mode, but for a large range of mode numbers. We observe that, even when the most unstable mode is an ion root, there can be unstable electron roots as well with comparable growth rates, and lower mode numbers (e.g. for $\delta = 0.005$). Conversely, dominant electron roots can coexist with ion roots with comparable growth rates (e.g. for $\delta = 0.02$).

Competition between ion and electron roots

Let us consider equilibrium profiles with comparable gradients, to study the competition between ion and electron roots of the trapped-ion-mode. We choose $\kappa_n = \kappa_T = 0.15$. The input parameters of the model are shown as *Case 3* in Table 6.1.

The numerical solution of the dispersion relation is shown in Fig. 6.4 against electron dissipation rate δ. In this regime, the growth rate is finite ($\gamma \approx 2\omega_d \approx 0.2\omega$) for $\delta = 0$. It peaks to $\gamma \approx 3\omega_d$ at $\delta \approx 0.02$. Propagation is in the ion diamagnetic direction. Dependence of the growth rate on electron dissipation is relatively weak.

6.2.2 Energy-space structure

Let us consider a flat density profile, $\kappa_n = 0$. The input parameters of the model are shown as *Case 1* in Table 6.1. In this case, the dispersion relation yields a branch with positive real frequency, which corresponds to propagation in the ion diamagnetic direction. It is often called as the ion root.

We investigate the linear energy-space structure for the ion root of the trapped-ion-mode. This eigenfunction is obtained from single-mode TERESA simulations by extracting at a fixed time t_1 a single m Fourier component of $f(\alpha, \psi_{1/2}, E, t_1)$, where $\psi_{1/2} = 0.5$ corresponds to the mid-radius of the simulation box. It is then normalized by the absolute value of the m component of $\phi(\alpha, \psi_{1/2}, t_1)$. The time of snapshot t_1 is chosen around the end of the exponential growth (and before the decrease of growth-rate due to nonlinear saturation), in order to give enough time for the eigenfunction to form from the initial arbitrary perturbation. In this section, the hat notation for Fourier components is omitted.

Fig. 6.6 shows the eigenfunction δf_n, for an arbitrary mode number, $n = 10$, obtained from a simulation with $N_E = 2048$ grid points in energy. We compare two cases, without ($\delta = 0$, left) and with ($\delta = 0.02$, right) electron dissipation. In both cases, there is a peak at $E/T_0 \approx \omega/(n\Omega_d)$, which corresponds to the resonance $\omega = n\omega_d(E)$. Interestingly, this peak becomes stronger as δ increases.

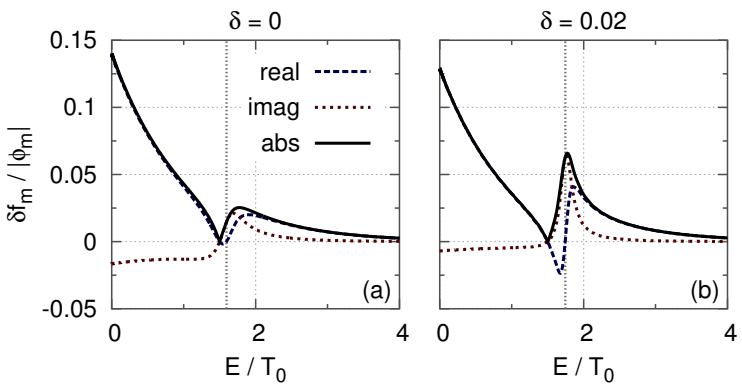

Figure 6.6 – Eigenfunction for Case 1 (flat density profile), $n = 10$, at $\psi = 0.5$. (a) No electron dissipation. (b) Finite electron dissipation $\delta = 0.02$. A dotted vertical line corresponds to the energy such that the resonance condition $\omega = n\omega_d(E) = n\Omega_d E$ is satisfied.

N_E	24	48	96	192	384
Linear growth rate	63	4.6	2.6	0.013	3.6×10^{-6}
Peak field amplitude	50	1.3	2.2	0.063	5.8×10^{-4}

Table 6.2 – Impact of sub-resolution in energy space. Relative error (in percent), taking a $N_E = 1536$ simulation as the reference case.

Note that the peak is narrow, especially for the imaginary part, with a full width at half maximum $\Delta E = 0.2\,T_0$ in the case of Fig. 6.6(b). We have performed a scan (restricted to powers of 2) in the number N_E of grid points in the energy direction. We found that obtaining the eigenfunction within a 10% accuracy requires $N_E = 256$ grid points (here, the energy cut-off is $E_{\max} = 20\,T_0$). A 1% accuracy requires $N_E = 1024$ grid points. That is true even though we adopted a regular grid spacing in $\sqrt{E}$ (rather than in E), which favors the resolving of small-scale structures at relatively low energies $E \sim T_0$.

We investigated the impact of sub-resolution of the resonance in the energy space on the linear growth rate, and the peak field amplitude (of mode $n = 10$ only). Table 6.2 gives the relative errors for $N_E = 24$, 48, 96, 192, and 384, taking a simulation with $N_E = 1536$ as a reference case. Here, the structure of the grid in energy is homogeneous in $E^{1/2}$. We have also performed simulations with different grid structures, namely homogeneous in E, or homogeneous in $E^{1/3}$, but these lead to slightly increased inaccuracies.

In the limit of small ρ_0 and δ_b, the eigenfunction can be estimated as

$$\delta f_{n,k} \;=\; -\frac{n\,\kappa_T\,e^{-E}\,(E-3/2)}{\omega - n\Omega_d E + \imath\gamma}\;\phi_{n,k}. \tag{6.18}$$

With the simple approximation $\phi_{n,k} = |\phi_{n,k}|$, the latter expression is in quantitative agreement with the values from numerical simulation (Fig. 6.6). The maximum absolute error in terms of $|\delta f_{n,k}|/|\phi_{n,k}|$ is 0.0016 for $\delta = 0$, and 0.0069 for $\delta = 0.02$. Eq. (6.18) does not depend explicitly on δ. In fact, here, the dominant cause of shrinking of the resonance with finite electron dissipation is a twice smaller γ/ω ratio for $\delta = 0.02$ compared to $\delta = 0$.

6.3 Single-mode saturation

The saturation of a single-mode was analyzed in Ref. [Dro15]. The time-evolution (see Fig.6.4 in the reference) is very similar to that of the simple bump-on-tail instability in the Vlasov-Poisson model, Fig. 4.2. Furthermore, the saturated amplitude qualitatively agrees with a mixing-length estimate.

Here, we investigate the impact of sub-resolution of the resonance in the energy space on the first peak of field amplitude (of mode $n = 10$ only). Table 6.2 includes the relative errors with $N_E = 1536$ as a reference case. We observe that the first peak of field amplitude is well evaluated with resolution as low as $N_E = 48$.

6.4 Turbulence and transport

6.4.1 Impacts of electron dissipation

We investigate the impact of electron dissipation on the peak radial particle flux. The results can be summarized as follows. The dependency of peak particle flux on δ is similar to that of the maximum linear growth rate. When density gradient and temperature gradient are similar, particle flux is of the order of a gyro-Bohm estimate for high enough electron dissipation, $\delta > 0.005$. When the density gradient is significantly larger than the temperature gradient, that is, when there are electron roots with growth-rates comparable to that of most unstable ion roots, particle flux peaks at an order-of-magnitude above the gyro-Bohm estimate for $\delta > 0.005$. Slight, transient particle pinch is observed in the case of higher density gradient, for smaller values of δ.

Let us consider a typical time evolution of an initial value TERESA simulation. After the linear phase, the electric field energy first saturates to some peak value, before decaying to a quasi-steady-state average value. We focus on the first, transient peaking of electric field amplitude, which corresponds also the highest peak of both field amplitude and particle flux. Understanding the first and strongest peak may serve the understanding of the quasi-steady state.

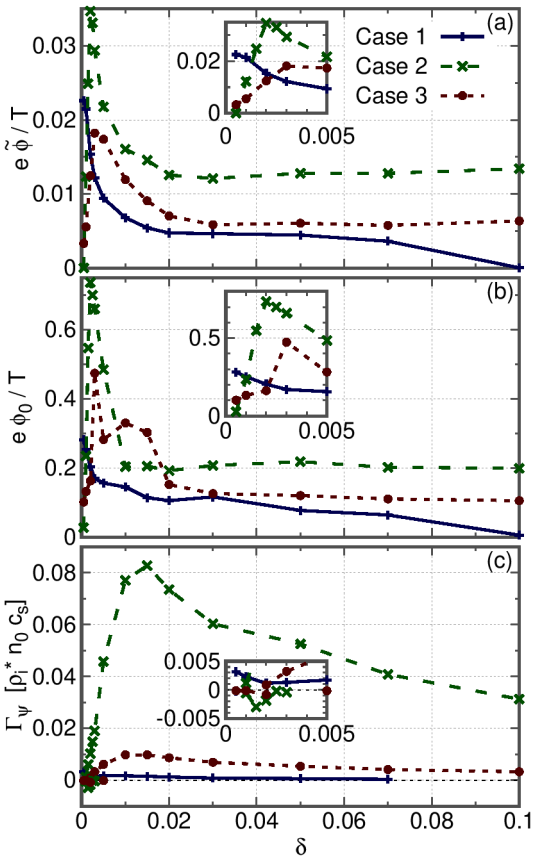

Figure 6.7 – Peak field energy (a), peak zonal flow energy (b), and peaks (minimum and maximum) of radial particle flux (c), as a function of electron dissipation. Inset: zoom in the low δ region. For clarity, the particle flux is not plotted when $|\Gamma_\psi| < 10^{-4}$.

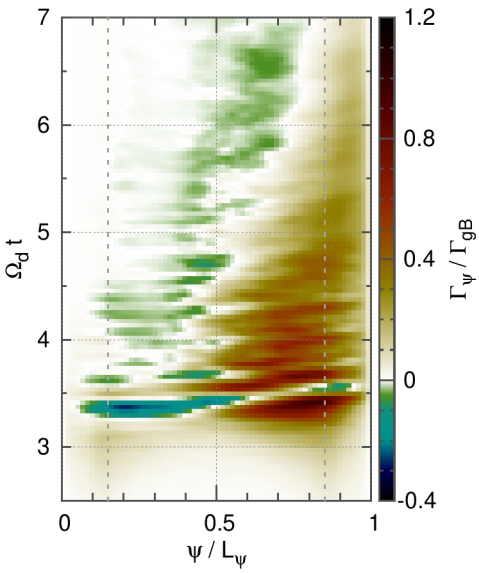

Figure 6.8 – Radial particle flux, as a function of radius and time, for Case 2 and $\delta = 0.0015$. Here, the flux is normalized by a gyro-Bohm estimate $\Gamma_{gB} = \rho^* T_0/(eB_0)\partial n/\partial r$, with $q_0\epsilon/\rho^* = 40$. Dashed vertical lines indicate the boundary with buffer regions, near the magnetic axis $\psi = 0$ and the outer region $\psi = L_\psi$, where artificial dissipation dominates.

We ran a series of TERESA simulations for the three cases of Table 6.1, and various values of electron dissipation rate δ. For these simulations, we use $N_\psi = 257$ grid points in radius, $N_\alpha = 513$ grid points in precession angle, and $N_E = 1024$ grid points in energy, with an energy cut-off $E_{\max} = 20$. This fine grid in energy is necessary to obtain the flux with good accuracy, at least in some cases. Fig. 6.7 shows the peak field energy (a), peak zonal flow energy (b), and peaks (minimum and maximum) of radial particle flux at $\psi = 0.5$ (c). Here, the field energy is defined as $e\tilde{\phi}/T$, where $\tilde{\phi}$ is the root mean square (rms) of $\phi - \langle\phi\rangle_\alpha$, over a radial domain $0.25 < \psi < 0.75$, which excludes the buffer regions. The zonal flow energy is defined as $e\phi_0/T$, where ϕ_0 is the rms of ϕ, over the same radial domain. The radial particle flux Γ_ψ is defined such that the angle-averaged density satisfies $\partial \langle n\rangle_\alpha / \partial t + \partial \Gamma_\psi / \partial \psi = 0$ in the absence of source.

Unsurprisingly, the dependency of peak particle flux on δ is similar to that of the maximum linear growth rate (see Fig. 6.4(b) for a graph of γ against δ). However, peak field and zonal energies show a different behavior, especially in the presence of a density gradient, peaking at $\delta \approx 0.005$ even though γ peaks at $\delta \approx 0.02$. In the case of flat density profile (Case 1), field energy, zonal energy and particle flux all decrease roughly monotonously with δ.

Let us compare the particle flux in Case 2 and Case 3, in the presence of finite dissipation, $\delta > 0.005$, after normalizing it by a gyro-Bohm estimate $\Gamma_{gB} = \rho^* T_0/(eB_0)\partial n/\partial r$. If we choose $q_0\epsilon/\rho^* = 40$, the flux peaks at $\Gamma_\psi/\Gamma_{gB} \approx 8$ for Case 2, and $\Gamma_\psi/\Gamma_{gB} \approx 1$ for Case 3. We note that from linear analysis, it can be concluded that electron roots have larger growth rates in Case 2 than in Case 3 for fixed δ. Therefore, electron roots may be responsible for pushing the particle flux up to an order-of-magnitude above the gyro-Bohm estimate.

Interestingly, when density gradient dominates (Case 2), we observe a slight pinch of particle ($\Gamma_\psi < 0$) for $\delta \approx 0.0015 - 0.002$, where the most unstable mode propagates in the electron diamagnetic direction. This can be seen in the inset of Fig. 6.7(c). The pinch can also be seen in Fig. 6.8, which shows a spatio-temporal map of the particle flux for Case 2 and $\delta = 0.0015$. The pinch is strongest at time $t \approx 3.3$, and stays significant in later times around the mid-radius of the simulation box ($\psi \approx 0.5$). To invoke a density pinch, we need to check that the negative flux is not due to a reversed density gradient. Between $t = 3.0$ and $t = 3.7$ (time period during which the negative flux is most significant), the density gradient is never reversed throughout all the simulation box. More precisely, the gradient $-\partial n/\partial\Psi$ stays larger than $0.1n_0/L_\Psi$ (about half of the initial κ_n) if we exclude the buffer regions, and larger than $0.078n_0/L_\Psi$ if we include them. When density gradient and temperature gradient are similar (Case 3), we observe a weaker pinch at $\delta = 0.002$.

As a caveat, the model does not allow to accurately characterize the nonlinear saturation. Indeed, it was shown that saturation is achieved via a spectral transfer that involves electron drift waves [DB90, KW94]. Investigating the quasi-steady-state obtained in our simulations may be relevant, for example to reveal hints of new physical mechanisms, but not for quantitative interpretation or prediction of experimental data.

To conclude, particle flux depends strongly on the ordering between equilibrium density gradient κ_n and equilibrium temperature gradient κ_T. The particle flux was compared to a gyro-Bohm estimate, Γ_{gB}. Particle flux peaks to $\sim \Gamma_{gB}$ and $\approx 8\Gamma_{gB}$, for $\kappa_n \approx \kappa_T$ and $\kappa_n \approx 2\kappa_T$, respectively, and for large-enough electron dissipation. Furthermore, it can take negative values, $\approx -0.4\Gamma_{gB}$, for small but finite electron dissipation $\delta_n \approx 0.005n$.

6.4.2 Anatomy of transport in energy space

A large part of the results summarized here were developed during the PhD thesis of my first PhD student, Julien Médina. More details can be found in Refs. [MLG+18] and [Méd19].

The gyrobounce approach allows one to study the details of the trapped particle dynamics in both real space and energy (or velocity) space, at reasonable computing cost. For collisionless TIM and TEM, we expect wave-particle resonances to play essential roles in transport. These modes being weakly dispersive, all resonances may be concentrated within a narrow range of energies. This raises the issue of the precision required to accurately describe turbulence and transport.

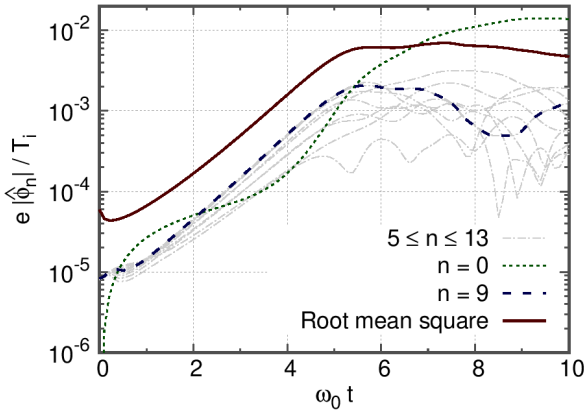

Figure 6.9 – Time-evolution of the amplitude of the dominant Fourier modes of the electric potential ϕ, at $\psi = 3L_\psi/8$. The modes $n = 5$ to $n = 13$ correspond to the 9 most intense modes. The linearly most unstable mode is $n = 9$. Here $\omega_0 = \Omega_d T_i$.

In this part, we describe the structure in energy-space of nonlinear radial fluxes of particles in TIM turbulence. This yields an estimate of the accuracy required in energy space.

We focus on one of the simulations investigated in subsection 6.4.1 : the one denoted as *Case 1* (kinetic ions, quasi-adiabatic electrons, flat density profile), whose input parameters are given in Table 6.1, and with electron dissipation parameter $\delta = 0.02$. We choose a grid with $N_\alpha \times N_\psi \times N_E = 256 \times 257 \times 1024$.

Fig. (6.9) shows the time-evolution of a selection of dominant modes. We observe a phase of linear growth of the plasma potential from $t = 0$ until $t \approx 4 - 5$ (For concision, time is normalized to the precession frequency of thermal ions, $\omega_0 = \Omega_d T_i$). Linearly, the most unstable mode is the mode number $n = 9$. Its linear frequency and growth rate are $\omega_{n=9} = 15.6$ and $\gamma_{n=9} = 0.987$. After $t = 5$ the modes saturate. The saturation amplitude in terms of the root mean square is of the order of $e\phi_{rms}/T_i \sim 5 \times 10^{-3}$.

Radial transport

Specialized to our model, Eq. (2.12) yields

$$\frac{\partial \langle f \rangle}{\partial t} + \frac{\partial \Lambda_\psi^{\mathrm{NL}}}{\partial \psi} = 0, \tag{6.19}$$

where $\Lambda_\psi^{\mathrm{NL}}(\psi, E, t) = \langle \dot{\psi}\, \delta f \rangle$ is the radial flux of phase-space density, and we added a superscript ^{NL} to emphasize that it contains all nonlinear terms. It is calculated directly within the TERESA simulation.

We can compare with the radial flux of phase-space density estimated by quasilinear theory, $\Lambda_\psi^{\mathrm{QL}}(\psi, E, t)$. Eqs. (2.25) and (2.26) yield

$$\Lambda_\psi^{\mathrm{QL}}(\psi, E, t) = -D^{\mathrm{QL}} \frac{\partial \langle f \rangle}{\partial \psi}, \tag{6.20}$$

where

$$D^{\mathrm{QL}}(\psi, E, t) = \sum_n n^2 \left| \hat{\phi}_n(\psi, E, t) \right|^2 \mathrm{Im} \frac{1 - e^{-i(\omega_{R,n} - \omega_n)t - |\gamma_n| t}}{(\omega_{R,n} - \omega_n) - \imath |\gamma_n(t)|}. \tag{6.21}$$

and

$$\omega_{R,n}(\psi, E, t) = n \left(\frac{\Omega_d E}{Z} + \frac{\partial \hat{\phi}_0}{\partial \psi} \right). \tag{6.22}$$

The term $\frac{\partial \langle \phi \rangle}{\partial \psi}$ shows that the mean flow (including zonal flow) induces a Doppler shift on the resonant frequency. To compute the quasilinear flux, the potential ϕ, the mean distribution function $\langle f \rangle$, the mode frequencies ω_n and growthrates γ_n are needed. In order to test fundamental aspects of QL formalism, we want to limit the sources of discrepancies between QL theory and NL simulations. Therefore, at each time we substitute ϕ and $\langle f \rangle$

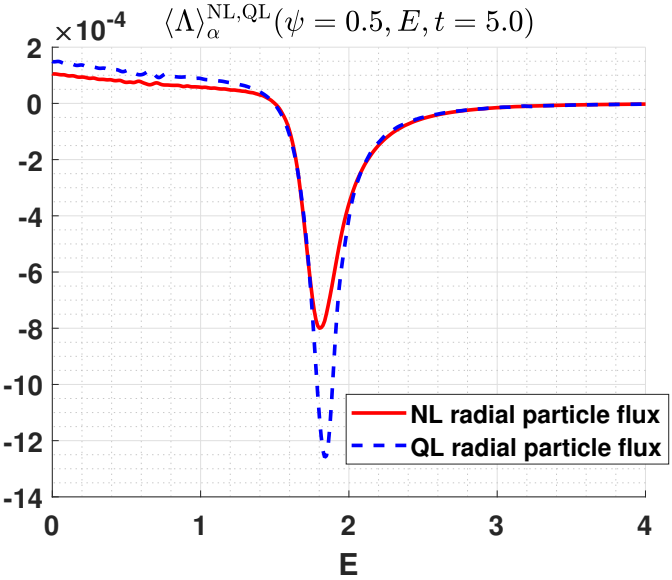

Figure 6.10 – Nonlinear and quasi-linear radial PS density fluxes against the energy (here normalized to T_i), at $t = 5$. Negative Λ means flux from core to edge.

extracted directly from nonlinear simulation, instead of using approximations such as the mixing length. Then, γ_n and ω_n are obtained by solving the linear dispersion relation.

The use of this version of quasilinear theory is justified for a time $\sim 1/\gamma$ after the start of the saturation phase. In our simulation, the fastest growing mode has a growthrate $\gamma \approx \omega_0$, where ω_0 is the precession frequency of thermal ions. Let us investigate the time $t = 5$, at the beginning of the turbulent phase, where the dominant modes have just achieved saturation. We choose an arbitrary radial location, $\psi_0 = L_\psi/2$. Quasilinear diffusion features one resonance for each mode n, when $\omega_n = \omega_{R,n}$. As expected, the resonant energies of the dominant modes ($n = 7 - 11$) are concentrated within a narrow range, $E/T_i \in [1.78, 1.83]$ (and the mean flow contribution is relatively small). Therefore we expect that the flux features a narrow peak of width $\Delta E \approx 0.05T_i$ around $E \approx 1.8T_i$. Fig. 6.10 shows the nonlinear flux of phase-space density obtained from simulation, as well as the quasilinear flux. The flux is positive (inbound) for $E/T_i < 3/2$ and negative (outbound) for $E/T_i > 3/2$. This can be simply explained by the sign of $\partial_\psi f_{\mathrm{eq}}$, which is negative for $E/T_i < 3/2$ and positive for $E/T_i < 3/2$. Therefore the sign is everywhere consistent with a flattening in ψ of $\langle f\rangle$, which remains close to f_{eq} at $t = 5$. As expected, we observe a narrow resonance negative peak. For the nonlinear flux, the width obtained by a gaussian fit is $\Delta E \approx 0.15T_i$. Strikingly, the flux at the resonance is one order of magnitude stronger than the flux for thermal particles. As a result, the resonance peak accounts for most of the flux, despite the small number of particles (7%) in the range $E/T_i \in [1.7, 2.0]$.

The nonlinear and quasilinear fluxes are in qualitative agreement, in terms of sign, energy of sign reversal, position of peak, width of peak, and behavior at large energies. However, there is quantitative discrepancy : 41% at $E = 0$, 55% at $E = T_i$, and 57% at the resonance peak. In the next part, we investigate the origin of this discrepancy, based on term-by-term comparison between kept and neglected terms in the Vlasov equation.

The moments of Eq. (6.19) yield the density flux,

$$\Gamma^{NL}(\psi, t) = \int_E \Lambda_\psi^{NL}(\psi, E', t) E'^{1/2} \mathrm{d}E', \tag{6.23}$$

and the heat flux,

$$q^{NL}(\psi, t) = \int_E \Lambda_\psi^{NL}(\psi, E', t) E'^{3/2} \mathrm{d}E'. \tag{6.24}$$

Note that we distinguish the flux of phase-space density Λ, and the flux of density (in the sense of fluid density) Γ. Fig. 6.11 shows both nonlinear and quasilinear density and heat fluxes at $t = 5$. The negative sign of both Γ and q is consistent with a flattening of the initial gradients. We observe a simple bell-shaped radial structure. This results from the constraining boundary conditions, coupled with the fact that the simulation box is

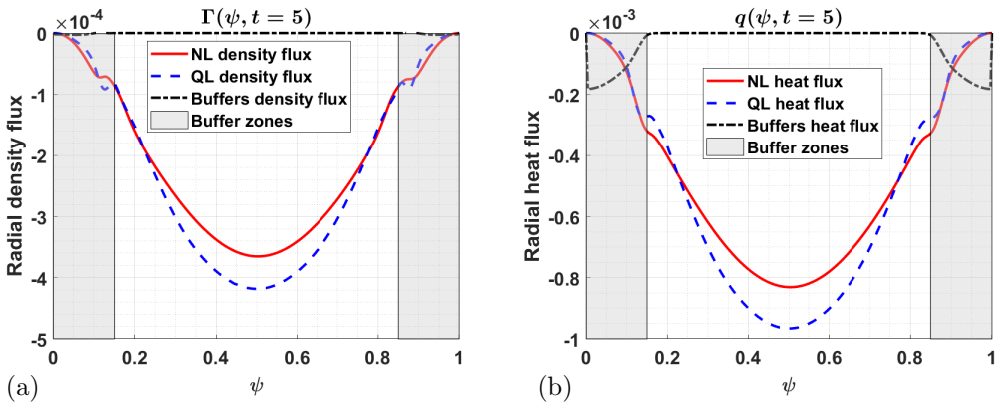

Figure 6.11 – Radial density (a) and heat (b) fluxes as a function of radius, at $t = 5$.

relatively small (10 banana widths). We confirmed this point with one simulation with larger box size, which yields flatter flux profiles except near the boundaries. We can separate the contribution from thermal particles and from resonant particles, by integrating over different ranges of energy E. This procedure shows that the resonant particles contribute more than 90% of the total heat flux. Overall, there is good qualitative and quantitative agreement between nonlinear and quasilinear density and heat fluxes, within a relative 16% inaccuracy. Surprisingly, the positive and negative errors in PS density flux compensate. Whether this is a coincidence or not remains to be investigated.

Term-by-term comparison for the Vlasov equation

To explain the discrepancy between the nonlinear and quasi-linear fluxes, let us compare the terms in Vlasov equation, including those that are included and those that are neglected in the quasi-linear theory. In our model, Eq. (2.15) takes the form

$$\mathrm{L}_{1,n} + \mathrm{L}_{2,n} + \mathrm{L}_{3,n} \;=\; \mathrm{NL}_{1,n} + \mathrm{NL}_{2,n} + \mathrm{NL}_{3,n}, \tag{6.25}$$

where we have noted the linear terms as

— $\mathrm{L}_{1,n} = \partial_t \hat{f}_n$,

— $\mathrm{L}_{2,n} = \imath n E \Omega_d \hat{f}_n$,

— $\mathrm{L}_{3,n} = -\imath n \hat{\phi}_n \partial_\psi \langle f \rangle$,

($\mathrm{L}_{3,n}$ is linear because $\langle f \rangle$ is taken as the new equilibrium distribution) , and the nonlinear terms as

— $\mathrm{NL}_{1,n} = -\imath n \hat{f}_n \partial_\psi \hat{\phi}_0$,

— $\mathrm{NL}_{2,n} = -\sum_{n' \neq n} \imath n' \hat{f}'_n \partial_\psi \hat{\phi}_{n-n'}$,

— $\mathrm{NL}_{3,n} = \sum_{n' \neq 0} \imath (n - n') \hat{\phi}_{n-n'} \partial_\psi \hat{f}_{n'}$.

The terms $\mathrm{L}_{1,n}$, $\mathrm{L}_{2,n}$, $\mathrm{L}_{3,n}$, and $\mathrm{NL}_{1,n}$ are taken into account in the quasilinear equation, while the terms $\mathrm{NL}_{2,n}$ and $\mathrm{NL}_{3,n}$ are neglected.

In order to compare the magnitude of all terms, we take their absolute value and sum them over all non zonal modes, which yields the terms L_1, L_2, L_3, NL_1, NL_2 and NL_3. For example,

$$\mathrm{L}_1 = \sum_{n \neq 0} |\mathrm{L}_{1,n}| \,. \tag{6.26}$$

Fig. 6.12 shows the linear and nonlinear terms of the system at $t = 5$, against energy (L_1 is not represented because we did not calculate it). We observe that $\mathrm{L}_2 \gg \mathrm{L}_3, \mathrm{NL}_1, \mathrm{NL}_2, \mathrm{NL}_3$ (except for $E \ll T_i$). This indicates that L_1 is of the same order of magnitude as L_2 and that these two terms, which correspond to free streaming, nearly cancel each other. L_2 corresponds to the banana precession around the toroidal direction and does not impact transport in the radial direction nor the QL radial fluxes. L_3 contributes directly to the radial QL fluxes since it involves $\partial_\psi \langle f \rangle$. NL_1 involves the zonal radial electric field $\partial_\psi \langle \phi \rangle$ and is responsible for a doppler-shift of the resonant frequencies. NL_2 and NL_3 correspond to

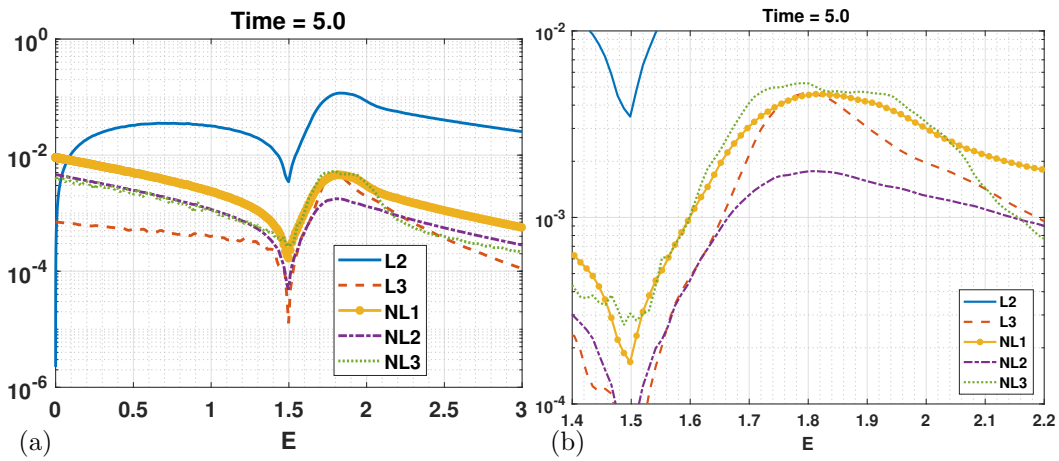

Figure 6.12 – (a) Comparison between linear and nonlinear terms of Vlasov equation. (b) Zoom around the resonance.

all the other nonlinear couplings that do not involve mean flow. NL_3 contributes directly to the radial transport since it involves $\partial_\psi \langle f \rangle$, but it is neglected in the framework of quasilinear theory.

The key terms influencing the radial fluxes are thus L_3 and NL_3. In the figure, we observe that $\mathrm{NL}_3 \gtrsim \mathrm{L}_3$ near the resonant energies. Therefore quasilinear theory discards an important term, corresponding to $\langle (\partial_\alpha \phi) \partial_\psi (f - \langle f \rangle) \rangle$, which may explain the discrepancies with nonlinear simulations.

Partial conclusion

To investigate how the radial turbulent transport depends on energy, the simulation was performed with a large number of grid points, $N_E = 1024$. We focused on a time in the simulation corresponding to the beginning of the turbulent phase. The flux features a narrow peak in the resonant region, with a width $\Delta E \approx 0.15 T_i$, around the energy $E \approx 1.8 T_i$. Strikingly, this resonant peak accounts for 90% of the density and heat fluxes. In contrast, the contribution from thermal particles is negligible. Based on these results, a fine mesh in the energy space ($\delta E \ll 0.1 T_i$), in the resonant region, is required to accurately describe the radial transport of density and heat.

Quasilinear theory (including the effect of mean flows) qualitatively agree with the simulation results, in terms of global structure in the radial direction, sign throughout the energy dimension, behavior at small and large energies, and for the resonant peak in terms of its shape, location and width in the energy dimension. However, quantitatively, there is a 57% overprediction at the peak, and a 55% overprediction at the thermal energy $E = T_0$. Since the flux is negative for resonant energies, and positive for thermal energies, these discrepancies can compensate each others. Indeed, there is quantitative agreement for the total density and heat fluxes, with only 16% overprediction. This may or may not be fortuitous.

We showed that the non-zonal nonlinear part of the radial advection in the Vlasov equation, which is neglected in quasilinear theory, is actually larger than the linear part. This explains the discrepancies.

As a caveat, we focused on collisionless trapped-particle-modes which are very weakly dispersive. In ITG turbulence, resonances may not play such a crucial role, and the coexistence and/or the coupling between TEM and ITG may mitigate the importance of the resonant peak in the radial fluxes.

Another important caveat is that boundary conditions consist of thermal baths, which strongly restrict the evolution of the profiles. As a result, the heat flux remains small in amplitude, and the relaxation of the initial temperature gradient is only marginal. A future analysis based on flux-driven simulations may provide new information about the role of resonant particles in turbulent transport.

	C_1	C_2	$q_0\rho_c/a$	δ_b/a	κ_T	κ_n	ϵ_ϕ	δ
Simulation A	0.1	0.1	0.001	0.01	0.15	0.05	1	0.02
Simulation B	0.05	0.1	ions 0.01 elec. 0.001	ions 0.1 elec. 0.01	0.15	0.05	0	0

Table 6.3 – Input parameters. Here $C_1 = a(1-f_p)/(f_pR_0)$, and $C_2 = a/R_0$.

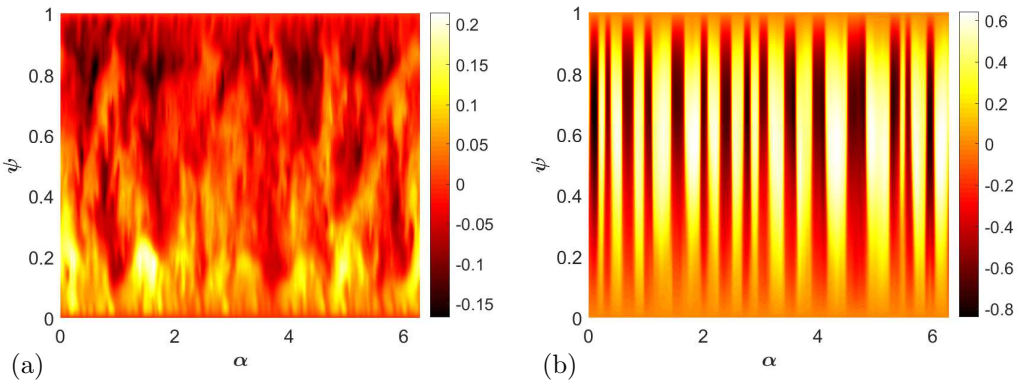

Figure 6.13 – Electric potential at $t = 6$. (a) Simulation A. (b) Simulation B.

6.4.3 Characterization by test particles

This subsection summarizes Ref. [MLG+19] and Chapter II of Ref. [Méd19]. We study the evolution of millions of test particles in a turbulent plasma simulation, as a method to get insights on the type of transport governing the plasma.

Turbulent transport may take various forms, such as diffusion [RR78, IGD95, HSPN02, ESG+18], hyper- or sub-diffusion [MRC+03], advection [IGD95, BPS+98, BRM+01, DPDG+10], particles draged along with self-trapped PS structures, and ballistic events such as avalanches [IUAT09, SGA+10, DPDG+10, SGA+11]. Test particle trajectories are useful to discriminate and investigate such processes.

Here, the goal is to discriminate the diffusive contribution from the non-diffusive contributions. We will compare two simulations: simulation A with quasi-adiabatic trapped electrons, and simulation B with fully kinetic trapped electrons. In simulation A, turbulence is more developed, and we find that transport is essentially diffusive. In constrast, simulation B is dominated by streamer-like structures, and we find that transport is dominated by non-diffusive processes.

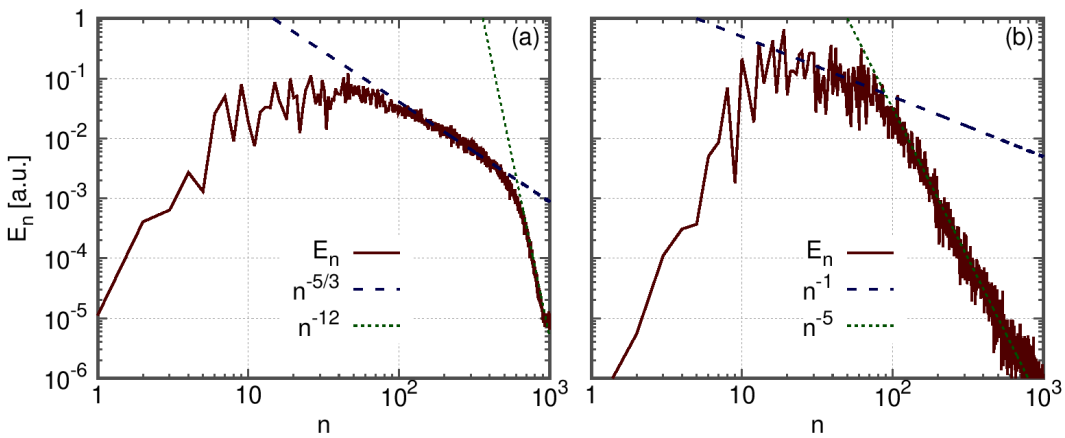

Figure 6.14 – Spectral energy density $E_n = n^3\phi_n^2$ [DGBG00], taken at $\psi = 0.5L_\psi$ and averaged over $t \in [6, 7]$. (a) Simulation A. (b) Simulation B.

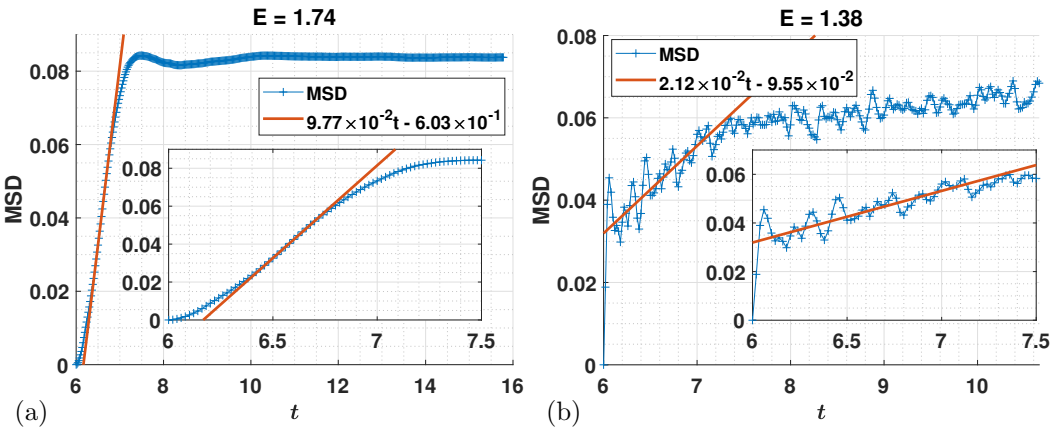

Figure 6.15 – Time-evolution of the test particles Mean Square Displacement (MSD). Here, time is normalized to the precession frequency of thermal ions, ω_0. (a) Simulation A, for $E = 1.74T_i$. (b) Simulation B, for $E = 1.38T_i$.

The input parameters of simulations A and B are given in Tab. 6.3. The modes saturate at $t \approx 2$ in simulation A, and $t \approx 3$ in simulation B. In both cases, we focus on an arbitrary time $t = 6$. Fig. 6.13 shows the electric potential in (α, ψ) space. In simulation A, of TIM turbulence, we observe no significant large structure such as zonal flow or streamer. In constrast, simulation B is dominated by streamer-like, radially-elongated modes. Both TIMs and TEMs are present. Fig. 6.14 shows the energy spectrum $E_n = n^3\phi_n^2$ averaged between $t = 6$ and $t = 7$. We observe that turbulence is more developed in simulation A than in simulation B. In simulation A, the most intense modes have mode number n in the order of 10, and the width of the spectrum is approximately 10 as well. For $100 \lesssim n \lesssim 400$, the energy spectrum roughly follows a power law $n^{-5/3}$ characteristic of a 2D turbulent cascade.

In both simulations, we compute the trajectories of one million test particles per energy grid. They are initialized at $t_0 = 6$ with a Gaussian distribution in ψ centered around $\psi = 0.5L_\psi$ and a standard deviation $\Delta\psi = 0.022L_\psi$, small enough to neglect the radial variations of turbulence. In the α direction they are distributed randomly with a uniform distribution. Then, TERESA computes the radial Mean Squared Displacement (MSD) of the test particles, $\langle(\psi(t) - \psi(t_0))^2\rangle$, where the average is over all the test particles of each energy E, as a function of time. A random walk diffusion coefficient can then be estimated as

$$D_{\mathrm{RW}} = \frac{1}{2}\frac{\mathrm{d}\langle(\psi(t) - \psi(t_0))^2\rangle}{\mathrm{d}t}. \tag{6.27}$$

Fig. 6.15 shows the time evolution of the radial MSD for one given value of energy for each simulation. In both subfigures, we may identify 3 phases in the evolution of the MSD, corresponding to different spatial and time scales.

1. Phase 1 corresponds to local convection on a small timescale ($\sim 0.1\omega_0^{-1}$) and small radial scale $\sim 10^{-2}L_\psi$.
2. Phase 2 corresponds to diffusion on a longer timescale $\sim \omega_0^{-1}$, of the order of the turbulent auto-correlation time. In this phase, the MSD grows rather linearly in time. The slope yields the randow-walk diffusion coefficient D_{RW}.
3. In phase 3 the MSD saturates because of reduced turbulence intensity near the boundaries, and ultimately because of boundary conditions, on a radial scale $\sim L_\psi$.

Fig. 6.15(a) corresponds to simulation A and $E = 1.74T_i$ (in the resonant region). Phase 1 appears from $t \approx 6$ to $t \approx 6.4$, phase 2 from $t \approx 6.4$ to $t \approx 6.8$, and phase 3 after $t \approx 6.8$. Fig. 6.15(b) corresponds to simulation B and $E = 1.38T_i$. Phase 1 appears from $t \approx 6$ to $t \approx 6.1$, phase 2 from $t \approx 6.1$ to $t \approx 7.5$, and phase 3 after $t \approx 6.8$.

From the random walk diffusion coefficient estimated from test-particles statistics, we

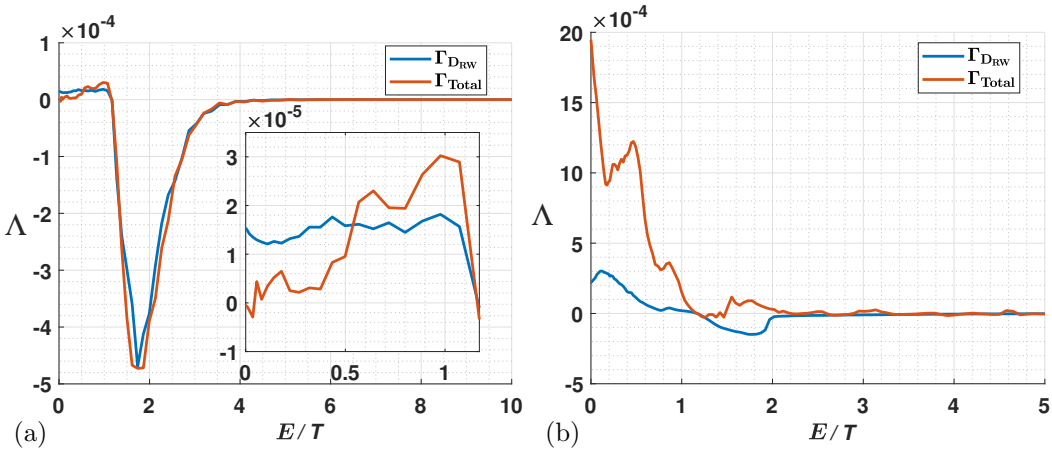

Figure 6.16 – Radial flux of phase-space density against energy. The total nonlinear flux averaged over an auto-correlation time τ_c and a radial range $\psi/L_\psi \in [0.4; 0.6]$ is compared with the diffusive part estimated from test-particles statistics. (a) Simulation A, $\tau_c \approx \omega_0^{-1}$. (b) Simulation B, $\tau_c \approx 4\omega_0^{-1}$.

calculate a radial diffusive flux as

$$\Gamma_{D_{\mathrm{RW}}} = -D_{\mathrm{RW}} \left\langle \frac{\partial \langle f \rangle}{\partial \psi} \right\rangle_{\psi/L_\psi \in [0.4;0.6]} . \tag{6.28}$$

Here, we averaged the radial gradient of $\langle f \rangle$ over $\psi/L_\psi \in [0.4; 0.6]$ in order to smooth out local variations, consistently with the radial extent of our analysis of test particles.

Let us compare the diffusive flux with the total flux calculated from f and ϕ. In principle, the two should coincide when transport is purely diffusive. To be consistent with the finite radial and time extents of our test particle analysis, the total flux is averaged over an auto-correlation time τ_c and a radial range $\psi/L_\psi \in [0.4; 0.6]$. Fig. 6.16 shows the diffusive flux and the total flux.

For simulation A, Fig. 6.16(a), we observe the same kind of resonance peak as found in subsection 6.4.2, around the energy $E \approx 1.74T_i$. In the resonant region, total flux and test-particle diffusive flux agree quantitatively, which indicates that the transport of resonant particles is diffusive. Since the resonance peak dominates transport overall, we also conclude that the whole radial transport is dominated by diffusion in this case. However, between $E = 0$ and $E \approx T_i$, there is significant discrepancy between total flux and diffusive flux, indicating that some non-diffusive mechanism may play a role for thermal particles, although the discrepancy may be due to uncertainties in measuring the slope of the MSD.

For simulation B, Fig. 6.16(b), we observe that both fluxes are fundamentally different from these of simulation A. Although there is a peak of diffusion coefficient near the resonant energies, which yields some negative flux around $E \approx 1.8T_i$, the diffusive flux is most intense around $E \approx 0.1T_i$. For low E the total flux is positive, i.e. from edge to core, which highlights a caveat of our constraining thermal baths boundary conditions: profile can spuriously stiffen. Nevertheless, the results indicate that transport in this case is mostly non diffusive.

To summarize, radial transport in well-developed TIM turbulence (simulation A) is mostly diffusive. In contrast, there are important non-diffusive contributions in TEM/TIM turbulence with strong streamer-like structures.

6.4.4 Control of turbulent transport

In Ref. [GLRD16], we reported on a new control method, which robustly stimulates the appearance of zonal flows, while minimizing the duration of the control process and the impact on plasma parameters.

The starting point of our work is a TERESA simulation where zonal flow transiently appears after the nonlinear saturation phase. We observe that zonal flow is strongly reduced

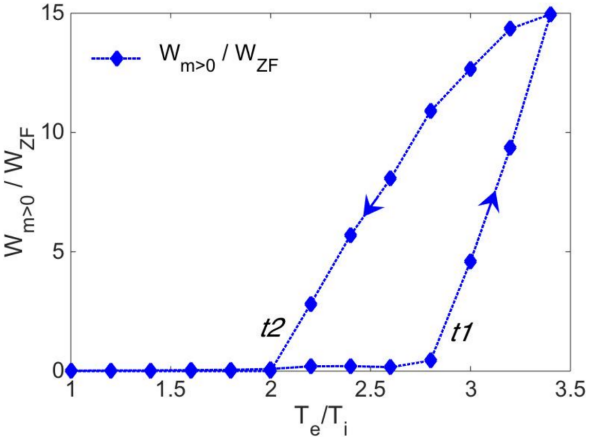

Figure 6.17 – Ratio of turbulent energy $W_{m>0}$ over zonal flow energy W_{ZF}, against electron/ion temperature ratio. Arrows indicate the direction of time.

in a later phase, permitting streamers-like structures to govern the plasma behaviour in the steady-state. By intervening for a short time during this latter state (after this transient growth and decay of zonal flow), we discovered a possibility to bifurcate to a new steady-state, in which zonal flows are strongly present and are maintained indefinitely, thereby allowing a significant reduction in radial heat fluxes. The intervention, or control method, is to increase the ion/electron temperature ratio for a short time. This is a crude model for experimental variations of the heating schemes. The required duration of control can be as short as a small fraction of the precession period of thermal ions, depending on the initial temperature ratio. Although, experimentally, the timescale of heating would enforce a longer lower limit on the duration of control. As a result of control, heat flux is reduced by a factor 15 on average.

In Ref. [GLR+17], we uncovered an hysteresis in the interplay between zonal flows and streamers, and a link between this hysteresis and the latter control method. We run a simulation where the electron/ion temperature ratio is artificially increased step-by-step from 1 to an arbitrary value of 3.4, on a slow timescale, $250\omega_0^{-1}$, and then decreased in a similar way. At each step, a quasi steady-state is achieved, and we measure a time-and-radial-average of zonal flow energy $\langle\partial_\psi\phi\rangle^2$, and turbulent energy $\langle\langle\partial_\psi\phi - \langle\partial_\psi\phi\rangle\rangle^2\rangle$. Fig. 6.17 shows the ratio between these energies, against the temperature ratio. We observe a clear hysteresis, with one or more order-of-magnitude difference between the two branches. Therefore, heat flux is sensitive to the history of T_e/T_i ratio. The transitions are associated with energy transfer between turbulence and zonal flow. The hysteresis clarifies how controlling T_e for a short duration can induce a drastic improvement of zonal flow in the steady-state: by switching from the higher branch of the hysteresis to the lower branch. We confirmed that this control method is effective as long as the initial temperature ratio is below its value at the transition marked $t1$ in the figure.

6.4.5 Impurity transport

The ideal plasma for fusion reactions in the core of ITER and future reactors is a mixture of deuterium and tritium. However, core Tokamak plasmas often contain other ion species, called impurities (e.g. helium, nitrogen, neon, argon, beryllium, carbon, or tungsten). Impurities are transported from edge to core by both collisional (neoclassical) and turbulent processes. Accumulation of impurities in the core threatens the viability of fusion. One issue is the dilution of fuel, which degrades the efficiency of fusion reactors. Another urgent issue is that heavy impurities, which are not fully ionized, radiate away the energy generated by fusion. The efficiency of fusion is very sensitive to core impurity concentration [PND+10]. Since slight contamination in the core can yield prohibitive energy losses, it is crucial to improve our lacking understanding of impurity transport.

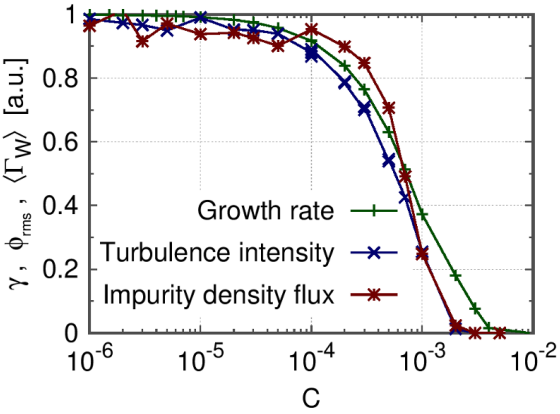

Figure 6.18 – Linear growth-rate, turbulence intensity (rms of the potential), and density flux, all versus tungsten concentration.

Impact of impurity density gradient

Recently we applied the TERESA code to study impurity transport [IGL+18]. We focused on impurities with high charge number Z. We showed that the direction of the radial gradient of impurities, even at a low concentration, could change the nature of turbulence, from TEM to TIM.

Limit of validity of the passive treatment

In gyrokinetic simulations of turbulent impurity transport, trace impurity species are often treated as passive species, in the sense that they are not included in Maxwell equations. This is consistent with the assumption that impurities with low enough concentrations are impacted by turbulence generated by electrons and main ions, but do not impact it significantly in return. Indeed, the relative contribution of impurity density in quasineutrality is of the order of CZ^2, where C is the impurity concentration, and Z its charge number. In the "trace" limit, $CZ^2 \ll 1$, the impurity behaves as a passive species, or test-particle, which means that its presence does not affect the turbulent state.

In Ref. [LDL+20], which we briefly summarize here, we relax this assumption, and investigate the active impacts of impurity, on impurity transport, as a function of its concentration, in the presence of TIM and TEM turbulence. We run a series of simulations with self-consistent (active) treatment of impurities for a wide range of concentrations, and compare the results with a series of simulations with passive impurities.

The impacts depend on the relationship between equilibrium density gradient and temperature gradient. Fig. 6.18 summarizes the impact of W^{40+} tungsten concentration in the case where these gradients are equal. It includes the linear growth rate, turbulence intensity, and impurity density flux, all normalized to their limit as C vanishes. There is a transition for all linear growth rate, turbulence intensity, and impurity density and heat fluxes, centered around $CZ^2 = 1.1$. However, the transition is significantly steeper for the fluxes.

We investigate the physical mechanism responsible for this difference in behavior between turbulence intensity and transport. We observe that phase-synchronization between impurity density fluctuations and electric potential fluctuations occurs for high enough impurity concentrations, which quenches impurity transport.

The steep transition for the turbulent flux may be viewed as a threshold, which gives the range of validity of the passive treatment, $C < 2 \times 10^{-4}$. When the temperature gradient is finite and the density profile is flat, we obtain qualitatively similar results, except for the density flux which vanishes. For the heat flux, the range of validity of the passive treatment is slightly smaller than for the case with equal gradients, $C < 10^{-4}$.

Finally, we performed a similar analysis for C^{6+} carbon (not shown here). There are two qualitative differences compared with the tungsten case: 1. the transition for the flux is centered around $CZ^2 = 0.5$; and 2. the transition for the flux is at lower concentration than the transition for turbulence intensity and growthrate, which is opposite to the tungsten case. However, our main conclusion stands: the transition is steeper for the flux than for turbulence, and steeper for turbulence than for the growth-rate.

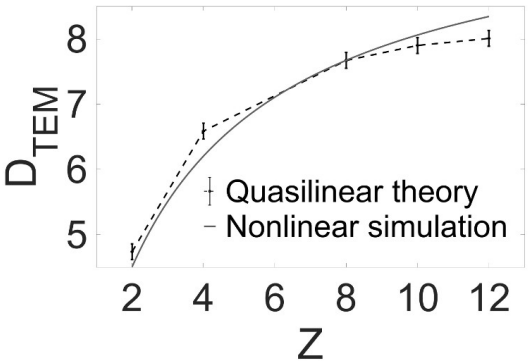

Figure 6.19 – Impurity diffusion coefficient D_{TEM} plotted against the impurity charge number Z in the case of TEM turbulence.

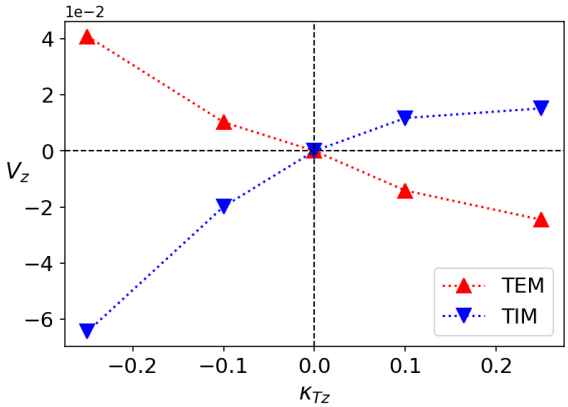

Figure 6.20 – Thermodiffusion velocity V_Z plotted against the impurity temperature gradient, for both TEM and TIM turbulent cases.

Diffusive impurity transport

In Ref. [GLG+19], we describe how impurity diffusive transport depends on the charge number, depending on the nature of the dominant instabilities. Here the impurity species are treated self-consistently but in the trace limit, so that impurity concentrations do not affect the nature of the turbulence.

Fig. 6.19 shows the diffusion coefficient for five different impurities with the same mass number ($A = 20$) but with 5 different charge numbers Z from 2 to 12 in the case of TEM turbulence. We observe that diffusion significantly increases with Z. In contrast, in TIM turbulence, it decreases with Z. Both results qualitatively agree with quasilinear theory. The dependency on mass number A is much weaker.

Thermo-diffusive and curvature-driven pinches

In Ref. [LGL+20], we use five different values of impurity temperature profiles to investigate the thermo-diffusive pinch. Fig. 6.20 shows that, as expected, the pinch velocity V_Z disappears when the temperature profile is flat. V_Z changes its sign when the temperature gradient does. We observe that the impurity pinch depends on the TIM or TEM nature of the turbulence.

Finally we demonstrate that the direction of the impurity curvature pinch is inward in the case of a positive magnetic shear, while a negative magnetic shear switches the sign of V_Z and therefore prevents impurity core accumulation, in agreement with quasilinear theory.

Chapter 7

Conclusions and outlook

In this chapter, let me summarize in Sec. 7.1 the analogies and differences between the models, and the main results developed in this manuscript, and propose in Sec. 7.2 a long-term research project to further our understanding of Vlasov turbulence.

7.1 Conclusions

In this manuscript, after introducing Vlasov plasmas in general action-angle formalism, and subcritical instabilities in neutral fluids and plasmas, we studied three main models (and some variants) of collisionless [1] plasmas:

1. the Berk-Breizman model for Langmuir waves driven by a supra-thermal population, including prescribed wave damping γ_d,
2. the 2-species, 1D Vlasov-Poisson model for sound waves driven by a velocity drift between thermal ions and thermal electrons, i.e. current-driven ion-acoustic (CDIA) instability,
3. the electrostatic bounce-averaged gyrokinetic model for trapped particle-driven 2D turbulence in tokamaks with simplified geometry.

Table 7.1 summarizes important analogies and differences between these models.

In both models 1. and 2., finite wave damping (externally applied in the BB model; due to ion Landau damping in the CDIA model) allows for the spontaneous creation of self trapped structures (holes and clumps) in the two-dimensional (2D) phase-space, whose median velocity evolves in time, resulting in spectral components with a frequency shift $\delta\omega(t)$ (chirping). The growth of phase-space structures results from momentum exchange between the structure and the wave, or between species, which is due to the dissipation acting on structures. The evolution of holes and clumps is a self-organization process, which provides the energy required to balance dissipation. In the project I propose in Sec. 7.2, an important objective is to investigate whether similar processes typically occur in model 3., and ultimately in tokamak core turbulence.

We developed a theory gives a simple relation between the growth of self-coherent PS structures and that of the wave energy (the energy-phasestrophy relation). Based on the theory, we explain the mechanism of subcritical instabilities as follows. Landau damping generates a seed phase-space structure, whose growth rate can be positive if the growth due to momentum exchange overcomes decay due to collisions. Not surprisingly, the theory for 1D Vlasov plasma has considerable overlap with those describing the evolution of flows in a quasi-geostrophic fluid. Both are 2D systems which supports waves, and are constrained by two invariants: energy and enstrophy in the fluid case, wave energy and phasestrophy in the Vlasov case. The mechanisms involved are relevant to many laboratory and space plasmas, where wave-particle interactions are essentially 1D. In the BB case, the energy-phasestrophy relation provides simple expressions of the nonlinear growthrate of a single hole of size Δv,

1. Although we demonstrated the importance of a qualitatively realistic collision operator in the context of the BB model, we focused on regimes which are collisionless in the sense that collision frequencies are much smaller than wave frequencies.

	BB model	Vlasov-Poisson e$^-$ & i$^+$	Bounce-averaged GK
Dim. of real space	1D	1D	2D
Dim. of PS of trajectories	2D	2D	2D
Dim. of PS of f	2D	2D	3D
Kinetic species	1	2	1, 2, or 3
Spatial boundary conditions	Periodic	Periodic	Periodic in α, thermal baths in Ψ
Collisions	Krook or drag+diff.	None	None
Angle	$kx - \omega t$ ($\sim m\theta + n\zeta - \omega t$)	$k_1 x$	$\alpha_3 = \alpha \approx \langle\zeta\rangle$
Action	$m(v - v_R)/k$	mv/k_1	$J_3 \approx q_s \Psi$
Eq. hamiltonian	$\frac{1}{2}\frac{k^2}{m}J^2$	$\frac{1}{2}\frac{k_1^2}{m}J^2$	$(1 + e\Omega_d\Psi)E$
Pert. hamiltonian	$e\phi_0 \cos\alpha$	$q_s\phi$	$q_s J_{0,s}(E)\phi$
Type of waves	Langmuir ($\sim$ AEs, EGAMs)	Ion-acoustic waves	TIM and TEM
Driving	Energetic particles	Current	Pressure gradient
Resonance	1D free streaming	1D free streaming	Precession
Dissipation	Prescribed γ_d	Ion Landau damping	Electrons ($\imath\delta$)
Turbulence	No (single wave)	CDIA turbulence	TIM/TEM turbulence
Subcr. instability[1]	Yes	Yes	Open-question
Threshold with:			
1% fluct.[2]	$\gamma > -0.5\gamma_L$	$v_d > 0.98 v_{d,\mathrm{cr}}$	Open-question
3% fluct.[3]	$\gamma > -1.5\gamma_L$	$v_d > 0.95 v_{d,\mathrm{cr}}$	Open-question
initial PS hole	$\gamma > -2\gamma_L$	$v_d > 0.5 v_{d,\mathrm{cr}}$	Open-question
Simulation code	COBBLES	COBBLES ou PICKLES	TERESA
Method	Semi-Lagrangian	Semi-Lagrangian ou PIC	Semi-Lagrangian

[1] self-trapping-driven
[2] with initial random fluctuations at level $e\tilde{\phi}/T \approx 1\%$, where $\tilde{\phi}$ is the potential r.m.s.
[3] with initial random fluctuations at level $e\tilde{\phi}/T \approx 3\%$

Table 7.1 – Analogies and differences between the 3 main models studied in this manuscript.

$\gamma^{\mathrm{NL}} \sim \gamma_d \Delta v \partial_v f_0$, of the initial perturbation threshold, and predicts the persistence of nonlinear instability in the marginally linear unstable regime. The theoretical arguments are in good agreement with numerical simulation results.

In the context of the BB model, we quantified several effects of finite collisions on chirping velocity and chirping period, in the ideal limit of a sine mode structure. Finite Krook collisions bend chirping branches. The discrepancy from square-root time dependency is 27% after one collision time. In the quiescent phase of the periodic chirping regime, relaxation oscillations are mainly due to collisional diffusion, which brings a hole/clump pair to a shape such that the linearized kinetic equation yields a negative growth rate, before the hole and clump are small enough (in amplitude, large in width) to recover a positive growth rate. The subsequent burst occurs before the velocity distribution completely recovers, leading to instantaneous growth rate about half the initial linear growth rate. Larger values of diffusion shorten the period by combining two effects: 1. structure dissipation during the burst and 2. faster recovery of a positive growth rate. Larger values of drag shorten the period if the quiescent phase is large enough, by deceleration of hole/clump pair, which yields larger nonlinear growth rate. Larger values of drag lengthen the period if the quiescent phase is short, by deepening the hole, which then survives longer.

We named and define sub-categories of chirping, namely periodic, bursty, intermittent, chaotic, steady hole, wavering hole, oscillating hole, hooked and sub-categories that characterize the asymmetry between downward and upward frequency sweeping. Then, the long-time nonlinear evolution was systematically categorized by an algorithm, which could be readily adapted to analyze experimental data. We investigated two complementary parameter spaces: 1. the (γ_d, ν_d) space for fixed drag/diffusion ratios; 2. the (ν_f, ν_d) space

for fixed damping rates, close to and relatively far from marginal stability; for a range of parameters including ITER-relevant collision frequencies, and parameters that can be used to reproduce magnetic signals of JT-60U and MAST experiments. We obtained behaviour bifurcation diagrams which provide the parameter range for each regime, and the relationship between regimes. When $\nu_f \ll \nu_d$, the phase diagram is qualitatively similar to what was obtained with Krook collisions, although chirping solutions can be intermittent, bursty or periodic, in addition to the chaotic behaviour found in the Krook case. We show that quasi-periodic chirping is a special case of bursty chirping, limited to a region relatively far from marginal stability ($\gamma_d/\gamma_{L0} = 0.2 - 0.7$). The presence of significant drag qualitatively modifies the nonlinear bifurcations. Steady-state, periodic and chaotic solutions, which are devoid of significant phase-space structure dynamics, are replaced by long-lived phase-space holes. The periodic chirping regime almost disappears. We didn't find any solution for which downward chirping is dominant.

These observations call for experiments, where collision frequencies may be used as a proxy to nonlinear regime, and/or chirping period, to mitigate energetic particle transport in Alfvén wave experiments.

By fitting the chirping velocity, lifetime and period, between COBBLES simulations of the BB model and TAEs in JT-60U and MAST, we estimated the local linear drive, external damping and collision frequencies, each within 10% inaccuracy. Our results shows the existence of modes with relatively large drive. The fact that we get the same results for two widely different tokamaks suggests that the existence of a relaxation oscillation around marginal stability, with the linear condition $\gamma \sim \gamma_L$, is a general feature of periodic chirping TAEs. Although significant work is needed to establish a one-to-one correspondence, we listed key points that suggest that it is reasonable to apply the BB model quantitatively to periodic, quasi-symmetric, slightly-chirping, small-amplitude TAEs on tokamaks. Our evidences for this bold claim are 1. a quantitative agreement of our simulations with the time-series of perturbation amplitude measured in JT-60U and MAST; 2. collision frequencies in agreement with independant estimations from equilibrium profiles measured in JT-60U, within experimental errorbars; 3. a reasonable agreement for the saturated bounce frequency estimated in Ref. [PBG$^+$04].

We extended the BB model to include fluid coupling between two modes. The model combines a 1D kinetic equation with equations for period doubling. Two regimes have been investigated. In a first regime, of successive fluid then kinetic growth, the dormant subcritical mode is first triggered by fluid coupling to the supercritical mode, which allows it to reach amplitudes of the same order of magnitude as the supercritical mode. This amplitude is above the threshold for the conventional kinetic subcritical instability. Then, the amplitude can keep growing by momentum exchange between the wave and PS structure(s), accompanied by significant chirping. This first regime is obtained for high collisional drag. In this case, the amplitude of the subcritical mode can grow orders-of-magnitude above the amplitude of the supercritical mode. In a second regime, of collaborative fluid-kinetic growth, the subcritical growth is due to an uninterrupted collaboration between fluid and kinetic nonlinearities. This is a new kind of instability mechanism, where fluid and kinetic nonlinearities have similar (in amplitude) contributions to the mode growth. Contrarily to the mechanism developed in earlier theories, the growth occurs much below the amplitude threshold, and without chirping. In this regime, the model reproduces key aspects of experimental observations of strong, abrupt EGAM burts on the LHD. We interpret the observation as a manifestation of the collaborative fluid-kinetic subcritical instability.

We considered a third variant of the BB model, where we relax the assumption of a single sine wave, and assume that dissipation depends on wavelength. We demonstrated the possibility of secondary instabilities of separate modes driven by gradients of the distribution function nearby the separatrix of the saturated PS island of a primary mode. The instantaneous nonlinear growthrate measured in simulations agrees with numerical solutions of the quasi-linear dispersion relation, with includes the primary PS island.

In the context of current-driven ion-acoustic waves in collisionless electron-ion plasmas,

we focused on nonlinear stability. Accurate Vlasov simulations of subcritical two-species plasma have shown that subcritical excitation of the ion-acoustic instability is much more sensitive to initial perturbation than was reported in the existing literature. In fact, earlier simulations were so noisy (suffering from the limited computing power of the 80s) that the initial distribution was linearly unstable. Our semi-Lagrangian simulation is the first simulation of subcritical ion-acoustic instability. If, on the one hand, the initial perturbation is an ensemble of wave, a system with finite ion-electron relative drift does not evolve if it is linearly stable. However, if it is close to marginal stability, and the initial perturbation is very large, the system absorbs the wave energy to form phase-space structures. These structures allow the system to relax by transporting trapped particles throughout the phase-space. In the final stage, a velocity plateau is formed in the electron distribution. If, on the other hand, the system has at least one initial PS structure, then it can drive subcritical instabilities by stirring the phase-space in its wake, even far from marginal stability. When the initial structure is unstable, the system may or may not ultimately relax into a velocity plateau, depending on the drift velocity and the parameters of the initial structure.

When the velocity drift is finite, a single electron phase-space hole can grow nonlinearly by climbing the velocity gradient. After it reaches the top of the electron distribution $v_{0,e}$, it decays while still accelerating. This process leaves a trail of negative f_e perturbations in the $v < v_{0,e}$ half of the phase-space, and a trail of positive perturbation in the other, $v > v_{0,e}$, half. Negative perturbations have a natural propensity to coalesce, and form many holes. This process can overcome ion Landau damping when $v_d > 0.5 v_{d,\mathrm{cr}}$ (roughly). When many holes are formed, a large region of phase-space becomes turbulent, and individual holes lose their identity, and so resemble granulations [Dup72]. Phase-space turbulence, which includes many structures, is much more efficient than an ensemble of waves or an isolated hole for driving subcritically particle redistribution, turbulent heating and anomalous resistivity.

We demonstrated that velocity-space redistribution and anomalous resistivity are due not only to PS vortices, but also to a new object called phase-space jets. The latter are highly anisotropic structures, with an extent in velocity of the order of the electron thermal velocity. Compared to phase-space holes, which are very robust structures, jets are relatively transient objects. However, they survive long enough for particles to scatter between low and high phase-space density regions, and drive significant particle redistribution. Jets and holes are associated with fundamentally different transport processes. Hole-driven transport is essentially convective, since trapped particles accelerate along with the hole. Jet-driven transport is essentially stochastic, since particles may accelerate or decelerate along the jet.

In the context of TIM turbulence, we investigated the impacts of electron dissipation on frequency, growth rate, and the energy-structure of the linear modes, as well as on turbulence and turbulent transport. We recovered the electron branch of TIMs. For moderate electron dissipation, each linear mode contains a narrow and strong peak at the resonant energy. Accurately resolving this narrow peak in numerical simulations yields a stringent lower bound on the number of grid points in the energy space: 256 for a 10% accuracy, 1024 for 1%.

The dependency of peak particle flux on electron dissipation is similar to that of the maximum linear growth rate. For high enough electron dissipation, $\delta > 0.005$, when density gradient and temperature gradient are similar, particle flux is of the order of a gyro-Bohm estimate. When the density gradient is significantly larger than the temperature gradient, that is, when there are electron roots with growth-rates comparable to that of most unstable ion roots, particle flux peaks at an order-of-magnitude above the gyro-Bohm estimate. Slight, transient particle pinch is observed in the case of higher density gradient, for smaller values of electron dissipation.

We analyzed the energy-space structure of transport. The flux features a narrow peak in the resonant region, with a width $\Delta E \approx 0.15 T_i$, around the resonant energies. Strikingly, this resonant peak accounts for 90% of the density and heat fluxes. In contrast, the contribution from thermal particles is negligible. Based on these results, a fine mesh in the energy space, in the resonant region, is required to accurately describe the radial transport of density and heat. Quasilinear theory (including the effect of mean flows) qualitatively agree with the simulation results, in terms of global structure in the radial direction, sign throughout the

energy dimension, behavior at small and large energies, and for the resonant peak in terms of its shape, location and width in the energy dimension. However, quantitatively, there is about 50% overprediction at the peak with a plus sign, and 50% overprediction at thermal energies with a minus sign. These errors with opposite sign compensate in such a way that the total density and heat fluxes are only overpredicted by 16%. A term-by-term analysis of the Vlasov equation shows that the non-zonal nonlinear part of radial advection, which is neglected in quasilinear theory, is actually larger than the included linear part. This explains the original discrepancies.

We developed a method for local, unambiguous characterization of transport, based on statistics of highly-accurate test particle trajectories. We tested it by recovering intuitive limits: radial transport in well-developed TIM turbulence is mostly diffusive, while there are important non-diffusive contributions in TEM/TIM turbulence with strong streamer-like structures.

We described a hysteresis between electron/ion temperature ratio and relative zonal flow energy, which indicates how confinement may be improved by short periods of control.

Finally, we investigated a few aspects of trapped impurity transport. The direction of radial gradient of heavy impurities, even at a low concentration, can change the nature of turbulence, between TEM and TIM. As impurity concentration increases, there is a transition for all linear growth rate, turbulence intensity, and impurity density and heat fluxes, centered around $CZ^2 \sim 1$. However, the transition is significantly steeper for the fluxes, because phase-synchronization between impurity density fluctuations and electric potential fluctuations occurs for high enough impurity concentrations, which quenches impurity transport. The steep transition for the turbulent flux may be viewed as a threshold, which gives the range of validity of the passive treatment, $C < 2 \times 10^{-4}$ for W^{40+} tungsten, and $C < 10^{-2}$ for C^{6+} carbon. For low to moderate charge numbers $2 < Z < 12$, diffusion significantly increases with Z in TEM turbulence, and decreases with Z in TIM turbulence, in agreement with quasilinear theory. The dependency on mass number A is much weaker. A scan in temperature gradient confirms that thermo-diffusive pinch vanishes for flat temperature profile, that the impurity pinch depends on the TIM or TEM nature of turbulence, and that the direction of the impurity curvature pinch is inward (outward) in the case of a positive (negative) magnetic shear, in agreement with quasilinear theory. These results reinforce the credibility of bounce-averaged gyrokinetics to investigate fundamental mechanisms and discover new trends.

7.2 Outlook

7.2.1 Phase-space turbulence, and granulation

State-of-the-art

More than four decades ago, Dupree proposed a novel turbulent state, characterized by the presence, not only of a collection of waves with random phases, but also of small-scale structures in the phase-space of particle distribution [Dup72]. In a limit of narrow wave spectrum, these structures would take the form of BGK modes, with a vortex structure in phase-space. For a wide wave spectrum, though, which is more relevant to drift-wave turbulence, there is a competition between the formation by wave-particle resonance of BGK modes, and their dispersion by the ambient turbulence. The result of this competition is predicted, by analytic theory, to take the form of a smaller scale (compared to BGK modes) random granulation of phase-space.

More recently, many authors (including myself) have discussed the importance of granulation in drift-wave turbulence and transport [TDH90, DST$^+$83, BDT88a, DII10, KID$^+$14a, KID$^+$14b, KID$^+$17], based on various analytic models. Numerical investigation remains to be performed. This poses a challenge for the conventional gyrokinetic approach, because resolving fine-scale structures in energy space makes such simulation very costly in terms of computing power. Attempts have been made to resolve fine-scale velocity-space structures in local gyrokinetic simulation [WS06]. Evidences of small-scale ($\Delta v_\parallel \ll v_{\rm th}$) structures were found, but the link to granulation was not discussed.

In the context of granulation, electron dissipation is an essential ingredient: it drives the nonlinear growth of phase-space structures [BDT88a], introduces dynamical friction associated with anomalous transport of ion heat and particles due to ion phase-space structures [BDT88a], and yields an important contribution to Reynolds stress, which can drive toroidal flows [KIDI13]. The trapped-ion reduced model with simple $\imath\delta$ electron dissipation is a promising tool to bootstrap the numerical study of granulation in drift-wave turbulence.

Objective

The objective of my project is to provide a new qualitative understanding of fundamental mechanisms at play in PS turbulence and granulation. To this aim, we will document, analyze, model, and if possible predict (via calculations, or scaling laws, or a combination) the statistical behavior of microscopic PS structures, and their macroscopic impacts, for Kubo numbers both $K \ll 1$ and $K \sim 1$. This encompasses the entirety of Fig. 1.1, at the expense of other aspects (e.g. detailed geometry, full dimensionality, and some classes of particles, which are known to have important qualitative impacts), which can be reintroduced later. To divide and conquer this ambitious objective, we can introduce two phases:

1. In phase 1, the objective is to characterize and develop a theory of PS turbulence, which corresponds to the limit $K \ll 1$, in both homogeneous and inhomogeneous plasmas. We will focus on regime where mean field evolution is governed by PS structures. In the context of granulation, phase 1 is a shortcut, because PS vortices may then be virtually decoupled from the background (phase-independent) wave turbulence.
2. In phase 2, the objective is to characterize and develop a theory of granulation (for $K \sim 1$).

To this aim, we will take advantage of both the COBBLES code and the TERESA code. This allows the investigation of new fundamental mechanisms in tractable analytic calculations, and tractable numerical simulations.

Homogeneous plasmas

The most fundamental concepts of PS turbulence in homogeneous plasma can be explored in simple 1D electron ion plasmas, with periodic boundary conditions, that is the model adopted in chapter 5. As can be seen in Fig. 5.24, we already witnessed cases with a turbulent phase-space, with many (~ 100) interacting vortices, whose sizes are distributed on a relatively broad range of scale. However, a caveat of this simulation is that it is a transient state in an initial-value simulation (without stirring - i.e. decaying turbulence). As a result, PS turbulence is only transient. PS holes eventually combine into a handful of large ones. We will need to apply a current drive to stir turbulence continuously and study the statistical steady-state.

Inhomogeneous plasmas

As for granulation in fusion plasmas, the bounce-averaged gyrokinetic model contains the essential ingredients:
— kinetic wave/particle interactions,
— free-energy, as well as a mechanism of energy dissipation,
— inhomogeneity of the mean fields.
However, important work is required to model the effects of collisions. By analogy with the BB model, we can expect collisional diffusion to smooth out PS structures above some value of collision frequency.

The plasma as a collection of PS vortices

To develop the analytic theory, we can attempt to adopt a new starting point. We will first assume a given distribution and dynamics of PS vortices, and adapt conventional and modern methods of statistical analysis [DII10, Kro15], to the distribution of PS vortices

instead of the distribution of particles. We will aim for a statistical description of plasmas as collections of PS vortices, and investigate the impacts of PS turbulence on the mean fields, such as turbulent mixing, or structure formation in real space. In other words, departing from the seminal work of Dupree, instead of attempting to develop from scratch a self-consistent turbulent theory for $K \sim 1$, we may attempt to build the foundations of a new theory upon the $K \ll 1$ limit, before aiming for $K \sim 1$.

In parallel with this approach, we can continue to build on Dupree's original granulation theory by confronting it to numerical simulations, and incorporating scaling laws found in the simulations. By creating artificial structures, we can gain crucial hints about favorable and unfavorable conditions

Subcritical regime

Characterizing granulation only requires adequate simulation codes, and numerical diagnostics. Distilling this knowledge into a deep understanding of granulation, however, is extremely challenging because granulation couples wave turbulence with PS turbulence. One may then aim at conditions where PS turbulence is decoupled from wave turbulence. We can expect these conditions to be met near marginal stability, and especially in a subcritical regime, if it exists. In these cases, PS vortices will dominate over wave turbulence.

7.2.2 Other projects

In parallel with the above main research programs, I plan to contribute to other research topics, mainly those already under development by the "High-temperature plasma" team in Institut Jean Lamour:

— We plan to further analyze impurity transport based on the gyrokinetic code GYSELA. This is the main task of my second PhD student, Kyungtak Lim, who started his PhD program in October 2018.

— Conception of a new plasma experiment: SPEKTRE, a cylindrical magnetized plasma device, with a length of a few meters, and a diameter of about one meter. I will also contribute to building the research program, including investigations of turbulence.

— Analytical and numerical investigation of plasma/wall interactions and plasma sheets based on kinetic models. We have published a first output based on a 1D/3V model [MLF+19], in the presence of a constant and oblique magnetic field, with an amplitude such the Debye length is intermediate between electron and ion Larmor radii. We are currently developing a 2D model, which in particular will allow the study of electric arc formation on walls.

— Application of a model of charged infinite planes, to study validity limits of the Vlasov equation.

Annexe A

Résumé en langue française (Summary in french)

Ce mémoire d'habilitation à diriger des recherches présente une synthèse de mes principaux travaux de recherche sur la physique des instabilités, de la turbulence et du transport turbulent dans les plasmas chauds, et notamment les processus non-linéaires sous-jacents.

A.1 Thèmes de recherche

A.1.1 Contexte

Mes recherches s'inscrivent principalement dans le contexte de la fusion thermonucléaire contrôlée par confinement magnétique (Fig. A.1), mais trouvent aussi des applications dans les plasmas astrophysiques et les interactions laser-plasma. La fusion thermonucléaire promet une énergie propre, renouvelable et universelle. Les réactions de fusion requièrent une température de l'ordre de 100 millions de degrés. La matière est alors sous forme de plasma, dans lequel les atomes sont ionisés et les électrons sont libres. Dans la chambre toroïdale d'un réacteur de fusion thermonucléaire, tel qu'un tokamak, le plasma est confiné grâce à un fort champ magnétique. La viabilité d'un tel réacteur requiert d'important progrès dans la compréhension du transport de particules, de chaleur et d'énergie entre le cœur et le bord du plasma, qui résulte principalement d'ondes électromagnétiques. Ces ondes électromagnétiques naissent en exploitant l'énergie libre qui se trouve dans les gradients de pression, de courant électrique, et de densité de l'espace des phases (ce qui inclue les anisotropies de température, et les gradients en vitesse). Ces instabilités peuvent prendre principalement deux formes :

— des modes macroscopiques,
— des fluctuations microscopiques qui forment une turbulence (Fig. A.2).

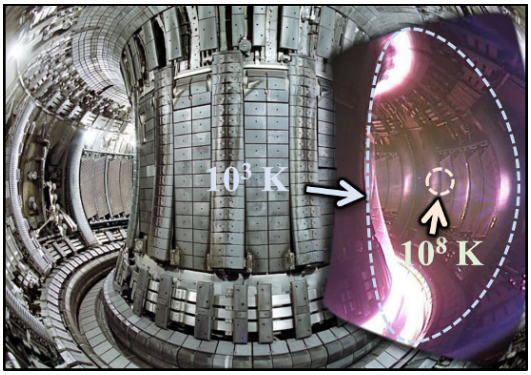

FIGURE A.1 – Composition de photographies de l'intérieur d'un tokamak. Les températures du coeur et du bord sont indiquées en ordre de grandeur. Photo : CCFE, EFDA-JET.

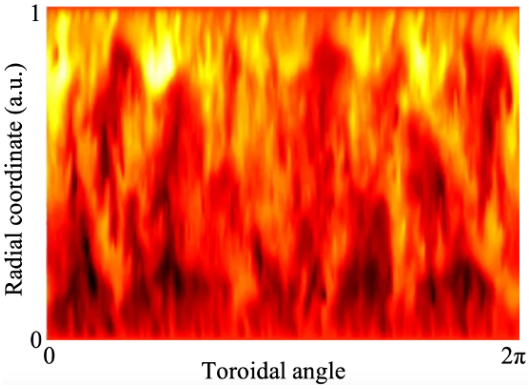

FIGURE A.2 – Illustration de la turbulence. Fluctuations du potentiel électrique obtenu dans une simulation TERESA.

Mes recherches visent à clarifier la physique de ces instabilités, et leurs effets sur les caractéristiques du plasma (notamment la turbulence et le transport turbulent), à l'aide de modèles cinétiques, qui prennent en compte de manière statistique la dynamique des particules dans l'espace des phases.

A.1.2 Vue d'ensemble

Mes recherches incluent les activités suivantes :

— Développement de théories analytiques et de modèles réduits pour les phénomènes non-linéaires dues aux particules énergétiques dans les plasmas de fusion [LIG09, NLG+10, LI12, Les13, LD13, SKI+16, SKI+17, SIH+17, DGLW19]. Application à l'interprétation de données expérimentales [LIS+10, NGG+10, IIO+16, LII+16b, IIK+16, LII+16a, IIL+17, HCY+18].

— Simulations numériques de très haute précision de plasmas unidimensionnels [LDK14a, LDK14b, Les16]. Applications à la turbulence acoustique ionique dans la magnétosphère, le vent solaire, et dans des contextes de reconnexion magnétique. Applications à la turbulence électrostatique dans les interactions laser-plasma.

— Simulations et analyses du transport turbulent en présence d'impuretés, telles que des particules de tungsten [IGL+18, GLG+19, LDL+20]. Ces particules qui proviennent de l'érosion de l'enceinte du tokamak peuvent, si elles sont transportées vers le coeur en quantité non négligeable, détériorer fortement l'efficacité de production d'énergie de fusion. Il est donc urgent de clarifier les mécanismes de transport des impuretés pour guider le développement de régimes d'opération efficaces.

— Simulations de méthodes de contrôle pour basculer d'un régime de mauvais confinement à un régime de bon confinement [GLRD16]. Ces nouvelles méthodes tirent avantage d'un phénomène d'hystérésis que nous avons découvert, entre la température des électrons et un écoulement fluide à large échelle appelé écoulement zonal [GLR+17].

— Caractérisation du transport turbulent dans les tokamaks [KID+14a, KID+14b, KID+17, LCMD+17, MLG+18, MLG+19] et les stellerators [III+15].

— Analyse des interactions entre turbulence et structures macroscopiques dans les plasma expérimentaux en géométrie cylindrique [MKS+13, IMK+14, YIK+14, KYI+15, AIS+16, IKK+16].

Dans la suite de ce document, je choisi de décrire les sujets qui ont menés à mes publications les plus citées.

A.1.3 Vortex dans l'espace des phases

Les plasmas chauds sont souvent le lieu d'importantes interactions résonantes entre ondes et particules. Mes contributions touchent à un effet cinétique non-linéaire, lié à ces résonances : l'auto-piégeage de particules par leur propre potentiel électrique. Ce phénomène donne lieu à la formation de structures semblables à des vortex, mais dans l'espace des phases de la fonction de distribution des particules (espace réel + espace des vitesses). En étudiant la dynamique des particules dans l'espace des phases, il est possible de clarifier les mécanismes de phénomènes qui semblent contre-intuitifs du point de vue d'un observateur de l'espace réel. Je me suis concentré sur trois types d'ondes, les ondes engendrées par la présence de particules supra-thermiques dans les plasmas de fusion, les ondes acoustiques ioniques dans les plasmas astrophysiques, et les ondes de dérives dues aux particules piégées dans les tokamaks. J'ai clarifié l'impact des structures de l'espace des phases sur la stabilité et l'évolution non-linéaire des ondes, ainsi que sur le transport de particules, la résistivité anormale, et le chauffage turbulent associés à ces ondes. Mes découvertes ont ouvert la voie à l'application expérimentale des structures de l'espace des phases comme diagnostic et moyen de contrôle.

En particulier, le confinement des ions énergétiques (supra-thermiques) produits par les réactions de fusion est primordial. En effet, les ions énergétiques doivent redistribuer leur énergie au reste des particules (thermiques), afin de perpétuer le chauffage, et d'éviter d'endommager l'enceinte. Or, les particules énergétiques excitent par résonance des perturbations électromagnétiques, appelés modes EP, qui induisent un transport important de ces

particules. Les structures de l'espace des phases ont un rôle essentiel dans l'évolution de ces modes EP, qui menacent la viabilité d'un réacteur de fusion.

Plus précisément, je me suis concentré sur les effets d'un phénomène cinétique non-linéaire : l'auto-piégeage de particules par leur propre potentiel électrique. La figure A.3 illustre comment un déficit local d'ions induit un puit de potentiel qui piège ces mêmes ions dans un vortex de l'espace des phases. Ce phénomène est essentiel dans les plasmas chauds, où les particules peuvent résonner fortement avec les ondes, du fait de la quasi-absence de collisions. L'existence de ces structures a été prédite par simulation numérique [RB67], interprétée par la théorie [Sch79], puis observée expérimentalement dans un vaste éventail de plasmas astrophysiques et de laboratoire [ES06]. Dans les plasmas de fusion, les structures de l'espace des phases dominent l'évolution des modes EP dans de nombreux cas. Ces structures sont alors observées, bien qu'indirectement, via l'effet de leur évolution sur les perturbations magnétiques [BBB+06]. En effet, un vortex peut accélérer ou décélérer, ce qui se traduit par une évolution temporelle de la fréquence du mode (selon la formule $\omega = kv$). Ce phénomène de sifflement non-linéaire sur une échelle de la milliseconde est régulièrement observé dans de nombreuses expériences. La figure A.4(b) montre un exemple de sifflement non-linéaire dans le plasma torique de MAST (CCFE, Royaume-Unis). Ici, deux structures coexistent dans l'espace des phases, et donnent lieu à deux branches dans le spectrogramme. L'une croît et l'autre décroît en fréquence. La majeure partie de la théorie non-linéaire, est basée sur un modèle communément appelé Berk-Breizman (BB) [BBP96]. Dans ce modèle, on utilise la séparation des échelles de temps entre l'évolution de la structure tridimensionnelle d'un mode ($\sim$ 100ms), d'une part, et de l'évolution de son amplitude et de sa phase par interaction non-linéaire avec les particules énergétiques ($\sim$ 1ms) d'autre part. Ces dernières interactions sont essentiellement 1D, et l'on peut alors modéliser l'évolution rapide du mode et de la fonction de distribution des particules énergétiques par un modèle cinétique 1D.

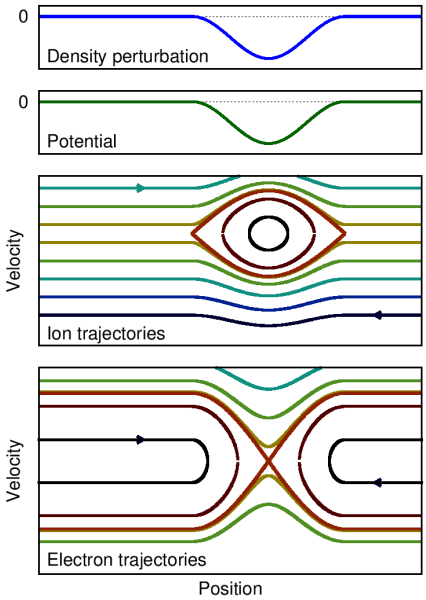

FIGURE A.3 – Schéma d'une structure auto-piégée dans l'espace des phases. Haut : perturbation de la densité ionique. Milieu : potentiel électrique généré par le vortex. Bas : trajectoires des ions dans l'espace des phases.

Questions ouvertes

De nombreux groupes de recherche ont pour objectif de prédire la stabilité des modes EP dans les futures expériences telles qu'ITER ou W7-X. Un problème majeur est que les phénomènes de dissipation sont si complexes que la théorie ne fournit qu'un ordre-de-grandeur du taux de dissipation γ_d. Cela ne permet pas de connaitre le signe du taux de croissance linéaire, $\gamma = \gamma_L - \gamma_d$, où γ_L est le taux d'excitation, lié à l'énergie libre. D'autre part, la mesure de γ_d ne se fait que très rarement, dans des expériences dédiées. La mesure de γ_L reste élusive, ou repose sur l'hypothèse $\gamma_L \approx \gamma_d$, que j'ai montré fausse en général. De plus, la théorie prédit la croissance de modes sous-critiques à seuil, c'est-à-dire non-linéairement instables même si $\gamma < 0$. Mais les théories existantes ne donnaient pas leurs conditions d'excitation. En 2010, j'ai donc entrepris de construire une théorie de stabilité non linéaire des modes EP, qui puisse s'appliquer facilement aux expériences, sans besoin d'un système de mesure dédié. L'idée est qu'un signal, même obtenu par une mesure non-intrusive (bobine de Mirnov), tel que celui de la figure A.4(a), contient une richesse d'informations qui n'étaient jusqu'alors que très peu exploitées.

Contribution

Mes activités incluent le développement de théories analytiques, le développement (à partir de zéro ou en collaboration) de simulations numériques, ainsi que l'analyse de données expérimentales. La première étape consistait à combler le fossé qui séparait les simulations BB de sifflement non-linéaire d'une riche variété d'observations. Il s'est avéré que les régimes expérimentaux n'étaient pas accessibles aux codes existants, car leurs conditions sont particulièrement problématiques du point de vue de la stabilité des codes cinétiques. J'ai donc développé un code basé sur une implémentation robuste (localement conservative), et un opérateur de collision plus sophistiqué que dans les codes existants [LIG09]. Cela m'a permis d'explorer pour la première fois les régimes expérimentaux, avec le modèle BB, et de reproduire les nombreuses formes que prennent dans les expériences le sifflement non-linéaire [LIS+10]. J'ai utilisé ce code pour approfondir notre compréhension des modes EP :

1. J'ai apporté des preuves numériques d'un transport non-diffusif des particules énergétiques, associé aux structures dans l'espace des phases, de magnitude comparable au transport diffusif. Cette analyse suggère que le transport peut être contrôlé efficacement en modifiant légèrement et localement les taux de collisions, afin de dissiper les structures (et non l'énergie de l'onde).
2. J'ai défini une catégorisation systématique des différents régimes de sifflement. J'ai exploré les bifurcations entre ces régimes [LI12]. J'ai indiqué comment les paramètres du plasma peuvent être ajustés pour bifurquer d'un régime à l'autre, et ainsi réduire le transport.
3. J'ai clarifié le mécanisme et les impacts des instabilités sous-critiques. J'ai démontré le comportement hystérétique des modes EP au voisinage de $\gamma = 0$.
4. J'ai réalisé les premières étapes du développement d'une théorie de la turbulence dans l'espace des phases. J'ai démontré un théorème qui fait le lien entre l'énergie des ondes et l'autocorrélation de la fonction de distribution des particules $\langle \delta f^2 \rangle$. Cette dernière quantité est une mesure des structures auto-piégées dans l'espace des phases. J'ai appliqué ce théorème au cas dominés par une structure isolée (un vortex de l'espace des phases), pour donner la première expression analytique du taux de croissance non-linéaire, et du seuil en amplitude [LD13].

J'avais enfin en main tous les éléments nécessaires pour exploiter les informations contenues dans une mesure des perturbations magnétiques telle que celle de la figure A.4(a). J'ai alors développé une méthode non-intrusive qui permet d'évaluer le taux de croissance, le taux de dissipation et les fréquences de collision de modes EP. La figure A.4(b) illustre cette méthode, qui consiste à faire coïncider les spectrogrammes de l'expérience et des simulations BB. Les paramètres d'entrée du modèle conduisent alors aux inconnues désirées. Comparée aux autres méthodes, même intrusives, on obtient alors des résultats très précis, car on exploite la sensibilité du comportement non linéaire aux caractéristiques linéaires, eux-mêmes sensibles aux paramètres du plasma. Grâce à trois collaborations successives, j'ai pu appliquer cette procédure à l'analyse des données des machines MAST (CCFE, Royaume-Unis), JT-60U (JAEA, Japon) et LHD (NIFS, Japon). Les résultats obtenus ont été vérifiés par deux autres méthodes indépendantes, basées sur une modélisation complètement tridimensionnelle, combinée à des mesures expérimentales pour l'une d'elles. Dans le cas du LHD, j'ai inclut le couplage fluide entre plusieurs modes, généralisant ainsi le modèle conventionnel de Berk-Breizman. Le nouveau modèle interprète l'expérience comme la première observation d'un mode sous-critique. Ces résultats ont fait

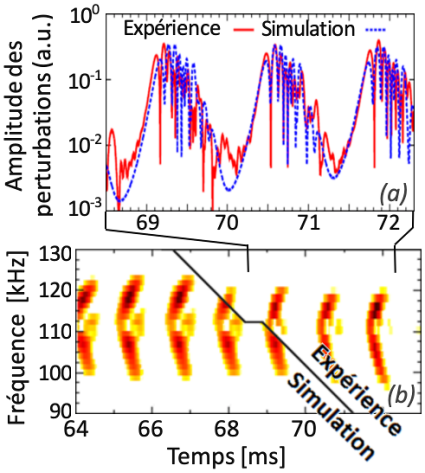

FIGURE A.4 – Enveloppe des perturbations magnétiques, filtrées entre 90 et 130 kHz (a) et spectrogramme (b). Comparaison entre l'expérience MAST et la simulation numérique.

l'objet de 2 articles dans le journal Physical Review Letters [IIO+16, LII+16b]. Ces résultats ont de fortes implications pour l'interprétation des expériences existantes, et la conception des futures machines, puisqu'il indique un fait pour la première fois supporté par l'expérience, selon lequel la stabilité des modes déstabilisés par résonance est une question cinétique et non-linéaire.

Application aux plasmas astrophysiques

J'ai également étudié les structures de l'espace des phases dans la turbulence due aux ondes acoustiques ioniques, dans le contexte de plasmas spatiaux, tels que la magnétosphère, la magnétopause, et le milieu interplanétaire. J'ai clarifié les conditions nécessaires à la croissance non-linéaire. J'ai montré que les structures ont des impacts importants sur la résistivité du plasma, et le chauffage turbulent des électrons [LDK14a]. J'ai découvert l'existence d'un nouveau type de structure dans l'espace des phases, qui s'apparente au filament qui relie deux galaxies en collision. J'ai montré que ces filaments sont responsables pour une partie importante du transport turbulent [LDK14b].

A.1.4 Anatomie du transport turbulent

Résumé

Le succès de la fusion thermonucléaire repose sur une meilleure compréhension du transport turbulent dans les plasmas chauds, qui découle principalement des ondes de dérive (oscillations microscopiques, déstabilisées par les gradients de densité ou de température). Mes recherches visent à clarifier les mécanismes sous-jacents à ce transport. Il s'agit d'étudier, par simulations numériques, les propriétés statistiques du transport turbulent en fonction des paramètres du plasma, ainsi que la formation de structures cohérentes à partir de la turbulence.

Contexte

Dans un plasma toroïdal de fusion par confinement magnétique, le transport de particules et d'énergie limite la pression, et donc les réactions de fusion, au cœur du plasma. Les observations expérimentales et les simulations numériques s'accordent sur le fait que les principaux coupables qui échappent encore au contrôle sont les ondes de dérive. Ces ondes ont une longueur d'onde ($\sim$ 1mm) bien plus petite que le libre parcours moyen des particules ($\sim$ 10km), ce qui implique d'importantes interactions résonantes. Pour prendre en compte ces effets de manière précise, il est nécessaire de déployer une modélisation cinétique. Par contraste avec la modélisation fluide, qui décrit l'évolution de grandeurs thermodynamiques (telles que la densité et la température) dans l'espace réel, la modélisation cinétique décrit l'évolution d'une fonction de distribution de particules dans un espace des phases à 6 dimensions (espace réel + espace des vitesses).

Approche numérique gyrocinétique

Dans un tokamak, les particules chargées ont tendances à s'enrouler autour des lignes du fort champ magnétique ambient. Les trajectoires peuvent alors être décomposées en un mouvement cyclotronique rapide, et un mouvement lent de dérive. L'approche gyrocinétique exploite cette caractéristique en moyennant le mouvement cyclotronique, ce qui permet de réduire la dimensionalité du problème de 6D à 5D. Dans le cadre de la thèse de Kyungtak Lim, que je co-encadre, nous utilisons le code gyrocinétique GYSELA, développé en collaboration avec l'Institut de Recherche sur la Fusion Magnétique (IRFM) du CEA Cadarache. Nous simulons un plasma de tokamak en présence d'une faible concentration d'impuretés telles que les particules de tungsten érodés de la paroi du réacteur. Le transport turbulent (et par collisions) du tungsten peut amener ces particules à contaminer le cœur du plasma, et fortement dégrader l'efficacité d'un réacteur. Il est donc urgent de développer la théorie du transport turbulent d'impuretés afin de pouvoir proposer des méthodes de contrôle. En 2019, nous avons analysé comment le transport d'une impureté dépend de sa charge et de

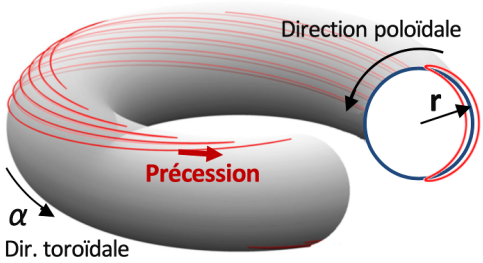

FIGURE A.5 – Trajectoire d'une particule piégée dans un plasma toroïdal magnétisé, et sa projection sur une coupe poloïdale.

sa masse. Un travail est en cours pour comparer ces résultats aux théories conventionnelles et proposer de nouvelles lois de comportement. Une simulation gyrocinétique nécessite des millions d'heures de calculs, réalisés en parallèle sur une dizaine de milliers de processeurs. Une part de mon travail consiste à répondre à des appels à l'exploitation de supercalculateurs. Sur la période 2019-2020 nous avons obtenu 30 millions d'heures de calcul sur le supercalculateur Marconi (21ème machine la plus puissante au monde).

Approche numérique réduite

Il est possible de réduire le temps de calcul de plusieurs ordres de grandeur, en sélectionnant un membre particulier parmi la famille des ondes de dérive qui constituent la turbulence. En effet, la variation d'amplitude du champ magnétique entre le centre du tore et l'extérieur implique qu'une partie importante des particules subit un effet de miroir magnétique. Ces particules piégées suivent un mouvement de rebond en forme de banane dans une projection poloïdale, accompagnée d'une précession dans la direction toroïdale, comme illustré en figure A.5. Ce piégeage magnétique est très différent de l'auto-piégeage électrostatique. Le premier défini les trajectoires d'équilibre, le deuxième est un effet non linéaire dû aux perturbations.

Le mouvement de précession des particules piégées peut résonner avec 2 types d'onde de dérive, appelés Trapped Ion-driven Mode (TIM) et Trapped Electron-driven Mode (TEM). La fréquence d'un tel mode est très inférieure à la fréquence de transit toroïdal des particules passantes et à la fréquence de rebond des particules piégées. L'invariance adiabatique de l'énergie des particules piégées permet alors de réduire l'espace des phases de 5 à 4 dimensions (en faisant une moyenne de rebond, en complément de la moyenne gyrocinétique). Le modèle se simplifie encore en faisant l'hypothèse que ce sont principalement les particules fortement piégés qui résonnent avec le mode. Cette hypothèse relie l'énergie et le moment magnétique. Le modèle est alors réduit à 3 dimensions (r, α, E) dans l'espace des phases de la fonction de distribution [DGBG00] :

— Position radiale moyenne r
— Angle de précession α
— Energie E

Ce modèle réduit 3D n'est valide que dans le cadre des hypothèses mentionnées, mais il a l'avantage de mettre l'étude des processus physiques fondamentaux sous-jacents à la portée des capacités de calcul numérique actuelles. Ce modèle est implémenté dans le code TERESA [CMGGL13], qui a été développé récemment en collaboration avec l'IJL et le CEA. Je contribue à son développement depuis 2013. Une première publication documente l'existence et l'effet de structures fines en énergie, dans la phase linéaire [LCMD+17]. Dans le cadre de la thèse de Julien Médina, que j'ai co-encadré, et qui a obtenu sa thèse en 2019, nous avons exploité le code TERESA pour améliorer la compréhension du transport turbulent. Nous avons montré que le transport peut être dominé par les effets de résonance, de manière étroitement localisée dans l'espace des énergies [MLG+18]. Nous avons ensuite développé un nouveau module de particules tests, qui permettent d'étudier avec précision les mécanismes de transport turbulent à partir des trajectoires et de leurs statistiques [MLG+19]. Plus récemment, nous avons utilisé le code TERESA pour étudier le transport d'impuretés. Nous avons montré qu'un phénomène de synchronisation induit une transition entre deux régimes de transport, avec un seuil en concentration [LDL+20]. Finalement, nous avons étudié comment le transport d'impuretés dépend des gradients de densité [LGL+20].

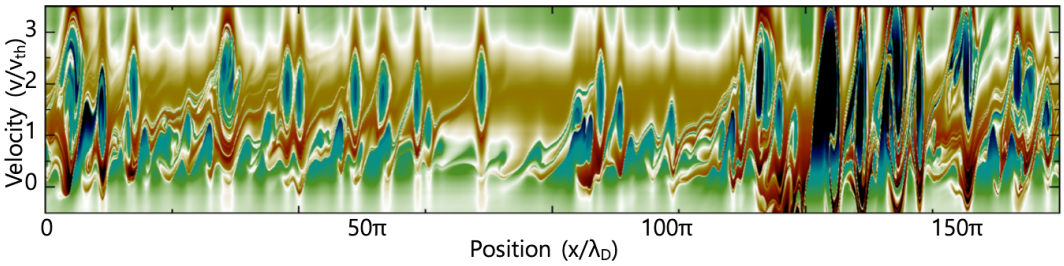

FIGURE A.6 – Phase-space turbulence in a large 1D plasma. Color map of a snapshot of fluctuations in the electron distribution (PS density) in a simulation of 1D turbulence.

A.2 Projet de recherche

A.2.1 Résumé

Mon projet vise à clarifier les mécanismes sous-jacents au transport turbulent dans les plasmas de fusion magnétique. Il consiste à étudier par simulations numériques l'auto-piégeage de particules et la formation de structures dans l'espace des phases associé à ces ondes de dérive, ainsi qu'un effet plus subtil de corrugation de la fonction de distribution, "granulation", qui résulte de la compétition entre formation de structures et dispersion turbulente. Selon la théorie analytique, la granulation a d'importants impacts sur la turbulence et le transport [KID+14a]. Nous utiliserons des simulations numériques pour quantifier les propriétés de la granulation et ses impacts. On se penchera ensuite sur les signatures de la granulation, qui seront susceptibles d'être mesurés.

A.2.2 Objectif

Je souhaite améliorer la prédictibilité des statistiques de la turbulence microscopique, et des impacts macroscopiques de la turbulence, tels que le transport. La figure A.6 illustre la présence de nombreux vortex de l'espace des phases dans une turbulence 1D. L'objectif est de généraliser ces résultats à une turbulence 2D, puis 3D. En passant de 1D à 2D, on s'attend également à une importante différence qualitative. La théorie analytique [Dup72] prévoit une corrugation ou granulation de l'espace des phases, résultat de la compétition entre la formation de structures (appelées alors drift-holes [TDH90]) par piégeage et la destruction des structures par la turbulence ambiante. En présence de granulation, les théories et modèles réduits conventionnels, qui supposent que les perturbations ne sont qu'un ensemble d'ondes incohérentes, trouvent leur limite. Cette limite pourrait expliquer pourquoi le calcul quantitatif du transport turbulent échappe toujours aux simulations numériques dans le cas général. En effet, la granulation induit de nouveaux effets, tel qu'une composante de friction, qui peut avoir d'importants impacts sur la turbulence et le transport, notamment via la génération d'écoulements zonaux [KID+14a]. La granulation de l'espace des phases reste inexplorée par les simulations.

A.2.3 Approche numérique

Les modèles gyrocinétiques, qui réduisent l'espace des phases de 6D à 5D en moyennant le rapide mouvement cyclotronique, incluent en principe la granulation. Cependant, en pratique, les fines échelles de la granulation échappent aux simulations gyrocinétiques, qui se limitent typiquement a quelques douzaines de points de grille dans l'espace de l'énergie. Résoudre la granulation nécessiterait quelques milliers de points, beaucoup trop coûteux en termes de temps de calcul.

L'approche adoptée par le code TERESA, en se focalisant sur les particules piégées, a l'avantage de mettre l'étude de la granulation à la portée des capacités de calcul numérique actuelles.

A.2.4 Approche expérimentale

La théorie analytique prédit des effets indirects macroscopiques. La difficulté est de distinguer le mécanisme responsable. Heureusement, il existe aussi des effets microscopiques qui semblent mesurables. En particulier, nos simulations permettent de préciser comment tirer parti de récents développements de la réflectométrie pour mesurer des pics de fluctuations de densité sur l'échelle de la granulation. Plus tard, notre analyse numérique de la granulation devrait indiquer comment manipuler les paramètres du plasma pour agir sur la granulation et leurs effets. Nous conduirons alors des expériences sur les machines de fusion magnétique pour tester ces idées.

A.2.5 Impacts

Ce projet constitue une extension naturelle de mes recherches de 2D à 3D (dans l'espace des phases). Il promet d'ouvrir la voie à de nouveaux diagnostics, et de nouvelles méthodes de contrôle dans le but de mitiger le transport et ainsi atteindre les conditions de fusion. Il contribuera également au développement de codes gyrocinétiques tels que GYSELA. De plus, puisque les structures de l'espace des phases sont omniprésentes dans les plasmas très peu collisionnels, ce projet aura également des retombées dans les contextes suivants où la turbulence joue un rôle majeur : l'espace entre la Terre et le Soleil (la couronne solaire, le vent solaire, la magnétosphère, et l'application à la météorologie de l'Espace), la propulsion électrique, et la radiation dans les ceintures de Van Allen.

Ce projet vient d'être sélectionné par l'Agence Nationale de la Recherche pour être financé à hauteur de 220 k€(ANR-JCJC) pour la période 2020-2023. Il me permettra de financer une thèse de 3 ans et un contrat postdoctoral de 18 mois, qui seront dédiés à ce projet. Le projet s'appuie aussi sur des collaborations internes, nationales (CEA Cadarache, LPIIM, et LPP) et internationales (UCSD, Kyushu U., et USTC en Chine). Ce projet est donc aussi une formidable opportunité de fédérer un consortium d'expert-e-s et de jeunes chercheu-se-r-s. L'idée est de construire, sur une échelle de la décennie, les fondations d'un vaste champ de recherche, puisque l'évolution exponentielle de la puissance de calcul devrait permettre d'envisager ensuite d'étudier les structures de l'espace des phases dans des modèles 4D, puis 5D.

A.2.6 Autres activités

En parallèle à ce projet de recherche principal, je prévois de contribuer aux autres activités de l'équipe "Plasmas chauds" de l'IJL :

- Conception d'une nouvelle expérience de plasma chaud : SPEKTRE, une machine linéaire de plasma cylindrique magnétisé, longue de plusieurs mètres et d'un diamètre d'environ un mètre. Je contribuerai aussi à la mise en place d'un programme de recherche qui inclut l'étude de la turbulence.
- étude numérique et analytique des interactions plasma/parois, et étude des gaines à l'aide de modèles cinétiques. Une première publication concerne un modèle 1D [MLF+19], et nous développons actuellement un modèle 2D qui nous permettra d'étudier la formation d'arcs électriques sur les parois.
- Développement d'un nouveau modèle de "plans chargés" pour quantifier le domaine de validité des modèles cinétiques conventionnels.

Bibliography

[ADC05] N Ananthkrishnan, Shardul Deo, and Fred Culick. Modeling and dynamics of nonlinear acoustic waves in a combustion chamber. *Combustion Science and Technology*, 177, 01 2005. (Cited on pages 30)

[AIS+16] H Arakawa, S Inagaki, Makoto Sasaki, Yusuke Kosuga, T Kobayashi, Naohiro Kasuya, Yoshihiko Nagashima, Takuma Yamada, M Lesur, A Fujisawa, et al. Eddy, drift wave and zonal flow dynamics in a linear magnetized plasma. *Scientific Rep.*, 6(1):1–7, 2016. (Cited on pages 149)

[ALP79] JC Adam, G Laval, and D Pesme. Reconsideration of quasilinear theory. *Phys. Rev. Lett.*, 43(22):1671, 1979. (Cited on pages 12)

[Arn78] Vladimir Igorevich Arnol'd. *Mathematical methods of classical mechanics.* Springer Verlag, New-York, 1978. (Cited on pages 9)

[Bal12] NJ Balmforth. Bgk states from the bump-on-tail instability. *Commun. Nonlinear Sc. Numerical Simulation*, 17(5):1989–1997, 2012. (Cited on pages 88)

[BB90a] H. L. Berk and B. N. Breizman. Saturation of a single mode driven by an energetic injected beam. i. plasma wave problem. *Phys. Fluids B*, 2(9):2226–2234, 1990. (Cited on pages 15, 27, 44)

[BB90b] H. L. Berk and B. N. Breizman. Saturation of a single mode driven by an energetic injected beam. iii. Alfvén wave problem. *Phys. Fluids B*, 2(9):2246–2252, 1990. (Cited on pages 44)

[BBB+02] D. Borba, H. L. Berk, B. N. Breizman, A. Fasoli, F. Nabais, S. D. Pinches, S. E. Sharapov, D. Testa, and the EFDA-JET Workprogramme. Modelling of Alfvén waves in jet plasmas with the castor-k code. *Nucl. Fusion*, 42:1029–1038, August 2002. (Cited on pages 66)

[BBB+06] H.L. Berk, C.J. Boswell, D. Borba, A.C.A. Figueiredo, T. Johnson, M.F.F. Nave, S.D. Pinches, S.E. Sharapov, and JET EFDA contributors. Explanation of the jet n = 0 chirping mode. *Nucl. Fusion*, 46(10):S888, 2006. (Cited on pages 51, 150)

[BBC+99] H. L. Berk, B. N. Breizman, J. Candy, M. Pekker, and N. V. Petviashvili. Spontaneous hole-clump pair creation. *Phys. Plasmas*, 6(8):3102–3113, 1999. (Cited on pages 27, 44, 50, 51, 72, 76, 85)

[BBP95a] H. L. Berk, B. N. Breizman, and M. Pekker. Numerical simulation of bump-on-tail instability with source and sink. *Phys. Plasmas*, 2(8):3007–3016, 1995. (Cited on pages 39, 44, 72)

[BBP95b] H. L. Berk, B. N. Breizman, and M. S. Pekker. Simulation of Alfvén-wave-resonant-particle interaction. *Nucl. Fusion*, 35:1713–1720, Decembre 1995. (Cited on pages 33)

[BBP96] H. L. Berk, B. N. Breizman, and M. Pekker. Nonlinear dynamics of a driven mode near marginal stability. *Phys. Rev. Lett.*, 76:1256–1259, February 1996. (Cited on pages 31, 32, 44, 45, 150)

[BBP97a] H. L. Berk, B. N. Breizman, and M. S. Pekker. Nonlinear theory of kinetic instabilities near threshold. *Plasma Phys. Rep.*, 23:778–788, sep 1997. (Cited on pages 31, 34, 44, 46)

[BBP97b] H. L. Berk, B. N. Breizman, and N. V. Petviashvili. Spontaneous hole-clump pair creation in weakly unstable plasmas. *Phys. Lett. A*, 234:213–218, feb 1997. (Cited on pages 32, 44, 46, 51, 58, 70, 91)

[BBP+97c] B. N. Breizman, H. L. Berk, M. S. Pekker, F. Porcelli, G. V. Stupakov, and K. L. Wong. Critical nonlinear phenomena for kinetic instabilities near threshold. *Phys. Plasmas*, 4(5):1559–1568, 1997. (Cited on pages 31, 46)

[BBP98] H. L. Berk, B. N. Breizman, and N. V. Petviashvili. Spontaneous hole-clump pair creation in weakly unstable plasmas. *Phys. Lett. A*, 238:408, 1998. (Cited on pages 44, 51)

[BBY93a] H. L. Berk, B. N. Breizman, and Huanchun Ye. Map model for nonlinear alpha particle interaction with toroidal Alfvén waves. *Phys. Fluids B*, 5(5):1506–1515, 1993. (Cited on pages 69)

[BBY93b] B.N. Breizman, H.L. Berk, and H. Ye. Collective transport of alpha particles due to Alfvén wave instability. *Phys. Fluids B*, 5:3217–3225, 1993. (Cited on pages 31, 38)

[BC13] Roberto Bruno and Vincenzo Carbone. The solar wind as a turbulence laboratory. *Living Rev. Solar Phys.*, 10(1):2, 2013. (Cited on pages 3)

[BDT88a] H. Biglari, P. H. Diamond, and P. W. Terry. Theory of trapped-ion temperature-gradient-driven turbulence and transport in low-collisionality plasmas. *Phys. Fluids*, 31(9):2644–2658, 1988. (Cited on pages 27, 118, 145, 146)

[BDT88b] H. Biglari, P. H. Diamond, and P. W. Terry. Theory of trapped-ion-temperature-gradient-driven turbulence and transport in low-collisionality plasmas. *Phys. Fluids*, 31(9):2644–2658, 1988. (Cited on pages 91, 105)

[Ber12] Herbert L Berk. Overview of nonlinear kinetic instabilities. In *AIP Conf. Proc.*, volume 1478, pages 29–49. Am. Inst. Phys., 2012. (Cited on pages 88)

[BF92] R. Betti and J. P. Freidberg. Stability of Alfvén gap modes in burning plasmas. *Phys. Fluids B*, 4(6):1465–1474, 1992. (Cited on pages 66)

[BFG+10] D. Borba, A. Fasoli, N. N. Gorelenkov, S. Gunter, Ph Lauber, N. Mellet, R. Nazikian, T. Panis, S. D. Pinches, D. Spong, D. Testa, and JET-EFDA Contributors. The influence of plasma shaping on the damping of toroidal Alfvén eigenmodes. In *in Fusion Energy 2010 (Proc. 23rd Int. Conf. Daejeon, 2010)*. Vienna: IAEA, 2010. CD-ROM file THW/P7-08 and http://www-naweb.iaea.org/napc/physics/FEC/FEC2010/html/index.htm. (Cited on pages 66)

[BFV+07] S. Briguglio, G. Fogaccia, G. Vlad, F. Zonca, K. Shinohara, M. Ishikawa, and M. Takechi. Particle simulation of bursting Alfvén modes in jt-60u. *Phys. Plasmas*, 14(5):055904, 2007. (Cited on pages 35, 67)

[BGK54] P.L. Bhatnagar, E.P. Gross, and M. Krook. A model for collision processes in gases. i. small amplitude processes in charged and neutral one-component systems. *Phys. Rev.*, 94(3):511–525, May 1954. (Cited on pages 37)

[BGK57] I.B. Bernstein, J.M. Greene, and M. D. Kruskal. Exact nonlinear plasma oscillations. *Phys. Rev.*, 108(3):546–550, Nov 1957. (Cited on pages 4, 14, 41)

[BNR70] H. L. Berk, C. E. Nielsen, and K. V. Roberts. Phase space hydrodynamics of equivalent nonlinear systems: Experimental and computational observations. *Phys. Fluids*, 13(4):980–995, 1970. (Cited on pages 104, 106)

[Bog46] Nikolaĭ Nikolaevich Bogoliubov. Problems of dynamic theory in statistical physics; problemy dinamicheskoi teorii v statisticheskoi fiziki. Technical Report AEC-tr-3852, Federal Publishing House for Technical-Theoretical Literature, Moscow-Leningrad, 1946. (Cited on pages 9)

[Bor14] Daniel Borrero. *Subcritical transition to turbulence in Taylor-Couette flow.* PhD thesis, Georgia Institute of Technology, 2014. (Cited on pages 22)

[BPS+98] JA Boedo, GD Porter, MJ Schaffer, R Lehmer, RA Moyer, JG Watkins, TE Evans, CJ Lasnier, AW Leonard, and SL Allen. Flow reversal, convection, and modeling in the diii-d divertor. *Phys. Plasmas*, 5(12):4305–4310, 1998. (Cited on pages 135)

[Bre10] B. N. Breizman. Nonlinear travelling waves in energetic particle phase space. *Nucl. Fusion*, 50(8):084014, 2010. (Cited on pages 66)

[BRM+01] Jose A Boedo, D Rudakov, R Moyer, S Krasheninnikov, D Whyte, G McKee, G Tynan, M Schaffer, P Stangeby, Philip West, et al. Transport by intermittent convection in the boundary of the diii-d tokamak. *Phys. Plasmas*, 8(11):4826–4833, 2001. (Cited on pages 135)

[BTD85] R. H. Berman, D. J. Tetreault, and T. H. Dupree. Simulation of phase space hole growth and the development of intermittent plasma turbulence. *Phys. Fluids*, 28:155–176, January 1985. (Cited on pages 91, 92, 93)

[BTDBG81] R.H. Berman, D.J. Tetreault, T.H. Dupree, and T. Boutros-Ghali. Computer simulation of nonlinear ion-electron instability. In *Bull. Am. Phys. Soc.*, volume 26, page 1060, 1981. (Cited on pages 93)

[BTDBG82] R. H. Berman, D. J. Tetreault, T. H. Dupree, and T. Boutros-Ghali. Computer simulation of nonlinear ion-electron instability. *Phys. Rev. Lett.*, 48:1249–1252, May 1982. (Cited on pages 29, 92, 93, 95)

[BTF00] DA Baver, PW Terry, and Eduardo Fernandez. Nonlinear instability driven by advection of electron density in collisionless plasmas. *Phys. Lett. A*, 267(2-3):188–193, 2000. (Cited on pages 26)

[Bun59] O. Buneman. Dissipation of currents in ionized media. *Phys. Rev.*, 115:503–517, Aug 1959. (Cited on pages 91)

[BW85] D. Biskamp and M. Walter. Suppression of shear damping in drift wave turbulence. *Phys. Lett. A*, 109(1–2):34 – 38, 1985. (Cited on pages 26)

[CBB+97] J. Candy, D. Borba, H. L. Berk, G. T. A. Huysmans, and W. Kerner. Nonlinear interaction of fast particles with Alfvén waves in toroidal plasmas. *Phys. Plasmas*, 4(7):2597–2611, 1997. (Cited on pages 66)

[CCC85] C. Z. Cheng, L. Chen, and M. S. Chance. High-n ideal and resistive shear Alfvén waves in tokamaks. *Annals Phys.*, 161:21–47, April 1985. (Cited on pages 31, 33)

[CD61] J. G. Charney and P. G. Drazin. Propagation of planetary-scale disturbances from the lower into the upper atmosphere. *J. Geophys. Research*, 66:83–109, January 1961. (Cited on pages 17)

[CD92] James A. Crotinger and Thomas H. Dupree. Trapped structures in drift wave turbulence. *Phys. Fluids B*, 4(9):2854–2870, 1992. (Cited on pages 122)

[CD93] J. R. Cary and I. Doxas. An explicit symplectic integration scheme for plasma simulations. *J. Comput. Phys.*, 107(1):98–104, 1993. (Cited on pages 39, 43)

[CDL+10] W. Chen, X.T. Ding, Yi. Liu, Q.W. Yang, X.Q. Ji, M. Isobe, G.L. Yuan, Y.P. Zhang, Y. Zhou, X.Y. Song, Y.B. Dong, W. Li, J. Zhou, G.J. Lei, J.Y. Cao, W. Deng, X.M. Song, X.R. Duan, and HL-2A Team. Features of ion and electron fishbone instabilities on hl-2a. *Nucl. Fusion*, 50(8):084008, 2010. (Cited on pages 51)

[CE77] F. V. Coroniti and A. Eviatar. Magnetic field reconnection in a collisionless plasma. *Astrophys. J. Suppl. Series*, 33:189–210, February 1977. (Cited on pages 91)

[CFLDA09] Giancarlo Consolo, Giovanni Finocchio, Luis Lopez-Diaz, and Bruno Azzerboni. Numerical analysis of the nonlinear excitation of subcritical spin-wave modes within a micromagnetic framework. *IEEE Transactions on Magnetics*, 45(11):5220, 2009. (Cited on pages 30)

[CH93] M. C. Cross and P. C. Hohenberg. Pattern formation outside of equilibrium. *Rev. Mod. Phys.*, 65:851–1112, Jul 1993. (Cited on pages 30)

[Cha99] Hubert Chanson. *The Hydraulics of Open Channel Flow: An Introduction. Physical Modelling of Hydraulics.* Butterworth-Heinemann, 1999. (Cited on pages 22)

[Che92] C. Z. Cheng. Kinetic extensions of magnetohydrodynamics for axisymmetric toroidal plasmas. *Phys. Rep.*, 211:1–51, February 1992. (Cited on pages 66)

[Che07] Shannon Yun-Ming Cheng. *Modeling of Hall thruster lifetime and erosion mechanisms.* PhD thesis, Massachusetts Institute of Technology, 2007. (Cited on pages 3)

[Chi60] Boris V Chirikov. Resonance processes in magnetic traps. *Sov. J. Atom. Energy*, 6(6):464–470, 1960. (Cited on pages 87)

[CHK86] R. Carrera, R. D. Hazeltine, and M. Kotschenreuther. Island bootstrap current modification of the nonlinear dynamics of the tearing mode. *Phys. Fluids*, 29(4):899–902, 1986. (Cited on pages 26)

[CMGGL13] T Cartier-Michaud, P Ghendrih, V Grandgirard, and G Latu. Optimizing the parallel scheme of the poisson solver for the reduced kinetic code teresa*. *ESAIM: Proc.*, 43:274–294, 2013. (Cited on pages 120, 153)

[CMGS+14] T Cartier-Michaud, P Ghendrih, Y Sarazin, G Dif-Pradalier, T Drouot, D Estève, X Garbet, V Grandgirard, G Latu, C Norscini, and C Passeron. Staircase temperature profiles and plasma transport self-organisation in a minimum kinetic model of turbulence based on the trapped ion mode instability. *J. Phys.: Conf. Series*, 561(1):012003, 2014. (Cited on pages 120)

[CN47] J. Crank and P. Nicolson. A practical method for numerical evaluation of solutions of partial differential equations of the heat-conduction type. *Proc. Camb. Phil. Soc.*, 43:50–67, 1947. (Cited on pages 40)

[Col65] Donald Coles. Transition in circular couette flow. *J. Fluid Mech.*, 21(3):385–425, 1965. (Cited on pages 22)

[Cou90] Maurice Couette. *Etudes sur le frottement des liquides.* PhD thesis, Faculté des sciences de Paris, 1890. (Cited on pages 22)

[CZ16] Liu Chen and Fulvio Zonca. Physics of alfvén waves and energetic particles in burning plasmas. *Rev. Mod. Phys.*, 88(1):015008, 2016. (Cited on pages 66)

[DB90] P. H. Diamond and H. Biglari. Theory of dissipative trapped-ion convective-cell turbulence. *Phys. Rev. Lett.*, 65:2865–2868, Dec 1990. (Cited on pages 130)

[DCSJ15] Tommy Dessup, Christophe Coste, and Michel Saint Jean. Subcriticality of the zigzag transition: A nonlinear bifurcation analysis. *Phys. Rev. E*, 91(3):032917, 2015. (Cited on pages 30)

[DD95] O. Dauchot and F. Daviaud. Finite amplitude perturbation and spots growth mechanism in plane couette flow. *Phys. Fluids*, 7(2):335–343, 1995. (Cited on pages 25)

[DGBG00] G Depret, X Garbet, P Bertrand, and A Ghizzo. Trapped-ion driven turbulence in tokamak plasmas. *Plasma Phys. Control. Fusion*, 42(9):949, 2000. (Cited on pages 118, 121, 124, 135, 153)

[DGLW19] AV Dudkovskaia, X Garbet, Maxime Lesur, and HR Wilson. Stability analysis of secondary modes, driven by the phase space island. *Nucl. Fusion*, 59(8):086010, 2019. (Cited on pages 90, 149)

[DGR+14] Thomas Drouot, Etienne Gravier, Thierry Reveille, Alain Ghizzo, Pierre Bertrand, Xavier Garbet, Yanick Sarazin, and Thomas Cartier-Michaud. A gyro-kinetic model for trapped electron and ion modes. *Euro. Phys. J. D*, 68(10):280, 2014. (Cited on pages 120, 121)

[DGR+15] T. Drouot, E. Gravier, T. Reveille, M. Sarrat, M. Collard, P. Bertrand, T. Cartier-Michaud, P. Ghendrih, Y. Sarazin, and X. Garbet. Global gyrokinetic simulations of trapped-electron mode and trapped-ion mode microturbulence. *Phys. Plasmas*, 22(8):082302, 2015. (Cited on pages 121)

[DGS+08] G. Darmet, Ph. Ghendrih, Y. Sarazin, X. Garbet, and V. Grandgirard. Intermittency in flux driven kinetic simulations of trapped ion turbulence. *Commun. Nonlinear Sc. Numerical Simulation*, 13(1):53 – 58, 2008. Vlasovia 2006: The Second International Workshop on the Theory and Applications of the Vlasov Equation. (Cited on pages 118)

[DIC04] Nick Dodd, Vicente Iranzo, and Miquel Caballería. A subcritical instability of wave-driven alongshore currents. *J. Geophys. Research: Oceans*, 109(C2), 2004. (Cited on pages 25)

[DII10] P.H. Diamond, S.I. Itoh, and K. Itoh. *Modern Plasma Physics: Volume 1, Physical Kinetics of Turbulent Plasmas*. Modern Plasma Physics. Cambridge University Press, Cambridge, 2010. (Cited on pages 3, 12, 14, 16, 145, 146)

[DIIH05] P H Diamond, S-I Itoh, K Itoh, and T S Hahm. Zonal flows in plasma—a review. *Plasma Phys. Control. Fusion*, 47(5):R35, 2005. (Cited on pages 30)

[DKL11] P. H. Diamond, Y. Kosuga, and M. Lesur. Dynamics of structures in configuration space and phase space: an introductory tutorial. Aix-en-Provence, 2011. Festival de Théorie. (Cited on pages 16)

[DKL15] P. H. Diamond, Y. Kosuga, and M. Lesur. Dynamics of structures in configuration space and phase space: an introductory tutorial. In *Rotation and Momentum Transport in Magnetized Plasmas*, pages 81–113, Aix-en-Provence, 2015. Festival de Théorie. (Cited on pages 49, 93, 122)

[DP61] WE Drummond and D Pines. Non-linear stability of plasma oscillation. Technical report, General Atomic Div., General Dynamics Corp., San Diego, Calif., 1961. (Cited on pages 3, 11)

[DP97] O. Dauchot and Manneville P. Local versus global concepts in hydrodynamic stability theory. *J. Phys. II France*, 7(2):371–389, 1997. (Cited on pages 19)

[DPDG+10] Guilhem Dif-Pradalier, PH Diamond, Virginie Grandgirard, Yanick Sarazin, J Abiteboul, Xavier Garbet, Ph Ghendrih, A Strugarek, S Ku, and CS Chang. On the validity of the local diffusive paradigm in turbulent plasma transport. *Phys. Rev. E*, 82(2):025401, 2010. (Cited on pages 135)

[DR81] PG Drazin and WH Reid. *Hydrodynamic Stability*. Cambridge University Press, Cambridge, 1981. (Cited on pages 22)

[Dro15] Thomas Drouot. *Study of turbulence associated with trapped particles in fusion plasmas*. PhD thesis, Université de Lorraine (Nancy), 2015. (Cited on pages 128)

[DSC+03] J. F. Drake, M. Swisdak, C. Cattell, M. A. Shay, B. N. Rogers, and A. Zeiler. Formation of electron holes and particle energization during magnetic reconnection. *Science*, 299(5608):873–877, 2003. (Cited on pages 91)

[DST+83] PH Diamond, PL Similon, PW Terry, CW Horton, SM Mahajan, JD Meiss, MN Rosenbluth, K Swartz, T Tajima, RD Hazeltine, and DW Ross. Theory of two-point correlation for trapped electrons and the spectrum of drift wave turbulence. *Plasma Phys. Controlled Fus. Res.*, IAEA-CN-41/D-1-2:259, 1983. (Cited on pages 145)

[Dup66] Thurman Henry Dupree. A perturbation theory for strong plasma turbulence. *Phys. Fluids*, 9(9):1773–1782, 1966. (Cited on pages 14)

[Dup70] T. H. Dupree. Theory of resistivity in collisionless plasma. *Phys. Rev. Lett.*, 25:789–792, Sep 1970. (Cited on pages 91, 93)

[Dup72] Thomas H. Dupree. Theory of phase space density granulation in plasma. *Phys. Fluids*, 15(2):334–344, 1972. (Cited on pages 5, 27, 144, 145, 154)

[Dup78] Thomas H. Dupree. Statistical mechanics of nonequilibrium fluctuations. In *Bull. Am. Phys. Soc.*, volume 23, page 869, 1978. (Cited on pages 27)

[Dup82] Thomas H. Dupree. Theory of phase-space density holes. *Phys. Fluids*, 25(2):277–289, 1982. (Cited on pages 4, 27, 49, 61, 91, 97, 108)

[Dup83] T. H. Dupree. Growth of phase-space density holes. *Phys. Fluids*, 26(9):2460–2481, 1983. (Cited on pages 27, 29, 93, 100)

[Dup86] Thomas H. Dupree. Growth of phase space holes near linear instability. *Phys. Fluids*, 29(6):1813–1819, 1986. (Cited on pages 93)

[DW+28] SJ Davies, CM White, et al. An experimental study of the flow of water in pipes of rectangular section. *Proc. R. Soc. Lond. A*, 119(781):92–107, 1928. (Cited on pages 22)

[DZB95] J. F. Drake, A. Zeiler, and D. Biskamp. Nonlinear self-sustained drift-wave turbulence. *Phys. Rev. Lett.*, 75:4222–4225, Dec 1995. (Cited on pages 26)

[EB02] D. Yu. Eremin and H. L. Berk. Frequency sweeping of phase space structures. *Physics of Plasmas*, 9(3):772–785, 2002. (Cited on pages 47)

[EDB+18] Dominik Ebi, Alexey Denisov, Giacomo Bonciolini, Edouard Boujo, and Nicolas Noiray. Flame dynamics intermittency in the bistable region near a subcritical hopf bifurcation. *Journal of Engineering for Gas Turbines and Power*, 140(6):061504, 2018. (Cited on pages 30)

[ES04] B. Eliasson and P. K. Shukla. Dynamics of electron holes in an electron–oxygen-ion plasma. *Phys. Rev. Lett.*, 93:045001, Jul 2004. (Cited on pages 105)

[ES05] B. Eliasson and P. K. Shukla. Solitary phase-space holes in pair plasmas. *Phys. Rev. E*, 71:046402, Apr 2005. (Cited on pages 105)

[ES06] B. Eliasson and P.K. Shukla. Formation and dynamics of coherent structures involving phase-space vortices in plasmas. *Phys. Rep.*, 422(6):225 – 290, 2006. (Cited on pages 4, 91, 150)

[ESG+18] Damien Estève, Yanick Sarazin, Xavier Garbet, Virginie Grandgirard, S Breton, P Donnel, Y Asahi, C Bourdelle, Guilhem Dif-Pradalier, C Ehrlacher, et al. Self-consistent gyrokinetic modeling of neoclassical and turbulent impurity transport. *Nucl. Fusion*, 58(3):036013, 2018. (Cited on pages 135)

[FA03] A. Fukuyama and T. Akutsu. Kinetic global analysis of Alfvén eigenmodes in toroidal plasmas. In *in Fusion Energy 2002 (Proc. 19th Int. Conf. Lyon, 2002)*, volume TH/P3-14, pages 1–5. Vienna: IAEA, 2003. CD-ROM file TH/P3-14 and http://www.iaea.org/programmes/ripc/physics/fec2002/html/fec2002.htm. (Cited on pages 66)

[FBB+95] A. Fasoli, D. Borba, G. Bosia, D. J. Campbell, J. A. Dobbing, C. Gormezano, J. Jacquinot, P. Lavanchy, J. B. Lister, P. Marmillod, J.-M. Moret, A. Santagiustina, and S. Sharapov. Direct measurement of the damping of toroidicity-induced Alfvén eigenmodes. *Phys. Rev. Lett.*, 75(4):645–648, Jul 1995. (Cited on pages 66)

[FBB+98] A. Fasoli, B. N. Breizman, D. Borba, R. F. Heeter, M. S. Pekker, and S. E. Sharapov. Nonlinear splitting of fast particle driven waves in a plasma: observation and theory. *Phys. Rev. Lett.*, 81:5564–5567, Decembre 1998. (Cited on pages 31, 35)

[FBB+00] A. Fasoli, D. Borba, B. Breizman, C. Gormezano, R. F. Heeter, A. Juan, M. Mantsinen, S. Sharapov, and D. Testa. Fast particles-wave interaction in the Alfvén frequency range on the joint european torus tokamak. *Phys. Plasmas*, 7:1816–1824, May 2000. (Cited on pages 66)

[FBD+06] ED Fredrickson, RE Bell, DS Darrow, GY Fu, NN Gorelenkov, BP LeBlanc, SS Medley, JE Menard, H Park, AL Roquemore, et al. Collective fast ion instability-induced losses in national spherical tokamak experiment. *Phys. Plasmas*, 13(5):056109, 2006. (Cited on pages 32)

[FBG+97] A Fasoli, D Borba, C Gormezano, R Heeter, A Jaun, J Jacquinot, W Kerner, Q King, J B Lister, S Sharapov, D Start, and L Villard. Alfvén eigenmode experiments in tokamaks and stellarators. *Plasma Phys. Control. Fusion*, 39(12B):B287, 1997. (Cited on pages 51)

[FC15] B Friedman and TA Carter. A non-modal analytical method to predict turbulent properties applied to the hasegawa-wakatani model. *Phys. Plasmas*, 22(1):012307, 2015. (Cited on pages 26)

[FE03] Holger Faisst and Bruno Eckhardt. Traveling waves in pipe flow. *Phys. Rev. Lett.*, 91(22):224502, 2003. (Cited on pages 25)

[FH99] BH Fong and TS Hahm. Bounce-averaged kinetic equations and neoclassical polarization density. *Phys. Plasmas*, 6(1):188–199, 1999. (Cited on pages 118, 119)

[Fu08] G. Y. Fu. Energetic-particle-induced geodesic acoustic mode. *Phys. Rev. Lett.*, 101:185002, Oct 2008. (Cited on pages 30)

[GBB05] N.N. Gorelenkov, H.L. Berk, and R.V. Budny. Beam anisotropy effect on alfvén eigenmode stability in iter-like plasmas. *Nucl. Fusion*, 45(4):226, 2005. (Cited on pages 57)

[GBC+00] N.N. Gorelenkov, S. Bernabei, C.Z. Cheng, K.W. Hill, R. Nazikian, S. Kaye, Y. Kusama, G.J. Kramer, K. Shinohara, T. Ozeki, and M.V. Gorelenkova. Stability properties of toroidal Alfvén modes driven by fast particles. *Nucl. Fusion*, 40(7):1311, 2000. (Cited on pages 69)

[GD90] FY Gang and PH Diamond. A nonlinear bounce-kinetic equation for trapped electrons. *Phys. Fluids B*, 2(12):2976–2985, 1990. (Cited on pages 118, 119)

[GDE+16] Xavier Garbet, P Donnel, C Ehrlacher, E Caschera, R Dumont, M Faganello, Virginie Grandgirard, Philippe Ghendrih, M Idouakass, M Lesur, and Y Sarazin. On the relationship between residual zonal flows and bump-on tail saturated instabilities. In *J. Phys.: Conf. Series*, volume 775, page 012004. IOP Publishing, 2016. (Cited on pages 43)

[GDPN+08] X. Garbet, G. Dif-Pradalier, C. Nguyen, P. Angelino, Y. Sarazin, V. Grandgirard, P. Ghendrih, and A. Samain. A minimal collision operator for implementing neoclassical transport in gyrokinetic simulations. In Olivier Sauter, X. Garbet, and Elio Sindoni, editors, *Proceedings of AIP conference on theory of fusion plasmas*, volume 1069, pages 271–276. AIP, Melville, NY, 2008. (Cited on pages 33)

[GDSR09] Alain Ghizzo, Daniele Del Sarto, and Thierry Reveille. Hamiltonian stochastic processes induced by successive wave-particle interactions in stimulated raman scattering. *Phys. Rev. E*, 79(4):046404, 2009. (Cited on pages 5)

[GEHBR81] Mohamed Gad-El-Hak, Ron F. Blackwelderf, and James J. Riley. On the growth of turbulent regions in laminar boundary layers. *J. Fluid Mech.*, 110:73–95, 9 1981. (Cited on pages 24)

[GIB+88] A Ghizzo, B Izrar, P Bertrand, E Fijalkow, MR Feix, and M Shoucri. Stability of bernstein–greene–kruskal plasma equilibria. numerical experiments over a long time. *Phys. Fluids*, 31(1):72–82, 1988. (Cited on pages 88)

[GIVW10] X. Garbet, Y. Idomura, L. Villard, and T.H. Watanabe. Gyrokinetic simulations of turbulent transport. *Nucl. Fusion*, 50(4):043002, 2010. (Cited on pages 120)

[GLG+19] Etienne Gravier, M Lesur, X Garbet, Y Sarazin, J Médina, K Lim, and M Idouakass. Diffusive impurity transport driven by trapped particle turbulence in tokamak plasmas. *Phys. Plasmas*, 26(8):082306, 2019. (Cited on pages 140, 149)

[GLR+17] Etienne Gravier, M Lesur, T Reveille, T Drouot, and J Médina. Transport hysteresis and zonal flow stimulation in magnetized plasmas. *Nucl. Fusion*, 57(12):124001, 2017. (Cited on pages 138, 149)

[GLRD16] Etienne Gravier, Maxime Lesur, Thierry Reveille, and Thomas Drouot. Stimulated zonal flow generation in the case of tem and tim microturbulence. *Phys. Plasmas*, 23(9):092507, 2016. (Cited on pages 137, 149)

[Gro00] Siegfried Grossmann. The onset of shear flow turbulence. *Rev. Mod. Phys.*, 72(2):603, 2000. (Cited on pages 22)

[GS92] N N Gorelenkov and S E Sharapov. On the collisional damping of tae-modes on trapped electrons in tokamaks. *Phys. Scr.*, 45(2):163, 1992. (Cited on pages 66)

[GS95a] R. G. Greaves and C. M. Surko. An electron-positron beam-plasma experiment. *Phys. Rev. Lett.*, 75:3846–3849, Nov 1995. (Cited on pages 105)

[GS95b] Yan Guo and Walter A Strauss. Instability of periodic bgk equilibria. *Commun. Pure App. Math.*, 48(8):861–894, 1995. (Cited on pages 88)

[GS98] Alexander Groisman and Victor Steinberg. Mechanism of elastic instability in couette flow of polymer solutions: experiment. *Phys. Fluids*, 10(10):2451–2463, 1998. (Cited on pages 23)

[GS04] M P Gryaznevich and S E Sharapov. Beta-dependence of energetic particle-driven instabilities in spherical tokamaks. *Plasma Phys. Control. Fusion*, 46(7):S15, 2004. (Cited on pages 51, 69)

[HA87] Dan S. Henningson and P. Henrik Alfredsson. The wave structure of turbulent spots in plane poiseuille flow. *J. Fluid Mech.*, 178:405–421, 5 1987. (Cited on pages 24)

[Haw10] Stephen Hawking. 10 questions for stephen hawking. *Time*, 2010. (Cited on pages 5)

[HB01] K. Hallatschek and D. Biskamp. Transport control by coherent zonal flows in the core/edge transitional regime. *Phys. Rev. Lett.*, 86:1223–1226, Feb 2001. (Cited on pages 74)

[HBP+11] EG Highcock, M Barnes, FI Parra, AA Schekochihin, CM Roach, and SC Cowley. Transport bifurcation induced by sheared toroidal flow in tokamak plasmas. *Phys. Plasmas*, 18(10):102304, 2011. (Cited on pages 26)

[HBS+10] EG Highcock, M Barnes, AA Schekochihin, FI Parra, CM Roach, and SC Cowley. Transport bifurcation in a rotating tokamak plasma. *Phys. Rev. Lett.*, 105(21):215003, 2010. (Cited on pages 26)

[HCH+94] C. T. Hsu, C. Z. Cheng, P. Helander, D. J. Sigmar, and R. White. Particle dynamics in chirped-frequency fluctations. *Phys. Rev. Lett.*, 72:2503–2507, Apr 1994. (Cited on pages 91)

[HCY+18] YM Hou, W Chen, Y Yu, M Lesur, XR Duan, M Xu, MY Ye, et al. Nonlinear wave-particle interaction behaviors driven by energetic ions in the hl-2a tokamak. *Nucl. Fusion*, 58(9):096028, 2018. (Cited on pages 149)

[Hei95] W W Heidbrink. Beam-driven chirping instability in diii-d. *Plasma Phys. Control. Fusion*, 37(9):937–949, 1995. (Cited on pages 32, 60)

[HF14] MJ Hole and Michael Fitzgerald. Resolving the wave–particle–plasma interaction: advances in the diagnosis, interpretation and self-consistent modelling of waves, particles and the plasma configuration. *Plasma Phys. Control. Fusion*, 56(5):053001, 2014. (Cited on pages 66)

[HFS00] R. F. Heeter, A. F. Fasoli, and S. E. Sharapov. Chaotic regime of Alfvén eigenmode wave-particle interaction. *Phys. Rev. Lett.*, 85:3177–3180, October 2000. (Cited on pages 31)

[HLJ93] Dan S Henningson, Anders Lundbladh, and Arne V Johansson. A mechanism for bypass transition from localized disturbances in wall-bounded shear flows. *J. Fluid Mech.*, 250:169–207, 1993. (Cited on pages 25)

[HM78] Akira Hasegawa and Kunioki Mima. Pseudo-three-dimensional turbulence in magnetized nonuniform plasma. *Phys. Fluids*, 21(1):87–92, 1978. (Cited on pages 13)

[HS02] P. Helander and D.J. Sigmar. *Collisional transport in magnetized plasmas.* Press Syndicate of the University of Cambridge, The Pitt Building, Trumpington Street, Cambridge, United Kingdom, 2002. (Cited on pages 34)

[HSC+12] EG Highcock, AA Schekochihin, SC Cowley, M Barnes, FI Parra, CM Roach, and W Dorland. Zero-turbulence manifold in a toroidal plasma. *Phys. Rev. Lett.*, 109(26):265001, 2012. (Cited on pages 26)

[HSPN02] RW Harvey, O Sauter, R Prater, and P Nikkola. Radial transport and electron-cyclotron-current drive in the tcv and diii-d tokamaks. *Physical review letters*, 88(20):205001, 2002. (Cited on pages 135)

[HvDW+04] Björn Hof, Casimir WH van Doorne, Jerry Westerweel, Frans TM Nieuwstadt, Holger Faisst, Bruno Eckhardt, Hakan Wedin, Richard R Kerswell, and Fabian Waleffe. Experimental observation of nonlinear traveling waves in turbulent pipe flow. *Science*, 305(5690):1594–1598, 2004. (Cited on pages 25)

[HW83] Akira Hasegawa and Masahiro Wakatani. Plasma edge turbulence. *Phys. Rev. Lett.*, 50(9):682, 1983. (Cited on pages 13)

[I+04] Blekhman Iliya et al. *Selected topics in vibrational mechanics*, volume 11. World Scientific, 2004. (Cited on pages 30)

[Ich68] Setsuo Ichimaru. Kinetic equations for turbulent plasmas. i. quasilinear theory. *Phys. Rev.*, 174(1):289, 1968. (Cited on pages 8)

[IGD95] MB Isichenko, AV Gruzinov, and PH Diamond. Invariant measure and turbulent pinch in tokamaks. *Phys. Rev. Lett.*, 74(22):4436, 1995. (Cited on pages 135)

[IGL+18] M Idouakass, Etienne Gravier, M Lesur, J Médina, T Réveillé, T Drouot, X Garbet, and Y Sarazin. Impurity density gradient influence on trapped particle modes. *Phys. Plasmas*, 25(6):062307, 2018. (Cited on pages 139, 149)

[IHI+05] K. Itoh, K. Hallatschek, S.-I. Itoh, P. H. Diamond, and S. Toda. Coherent structure of zonal flow and onset of turbulent transport. *Phys. Plasmas*, 12(6):062303, 2005. (Cited on pages 74, 85)

[IIF92] K. Itoh, S.-I. Itoh, and A. Fukuyama. Theory of anomalous transport in high-aspect-ratio toroidal helical plasmas. *Phys. Rev. Lett.*, 69:1050–1053, Aug 1992. (Cited on pages 26)

[III+15] Shigeru Inagaki, Kimitaka Itoh, Sanae-I Itoh, Yusuke Kosuga, Maxime Lesur, and Naohiro Kasuya. Test of the telegraph equation for transport dynamics in plasma. *Plasma Fusion Res.*, 10:1203002–1203002, 2015. (Cited on pages 149)

[IIK+16] K Itoh, S-I Itoh, Y Kosuga, M Lesur, and T Ido. Onset condition of the subcritical geodesic acoustic mode instability in the presence of energetic-particle-driven geodesic acoustic mode. *Plasma Phys. Rep.*, 42(5):418–423, 2016. (Cited on pages 30, 77, 78, 85, 149)

[IIL+17] T Ido, K Itoh, M Lesur, M Osakabe, A Shimizu, K Ogawa, M Nishiura, I Yamada, R Yasuhara, Yusuke Kosuga, et al. Observation of subcritical geodesic acoustic mode excitation in the large helical device. *Nucl. Fusion*, 57(7):072009, 2017. (Cited on pages 149)

[IIO+16] T. Ido, K. Itoh, M. Osakabe, M. Lesur, A. Shimizu, K. Ogawa, K. Toi, M. Nishiura, S. Kato, M. Sasaki, K. Ida, S. Inagaki, and S.-I. Itoh. Strong destabilization of stable modes with a half-frequency associated with chirping geodesic acoustic modes in the large helical device. *Phys. Rev. Lett.*, 116:015002, Jan 2016. (Cited on pages 30, 73, 74, 75, 81, 82, 83, 86, 149, 152)

[IIYF96] Kimitaka Itoh, Sanae I. Itoh, Masatoshi Yagi, and Atsushi Fukuyama. Subcritical excitation of plasma turbulence. *J. Physical Soc. Japan*, 65(9):2749–2752, 1996. (Cited on pages 26)

[IKK+16] S Inagaki, T Kobayashi, Yusuke Kosuga, S-I Itoh, T Mitsuzono, Yoshihiko Nagashima, H Arakawa, Takuma Yamada, Y Miwa, Naohiro Kasuya, et al. A concept of cross-ferroic plasma turbulence. *Scientific Rep.*, 6:22189, 2016. (Cited on pages 149)

[IMK+14] Shigeru Inagaki, Yudai Miwa, Tatsuya Kobayashi, Takuma Yamada, Yoshihiko Nagashima, Tomohiro Mitsuzono, Hiromitsu Fujino, Makoto Sasaki, Naohiro Kasuya, Maxime Lesur, et al. Identification of quasi-periodic nonlinear waveforms in turbulent plasmas. *Plasma Fusion Res.*, 9:1201016–1201016, 2014. (Cited on pages 149)

[IOS+15] T. Ido, M. Osakabe, A. Shimizu, T. Watari, M. Nishiura, K. Toi, K. Ogawa, K. Itoh, I. Yamada, R. Yasuhara, Y. Yoshimura, S. Kato, and The LHD Experiment Group. Identification of the energetic-particle driven gam in the lhd. *Nucl. Fusion*, 55(8):083024, 2015. (Cited on pages 73, 82, 83)

[IUAT09] Yasuhiro Idomura, H Urano, Nobuyuki Aiba, and S Tokuda. Study of ion turbulent transport and profile formations using global gyrokinetic full-f vlasov simulation. *Nucl. Fusion*, 49(6):065029, 2009. (Cited on pages 135)

[JAD15] Miho Janvier, Guillaume Aulanier, and Pascal Démoulin. From coronal observations to mhd simulations, the building blocks for 3d models of solar flares (invited review). *Solar Phys.*, 290(12):3425–3456, 2015. (Cited on pages 3)

[Jar89] A Jarmén. Toroidal ion temperature gradient driven modes with dissipation and trapped electron effects. *Phys. Scr.*, 40(5):658, 1989. (Cited on pages 121)

[JAVV95] A. Jaun, K. Appert, J. Vaclavik, and L. Villard. Global waves in resistive and hot tokamak plasmas. *Comput. Phys. Commun.*, 92:153–187, Decembre 1995. (Cited on pages 66)

[Jea15] JH Jeans. On the theory of star-streaming and the structure of the universe. *Monthly Notices Roy. Astr. Soc.*, 76:70–84, 1915. (Cited on pages 8)

[JG05] Bryan M Johnson and Charles F Gammie. Linear theory of thin, radially stratified disks. *Astr. J.*, 626(2):978, 2005. (Cited on pages 26)

[KA90] Barbro G. B. Klingmann and P. Henrik Alfredsson. Turbulent spots in plane poiseuille flow — measurements of the velocity field. *Phys. Fluids A*, 2(12):2183–2195, 1990. (Cited on pages 25)

[Kad64] BB Kadomtsev. Voprosy teorii plasmy. *Vol 4 Gosatomizdat, Moscow*, page 188, 1964. (Cited on pages 3)

[Kau72] Allan N Kaufman. Quasilinear diffusion of an axisymmetric toroidal plasma. *Phys. Fluids*, 15(6):1063–1069, 1972. (Cited on pages 119)

[KBS+15] J Kühnen, P Braunshier, M Schwegel, HC Kuhlmann, and B Hof. Subcritical versus supercritical transition to turbulence in curved pipes. *J. Fluid Mech.*, 770, 2015. (Cited on pages 23)

[KD11] Y. Kosuga and P. H. Diamond. On relaxation and transport in gyrokinetic drift wave turbulence with zonal flow. *Phys. Plasmas*, 18(12):122305, 2011. (Cited on pages 91, 106)

[KD12] Yusuke Kosuga and PH Diamond. Drift hole structure and dynamics with turbulence driven flows. *Phys. Plasmas*, 19(7):072307, 2012. (Cited on pages 5, 106)

[KDW+13] Y. Kosuga, P.H. Diamond, L. Wang, Ö.D. Gürcan, and T.S. Hahm. Progress on theoretical issues in modelling turbulent transport. *Nucl. Fusion*, 53(4):043008, 2013. (Cited on pages 106)

[Ken08] Alexander Kendl. Two-dimensional turbulence in magnetized plasmas. *Euro. J. Phys.*, 29(5):911, 2008. (Cited on pages 117)

[KID+14a] Y. Kosuga, S.-I. Itoh, P. H. Diamond, K. Itoh, and M. Lesur. Ion temperature gradient driven turbulence with strong trapped ion resonance. *Phys. Plasmas*, 21(10):102303, 2014. (Cited on pages 27, 145, 149, 154)

[KID+14b] Y. Kosuga, S.-I. Itoh, P. H. Diamond, K. Itoh, and M. Lesur. Relative dispersion of trapped ion granulations in sheared flows. *Plasma Fusion Res.*, 9:3403018, 2014. (Cited on pages 106, 145, 149)

[KID+17] Y Kosuga, S-I Itoh, PH Diamond, K Itoh, and M Lesur. Role of phase space structures in collisionless drift wave turbulence and impact on transport modeling. *Nucl. Fusion*, 57(7):072006, 2017. (Cited on pages 5, 27, 30, 145, 149)

[KIDI13] Y Kosuga, S-I Itoh, P H Diamond, and K Itoh. Conversion of poloidal flows into toroidal flows by phase space structures in trapped ion resonance driven turbulence. *Plasma Phys. Control. Fusion*, 55(12):125001, 2013. (Cited on pages 146)

[KKK+99] Y. Kusama, G. J. Kramer, H. Kimura, M. Saigusa, T. Ozeki, K. Tobita, T. Oikawa, K. Shinohara, T. Kondoh, M. Moriyama, F. V. Tchernychev, M. Nemoto, A. Morioka, M. Iwase, N. Isei, T. Fujita, S. Takeji, M. Kuriyama, R. Nazikian, G. Y. Fu, K. W. Hill, and C. Z. Cheng. Characteristics of Alfvén eigenmodes, burst modes and chirping modes in the Alfvén frequency range driven by negative ion based neutral beam injection in jt-60u. *Nucl. Fusion*, 39:1837–1843, Novembre 1999. (Cited on pages 32, 35, 51, 66, 68)

[KLP+97] T Klinger, A Latten, A Piel, G Bonhomme, Th Pierre, and T Dudok de Wit. Route to drift wave chaos and turbulence in a bounded low-β plasma experiment. *Phys. Rev. Lett.*, 79(20):3913, 1997. (Cited on pages 3)

[Kol41a] Andrey Nikolaevich Kolmogorov. Dissipation of energy in locally isotropic turbulence. In *Akademiia Nauk SSSR Doklady*, volume 32, page 16, 1941. (Cited on pages 17)

[Kol41b] Andrey Nikolaevich Kolmogorov. The local structure of turbulence in incompressible viscous fluid for very large reynolds numbers. *Cr Acad. Sci. URSS*, 30:301–305, 1941. (Cited on pages 3, 17)

[KP71] B.B. Kadomtsev and O.P. Pogutse. Trapped particles in toroidal magnetic systems. *Nucl. Fusion*, 11(1):67, 1971. (Cited on pages 117, 121, 124)

[Kra67] Robert H Kraichnan. Inertial ranges in two-dimensional turbulence. *Phys. Fluids*, 10(7):1417–1423, 1967. (Cited on pages 17)

[Kro15] John A Krommes. A tutorial introduction to the statistical theory of turbulent plasmas, a half-century after kadomtsev's plasma turbulence and the resonance-broadening theory of dupree and weinstock. *J. Plasma Phys.*, 81(6), 2015. (Cited on pages 3, 146)

[Kru88] W. L. Kruer. *The physics of laser plasma interactions.* Reading, MA, Addison-Wesley Publishing Co. (Frontiers in Physics. Volume 73), 1988, 199 p., 1988. (Cited on pages 91)

[KW94] O. T. Kingsbury and R. E. Waltz. Numerical simulation of drift waves and trapped ion modes. *Phys. Plasmas*, 1(7):2319–2328, 1994. (Cited on pages 130)

[KYI+15] Fumiyoshi Kin, Takuma Yamada, Shigeru Inagaki, Hiroyuki Arakawa, Yoshihiko Nagashima, Naohiro Kasuya, Akihide Fujisawa, Kousuke Nakanishi, Hikaru Kono, Takaaki Mizokami, et al. Evaluation of non-linear mode coupling during end-plate biasing experiment in panta. *Plasma Fusion Res.*, 10:3401043–3401043, 2015. (Cited on pages 149)

[Lan46] L. Landau. On the vibrations of the electronic plasma. *J. Phys.*, 10:25–34, 1946. (Cited on pages 8, 10, 30, 32)

[LB67] Donald Lynden-Bell. Statistical mechanics of violent relaxation in stellar systems. *mnras*, 136:101, 1967. (Cited on pages 16)

[LBS09] M. K. Lilley, B. N. Breizman, and S. E. Sharapov. Destabilizing effect of dynamical friction on fast-particle-driven waves in a near-threshold nonlinear regime. *Phys. Rev. Lett.*, 102(19):195003, May 2009. (Cited on pages 34, 41, 51, 55, 57)

[LBS10] M. K. Lilley, B. N. Breizman, and S. E. Sharapov. Effect of dynamical friction on nonlinear energetic particle modes. *Phys. Plasmas*, 17(9):092305, 2010. (Cited on pages 48, 64, 91)

[LCMD+17] Maxime Lesur, Thomas Cartier-Michaud, Thomas Drouot, PH Diamond, Y Kosuga, Thierry Reveille, Etienne Gravier, Xavier Garbet, S-I Itoh, and K Itoh. A simple model for electron dissipation in trapped ion turbulence. *Phys. Plasmas*, 24(1):012511, 2017. (Cited on pages 121, 122, 125, 149, 153)

[LD13] M. Lesur and P. H. Diamond. Nonlinear instabilities driven by coherent phase-space structures. *Phys. Rev. E*, 87:031101, Mar 2013. (Cited on pages 16, 48, 76, 77, 85, 93, 149, 151)

[LDK14a] M Lesur, P H Diamond, and Y Kosuga. Nonlinear current-driven ion-acoustic instability driven by phase-space structures. *Plasma Phys. Control. Fusion*, 56(7):075005, 2014. (Cited on pages 5, 29, 30, 76, 93, 149, 152)

[LDK14b] M. Lesur, P. H. Diamond, and Y. Kosuga. Phase-space jets drive transport and anomalous resistivity. *Phys. Plasmas*, 21(11):–, 2014. (Cited on pages 30, 47, 106, 149, 152)

[LDL+20] M. Lesur, C. Djerroud, K. Lim, E. Gravier, M. Idouakass, J. Moritz, J. Médina, T. Réveillé, T. Drouot, T. Cartier-Michaud, and X. Garbet. Validity limits of the passive treatment of impurities in gyrokinetic tokamak simulations. *Nucl. Fusion*, 60(3):036016, feb 2020. (Cited on pages 139, 149, 153)

[Les11] M. Lesur. *The Berk-Breizman model as a paradigm for energetic particle-driven Alfvén eigenmodes.* PhD thesis, Ecole Polytechnique, France, 2011. (Cited on pages 44, 46)

[Les13] M. Lesur. Effects of collisions on energetic particle-driven chirping bursts. *Phys. Plasmas*, 20(5):055905, 2013. (Cited on pages 149)

[Les16] Maxime Lesur. Method- and scheme-independent entropy production in turbulent kinetic simulations. *Comput. Phys. Commun.*, 200:182 – 189, 2016. (Cited on pages 15, 29, 41, 149)

[LGKP07] P. Lauber, S. Günter, A. Könies, and S.D. Pinches. Ligka: A linear gyrokinetic code for the description of background kinetic and fast particle effects on the mhd stability in tokamaks. *J. Comput. Phys.*, 226(1):447–465, 2007. (Cited on pages 66)

[LGL+20] K. Lim, E. Gravier, M. Lesur, X. Garbet, Y. Sarazin, and J. Médina. Impurity pinch generated by trapped particle driven turbulence. submitted, 2020. (Cited on pages 140, 153)

[LI12] M. Lesur and Y. Idomura. Nonlinear categorization of the energetic-beam-driven instability with drag and diffusion. *Nucl. Fusion*, 52(9):094004, 2012. (Cited on pages 27, 41, 51, 52, 76, 78, 149, 151)

[Lic69] A.J. Lichtenberg. *Phase-space dynamics of particles.* Wiley series in plasma physics. Wiley, 1969. (Cited on pages 33)

[LIG09] M. Lesur, Y. Idomura, and X. Garbet. Fully nonlinear features of the energetic beam-driven instability. *Phys. Plasmas*, 16(9):092305–+, September 2009. (Cited on pages 27, 41, 44, 45, 51, 60, 72, 76, 149, 151)

[LII+16a] M Lesur, K Itoh, T Ido, S-I Itoh, Y Kosuga, M Sasaki, S Inagaki, M Osakabe, K Ogawa, A Shimizu, K Ida, and the LHD experiment group. Nonlinear excitation of subcritical fast ion-driven modes. *Nucl. Fusion*, 56(5):056009, 2016. (Cited on pages 30, 33, 84, 85, 149)

[LII+16b] M. Lesur, K. Itoh, T. Ido, M. Osakabe, K. Ogawa, A. Shimizu, M. Sasaki, K. Ida, S. Inagaki, S.-I. Itoh, and the LHD Experiment Group. Nonlinear excitation of subcritical instabilities in a toroidal plasma. *Phys. Rev. Lett.*, 116:015003, Jan 2016. (Cited on pages 30, 72, 73, 81, 149, 152)

[Lil09] M. K. Lilley. *Resonant interaction of fast particles with Alfvén waves in spherical tokamaks.* PhD thesis, Imperial College, UK, 2009. (Cited on pages 41)

[LIS+10] M. Lesur, Y. Idomura, K. Shinohara, X. Garbet, and the JT-60 Team. Spectroscopic determination of kinetic parameters for frequency sweeping Alfvén eigenmodes. *Phys. Plasmas*, 17(12):122311, 2010. (Cited on pages 27, 34, 47, 51, 55, 57, 58, 62, 66, 149, 151)

[LIT07] M. Lesur, Y. Idomura, and S. Tokuda. Kinetic simulations of electrostatic plasma waves using cubic-interpolated-propagation scheme. *JAEA-Research*, 2006-089:1–29, 2007. (Cited on pages 40)

[LJ91] Anders Lundbladh and Arne V Johansson. Direct simulation of turbulent spots in plane couette flow. *J. Fluid Mech.*, 229:499–516, 1991. (Cited on pages 22)

[LMSS18] Maxime Lesur, Julien Médina, Makoto Sasaki, and Akihiro Shimizu. Subcritical instabilities in neutral fluids and plasmas. *Fluids*, 3(4):89, 2018. (Cited on pages 18)

[LN14] MK Lilley and RM Nyqvist. Formation of phase space holes and clumps. *Phys. Rev. Lett.*, 112(15):155002, 2014. (Cited on pages 88)

[LSC04] TT Lim, TK Sengupta, and M Chattopadhyay. A visual study of vortex-induced subcritical instability on a flat plate laminar boundary layer. *Experiments in Fluids*, 37(1):47–55, 2004. (Cited on pages 25)

[LSS16] Maxime Lesur, Makoto Sasaki, and Akihiro Shimizu. Subcritical instabilities in neutral fluids and plasmas. *J. Plasma Fusion Research*, 92(9), 2016. (Cited on pages 18)

[Man77] W.M. Manheimer. *Introduction to trapped-particle instability in tokamaks. ERDA Critical Review Series.* University of Michigan Library, Jan 1977. (Cited on pages 121)

[Man04] P Manneville. *Instabilités, Chaos et Turbulence.* Editions de l'Ecole Polytechnique, 2004. (Cited on pages 23)

[Man08] Paul Manneville. Understanding the sub-critical transition to turbulence in wall flows. *Pramana*, 70(6):1009–1021, 2008. (Cited on pages 25)

[Man15] Paul Manneville. On the transition to turbulence of wall-bounded flows in general, and plane couette flow in particular. *European J. Mech.-B*, 49:345–362, 2015. (Cited on pages 22)

[Maz65] R. Mazitov. Damping of plasma waves. *J. Applied Mech. Tech. Phys.*, 6:22–25, 1965. 10.1007/BF00914365. (Cited on pages 43)

[MB00] Giovanni Manfredi and Pierre Bertrand. Stability of bernstein–greene–kruskal modes. *Phys. Plasmas*, 7(6):2425–2431, 2000. (Cited on pages 88)

[Mcw84] James C. Mcwilliams. The emergence of isolated coherent vortices in turbulent flow. *J. Fluid Mech.*, 146:21–43, 8 1984. (Cited on pages 16)

[Méd19] Julien Médina. *Transport processes in phase space driven by trapped particle turbulence in tokamak plasmas.* PhD thesis, Université de Lorraine (Nancy), 2019. (Cited on pages 130, 135)

[MGRQR03] L. Meignin, P. Gondret, C. Ruyer-Quil, and M. Rabaud. Subcritical kelvin-helmholtz instability in a hele-shaw cell. *Phys. Rev. Lett.*, 90:234502, Jun 2003. (Cited on pages 23, 24)

[MGS+99] K. G. McClements, M. P. Gryaznevich, S. E. Sharapov, R. J. Akers, L. C. Appel, G. F. Counsell, C. M. Roach, and R. Majeski. Physics of energetic particle-driven instabilities in the start spherical tokamak. *Plasma Phys. Control. Fusion*, 41:661–678, May 1999. (Cited on pages 32)

[MIW+15] S Maeyama, Y Idomura, T-H Watanabe, M Nakata, M Yagi, N Miyato, A Ishizawa, and M Nunami. Cross-scale interactions between electron and ion scale turbulence in a tokamak plasma. *Phys. Rev. Lett.*, 114(25):255002, 2015. (Cited on pages 6)

[MKS+13] Yudai Miwa, Naohiro Kasuya, Makoto Sasaki, Shigeru Inagaki, Kimitaka Itoh, Masatoshi Yagi, Akihide Fujisawa, Yoshihiko Nagashima, Maxime Lesur, Tatsuya Kobayashi, et al. Evaluation of excitation conditions of itg modes in the panta. *Plasma Fusion Res.*, 8:2403133–2403133, 2013. (Cited on pages 149)

[MLF+19] J Moritz, M Lesur, E Faudot, S Devaux, S Heuraux, and J Ledig. The plasma-wall transition with collisions and an oblique magnetic field: Reversal of potential drops at grazing incidences. *Phys. Plasmas*, 26(1):013507, 2019. (Cited on pages 147, 155)

[MLG+18] Julien Médina, M Lesur, Etienne Gravier, Thierry Reveille, M Idouakass, T Drouot, Pierre Bertrand, T Cartier-Michaud, X Garbet, and PH Diamond. Radial density and heat fluxes description in the velocity space: Nonlinear simulations and quasi-linear calculations. *Phys. Plasmas*, 25(12):122304, 2018. (Cited on pages 130, 149, 153)

[MLG+19] J Médina, M Lesur, Etienne Gravier, T Réveillé, and P Bertrand. Test particle dynamics in low-frequency tokamak turbulence. *Phys. Plasmas*, 26(10):102301, 2019. (Cited on pages 135, 149, 153)

[MM92] R. R. Mett and S. M. Mahajan. Kinetic theory of toroidicity-induced Alfvén eigenmodes. *Phys. Fluids B*, 4(9):2885–2893, 1992. (Cited on pages 35, 66)

[MP94] H.E. Mynick and N. Pomohrey. Frequency sweeping: a new technique for energy-selective transport. *Nucl. Fusion*, 34(9):1277, 1994. (Cited on pages 91)

[MPT18] Ben F McMillan, Chris CT Pringle, and Bogdan Teaca. Simple advecting structures and the edge of chaos in subcritical tokamak plasmas. *arXiv preprint arXiv:1802.08519*, 2018. (Cited on pages 26)

[MQBH20] Hooman Hezaveh Hesar Maskan, Zhisong Qu, Boris N Breizman, and Matthew J Hole. Long range frequency chirping of alfvén eigenmodes. *Nuclear Fusion*, 2020. (Cited on pages 35)

[MR56] J.M. Manley and H.E. Rowe. Some general properties of nonlinear elements-part i. general energy relations. *Proceedings of the IRE*, 44(7):904–913, July 1956. (Cited on pages 73)

[MRC+03] JH Misguich, J-D Reuss, D Constantinescu, G Steinbrecher, M Vlad, F Spineanu, B Weyssow, and R Balescu. Noble internal transport barriers and radial subdiffusion of toroidal magnetic lines. *Ann. Phys. Fr*, 28(6), 2003. (Cited on pages 135)

[MSS70] S. Q. Mah, H. M. Skarsgard, and A. R. Strilchuk. Current-induced ion heating in a toroidal plasma. *Phys. Rev. Lett.*, 25:1409–1413, Nov 1970. (Cited on pages 91)

[MV11] Clément Mouhot and Cédric Villani. On landau damping. *Acta Mathematica*, 207(1):29–201, 2011. (Cited on pages 14)

[MvS07] Alexander N Morozov and Wim van Saarloos. An introductory essay on subcritical instabilities and the transition to turbulence in visco-elastic parallel shear flows. *Phys. Rev.*, 447(3-6):112–143, 2007. (Cited on pages 23)

[NFA+08] R. Nazikian, G. Y. Fu, M. E. Austin, H. L. Berk, R. V. Budny, N. N. Gorelenkov, W. W. Heidbrink, C. T. Holcomb, G. J. Kramer, G. R. McKee, M. A. Makowski, W. M. Solomon, M. Shafer, E. J. Strait, and M. A. Van Zeeland. Intense geodesic acousticlike modes driven by suprathermal ions in a tokamak plasma. *Phys. Rev. Lett.*, 101:185001, Oct 2008. (Cited on pages 51)

[NGG+10] C Nguyen, X Garbet, V Grandgirard, J Decker, Z Guimarães-Filho, M Lesur, H Lütjens, A Merle, and R Sabot. Nonlinear modification of the stability of fast particle driven modes in tokamaks. *Plasma Phys. Control. Fusion*, 52(12):124034, 2010. (Cited on pages 27, 36, 105, 149)

[NLB12] R.M. Nyqvist, M.K. Lilley, and B.N. Breizman. Adiabatic description of long range frequency sweeping. *Nucl. Fusion*, 52(9):094020, 2012. (Cited on pages 47, 91)

[NLG+10] C. Nguyen, H. Lütjens, X. Garbet, V. Grandgirard, and M. Lesur. Existence of metastable kinetic modes. *Phys. Rev. Lett.*, 105(20):205002, Nov 2010. (Cited on pages 27, 36, 105, 149)

[NTYT01] T. Nakamura, R. Tanaka, T. Yabe, and K. Takizawa. Exactly conservative semi-lagrangian scheme for multi-dimensional hyperbolic equations with directional splitting technique. *J. Comput. Phys.*, 174(1):171–207, 2001. (Cited on pages 40, 41)

[OH03] Wataru Oohara and Rikizo Hatakeyama. Pair-ion plasma generation using fullerenes. *Phys. Rev. Lett.*, 91:205005, Nov 2003. (Cited on pages 105)

[OKWZ16] J Ongena, R Koch, R Wolf, and H Zohm. Magnetic-confinement fusion. *Nat. Phys.*, 12(5):398–410, 2016. (Cited on pages 3)

[OMMK96] Y. Omura, H. Matsumoto, T. Miyake, and H. Kojima. Electron beam instabilities as generation mechanism of electrostatic solitary waves in the magnetotail. *J. Geophys. Research*, 101(A2):2685–2697, 1996. (Cited on pages 92)

[O'N65] T. O'Neil. Collisionless damping of nonlinear plasma oscillations. *Phys. Fluids*, 8:2255–2262, 1965. (Cited on pages 15, 43)

[O'N67] T. M. O'Neil. Nonlinear instability. *Phys. Fluids*, 10(5):1027–1030, 1967. (Cited on pages 27)

[OVNG01] M. M. Oppenheim, G. Vetoulis, D. L. Newman, and M. V. Goldman. Evolution of electron phase-space holes in 3d. *Geophys. Rev. Lett.*, 28(9):1891–1894, 2001. (Cited on pages 92)

[OWM71] T. M. O'Neil, J. H. Winfrey, and J. H. Malmberg. Nonlinear interaction of a small cold beam and a plasma. *Phys. Fluids*, 14(6):1204–1212, 1971. (Cited on pages 43)

[OYT+06] M. Osakabe, S. Yamamoto, K. Toi, Y. Takeiri, S. Sakakibara, K. Nagaoka, K. Tanaka, K. Narihara, and the LHD Experimental Group. Experimental observations of enhanced radial transport of energetic particles with Alfvén eigenmode on the lhd. *Nucl. Fusion*, 46(10):S911, 2006. (Cited on pages 32)

[PAC+98] S. D. Pinches, L. C. Appel, J. Candy, S. E. Sharapov, H. L. Berk, D. Borba, B. N. Breizman, T. C. Hender, K. I. Hopcraft, G. T. A. Huysmans, and W. Kerner. The hagis self-consistent nonlinear wave-particle interaction model. *Comput. Phys. Commun.*, 111:133–149, June 1998. (Cited on pages 66)

[PBF+10] M. Podestà, R. E. Bell, E. D. Fredrickson, N. N. Gorelenkov, B. P. LeBlanc, W. W. Heidbrink, N. A. Crocker, S. Kubota, and H. Yuh. Effects of toroidal rotation shear on toroidicity-induced alfv[e-acute]n eigenmodes in the national spherical torus experiment. *Physics of Plasmas*, 17(12):122501, 2010. (Cited on pages 51)

[PBG+04] S. D. Pinches, H. L. Berk, M. P. Gryaznevich, S. E. Sharapov, and the JET-EFDA Contributors. Spectroscopic determination of the internal amplitude of frequency sweeping tae. *Plasma Phys. Control. Fusion*, 46:S47–S57, July 2004. (Cited on pages 31, 32, 46, 66, 69, 70, 143)

[PCL+15] SD Pinches, IT Chapman, Ph W Lauber, HJC Oliver, SE Sharapov, K Shinohara, and K Tani. Energetic ions in iter plasmas. *Phys. Plasmas*, 22(2):021807, 2015. (Cited on pages 66)

[PMT17] Chris CT Pringle, Ben F McMillan, and Bogdan Teaca. A nonlinear approach to transition in subcritical plasmas with sheared flow. *Phys. Plasmas*, 24(12):122307, 2017. (Cited on pages 26)

[PND+10] Th Pütterich, R Neu, R Dux, AD Whiteford, MG O'Mullane, HP Summers, et al. Calculation and experimental test of the cooling factor of tungsten. *Nucl. Fusion*, 50(2):025012, 2010. (Cited on pages 138)

[Pom86] Y Pomeau. Front motion, metastability and subcritical bifurcations in hydrodynamics. *Physica D*, 23:3, 1986. (Cited on pages 25)

[Pra25] Ludwig Prandtl. Bericht über untersuchungen zur ausgebildeten turbulenz. *J. Applied Math. Mech.*, 5(2):136–139, 1925. (Cited on pages 3)

[PWHF03] P. Petkaki, C. E. J. Watt, R. B. Horne, and M. P. Freeman. Anomalous resistivity in non-maxwellian plasmas. *J. Geophys. Research*, 108(A12):n/a–n/a, 2003. (Cited on pages 92)

[RB67] K. V. Roberts and H. L. Berk. Nonlinear evolution of a two-stream instability. *Phys. Rev. Lett.*, 19:297–300, Aug 1967. (Cited on pages 4, 5, 91, 104, 150)

[RF61] Yu A Romanov and GF Filippov. The interaction of fast electron beams with longitudinal plasma waves. *Sov. Phys. JETP*, 13:87–92, 1961. (Cited on pages 11)

[RR60] Norman Rostoker and MN Rosenbluth. Test particles in a completely ionized plasma. *Phys. Fluids*, 3(1):1–14, 1960. (Cited on pages 9, 14)

[RR78] AB Rechester and MN Rosenbluth. Electron heat transport in a tokamak with destroyed magnetic surfaces. *Phys. Rev. Lett.*, 40(1):38, 1978. (Cited on pages 135)

[Sag66] RZ Sagdeev. Cooperative phenomena and shock waves in collisionless plasmas. *Rev. Plasma Phys.*, 4:23, 1966. (Cited on pages 14)

[Sak72] P. H. Sakanaka. Formation and interaction of ion-acoustic solitary waves in a collisionless warm plasma. *Phys. Fluids*, 15(2):304–310, 1972. (Cited on pages 91)

[SBP+15] BN Sorbom, J Ball, TR Palmer, FJ Mangiarotti, JM Sierchio, P Bonoli, C Kasten, DA Sutherland, HS Barnard, CB Haakonsen, et al. Arc: A compact, high-field, fusion nuclear science facility and demonstration power plant with demountable magnets. *Fusion Engineering and Design*, 100:378–405, 2015. (Cited on pages 6)

[Sch79] H Schamel. Theory of electron holes. *Phys. Scr.*, 20(3-4):336, 1979. (Cited on pages 4, 91, 93, 150)

[Sch86] Hans Schamel. Electron holes, ion holes and double layers: Electrostatic phase space structures in theory and experiment. *Phys. Rep.*, 140(3):161 – 191, 1986. (Cited on pages 14, 27, 91)

[Sch07] Peter J Schmid. Nonmodal stability theory. *Annu. Rev. Fluid Mech.*, 39:129–162, 2007. (Cited on pages 19)

[Sco90] Bruce D. Scott. Self-sustained collisional drift-wave turbulence in a sheared magnetic field. *Phys. Rev. Lett.*, 65:3289–3292, Dec 1990. (Cited on pages 26)

[SdS03] T. K. Sengupta, S. de, and S. Sarkar. Vortex-induced instability of an incompressible wall-bounded shear layer. *Journal of Fluid Mechanics*, 493:277–286, October 2003. (Cited on pages 25)

[SDSGL13] Arthur V Straube, Roel PA Dullens, Lutz Schimansky-Geier, and Ard A Louis. Zigzag transitions and nonequilibrium pattern formation in colloidal chains. *J. Chem. Phys.*, 139(13):134908, 2013. (Cited on pages 30)

[SG69] R.Z. Sagdeev and A.A. Galeev. *Nonlinear plasma theory.* W.A.Benjamin, New York, 1969. (Cited on pages 11, 12)

[SGA+10] Yanick Sarazin, Virginie Grandgirard, Jérémie Abiteboul, S Allfrey, Xavier Garbet, Ph Ghendrih, Guillaume Latu, A Strugarek, and Guilhem Dif-Pradalier. Large scale dynamics in flux driven gyrokinetic turbulence. *Nucl. Fusion*, 50(5):054004, 2010. (Cited on pages 135)

[SGA+11] Y Sarazin, V Grandgirard, J Abiteboul, S Allfrey, X Garbet, Ph Ghendrih, G Latu, A Strugarek, G Dif-Pradalier, PH Diamond, et al. Predictions on heat transport and plasma rotation from global gyrokinetic simulations. *Nucl. Fusion*, 51(10):103023, 2011. (Cited on pages 135)

[SGF+05] Y Sarazin, V Grandgirard, E Fleurence, X Garbet, Ph Ghendrih, P Bertrand, and G Depret. Kinetic features of interchange turbulence. *Plasma Phys. Control. Fusion*, 47(10):1817, 2005. (Cited on pages 118)

[SHC95] D.A. Spong, C.L. Hedrick, and B.A. Carreras. Strategies for modifying alpha driven tae thresholds through q profile and ion temperature control. *Nucl. Fusion*, 35(12):1687, 1995. (Cited on pages 35)

[SHWC92] D. J. Sigmar, C. T. Hsu, R. White, and C. Z. Cheng. Alpha-particle losses from toroidicity-induced Alfvén eigenmodes. part ii: Monte carlo simulations and anomalous alpha-loss processes. *Phys. Fluids B*, 4(6):1506–1516, 1992. (Cited on pages 69)

[SIH+17] Makoto Sasaki, K Itoh, K Hallatschek, Naohiro Kasuya, M Lesur, Yusuke Kosuga, and S-I Itoh. Enhancement and suppression of turbulence by energetic-particle-driven geodesic acoustic modes. *Scientific Rep.*, 7(1):1–7, 2017. (Cited on pages 149)

[SIN+09] M. Sasaki, K. Itoh, Y. Nagashima, A. Ejiri, and Y. Takase. Nonlinear self-interaction of geodesic acoustic modes in toroidal plasmas. *Phys. Plasmas*, 16(2):022306, 2009. (Cited on pages 74)

[SK96] H Schamel and J Korn. Plasma transport in the presence of selfgenerated phasespace structures. *Phys. Scr.*, 1996(T63):63, 1996. (Cited on pages 106)

[SKI+16] Makoto Sasaki, Naohiro Kasuya, K Itoh, K Hallatschek, M Lesur, Yusuke Kosuga, and S-I Itoh. A branch of energetic-particle driven geodesic acoustic modes due to magnetic drift resonance. *Phys. Plasmas*, 23(10):102501, 2016. (Cited on pages 149)

[SKI+17] Makoto Sasaki, Naohiro Kasuya, K Itoh, Yusuke Kosuga, M Lesur, K Hallatschek, and S-I Itoh. Toroidal momentum channeling of geodesic acoustic modes driven by fast ions. *Nucl. Fusion*, 57(3):036025, 2017. (Cited on pages 149)

[SKT+01] K. Shinohara, Y. Kusama, M. Takechi, A. Morioka, M. Ishikawa, N. Oyama, K. Tobita, T. Ozeki, S. Takeji, S. Moriyama, T. Fujita, T. Oikawa, T. Suzuki, T. Nishitani, T. Kondoh, S. Lee, M. Kuriyama, JT-60 Team, G. J. Kramer, N. N. Gorelenkov, R. Nazikian, C. Z. Cheng, G. Y. Fu, and A. Fukuyama. Alfvén eigenmodes driven by Alfvénic beam ions in jt-60u. *Nucl. Fusion*, 41:603–612, May 2001. (Cited on pages 35, 67)

[SLC01] TK Sengupta, TT Lim, and M Chattopadhyay. An experimental and theoretical investigation of a by-pass transition mechanism, iit kanpur report no. iitk/aero. Technical report, AD/2001/02, 2001. (Cited on pages 25)

[SMPR79] K. Saeki, P. Michelsen, H. L. Pécseli, and J. Juul Rasmussen. Formation and coalescence of electron solitary holes. *Phys. Rev. Lett.*, 42:501–504, Feb 1979. (Cited on pages 91)

[STI+02] K. Shinohara, M. Takechi, M. Ishikawa, Y. Kusama, A. Morioka, N. Oyama, K. Tobita, T. Ozeki, the JT-60 Team, N. N. Gorelenkov, C. Z. Cheng, G. J. Kramer, and R. Nazikian. Recent progress of Alfvén eigenmode experiments using N-NB in JT-60U tokamak. *Nucl. Fusion*, 42:942–948, August 2002. (Cited on pages 35, 63, 67)

[Str68] G. Strang. On the construction and comparison of difference schemes. *SIAM J. Numerical Analysis*, 5:506–517, 1968. (Cited on pages 40)

[SVK97] VI Shrira, VV Voronovich, and NG Kozhelupova. Explosive instability of vorticity waves. *J. Phys. Oceanography*, 27(4):542–554, 1997. (Cited on pages 25)

[TA92] Nils Tillmark and P Henrik Alfredsson. Experiments on transition in plane couette flow. *J. Fluid Mech.*, 235:89–102, 1992. (Cited on pages 22)

[TBG06] PW Terry, DA Baver, and Sangeeta Gupta. Role of stable eigenmodes in saturated local plasma turbulence. *Phys. Plasmas*, 13(2):022307, 2006. (Cited on pages 26)

[TDH90] P. W. Terry, P. H. Diamond, and T. S. Hahm. The structure and dynamics of electrostatic and magnetostatic drift holes. *Phys. Fluids B*, 2(9):2048–2063, 1990. (Cited on pages 5, 27, 91, 105, 145, 154)

[TDM87] S. I. Tsunoda, F. Doveil, and J. H. Malmberg. Nonlinear interaction between a warm electron beam and a single wave. *Phys. Rev. Lett.*, 59:2752–2755, Dec 1987. (Cited on pages 32)

[TDS+09] T Tatsuno, W Dorland, AA Schekochihin, GG Plunk, Michael Barnes, SC Cowley, and GG Howes. Nonlinear phase mixing and phase-space cascade of entropy in gyrokinetic plasma turbulence. *Phys. Rev. Lett.*, 103(1):015003, 2009. (Cited on pages 6)

[Tet83] David J. Tetreault. Growth rate of the clump instability. *Phys. Fluids*, 26(11):3247–3261, 1983. (Cited on pages 29)

[TLP77] M. Tagger, G. Laval, and R. Pellat. Trapped ion mode driven by ion magnetic drift resonance in a fat torus. *Nucl. Fusion*, 17(1):109, 1977. (Cited on pages 118, 124)

[TOI+11] K Toi, K Ogawa, M Isobe, M Osakabe, D A Spong, and Y Todo. Energetic-ion-driven global instabilities in stellarator/helical plasmas and comparison with tokamak plasmas. *Plasma Phys. Control. Fusion*, 53(2):024008, 2011. (Cited on pages 51)

[TRC86] W. M. Tang, G. Rewoldt, and Liu Chen. Microinstabilities in weak density gradient tokamak systems. *Phys. Fluids*, 29(11):3715–3718, 1986. (Cited on pages 121)

[TSTI03] Y. Todo, K. Shinohara, M. Takechi, and M. Ishikawa. Computer simulation of frequency sweeping of energetic particle mode in a JT-60U experiment. *J. Plasma Fusion Research*, 79:1107–1108, 2003. (Cited on pages 32)

[TSW+95] Y. Todo, T. Sato, K. Watanabe, T. H. Watanabe, and R. Horiuchi. Magnetohydrodynamic vlasov simulation of the toroidal Alfvén eigenmode. *Phys. Plasmas*, 2(7):2711–2716, 1995. (Cited on pages 66)

[TTRD93] Lloyd N Trefethen, Anne E Trefethen, Satish C Reddy, and Tobin A Driscoll. Hydrodynamic stability without eigenvalues. *Science*, 261(5121):578–584, 1993. (Cited on pages 22)

[TTT+99] M. Takechi, K. Toi, S. Takagi, G. Matsunaga, K. Ohkuni, S. Ohdachi, R. Akiyama, D. S. Darrow, A. Fujisawa, M. Gotoh, H. Idei, H. Iguchi, M. Isobe, T. Kondo, M. Kojima, S. Kubo, S. Lee, T. Minami, S. Morita, K. Matsuoka, S. Nishimura, S. Okamura, M. Osakabe, M. Sasao, M. Shimizu, C. Takahashi, K. Tanaka, and Y. Yoshimura. Energetic-ion-driven toroidal Alfvén eigenmodes observed in a heliotron/torsatron plasma. *Phys. Rev. Lett.*, 83:312–315, July 1999. (Cited on pages 32)

[Van02] R. G. L. Vann. *Characterisation of fully nonlinear Berk-Breizman phenomenology.* PhD thesis, University of Warwick, UK, 2002. (Cited on pages 40)

[VDR+03] R. G. L. Vann, R. O. Dendy, G. Rowlands, T. D. Arber, and N. d'Ambrumenil. Fully nonlinear phenomenology of the berk-breizman augmentation of the vlasov-maxwell system. *Phys. Plasmas*, 10(3):623–630, 2003. (Cited on pages 40, 41, 51)

[Vil14] Cédric Villani. Particle systems and nonlinear landau damping. *Phys. Plasmas*, 21(3):030901, 2014. (Cited on pages 14)

[Vla38] A A Vlasov. On vibration properties of electron gas. *J. Exp. Theor. Phys.*, 8(3):291, 1938. (in Russian). (Cited on pages 8)

[Vla68] A A Vlasov. The vibrational properties of an electron gas. *Sov. Phys. Uspekhi*, 10(6):721–733, jun 1968. (Cited on pages 8)

[VVS61] AA Vedenov, EP Velikhov, and RZ Sagdeev. Nonlinear oscillations of rarified plasma. *Nucl. Fusion*, 1(2):82, 1961. (Cited on pages 3, 11)

[vWHF+17] F van Wyk, EG Highcock, AR Field, CM Roach, AA Schekochihin, FI Parra, and W Dorland. Ion-scale turbulence in mast: anomalous transport, subcritical transitions, and comparison to bes measurements. *Plasma Phys. Control. Fusion*, 59(11):114003, 2017. (Cited on pages 26)

[VWHS+16] F Van Wyk, EG Highcock, AA Schekochihin, CM Roach, AR Field, and W Dorland. Transition to subcritical turbulence in a tokamak plasma. *J. Plasma Phys.*, 82(6), 2016. (Cited on pages 26)

[Wal97] Fabian Waleffe. On a self-sustaining process in shear flows. *Phys. Fluids*, 9(4):883–900, 1997. (Cited on pages 25)

[WB98] H. V. Wong and H. L. Berk. Growth and saturation of toroidal Alfvén eigenmode modes destabilized by ion cyclotron range of frequency produced tails. *Phys. Plasmas*, 5(7):2781–2796, 1998. (Cited on pages 31)

[Wei79] M. A. Weissman. Nonlinear wave packets in the kelvin-helmholtz instability. *Philos. Trans. R. Soc. London A*, 290(1377):639–681, 1979. (Cited on pages 23)

[WHF02] C. E. J. Watt, R. B. Horne, and M. P. Freeman. Ion-acoustic resistivity in plasmas with similar ion and electron temperatures. *Geophys. Rev. Lett.*, 29(1):4–1–4–4, 2002. (Cited on pages 92)

[WHT05] G.-P. Wu, G.-L. Huang, and Y.-H. Tang. The Influence of Ion-Acoustic Turbulence on the Electron Acceleration in the Reconnecting Current Sheet. *Chinese J. of Astr. and Astrophys.*, 5:99–109, February 2005. (Cited on pages 91)

[WK04] Hakan Wedin and Rich R Kerswell. Exact coherent structures in pipe flow: travelling wave solutions. *J. Fluid Mech.*, 508:333–371, 2004. (Cited on pages 25)

[WS06] T.-H. Watanabe and H. Sugama. Velocity–space structures of distribution function in toroidal ion temperature gradient turbulence. *Nucl. Fusion*, 46(1):24, 2006. (Cited on pages 6, 145)

[WT13] Hao Wang and Yasushi Todo. Linear properties of energetic particle driven geodesic acoustic mode. *Phys. Plasmas*, 20(1):012506, 2013. (Cited on pages 74, 85)

[WW05] Fabian Waleffe and Jue Wang. Transition threshold and the self-sustaining process. In *IUTAM Symposium on Laminar-Turbulent Transition and Finite Amplitude Solutions*, pages 85–106. Springer, 2005. (Cited on pages 25)

[XjTL15] Gao Xue-jun, Hans True, and Yong Li. Lateral dynamic features of a railway vehicle. *Proceedings of the Institution of Mechanical Engineers, Part F: Journal of Rail and Rapid Transit*, 230, 02 2015. (Cited on pages 30)

[YII+95] M. Yagi, S.-I. Itoh, K. Itoh, A. Fukuyama, and M. Azumi. Self-sustained plasma turbulence due to current diffusion. *Phys. Plasmas*, 2(11):4140–4148, 1995. (Cited on pages 26)

[YII02a] A. Yoshizawa, S.I. Itoh, and K. Itoh. *Plasma and Fluid Turbulence: Theory and Modelling*. Series in Plasma Physics and Fluid Dynamics. CRC Press, 2002. (Cited on pages 19)

[YII02b] Akira Yoshizawa, Sanae I Itoh, and Kimitaka Itoh. *Plasma and Fluid Turbulence: Theory and Modelling*. CRC Press, 2002. (Cited on pages 3)

[YIK+14] Takuma Yamada, S Inagaki, T Kobayashi, Yoshihiko Nagashima, T Mitsuzono, Y Miwa, K Nakanishi, H Fujino, Makoto Sasaki, Naohiro Kasuya, et al. End plate biasing experiments in linear magnetized plasmas. *Nucl. Fusion*, 54(11):114010, 2014. (Cited on pages 149)

[ZC92] Fulvio Zonca and Liu Chen. Resonant damping of toroidicity-induced shear-Alfvén eigenmodes in tokamaks. *Phys. Rev. Lett.*, 68(5):592–595, Feb 1992. (Cited on pages 66)

[ZCS96] Fulvio Zonca, Liu Chen, and R. A Santoro. Kinetic theory of low-frequency Alfvén modes in tokamaks. *Plasma Phys. Control. Fusion*, 38(11):2011, 1996. (Cited on pages 66)

[ZK62] VE Zakharov and VI Kariman. On the non-linear theory of plasma wave damping. *Zh. éksp. teor. Fiz.*, 43(2):490–499, 1962. (Cited on pages 43)

[ZK63] VE Zakharov and VI Karpman. On the nonlinear theory of the damping of plasma waves. *Sov. J. Experim. Th. Phys.*, 16:351, 1963. (Cited on pages 43)